Design Aspects of High Performance Synchronous Reluctance Machines with and without Permanent Magnets

Ontwerpaspecten van performante synchrone reluctantiemachines met en zonder permanente magneten

Mohamed Nabil Fathy Ibrahim

Promotoren: prof. dr. ir. P. Sergeant, prof. dr. eng. E. Rashad
Proefschrift ingediend tot het behalen van de graad van
Doctor in de ingenieurswetenschappen: werktuigkunde-elektrotechniek

UNIVERSITEIT GENT

Vakgroep Elektrische Energie, Metalen, Mechanische Constructies en Systemen
Voorzitter: prof. dr. ir. L. Dupré
Faculteit Ingenieurswetenschappen en Architectuur
Academiejaar 2017 - 2018

ISBN 978-94-6355-070-3
NUR 950, 959
Wettelijk depot: D/2017/10.500/105

Ghent University
Faculty of Engineering and Architecture (FEA)
Department of of Electrical Energy,
Metals, Mechanical Constructions & Systems (EEMMeCS)
Electrical Energy Laboratory (EELAB)

Design Aspects of High Performance Synchronous Reluctance Machines with and without Permanent Magnets

Ontwerpaspecten van performante synchrone reluctantiemachines met en zonder permanente magneten

Mohamed Nabil Fathy Ibrahim

Dissertation submitted to obtain the academic degree of
Doctor of Electromechanical Engineering

Promotors

Prof. dr. ir. Peter Sergeant (UGent- EEMMeCS)

Prof. dr. eng. Essam Rashad (Tanta university- Egypt)

Examination board

Prof. dr. ir. Daniël De Zutter (Chairman)	Ghent University, Belgium
Prof. dr. ir. Nicola Bianchi	Padova University, Italy
Prof. dr. ir. Guillaume Crevecoeur	Ghent University, Belgium
Prof. dr. ir. Omar Hegazy	Free University of Brussels, Belgium
Prof. dr. ir. Pieter Rombouts	Ghent University, Belgium
Prof. dr. ir. Luc Dupré	Ghent University, Belgium
Prof. dr. ir. Peter Sergeant	Ghent University, Belgium
Prof. dr. eng. Essam Rashad	Tanta University, Egypt

The research presented in this thesis has been funded by the Egyptian Ministry of Higher Education (Cultural Affairs and Missions Sector) and the Special Research Fund (BOF) of Ghent University.

For the pure soul of my grandfathers (Fathy and Hadeia)

For my dear parent (Nabil and Samia)

For my lovely wife (Nahla)

For my lovely kids (Lojain and Osama)

For my brothers and sister (Ahmed, Safwat and Safaa)

Acknowledgment

Without an electric charge, there would not be electricity. Likewise, this PhD thesis would not exist without the help of so many people. This thesis was not a work of one day, but it is a work of more than three years. In this period, I met many friends, colleagues and others. To them, I would like to say…..thank you!

In the first place, I would like to express my sincere thanks and gratitude to my promotor Prof. dr. ir. Peter Sergeant for his continuous support and encouragement during this work and for the countless hours spent on discussions, thinking and proofreading of all my work. Dear Peter, it took me long time to call you Peter. I am very grateful also that you were always very fast to reply to my e-mails. Peter, bedankt voor je geduld gedurende mijn doctoraat en voor de vrijheid waarin ik mocht werken.

I would like to thank my supervisor Prof. dr. eng. Essam Rashad for his support and encouragement through this work. I would never forget the delicious dinner together at my last night at Sydney, Australia, Aug. 2017.

I would like to thank all the members of the examination board: Prof. Daniël De Zutter, Prof. Nicola Bianchi, Prof. Guillaume Crevecoeur, Prof. Omar Hegazy, Prof. Pieter Rombouts and Prof. Luc Dupré for their effort to evaluate my work.

I would like to thank my colleagues at EELAB for the help during my work, in particular dr. Ahmed Abdallh, dr. Ahmed Hemeida, dr. Kristof de koker, dr. Bishal Silwal, dr. Bart Meersman, ir. Dimitar Bozalakov, ir. Joachim Druant, ing. Bert Hannon, ir. Bart Wymeersch, dr. Mohamed Taha, Eng. Mohannad Manti, ir. Marriem and Eng. Abdallah.

In addition, I would like to thank Mrs. Marilyn and Mrs. Ingrid for their essential administrative work and for the nice coffee, and ing. Nic Vermeulen for his continuous help to solve my computer problems.

I would like to offer my special thanks to EELAB technicians Tony, Vincent and Stefaan for helping me a lot during my experimental tests. They replaced between the prototypes several times. Indeed, it was very difficult without their help.

I would like to thank Prof. Ayman S. Abdel-Khalik for the good collaboration.

Moreover, I am very grateful to my colleagues and staff members at Electrical Engineering Department at my home university (Kafrelshiekh University) in Egypt.

In Ghent, I met, enjoyed, talked and worked with several people from several countries. I cannot forget them.

Finally, I would like to thank my family: mom, dad, my brothers and my sister; I have no words to acknowledge their sacrifices not only during this work but also during the whole life. I would like to give my special thanks to my lovely wife (Nahla) and our little kids (Lojain and Osama) for their patience, support and encouragement.

Mohamed Nabil Fathy Ibrahim,

Gent, December 2017

Contents

Summary

Recently, a growing interest in the efficiency and the cost of electrical machines has been observed. The efficiency of electric motors is important because electric motors consume about 40%-45% of the produced electricity worldwide and about 70% of the industrial electricity[1]. Therefore, some types of electric motors have been classified in proposed standard classes[1] based on their efficiency. By consequence, efficient and low cost electric motors are necessary on the market.

Several types of electric motors are used in industrial applications such as permanent magnet synchronous motors (PMSMs), induction motors (IMs) and reluctance motors (RMs). Due to the high cost of PMSMs and due to the rotor losses of the IMs, the RMs can be considered as promising and attractive candidates. Moreover, they have a robust and simple structure, and a low cost as there are no cage, windings and magnets in the rotor. There are two main types of RMs: switched reluctance motors (SRMs) and synchronous reluctance motors (SynRMs). However, there are some disadvantages of these types of machines. On the one hand, the SRMs have problems of torque ripple, vibrations and noise. In addition, their control is more complicated than that of three-phase conventional motor drives, a.o. because of the high non-linearity of the inductance. On the other hand, the SynRMs have a low power factor, so that an inverter with a high Volt-Ampère rating is required to produce a given motor output power. Therefore, adding a proper amount of low cost permanent magnet (PM) material - such as ferrite - may be a good option to boost the power factor. The PMs also increase the efficiency and torque density. These types of motors are

[1]Waide, P. and C. Brunner (2011),"Energy-Efficiency Policy Opportunities for Electric Motor Driven Systems", IEA Energy Papers, No. 2011/07, OECD Publishing, Paris.

called permanent magnet-assisted synchronous reluctance motors (PMaSynRMs).

In this thesis, both SynRMs and PMaSynRMs are investigated. The main focus is given to the rotor design, magnetic material grade and winding configuration. In addition, the modelling and control of SynRMs and PMaSynRMs is also investigated.

First, parametrized models are made of the machines. The finite element method (FEM) is used to obtain the dq-axis flux-linkages $\lambda_d(i_d, i_q, \theta_r)$ and $\lambda_q(i_d, i_q, \theta_r)$ of the SynRM in static 2D simulations, as a function of d-axis current i_d, and q-axis current i_q and rotor position θ_r. As known, the performance (output torque, power factor and efficiency) of SynRMs depends mainly on the ratio between the direct (d) and quadrature (q) axis inductances (L_d/L_q). This ratio is well-known as the saliency ratio of the SynRM. As magnetic saturation causes significant changes in the inductances and by consequence in the saliency ratio during operation, a SynRM model based on constant inductances (L_d and L_q) is not good enough. It can lead to large deviations in the prediction of the torque capability compared with the real motor. How large these deviations are, is clarified in this thesis by comparing several models that do or do not take into account saturation, cross-saturation and rotor position effects. It is found that saturation and cross saturation must be included in the model for an accurate representation of the SynRM performance and control. This means the flux linkages should be function of i_d and i_q. The rotor position needn't be included. Apart from the currents, the FEM contains many parameters for the flux barrier geometry, which have a strong influence on the torque and torque ripple of the machine. Next to static simulations, also dynamic simulations are done. In these simulations, the flux-linkages are stored in lookup tables, created a priori by FEM, to speed up the simulations.

Based on the SynRM FEM model, the design of the SynRM rotor is investigated. Choosing the flux-barrier geometry parameters is very complex because there are many parameters that play a role. Therefore, an optimization technique is always necessary to select the flux-barrier parameters that optimize the SynRM performance indicators (maximize the saliency ratio and output torque and minimize the torque ripple). To gain insight in the relevant parameters, first a sensitivity analysis is done: the influence of the flux-barrier parameters is studied on the SynRM performance indicators. These indicators are again saliency ratio, output torque and torque ripple. In addition, easy-to-use

parametrized equations are proposed to select the value of the two most crucial parameters of the rotor i.e. the flux-barrier angle and width. The proposed equations are compared with three existing literature equations. At the end, an optimal rotor design is obtained based on an optimized technique coupled with FEM. The optimal rotor is checked mechanically for the robustness against mechanical stresses and deformations.

Apart from the geometry, the electric steel grade plays a major role in the losses and efficiency of an electric machine. Therefore, several steel grades are compared with respect to the SynRM performance i.e. output torque, power factor, torque ripple, iron losses and efficiency. Four different steel grades NO20, M330P-50A, M400-50A and M600-100A are considered. The steel grades differ in thickness and in the losses they produce. It was found that the "best" grade NO20 had in the rated operating point of the considered SynRM 9.0% point more efficiency than the "worst" grade M600-100A.

Next to energy-efficiency, a large interest in recent research is dedicated to obtain a high torque density. One of the main techniques to improve the machine torque density is to increase the fundamental winding factor through an innovative winding layout. Among several configurations, the so-called combined star-delta winding layout was proposed in literature several years ago. In the PhD, the combined star-delta winding is compared with the conventional star winding in terms of output torque, torque ripple and efficiency. A simple method to calculate the equivalent winding factor of the different winding connections is proposed. In addition, the modelling of a SynRM with combined star-delta winding is given. Furthermore, the effect of different winding layouts on the performance of the SynRM is presented. To compare both windings experimentally, two stators are made, one with combined star-delta windings and one with conventional star windings, having the same copper volume. Measurements revealed a 5.2% higher output torque of the first machine at rated current and speed.

In order to even further improve the power factor and the output torque of the SynRM, ferrite PMs are inserted in the center of the rotor flux-barriers. The rotor geometry of the resulting PMaSynRM is the same as the conventional SynRM. Hence, two rotors with identical iron lamination stack were built: one with PMs and a second one without magnets. Having the two stators and two rotors, a comparison of four

prototype SynRMs is done in the PhD, each of 5.5 kW. Several validation measurements have been obtained. The combined-star delta SynRM with PMs in the rotor had up to 1.5 % point more efficiency than the SynRM with star winding and rotor without magnets at the rated current and speed.

As an application of SynRM, an efficient and low cost photovoltaic (PV) pumping system employing a SynRM is studied. The proposed system does not have a DC-DC converter that is often used to maximize the PV output power, nor has it storage (battery). Instead, the system is controlled in such a way that both the PV output power is maximized and the SynRM works at the maximum torque per Ampère, using a conventional three phase pulse width modulated inverter. The design and the modelling of all the system components are given. The performance of the proposed PV pumping system is presented, showing the effectiveness of the system.

Samenvatting

De laatste jaren is er een groeiende interesse in het rendement en de kost van elektrische machines. Het rendement van elektrische motoren is belangrijk omdat niet minder dat 40%-50% van de wereldwijd geproduceerde elektriciteit wordt verbruikt door elektrische motoren, en ongeveer 70% van de industriële elektriciteit[1]. Daarom werden sommige types motoren op basis van hun rendement ingedeeld in een aantal standaardklasses[1]. Het hoge rendement en de lage kost van elektrische motoren zijn dan ook belangrijk op de markt.

Verschillende types van elektrische motoren worden gebruikt in industriële toepassingen zoals permanentemagneetbekrachtigde synchrone machines (PMSMs), inductiemotoren (IMs) en reluctantiemotoren (RMs). Door de hoge kost van PMSMs en door de hoge rotorverliezen van inductiemotoren, kunnen reluctantiemotoren beschouwd worden als een veelbelovend en aantrekkelijk alternatief. Bovendien hebben deze machines een robuuste en eenvoudige opbouw en een lage kost. Dit komt doordat er geen rotorkooi, wikkelingen of magneten zijn in de rotor. Er zijn twee types reluctantiemachines: geschakelde reluctantiemachines (SRMs) en synchrone reluctantiemachines (SynRMs). Nochtans hebben deze machines ook een aantal nadelen. Enerzijds hebben geschakelde reluctantiemotoren problemen wat betreft koppelrimpel, trillingen en geluid. Bovendien is hun controle ingewikkelder dan deze van conventionele driefasige aandrijvingen, o.a. door de sterk niet-lineaire inductantie. Anderzijds hebben synchrone reluctantiemotoren een lage arbeidsfactor, zodat een invertor met hoog schijnbaar vermogen nodig is om een gegeven

[1]Waide, P. and C. Brunner (2011),"Energy-Efficiency Policy Opportunities for Electric Motor Driven Systems", IEA Energy Papers, No. 2011/07, OECD Publishing, Paris.

motorvermogen te realiseren. Daarom kan het toevoegen van een geschikte hoeveelheid goedkoop permanent-magneetmateriaal - zoals ferriet - een goede oplossing zijn om de arbeidsfactor te verbeteren. De permanente magneten verhogen ook het rendement en de koppeldichtheid. These types motoren worden in de Engelstalige literatuur "permanent magnet-assisted synchronous reluctance motors" (PMaSynRMs) genoemd.

In deze thesis worden zowel SynRMs als PMaSynRMs onderzocht. De focus ligt vooral op het rotorontwerp, het type van magnetisch materiaal en de wikkelconfiguratie. Daarenboven wordt ook het modelleren en de controle van SynRMs en PMaSynRMs onderzocht.

Ten eerste worden geparametrizeerde modellen gemaakt van de machines. De eindige-elementenmethode (EEM) wordt gebruikt om de gekoppelde fluxen $\lambda_d(i_d, i_q, \theta_r)$ en $\lambda_q(i_d, i_q, \theta_r)$ te berekenen langs de *d*- en *q*-as van de SynRM. Dit gebeurt in statische 2D simulaties, als functie van de *d*-as component van de stroom i_d, de *q*-as component van de stroom i_q, en de rotorpositie θ_r. Zoals geweten is de performantie (koppel, arbeidsfactor en rendement) van SynRMs vooral afhankelijk van de verhouding tussen de directe component (*d*) en de kwadratuurcomponent (*q*) van de inductanties (L_d/L_q). Deze verhouding wordt in het Engels de "saliency ratio" van de SynRM genoemd. Omdat magnetische verzadiging aanzienlijke wijzigingen veroorzaakt in de inductanties en dus in deze verhouding gedurende de werking van de machine, is een model van de SynRM op basis van constante inductanties niet goed genoeg. Het kan leiden tot grote afwijkingen in de voorspelling van het koppel, in vergelijking met de echte motor. Hoe groot deze afwijkingen zijn, wordt verduidelijkt in deze thesis door verschillende modellen met elkaar te vergelijken die wel of niet rekening houden met verzadiging, mutuele verzadiging en de rotorpositie. De conclusie is dat verzadiging en mutuele verzadiging in rekening moeten gebracht zijn in het model, om een nauwkeurige voorstelling van de SynRM-performantie en controle te bekomen. Dit betekent dat de inductanties functie worden van i_d en i_q. De rotorpositie echter moet niet in rekening gebracht worden. Naast de stroomparameters bevat het EEM ook vele parameters voor de geometrie van de fluxbarrières, die zeer veel invloed hebben op het koppel en de koppelrimpel van de machine. Behalve statische simulaties werden ook dynamische simulaties gedaan. Om de rekentijd te verlagen wordt hiervoor gebruikt gemaakt van opzoektabellen voor

de gekoppelde flux, die vooraf opgesteld zijn via de EEM.Op basis van het SynRM model wordt het des ign van de SynRM bestudeerd. Het kiezen van de geometrieparameters van de fluxbarrières is zeer complex doordat er vele parameters zijn die een rol spelen. Daarom is altijd een optimalisatietechniek vereist om de optimale parameters van de fluxbarrières te selecteren die de performantie-indicatoren optimaliseren (maximale verhouding L_d/L_q, maximaal koppel en minimale koppelrimpel). Om inzicht te krijgen in de relevante parameters is eerst een sensitiviteitsanalyse gedaan: de invloed van de fluxbarrières op de performantie-indicatoren wordt bekeken. Deze indicatoren zijn opnieuw de verhouding L_d/L_q, koppel en koppelrimpel. Daarenboven worden eenvoudige geparametrizeerde vergelijkingen voorgesteld om de waarde van de meest cruciale parameters van de rotor te kiezen: de hoek en de breedte van de fluxbarrières. De voorgestelde vergelijkingen worden vergeleken met drie bestaande uitdrukkingen in de literatuur. Tenslotte wordt een optimale rotor ontworpen op basis van een optimalisatietechniek in combinatie met de EEM. De optimale rotor is mechanisch gecontroleerd wat betreft robuustheid tegen mechanische spanning en deformaties.

Naast de geometrie speelt ook het magnetisch materiaal een belangrijke rol in de verliezen en het rendement van de machine. Daarom worden verschillende soorten magnetisch blik vergeleken wat betreft de performantie-indicatoren van de SynRM: koppel, arbeidsfactor, koppelrimpel, ijzerverliezen en rendement. Vier soorten staal worden vergeleken: M600-100A, M400-50A, M330P-50A en NO20. De viertypes verschillen in dikte en in verliezen die ze produceren. Het resultaat van de simulaties was dat de "beste" staalsoort NO20 in het nominaal werkingspunt een rendement had dat 9.0% hoger was dan de "slechtste" staalsoort M600-100A.

Bijkomend aan het streven naar energie-efficiëntie van de motor, wordt veel onderzoek gedaan naar het bekomen van hoge koppeldichtheid. Eén van de technieken om de koppeldichtheid te verbeteren is om de fundamentele wikkelfactor te verhogen, via een innovatieve lay-out van de wikkeling. Onder verschillende mogelijke configuraties is de zogenaamde "gecombineerde ster-driehoekwikkeling" reeds vele jaren terug voorgesteld in de literatuur. In het PhD wordt deze wikkeling vergeleken met de conventionele ster-wikkeling. Een eenvoudige methode om de equivalente wikkelfactor te bepalen is eveneens uitgelegd. Daarnaast wordt het effect van

verschillende lay-outs van wikkelingen bestudeerd op de performantie van de SynRM. Om de twee wikkelconfiguaties experimenteel te vergelijken, werden twee statoren gemaakt. De ene heeft een gecombineerde ster-driehoekwikkeling, en de andere heeft een conventionele ster-wikkeling. Uit metingen en simulaties bleek de eerste machine 5.2% meer koppel bij nominale stroom en snelheid.

Om de arbeidsdfactor en het koppel van de SynRM nog verder op te drijven, werden ferrietmagneten toegevoegd in het centrum van de fluxbarrières op de rotor. De rotorgeometrie van de resulterende PMaSynRM is dezelfde als de conventionele SynRM. Bijgevolg werden twee rotoren gebouwd met identieke magnetische lamellen: één met permanente magneten en één zonder magneten. Met deze twee statoren en twee rotoren konden in dit doctoraat vier prototype SynRMs bestudeerd worden, elk van 5.5kW. Verschillende metingen werden uitgevoerd ter validatie van de modellen. De SynRM met gecombineerde ster-driehoekwikkeling en met magneten in de rotor had tot 1.5% punt meer rendement dan de SynRM met conventionele wikkeling en rotor zonder magneten bij nominale stroom en snelheid.

Als een toepassing van de SynRM werd een efficiënt en goedkoop fotovoltaïsch (PV) pompsysteem bestudeerd, dat gebruik maakt van een SynRM. Het voorgestelde systeem heeft geen DC-DC omzetter die vaak gebruikt wordt om de output van het PV systeem te maximaliseren. Het systeem heeft ook geen batterij-opslag, maar het wordt gestuurd op zo een manier dat enerzijds het uitgangsvermogen van de PV-panelen wordt gemaximaliseerd, en dat anderzijds de SynRM werkt in het punt van maximaal koppel per Ampère. Hiervoor wordt een conventionele driefasige invertor gebruikt met pulsbreedtemodulatie. Het ontwerp en de modellering van alle componenten is beschreven in het PhD. Ook de performantie van het voorgestelde PV pompsysteem is gepresenteerd, en de effectiviteit van het systeem is aangetoond.

List of Abbreviations

BDCM	Brushless dc motor/machine
C	Capacitor
d-axis	Direct-axis
DC	Direct current
DTC	Direct torque control
EMF	Electro-motive force
Exp.	Experimental
FEM	Finite element method/model
FOC	Field-oriented control
GO	Grain oriented
IGBT	Insulated-gate bipolar transistor
IM	Induction motor/machine
MMF	Magneto-motive force
MTPA	Maximum torque per Ampère
NdFeB	Neodymium iron boron
NO	Non oriented
PM	Permanent magnet
PMaSynRM	Permanent magnet assisted synchronous reluctance motor/machine

PMSM	Permanent magnet synchronous motor/machine
PV	Photovoltaic
PWM	Pulse width modulation
q-axis	Quadrature-axis
Rel	Reluctance
S	Star connection
Sd	Star-delta connection
Sim.	Simulation
SmCo	Samarium cobalt
SRM	Switched reluctance motor/machine
SoS	Star of slot
SynRM	Synchronous reluctance motor/machine
VSI	Voltage source inverter
2D	Two dimensional space

List of Symbols

B	Magnetic flux density, T.
f	Frequency, Hz.
g	Gravitational constant, 9.81 m/s^2.
G	Solar Irradiation level, W/m^2.
H	Magnetic flux intensity, A/m.
H_p	Total head of the pump, m.
i_{abc}	Three phase stator currents, A.
i_d, i_q	Instantaneous direct (d) and quadrature (q) axis stator current respectively, A.
I_d, I_q	Steady-state direct (d) and quadrature (q) axis stator current respectively, A.
K_p	Proportionality constant of the pump, N.m/(rad/s)^2.
K_w	Winding factor.
L_b	Flux-barrier length of SynRM rotor, m.
L_d, L_q	Direct and quadrature axis inductance of SynRM respectively, H.
L_d/L_q	Saliency ratio.
L_{dd}, L_{qq},	Direct and quadrature axis self inductance of SynRM respectively, H.
L_{dq}, L_{qd},	Direct and quadrature axis mutual inductance of SynRM respectively, H.

N_c	Number of turns per coil.
P	Number of pole pairs.
p	Differential operator (d/dt).
p_b	Flux-barrier position of SynRM rotor, m.
P_{class}	Classic losses, W.
P_{exc}	Excess losses, W.
PF	Power factor.
PF_m	Power factor at the maximum torque.
P_{hyst}	Hysteresis losses, W.
P_{iron}	Iron losses, W.
P_o	Output power of SynRM, W.
P_{PV}	Output power of the PV array, V
q	Number of slots per pole per phase
Q	Flow rate of the pump, m^3/h.
R_s	Stator resistance of the SynRM, Ω.
R_{sm}, R_{pm}	Series and parallel resistance of the PV module, Ω.
T_e	Electromagnetic torque, N.m.
T_l	Load torque, N.m.
T_m	Maximum torque, N.m.
$T_r\%$	Torque ripple, in percent.
v_d, v_q	Instantaneous direct and quadrature component of stator voltage respectively, V.
V_d, V_q	Steady-state direct and quadrature component of stator voltage respectively, V.
V_{dc}	DC bus voltage of the inverter, V.

V_m, I_m	Maximum input voltage and current of the SynRM, V and A respectively.
V_{PV}, I_{PV}	Output voltage and current of the PV array, V and A respectively.
W_b	Flux-barrier width of SynRM rotor, m.
α	Angle between current vector and d-axis, Deg.
δ	Angle between voltage vector and q-axis, Deg.
$\eta\%$	Efficiency, in percent.
θ_b	Flux-barrier angle of SynRM rotor, Deg.
θ_r	Mechanical rotor position, Deg.
λ_d, λ_q	Direct and quadrature axis flux-linkages of the SynRM as a function of i_d, i_q and θ_r resp., V.s.
μ_r	Relative permeability.
ρ_i	Iron density, kg/m^3.
ρ_w	Water density, kg/m^3.
ϕ	Power factor angle, rad.
ψ_d, ψ_q	Direct and quadrature axis flux-linkages of the SynRM as a function of i_d and i_q, averaged with respect to θ_r, V.s.
ω_r, N_r	Mechanical speed of the rotor, rad/s and r/min respectively.

List of scientific publications during my PhD research

1. Articles under review in international SCI journals

Here, the papers under review in international journals are given:

[1] **M. N. Ibrahim**, A. S. Abdelkader, E. M. Rashad and P. Sergeant, "An improved torque density synchronous reluctance machine with combined star-delta winding layout,'' *Under review, IEEE Trans. Energy Convers.*

2. Articles published in international SCI journals

Here, the journal papers published in peer-reviewed international journals are listed:

[1] **M. N. Ibrahim**, E. M. Rashad and P. Sergeant, "Performance comparison of conventional synchronous reluctance machine and PM-assisted type with combined star-delta winding," *Energies* 10 (1500):1-18, Oct. 2017.

[2] **M. N. Ibrahim**, P. Sergeant, E. M. Rashad, "Relevance of including saturation and position dependence in the inductances for accurate dynamic modelling and control of SynRMs," *IEEE Trans. Ind. Appl.* vol. 53, no. 1, pp. 151-160, Jan.-Feb. 2017.

[3] **M. N. Ibrahim**, P. Sergeant, and E. M. Rashad, "Combined star-delta windings to improve synchronous reluctance motor performance," *IEEE Trans. Energy Convers*. vol. 31, no. 4, pp. 1479-1487, Dec. 2016.

[4] **M. N. Ibrahim**, P. Sergeant, and E. M. Rashad, "Simple design approach for low torque ripple and high output torque

synchronous reluctance motors," *Energies 9* (942): 1–14, Nov. 2016.

[5] **M. N. Ibrahim**, P. Sergeant and E. M. Rashad, "Synchronous reluctance motor performance based on different electrical steel grades," *IEEE Trans. Magn.* vol. 51, no. 11, pp. 1-4, Nov. 2015.

[6] A. Salem, A. Abdallh, P. Rasilo, F. De Belie, **M. N. Ibrahim**, L. Dupré, and J. Melkebeek, "The effect of common-mode voltage elimination on the iron loss in machine core laminations of multilevel drives," *IEEE Trans. Magn.*, vol. 51, no. 11, pp. 1-4, Nov. 2015.

3. Publications in the proceeding of international conferences

An overview of conference papers is given here:

[1] **M. N. Ibrahim**, A. S. Abdelkader, E. M. Rashad and P. Sergeant, "Comparison between two combined star-delta configurations on synchronous reluctance motors performance," in proc. *20th International Conference on Electrical Machines and Systems (ICEMS), Sydney,* 2017, pp. 1-7.

[2] **M. N. Ibrahim**, P. Sergeant, and E. M. Rashad, " Design of low cost and efficient photovoltaic pumping system utilizing synchronous reluctance motor" in proc. *International Electric Machines and Drives Conference (IEMDC), Miami, FL,* 2017, pp. 1-7.

[3] **M. N. Ibrahim**, P. Sergeant and E. M. Rashad, "Rotor design with and without permanent magnets and performance evaluation of synchronous reluctance motors," in proc. *19th International Conference on Electrical Machines and Systems (ICEMS), Chiba,* 2016, pp. 1-7.

[4] **M. N. Ibrahim**, P. Sergeant and E. M. Rashad, "Influence of rotor flux-barrier geometry on torque and torque ripple of permanent-magnet-assisted synchronous reluctance motors," in proc. *XXII International Conference on Electrical Machines (ICEM), Lausanne,* 2016, pp. 398-404.

[5] **M. N. Ibrahim**, P. Sergeant and E. M. Rashad, "Performance evaluation of synchronous reluctance motors with and without permanent magnets," in proc. *Young Researchers Symposium, Eindhoven, The Netherlands,* 2016, pp.1-6.

[6] **M. N. Ibrahim**, E. M. Rashad and P. Sergeant, "Transient analysis and stability limits for synchronous reluctance motors considering saturation effects," in proc. *18th International Conference on Electrical Machines and Systems (ICEMS), Pattaya,* 2015, pp. 1812-1816.

[7] **M. N. Ibrahim**, E. M. Rashad and P. Sergeant, "Steady-state analysis and stability of synchronous reluctance motors considering saturation effects," in proc. *10th International Symposium on Diagnostics for Electrical Machines, Power Electronics and Drives (SDEMPED), Guarda,* 2015, pp. 345-350.

Chapter 1
Introduction

1.1 Introduction

This chapter presents an introduction about the synchronous reluctance machines. In addition, the motivation, objectives and outlines of this thesis are given.

1.2 SynRM state of art

Recently, Synchronous Reluctance Motors (SynRMs) have been a subject of interest for many variable speed industrial applications. This is thanks to the following main features [1]–[5]:

- There are no windings, magnets or cages in the rotor. Hence, the rotors of SynRMs are cheaper and lighter than the rotors of induction machines (IMs) and permanent magnet synchronous machines (PMSMs) with the same size.
- The rotor temperature is very low. Consequently, the torque/Ampère ratio is independent of rotor temperature, unlike that of both IMs and PMSMs [1], [2].
- The stators of SynRMs and the inverters to supply them are identical to those of both IMs and PMSMs.
- The control methods of SynRMs are similar to those of IMs. The speed control without encoders (sensorless control) is much easier owing to the anisotropy of the rotor design [6], [7].

However, the power factor of SynRMs is rather poor compared to both IMs and PMSMs, requiring a high inverter rating. On the other hand, the efficiency of SynRMs -e.g. as shown in Fig. 1.1- is much better than that of IMs and is inferior to that of PMSMs of the same power rating [8], [9]. Figure 1.1 shows the measured efficiency of prototype commercial SynRM drive, measured in the framework of the ESMADS[1] project at Ghent University.

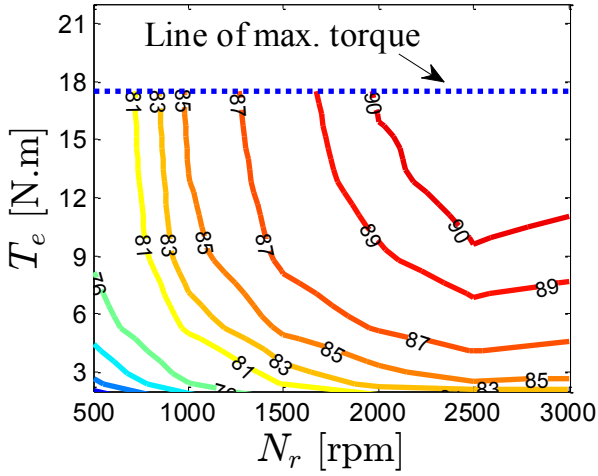

Figure 1.1: Measured efficiency map of the whole drive system using SynRM machine at optimal current angles. SynRM rating is 5.5 kW and 3000 rpm.

The first SynRM is initiated in 1923 by Kostko and is called "salient pole rotor reactions synchronous motor without field coils" [10]. Basically, SynRMs were used as a direct online motor with a cage in the rotor because a pure reluctance machine does not have the self-starting capability. Up to the 1980's, SynRMs were ignored by researchers due to the complex rotor design, poor power factor and low efficiency compared to IMs [2], [11]. Thanks to the advancement in the manufacturing technology and the development in the power semiconductor devices, the SynRM performance has been dramatically

[1] IWT Tetra project nr. 130201, "Efficiëntieverhoging van Snelheidsgeregelde Motor Aangedreven Systemen (ESMADS)"

improved. In addition, by controlling the inverter driven SynRM, there is no longer need to add a cage in the SynRM rotor. In recent SynRMs, an amount of permanent magnets is inserted in the rotor to further improve the torque density and the power factor. This machine is called a permanent magnet assisted SynRM (PMaSynRM) [9], [12].

The SynRM geometry consists of two main parts: stator and rotor. The stator structure is similar to the stator of AC machines. In general, several slots with distributed windings are used as seen in Fig. 1.2.

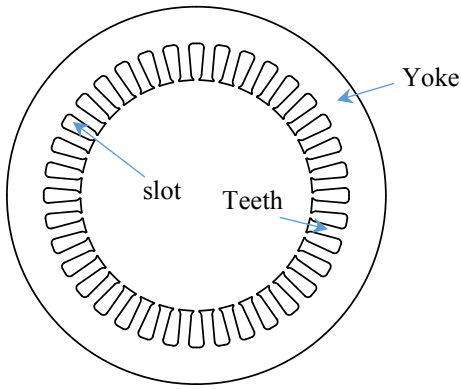

Figure 1.2: SynRM stator.

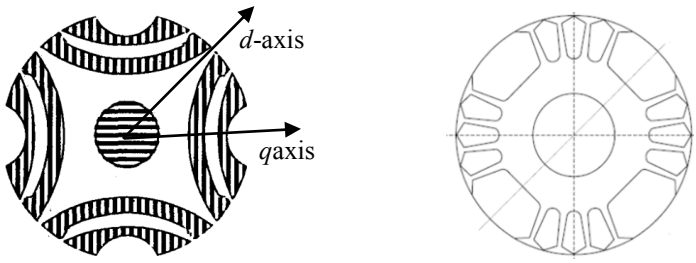

(a) Kostko rotor (b) IM rotor with a few teeth removed

Figure 1.3: First SynRM rotor generation.

The rotor geometry of a SynRM has different shapes [13]. The first rotor geometry was introduced by Kostko in 1923 with segmental iron pieces and flux-barriers as shown in Fig. 1.3-a. The iron is the dark coloured material. In the 1930's, the anisotropic rotor structure was obtained by a typical rotor punching identical to IMs but with cutting

out a few teeth as seen in Fig. 1.3-b [14]. These motors have generally a low power factor and efficiency because the saliency ratio is too small. The saliency ratio is the ratio between two inductances: the inductance measured along the "easy magnetic axis" or *d*-axis, and the inductance measured along the "difficult magnetic axis" or *q*-axis: see Fig. 1.3. It will be shown in **Chapter 2** that the saliency ratio is crucial with respect to the performance and power factor of the SynRM. Consequently, they have a larger size than IMs for similar power ratings.

In the 1960's, a second generation of SynRM rotors was introduced. It utilizes a segmental rotor construction as sketched in Fig. 1.4 [14]. The SynRM of this rotor type was started via a soft starter, not using a cage in the rotor. The saliency ratio of this machine was much better than of the first rotor generation (Fig. 1.3): about five or more. This rotor type enabled the SynRM to fit in the same frame size as their IMs counterpart. However, the efficiency and the power factor are still poor, refraining the widespread use of this machine. In addition, the manufacturing cost was a cumbersome. This is because the rotor laminations were constructed with many small laminations that had to be connected to each other and then bolted on the rotor shaft.

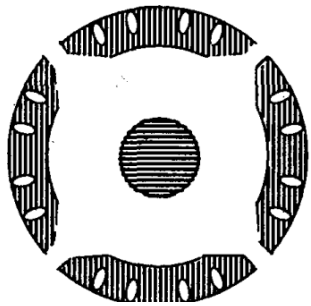

Figure 1.4: Isolated segmented rotor.

In 1970's, a modern rotor geometry was created as shown in Fig. 1.5 [15]. The rotor is constructed of several axially laminated steel sheets of "u" or "v" shape. These sheets are stacked in the radial direction as seen in Fig. 1.5. With this rotor structure, the saliency ratio of the SynRM has been reported to be about seven or more. It is not surprising that this improved the overall performance of SynRM significantly. This enabled the SynRM to be considered as a possible alternative for

the other electric machines on the market. However, the main difficulty with such a rotor is the complexity of the mechanical design, hence the increased manufacturing cost. This issue blocked the mass production of this machine in the 1970's [16].

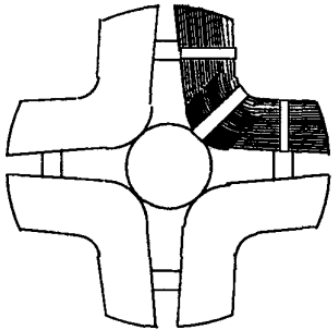

Figure 1.5: Axially laminated rotor.

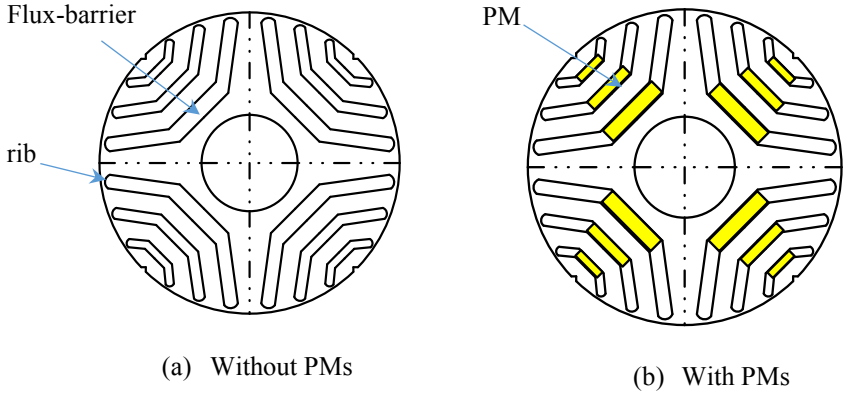

Figure 1.6: Transversally (flux-barrier) laminated rotor.

More recently, around the year 2000, a transversally laminated rotor has been introduced [17], [18], [19]. This rotor has several flux-barriers as shown in Fig. 1.6(a). The lamination of this rotor is similar to that of IMs by traditional punching of wire cutting. This means that the construction and the manufacturing are easy and cheap. However, the saliency ratio of SynRM using the flux-barrier rotor (Fig. 1.6(a)) is lower than using the axially laminated rotor (Fig. 1.5). This is because of more leakage flux in the flux-barrier rotor than in the axially

laminated one. Especially the "ribs" – see Fig 1.6(a) – that mechanically connect the different iron parts of the rotor, are an unwanted path for leakage flux that explains why the output torque and power factor are lower [20]. However, there are several advantages using the flux-barrier rotor, such as easy mass production and suitability for rotor skewing to reduce the torque ripple. In addition, the flux-barrier geometry can be optimized in order to obtain an optimal SynRM performance [21]. This can be done by a proper selection of the flux-barrier and rib dimensions, see Fig. 1.6(a). Moreover, to further increase the SynRM performance (output torque, power factor and efficiency), low flux density and cheap ferrite permanent magnets (PMs) can be inserted in the flux-barriers of the rotor as shown in Fig. 1.6(b) [22]. It is possible to fully or partially fill the flux-barriers with PMs [23], resulting in a so-called PM assisted SynRM. The more PMs are inserted in the flux-barriers, the more improved output torque and power factor are obtained. However, this is again a compromise between the cost and the performance of the machine.

1.3 SynRM principle of operation

In this introduction chapter, we give the intuitive operation principle of a SynRM. The detailed operation and the mathematical model of the SynRM will be given in **Chapter 2**.

Basically, the SynRM stator has three phase sinusoidally distributed windings. The SynRM operation is similar to that of a salient pole synchronous motor without excitation winding in the rotor as shown in Fig. 1.7. The three phase windings create a magneto-motive force (MMF) rotating synchronously with the supply frequency. The electromagnetic torque is then produced by the variations in the inductances due to the rotation of the rotor. The rotor is magnetically asymmetric between the *d*-axis (minimum reluctance) and *q*-axis (maximum reluctance) as sketched in Fig. 1.7. According to the rotating MMF, the rotor moves in such a way that the magnetic reluctance is minimum [24], [25].

In the past, it was necessary to include a cage in the rotor to provide the stating torque of the line-start SynRM [26], [27]. Otherwise, the rotor could not accelerate and synchronize with the rotating field of the supply. In addition, the cage was also necessary to maintain

synchronism of the machine under sudden loads. Recently thanks to the advancement in the power electronics drives, there is no longer need for a cage in the rotor because the motor can work stably under control.

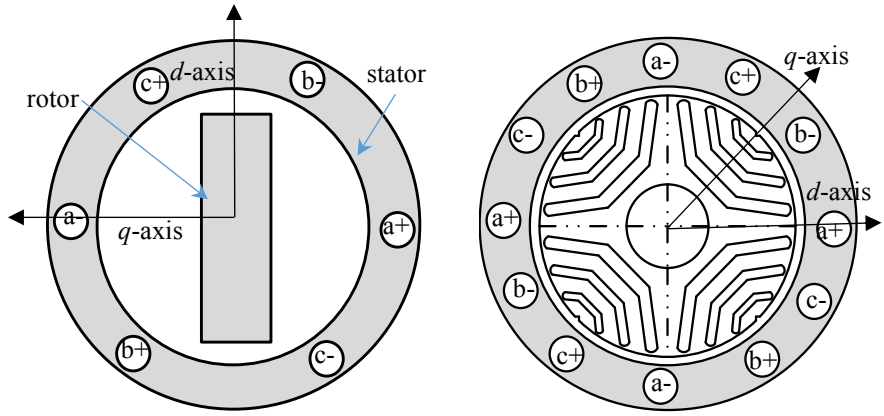

(a) Three phase two pole salient pole synchronous machine.

(b) Three phase four pole SynRM.

Figure 1.7: Synchronous machines.

1.4 Motivation

Recently, a growing interest in the efficiency and the cost of electric machines has been observed. The efficiency of electric motors has been classified based on proposed standard classes as given in [8]. This is caused by the fact that electric motors consume about 40%-45% of the produced electricity and about 70% of the industrial electricity. Therefore, efficient and low cost electric motors are necessary and unavoidable [28].

Several types of motors are used in industrial applications, such as permanent magnet synchronous motors (PMSMs), induction motors (IMs) and reluctance motors (RMs) [29]–[31]. The cost of PMSMs is always high due to the high prices of the rare-earth magnets. Although IMs have a low price, their efficiency is not high as a result of the losses in the rotor. This made RMs to be promising and attractive candidates [32]. There are two main types of RM machines: the switched reluctance machine (SRM) and the synchronous reluctance machine (SynRM). Both have a robust, simple structure and low cost because there are no cage, windings and magnets in the rotor. However, there

are some disadvantages of these types of machines. On the one hand, switched reluctance motors (SRMs) have problems of torque ripple, vibrations and noise. In addition, their control is more complicated than that of a three-phase conventional motor drive, due to the dependency of the current-switching angle on the high non-linearity of the inductance variation [32]. On the other hand, synchronous reluctance motors (SynRMs) have a low power factor, i.e. an inverter with a high Volt-Ampère rating is required to produce a given motor output power. As already mentioned, adding a proper amount of low cost permanent magnets (PMs) to boost the power factor of SynRM may be a good option. The PMs not only enhance the power factor but also increase the efficiency and torque density of the PMaSynRM [22].

This research focuses on the design of SynRMs and PMaSynRMs in order to improve their performance. An accurate mathematical model of the SynRMs is necessary. The models provided in the literature- up to our knowledge- do not investigate the influence of rotor position on the SynRM performance and stability. In addition, the efficiency and torque density of these machines are still addressed for an improvement.

1.5 Objectives

To differ this research among the other scientific contributions on SynRMs and PMaSynRMs, the objectives of this PhD research are summarized as follows:

- The relevance of including magnetic saturation and rotor position effects in the mathematical *dq*-axis model of SynRMs is investigated. Consequently, an accurate model for SynRMs is proposed. In addition, the modelling of SynRMs is studied in both open loop and closed loop controlled methods, considering and neglecting the influence of the magnetic saturation and rotor position effects.
- The influence of flux-barrier parameters on the performance indicators (saliency ratio, output torque and torque ripple) of a SynRM is studied; compared to the literature, this PhD investigates more flux-barrier parameters. In addition, easy-to-use parametrized equations to select appropriate values for the most crucial geometrical parameters of the rotor are proposed.

Moreover, an optimal rotor design is provided and checked both electromagnetically and mechanically.

- A comparison of the SynRM performance based on different electrical steel grades is given.
- Different combined star-delta winding configurations are proposed and compared to the conventional star connection. In addition, a simple mathematical formula is proposed to calculate the equivalent winding factor of the different winding connections. The performance of SynRMs based on the different winding configurations is compared.
- PMaSynRMs and SynRMs using different winding connections are compared. Two different winding configurations in the stator and two different optimal rotor designs are considered. The two windings are the combined star-delta windings and the conventional star windings. The two rotors are one with PMs in the rotor flux-barriers and the second one without PMs. Eventually, four machines are compared.
- Five SynRM prototypes (different windings and rotors with and without PMs) are manufactured and tested in a laboratory setup. A parametrized control algorithm is implemented on the setup in order to test the machine in different loading conditions, for open loop control and closed loop control. Also the influence of several control parameters such as the PI controller parameters and the current angle are investigated experimentally. The efficiency maps of these prototypes are constructed. The experimental results are used to validate the models and the theoretical analysis.
- An application case of PV pumping system using the SynRM is studied. This system does not include the conventional DC-DC converter and the batteries. This results in a low cost and efficient PV pumping system using a SynRM.

1.6 Outline

This thesis is organized in nine chapters.

Chapter 1 gives a brief introduction about SynRMs. The motivations, objectives and outlines of this thesis are provided as well.

In **Chapter 2**, an accurate modelling of the SynRM is presented, showing the influence of the magnetic saturation and rotor position on the SynRM behavior in both open and closed loop controlled methods.

Chapter 3 introduces the design of a SynRM, focusing on the rotor flux-barriers. In addition, an optimal rotor design is provided.

The comparison of a SynRM performance based on different electrical steel grades is given in **Chapter 4**.

Chapter 5 compares the conventional star connection with combined star-delta winding configurations. In addition, the performance of SynRM based on these different winding configurations is addressed.

The influence of adding PMs in the rotor of SynRMs is presented in **Chapter 6**. Furthermore, a complete comparison of SynRMs and PMaSynRMs with different winding connections is given.

Five experimental prototypes are manufactured and tested in **Chapter 7**. Several measurements on the prototypes are performed as well.

Chapter 8 uses one prototype to drive a centrifugal pump in a photovoltaic pumping system, intended for irrigation in rural areas in developing countries. In this chapter, a low cost and efficient PV pumping system is proposed.

Chapter 9 concludes this work and gives some proposals for future research in the topic of SynRMs.

Biography

[1] A. Vagati, M. Pastorelli, G. Francheschini, and S. C. Petrache, "Design of low-torque-ripple synchronous reluctance motors," *IEEE Trans. Ind. Appl.*, vol. 34, no. 4, pp. 758–765, 1998.

[2] A. Vagati, "The synchronous reluctance solution: a new alternative in AC drives," in *Proceedings of IECON'94 - 20th Annual Conference of IEEE Industrial Electronics*, vol. 1, pp. 1–13.

[3] N. Bianchi, E. Fornasiero, and W. Soong, "Selection of PM flux linkage for maximum low-speed torque rating in a PM-assisted

synchronous reluctance machine," *IEEE Trans. Ind. Appl.*, vol. 51, no. 5, pp. 3600–3608, Sep. 2015.

[4] H. Mahmoud and N. Bianchi, "Eccentricity in synchronous reluctance motors-Part I: analytical and finite-element models," *IEEE Trans. Energy Convers.*, vol. 30, no. 2, pp. 745–753, Jun. 2015.

[5] M. Ferrari, N. Bianchi, and E. Fornasiero, "Analysis of rotor saturation in synchronous reluctance and PM-assisted reluctance motors," *IEEE Trans. Ind. Appl.*, vol. 51, no. 1, pp. 169–177, Jan. 2015.

[6] E. Capecchi, P. Guglielmi, M. Pastorelli, and A. Vagati, "Position-sensorless control of the transverse-laminated synchronous reluctance motor," *IEEE Trans. Ind. Appl.*, vol. 37, no. 6, pp. 1768–1776, Nov. 2001.

[7] A. Consoli, F. Russo, G. Scarcella, and A. Testa, "Low- and zero-speed sensorless control of synchronous reluctance motors," *IEEE Trans. Ind. Appl.*, vol. 35, no. 5, pp. 1050–1057, 1999.

[8] A. T. De Almeida, F. J. T. E. Ferreira, and A. Q. Duarte, "Technical and economical considerations on super high-efficiency three phase motors," *IEEE Trans. Ind. Appl.*, vol. 50, no. 2, pp. 1274–1285, Mar. 2014.

[9] S. Morimoto, Shohei O., Y. Inoue, and M. Sanada, "Experimental evaluation of a rare-earth-free PMASynRM with ferrite magnets for automotive applications," *IEEE Trans. Ind. Electron.*, vol. 61, no. 10, pp. 5749–5756, Oct. 2014.

[10] J. K. Kostko, "Polyphase reaction synchronous motors," *J. Am. Inst. Electr. Eng.*, vol. 42, no. 11, pp. 1162–1168, Nov. 1923.

[11] T. A. Lipo, "Synchronous reluctance machines-A viable alternative for AC drives?," *Electr. Mach. Power Syst.*, vol. 19, no. 6, pp. 659–671, Nov. 1991.

[12] M. N. Ibrahim, P. Sergeant, and E. M. Rashad, "Influence of rotor flux-barrier geometry on torque and torque ripple of permanent-magnet-assisted synchronous reluctance motors," in *2016 XXII International Conference on Electrical Machines (ICEM)*, 2016, pp. 398–404.

[13] T. Matsuo and T. A. Lipo, “Rotor design optimization of synchronous reluctance machine,” *IEEE Trans. Energy Convers.*, vol. 9, no. 2, pp. 359–365, Jun. 1994.

[14] P. J. Lawrenson and S. K. Gupta, “Developments in the performance and theory of segmental-rotor reluctance motors,” *Proc. Inst. Electr. Eng.*, vol. 114, no. 5, p. 645, 1967.

[15] A. J. O. Cruickshank, A. F. Anderson, and R. W. Menzies, “Theory and performance of reluctance motors with axially laminated anisotropic rotors,” *Proc. Inst. Electr. Eng.*, vol. 118, no. 7, p. 887, 1971.

[16] N. Bianchi and B. J. Chalmers, “Axially laminated reluctance motor: analytical and finite-element methods for magnetic analysis,” *IEEE Trans. Magn.*, vol. 38, no. 1, pp. 239–245, 2002.

[17] T. J. E. Miller, A. Hutton, C. Cossar, and D. A. Staton, “Design of a synchronous reluctance motor drive,” *IEEE Trans. Ind. Appl.*, vol. 27, no. 4, pp. 741–749, 1991.

[18] T. A. Lipo, “Novel reluctance machine concepts for variable speed drives,” in *[1991 Proceedings] 6th Mediterranean Electrotechnical Conference*, pp. 34–43.

[19] M. N. Ibrahim, P. Sergeant, and E. M. Rashad, “Simple design approach for low torque ripple and high output torque synchronous reluctance motors,” *Energies*, vol. 9, no. 11, p. 942, Nov. 2016.

[20] F. Leonardi, P. J. McCleer, and A. Elantably, “Rotors for synchronous reluctance traction motors: a comparative study,” in *Conference Record of the 1999 IEEE Industry Applications Conference. Thirty-Forth IAS Annual Meeting (Cat. No.99CH36370)*, vol. 2, pp. 835–839.

[21] G. Pellegrino, F. Cupertino, and C. Gerada, “Automatic design of synchronous reluctance motors focusing on barrier shape optimization,” *IEEE Trans. Ind. Appl.*, vol. 51, no. 2, pp. 1465–1474, Mar. 2015.

[22] P. Guglielmi, B. Boazzo, E. Armando, G. Pellegrino, and A. Vagati, “Permanent-magnet minimization in PM-assisted synchronous reluctance motors for wide speed rang,” *IEEE Trans. Ind. Appl.*, vol. 49, no. 1, pp. 31–41, Jan. 2013.

[23] M. N. Ibrahim, P. Sergeant, and E. M. Rashad, “Rotor design with and without permanent magnets and performance evaluation of synchronous reluctance motors,” *ICEMS2016*, pp. 1–7, 2016.

[24] R. Mathur, H. Lee, and R. Menzies, “Theory and operation of reluctance motors with magnetically anisotropic rotors II - synchronous performance,” *IEEE Trans. Power Appar. Syst.*, vol. PAS-91, no. 1, pp. 42–45, Jan. 1972.

[25] R. Menzies, “Theory and operation of reluctance motors with magnetically anisotropic rotors part I analysis,” *IEEE Trans. Power Appar. Syst.*, vol. PAS-91, no. 1, pp. 35–41, Jan. 1972.

[26] M. Nabil, S. M. Allam, and E. M. Rashad, “Modeling and design considerations of a photovoltaic energy source feeding a synchronous reluctance motor suitable for pumping systems,” *Ain Shams Eng. J.*, vol. 3, no. 4, pp. 375–382, Dec. 2012.

[27] M. Nabil, S. M. Allam, and E. M. Rashad, “Performance improvement of a photovoltaic pumping system using a synchronous reluctance motor,” *Electr. Power Components Syst.*, vol. 41, no. 4, pp. 447–464, Feb. 2013.

[28] P. Waide and C. U. Brunner, “Energy-efficiency policy opportunities for electric motor-driven systems,” OECD Publishing, May 2011.

[29] K. Kiyota and A. Chiba, “Design of switched reluctance motor competitive to 60-kW IPMSM in third-generation hybrid electric vehicle,” *IEEE Trans. Ind. Appl.*, vol. 48, no. 6, pp. 2303–2309, Nov. 2012.

[30] T. Wang, P. Zheng, Q. Zhang, and S. Cheng, “Design characteristics of the induction motor used for hybrid electric vehicle,” *IEEE Trans. Magn.*, vol. 41, no. 1, pp. 505–508, Jan. 2005.

[31] L. Dang, N. Bernard, N. Bracikowski, and G. Berthiau, “Design optimization with flux-weakening of High-Speed PMSM for electrical vehicle considering the driving cycle,” *IEEE Trans. Ind. Electron.*, pp. 1–1, 2017.

[32] Z. Yang, F. Shang, I. P. Brown, and M. Krishnamurthy, “Comparative study of interior permanent magnet, induction,

and switched reluctance motor drives for EV and HEV applications," *IEEE Trans. Transp. Electrif.*, vol. 1, no. 3, pp. 245–254, Oct. 2015.

Chapter 2
SynRM Modelling and Control

2.1 Introduction

In literature, several techniques are described for modelling SynRM drives. Modelling the drive requires both an electromagnetic machine model and a control model. Both can be found in literature. After giving an overview of existing techniques, this chapter presents two conventional dynamic models in the *dq*-reference frame: one with an open loop control and one with a closed loop control. The electromagnetic behavior in these two dynamic control models is represented by the L_d and L_q inductances. These inductances are computed by finite element model (FEM) in 2D.

In a SynRM, the inductances depend on saturation, cross saturation and rotor position. Taking these effects into account is expected to make the model more accurate, but also more complicated and more computationally expensive. Therefore, the relevance of including these features in models is investigated in this chapter for an example SynRM. Three models for the L_d and L_q are compared: model 1 takes into account saturation and rotor position effects on the *dq*-axis flux linkages; model 2 considers only influence of saturation; model 3 takes into account none of the aforementioned aspects, and hence uses a constant L_d and L_q. The comparison of the three inductance models is done for both dynamic models: open loop and closed loop.

At the end of the chapter, the SynRM torque capability and power factor of the example SynRM are shown for several speeds up to double

the rated value, considering and neglecting the saturation effect on the inductances (L_d and L_q).

2.2 Overview of the SynRM modelling

The performance (output torque, power factor and efficiency) of synchronous reluctance motors (SynRMs) depends mainly on the ratio between the direct (d) and quadrature (q) axis inductances (L_d/L_q). This ratio is well-known as the saliency ratio of the SynRM [1]. The saliency ratio is affected by the rotor geometry design and the magnetic material grade of the motor core. Therefore, an optimization for the rotor geometrical parameters is always necessary [2]. The dq-axis inductances of SynRMs are not constant values but they depend on the self-axis current (saturation) as well as on the other axis current (cross-saturation). Furthermore, the position of the rotor with respect to the stator has an influence on the value of L_d and L_q due to the variation of the magnetic reluctance with respect to the teeth [3]. The aforementioned aspects of the behavior of the inductances definitely will have an influence on the modelling and hence the whole performance of the machine and control system.

In literature, a lot of papers have investigated the saturation and cross-saturation effects with respect to SynRM modelling. Several models have been suggested to include the effect of the magnetic saturation in SynRM modelling for accurate prediction of the machine performance and control [4]-[10]. For example in [4], a saturation model was proposed, considering a single saturation factor to include the magnetic saturation of the dq-axis inductances of salient pole synchronous machines. In [5], the effect of the magnetic saturation on the control of a SynRM was studied based on a single saturation factor and on measured values. However, [4] and [5] assumed that the dq-axis inductances saturate to the same level at all the operating conditions. In [6], mathematical relations based on experimental measurements were proposed to include the magnetic saturation effect of the dq-axis inductances of the SynRM. However, this model is complex and several mathematical constants have to be obtained. In [7], the impact of cross saturation in SynRMs of the transverse-laminated type is studied with a mixed theoretical and experimental approach, considering assumptions in the measurement data of the dq-axis flux linkages. In [8], the authors obtained L_d as function only of i_d by experimental

measurements, neglecting the cross-saturation effect. In addition, they assumed a constant L_q.

Recently, analytical and finite element (FE) models have been developed to investigate the influence of the magnetic saturation on the electric machines modelling, in particular SynRMs. However, the FE models are much simpler to make and more accurate than the analytical ones. Several analytical models for SynRMs can be found in the literature [9]–[14]. These models differ in accuracy and mathematical complexity. For example in [9], the authors presented an analytical model to study the eccentricity of SynRMs. However, this analytical model assumes current sheets in the stator. This means that the slotting effect is neglected. In addition, the magnetic saturation in both the stator and rotor is neglected. Consequently, the accuracy of that model is not enough for expecting an accurate SynRM performance, in particular for high currents where the saturation effect is huge. Later on in [10], the authors improved the analytical model presented in [9]. They considered the magnetic saturation and the slotting effects. However, the model becomes more complex. The influence of rotor saturation on SynRMs was investigated in [15] using FE models. The paper proved that the level of saturation in the rotor causes a different output torque and power.

A fast model considering the saturation, cross-saturation and the rotor position effects is necessary for an accurate representation of the SynRM performance and control. Such a model will be used for this PhD. It is not analytical but it uses look-up tables based on FEM.

2.3 SynRM dynamic model

In order to eliminate the variation of the SynRM inductances as a function of time, the model of the SynRM is represented by the conventional *dq*-axis transformation in the rotor reference frame. A schematic representation of the *abc* variables (voltage, current and flux-linkage) and *dqo* components is shown in Fig. 2.1 [16].

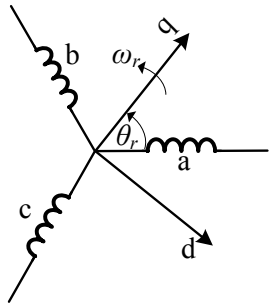

Figure 2.1: A schematic representation of the *abc* variables and *dq* components.

The transformation of *abc* variables to *qdo* components can be obtained by [17]:

$$\begin{bmatrix} Y_q \\ Y_d \\ Y_o \end{bmatrix} = K_s \begin{bmatrix} Y_a \\ Y_b \\ Y_c \end{bmatrix} \tag{2.1}$$

where the variable Y can be the phase voltages, currents and flux linkages. The transformation matrix K_s represents the combined matrices of both Park and Clarke transformations and it is given by [17]:

$$K_s = \frac{2}{3}\begin{bmatrix} \cos(\theta_r) & \cos\left(\theta_r - \frac{2\pi}{3}\right) & \cos\left(\theta_r + \frac{2\pi}{3}\right) \\ \sin(\theta_r) & \sin\left(\theta_r - \frac{2\pi}{3}\right) & \sin\left(\theta_r + \frac{2\pi}{3}\right) \\ \frac{1}{2} & \frac{1}{2} & \frac{1}{2} \end{bmatrix} \tag{2.2}$$

The *dq*-axis voltage equations of a SynRM can be formulated by [7], [18]:

$$\begin{cases} v_d = R_s i_d + p\lambda_d(i_d, i_q, \theta_r) - \omega_r P\lambda_q(i_d, i_q, \theta_r) \\ v_q = R_s i_q + p\lambda_q(i_d, i_q, \theta_r) + \omega_r P\lambda_d(i_d, i_q, \theta_r) \end{cases} \tag{2.3}$$

where λ_d and λ_q are the *dq*-axis flux linkages.

The electromagnetic torque of the SynRM can obtained by:

$$T_e = \frac{3}{2} P \left(\begin{array}{l} (\lambda_d(i_d, i_q, \theta_r) i_q - \lambda_q(i_d, i_q, \theta_r) i_d) + \\ \frac{i_d}{P} \frac{\partial \lambda_d(i_d, i_q, \theta_r)}{\partial \theta_r} + \frac{i_q}{P} \frac{\partial \lambda_q(i_d, i_q, \theta_r)}{\partial \theta_r} \end{array} \right) \tag{2.4}$$

The terms on the second line of (2.4) only occur if the rotor position (θ_r) is taken into account, and their numerical value is small compared to the terms on the first line.

In steady state, the differential operator p in (2.3) is equal to zero, with an averaging with respect to the rotor position θ_r. Therefore, v_d, v_q, i_d, i_q, λ_d, and λ_q become constant values i.e. V_d, V_q, I_d, I_q and ψ_d and ψ_q respectively:

$$\begin{cases} V_d = R_s I_d - \omega_r P \psi_q(I_d, I_q) \\ V_q = R_s I_q + \omega_r P \psi_d(I_d, I_q) \end{cases} \tag{2.5}$$

$$T_e = \frac{3}{2} P(\psi_d(I_d, I_q) I_q - \psi_q(I_d, I_q) I_d) \tag{2.6}$$

The vector diagram of the SynRM is shown in Fig. 2.2 [7], [16], [18].

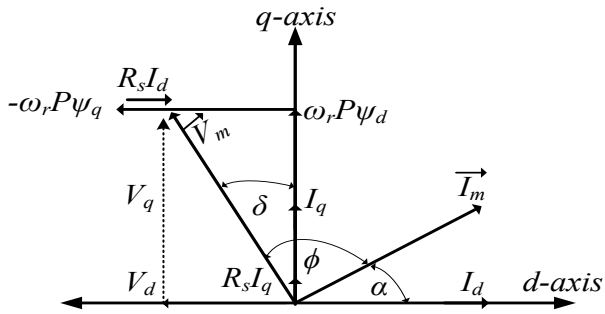

Figure 2.2: Vector diagram of the SynRM in steady state.

From the SynRM vector diagram, the dq-axis voltages and currents can be represented by:

$$\begin{cases} V_d = -V_m \sin(\delta) \\ V_q = V_m \cos(\delta) \end{cases} \tag{2.7}$$

$$\begin{cases} I_d = I_m \cos(\alpha) \\ I_q = I_m \sin(\alpha) \end{cases} \tag{2.8}$$

where δ is the machine load angle and α is the current angle as shown in Fig. 2.2.

The power factor of the SynRM can be expressed by:

$$PF = \cos(\phi) = \frac{V_d \cos(\alpha) + V_q \sin(\alpha)}{\sqrt{{V_d}^2 + {V_q}^2}} \tag{2.9}$$

The torque ripple percentage value of the machine can be computed by:

$$T_r\% = \frac{Max(T_e) - Min(T_e)}{Avg(T_e)} * 100 \tag{2.10}$$

2.4 Finite element model (FEM)

In this thesis, all the electromagnetic analysis is done using FE models in 2D. Although the FEM is a time consuming model for solving the electromagnetic quantities of electric machines, it is accurate and simple. To reduce the time computation of FEM, several possible techniques can be used [19]. For a symmetrical geometry of an electric machine, only a part of the geometry needs to be modeled. The mesh of FEM plays an important role in the accuracy of the solution as well as in the computation time. The number of mesh nodes and elements is a compromise between the accuracy and the computation time. Figure 2.3 shows the mesh of a part of the SynRM geometry: the total number of nodes and elements are 28323 and 56204 respectively. In this thesis, to compute the electromagnetic performance of the SynRM, sinusoidal currents are injected in the stator windings to emulate the current controlled inverter that supplies the SynRM. This means that PWM harmonics are not taken into account. The rotor is rotated at a fixed speed.

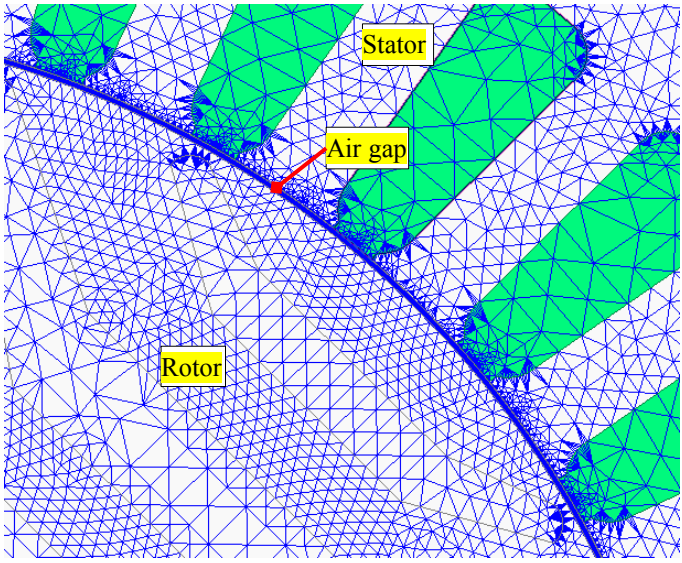

Figure 2.3: Mesh of a part of the SynRM geometry.

2.5 Saturation, cross-saturation and rotor position effects on the flux linkage

A shown in **Section 2.3,** the SynRM model depends mainly on the *dq*-axis flux linkages, which are sensitive to saturation and rotor position. In order to investigate the relevance of the magnetic saturation, cross-saturation and rotor position with respect to the SynRM model and control, at first we study the influence of the magnetic saturation and rotor position on the *dq*-axis flux linkages (λ_d, λ_q). Let us refer to a 3 phase-SynRM having 36 slots and 4 poles with the parameters listed in Table 2.1. The number of turns per slot is 15 with two parallel groups. The FEM presented in **Section 2.4** is used to obtain $\lambda_d(i_d, i_q, \theta_r)$ and $\lambda_q(i_d, i_q, \theta_r)$. Three phase sinusoidal currents are injected in the SynRM windings while the rotor rotates at a fixed speed. Then, i_d and i_q are obtained by the conventional *dq*-axis transformation (2.2) of the three phase currents (i_{abc}). The flux linkage of the phases (λ_{abc}) is computed by FEM and hence the *dq*-axis flux linkages (λ_d, λ_q) are calculated. Thanks to the symmetry of the 4 poles of the machine, modelling of one pole is enough in the FEM. One pole of the SynRM geometry is shown in Fig. 2.4.

Table 2.1: Parameters of the reference SynRM

Parameter	Value	Parameter	Value
Number of rotor flux barriers/ pole	3	Active axial length	140 mm
Number of stator slots/ pole pairs	36/2	Air gap length	0.3 mm
Number of phases	3	Stator /Rotor steel	M400-50A
Stator outer/inner diameter	180/110 mm	Rated frequency	200 Hz
Rotor shaft diameter	35 mm	Rated speed	6000 RPM
Rotor outer diameter	109.4 mm	Rated current	21.21 A
Rated output power	10 kW	Rated voltage	380 V

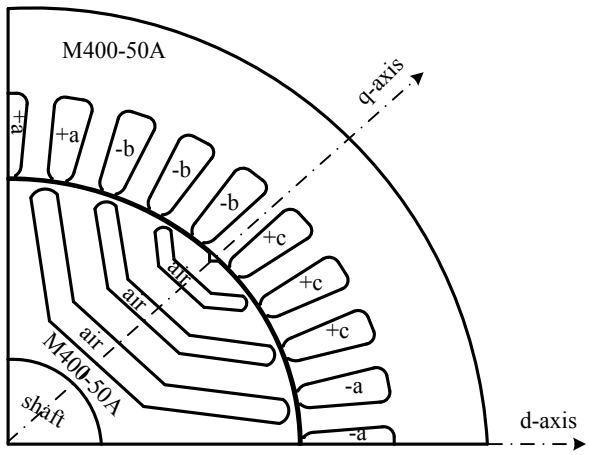

Figure 2.4: One pole of the SynRM geometry.

Figures 2.5 and 2.6 illustrate the variation of the λ_d and λ_q of the SynRM for several rotor positions θ_r at several i_d and i_q at the rated speed (6000 rpm). It is evident that, for a constant current along one axis, the flux linkage of that axis decreases with increasing the current of the other axis. For example, in Fig. 2.5-a, at i_d=10 A, λ_d decreases by about 12% when i_q increases from 0 A to 30 A. The reduction in the

flux linkage as a result of the increase of the other axis current is the well-known cross saturation effect. In fact, the amount of reduction in the flux linkage depends on the value of the currents. This can be seen by comparing e.g Fig. 2.5-a and c. The reduction in λ_d of Fig. 2.5-c is about 3.5% compared to about 12% in Fig. 2.5-a. The effect of the cross saturation is lower at high currents. This is because at higher currents, the machine becomes more saturated. In addition, it is observed that the cross-saturation effect on λ_q (Fig. 2.6) is much stronger than on λ_d (Fig. 2.5). Notice that increasing i_d leads to an impressive reduction in the λ_q of about 35% for low i_q (Fig. 2.6-a) and of about 22% for high i_q (Fig. 2.6-c). This is due to the rather low value of λ_q compared with λ_d (saliency factor equals about 5 at the rated stator current).

An interesting notice here is that the cross saturation does not influence the value of the flux linkage only, but also the value of the ripple of the flux linkage as a function of the rotor position θ_r. The ripples of λ_d and λ_q increase with increasing the currents (i_d, i_q). For instance, in Fig. 2.6-a, at i_q=10 A, the ripple of λ_q is increased from 3.4% to 20% when i_d increases from 0 A to 30 A. The variation of λ_d and λ_q with the rotor position θ_r is due to the magnetic reluctance variation between the rotor (mainly the flux-barriers of the rotor) with respect to the teeth of the stator as reported in Fig. 2.7. For the same current level, the flux density level changes with the rotor position. For small currents, the flux chooses paths of minimum reluctance in the air gap as shown in Fig. 2.7-a and b. For larger currents, these paths are saturated in the same rotor positions, forcing the flux to choose paths with larger reluctance in these rotor positions as seen in Fig. 2.7-c and d. The ripples in λ_d and λ_q will have an effect on the ripple of the SynRM output torque. Hence, it is important to reduce the ripples of the flux-linkage to obtain a low ripple in the output torque of the machine as well as low iron losses. This can be done mainly by optimizing the design of the rotor flux-barrier angle with respect to the stator teeth.

Figure 2.8 shows the *dq*-axis flux linkages ($\psi_d(I_d, I_q)$, $\psi_q(I_d, I_q)$) of the SynRM averaged with respect to the rotor positon θ_r. The nonlinearity of the *dq*-axis flux linkages as function of the currents is clearly visible, mainly for the *d*-axis flux linkage. The effect of the saturation on λ_q is not significant and can be neglected because of the high magnetic reluctance of the *q*-axis. From Figs. 2.5 to 2.8, it is evident that the λ_d and λ_q vary with both i_d, i_q and θ_r. The question is: how accurate should the model of λ_d and λ_q be for accurate prediction

of the SynRM performance and control? The answer to this question will be given further in this chapter.

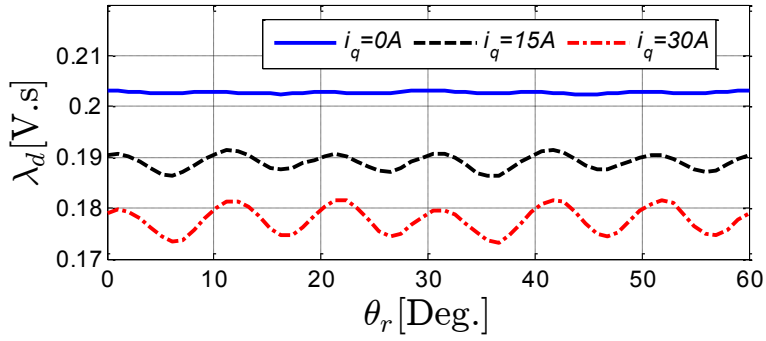

(a) λ_d versus θ_r for constant i_d=10 A and different i_q (0, 15 and 30 A).

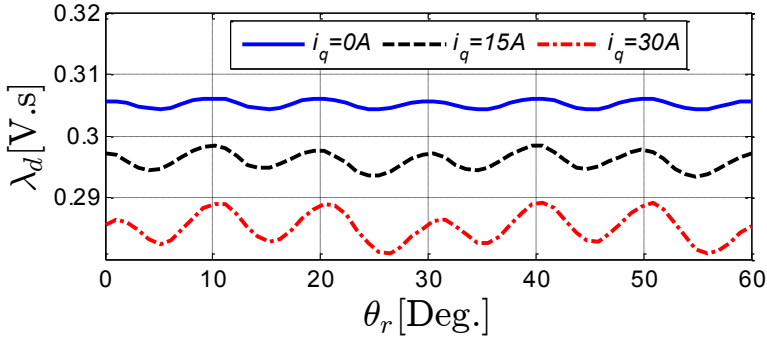

(b) λ_d versus θ_r for constant i_d=20 A and different i_q (0, 15 and 30 A).

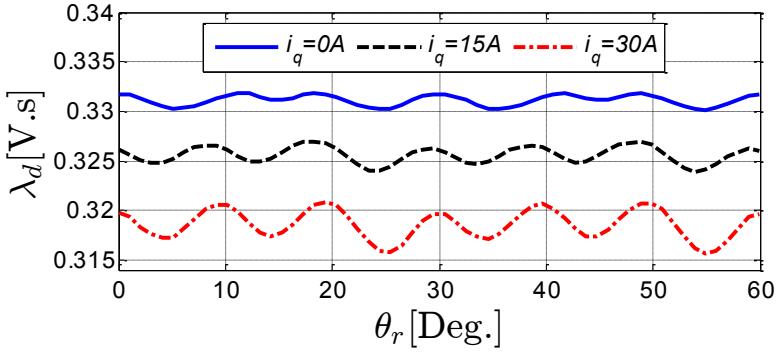

(c) λ_d versus θ_r for constant i_d=30 A and different i_q (0, 15 and 30 A).

Figure 2.5: *d*-axis flux linkage ($\lambda_d(i_d, i_q, \theta_r)$) for the SynRM at rated speed (6000 rpm) using FEM.

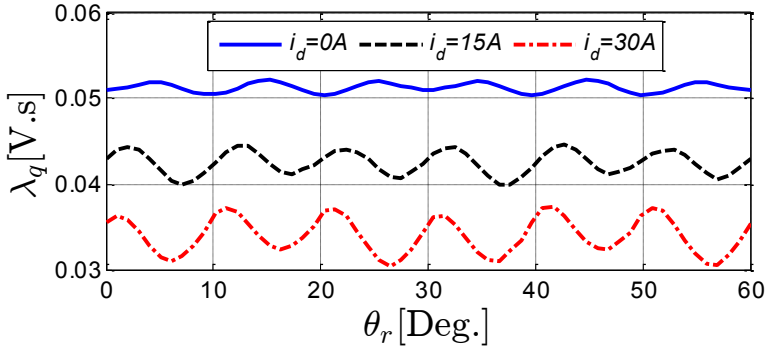

(a) λ_q versus θ_r for constant i_q=10 A and different i_d (0, 15 and 30 A).

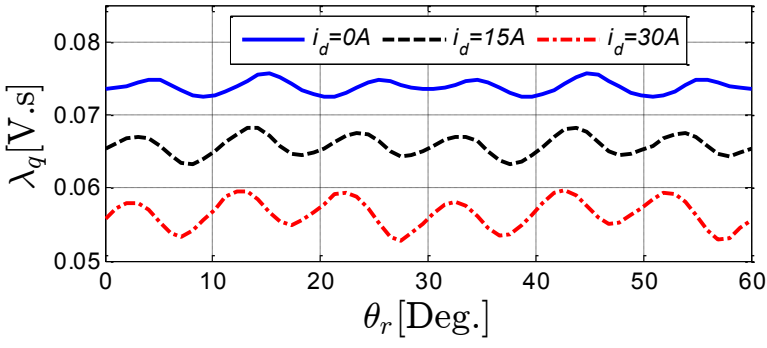

(b) λ_q versus θ_r for constant i_q=20 A and different i_d (0, 15 and 30 A).

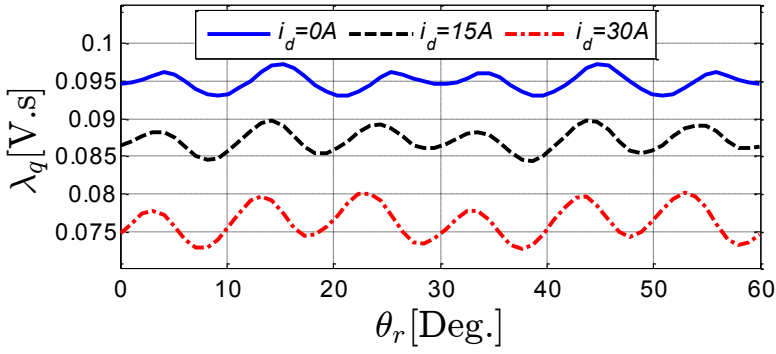

(c) λ_q versus θ_r for constant i_q=30 A and different i_d (0, 15 and 30 A).

Figure 2.6: q-axis flux linkage ($\lambda_q(i_d, i_q, \theta_r)$) for the SynRM at rated speed (6000 rpm) using FEM.

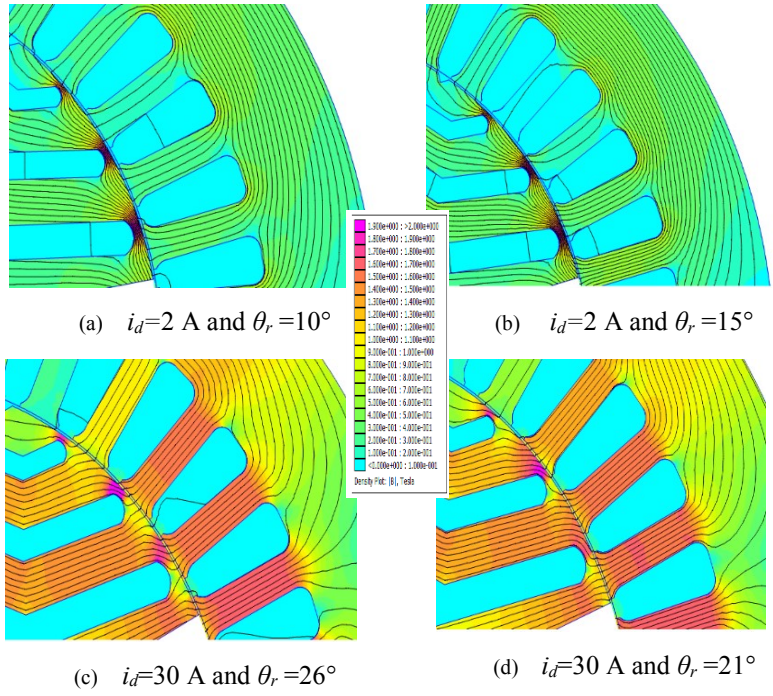

(a) i_d=2 A and θ_r =10° (b) i_d=2 A and θ_r =15°

(c) i_d=30 A and θ_r =26° (d) i_d=30 A and θ_r =21°

Figure 2.7: Flux paths of the SynRM for i_q=10 A and different values for i_d and θ_r. The flux density scale ranges from 0 T (cyan colour) to 2 T (magenta colour).

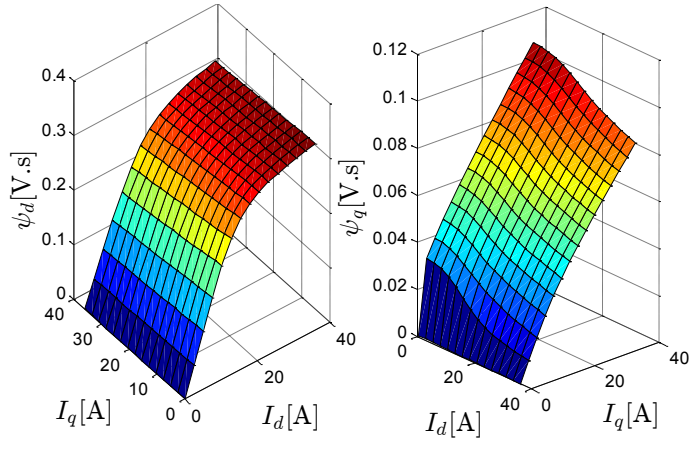

Figure 2.8: *dq*-axis flux linkages ($\psi_d(I_d, I_q)$, $\psi_q(I_d, I_q)$) averaged with respect to the rotor position (θ_r) using FEM.

2.6 Three different models for the flux linkages

It is shown before that both λ_d and λ_q depend on the current components (i_d, i_q) and rotor position (θ_r) of the SynRM. Therefore, we compare three different models for λ_d and λ_q to show their influence on the SynRM performance and control. The three models of λ_d and λ_q are as follows:

- **Model 1**: Both magnetic saturation and rotor position effects are taken into account (the general and most accurate model). The λ_d, and λ_q can be expressed by:

$$\begin{cases} \lambda_d(i_d, i_q, \theta_r) = L_{dd}(i_d, \theta_r) i_d + L_{dq}(i_d, i_q, \theta_r) i_q \\ \lambda_q(i_d, i_q, \theta_r) = L_{qd}(i_d, i_q, \theta_r) i_d + L_{qq}(i_q, \theta_r) i_q \end{cases} \tag{2.11}$$

- **Model 2:** Magnetic saturation effect only is taken into account, neglecting the rotor position effect. The λ_d, and λ_q can be written by:

$$\begin{cases} \lambda_d(i_d, i_q) = L_{dd}(i_d) i_d + L_{dq}(i_d, i_q) i_q \\ \lambda_q(i_d, i_q) = L_{qd}(i_d, i_q) i_d + L_{qq}(i_q) i_q \end{cases} \tag{2.12}$$

- **Model 3:** Unsaturated case where both the magnetic saturation and rotor position effects are neglected. The λ_d, and λ_q can be represented by:

$$\begin{cases} \lambda_d = L_d i_d \\ \lambda_q = L_q i_q \end{cases} \tag{2.13}$$

  Here, the *d* and *q*-axis inductances (L_d, L_q) are constant values.

The *dq*-axis flux linkage relations (2.11) may be obtained by experimental measurements, analytical equations, numerical calculation or by a combined solution of the analytically and experimentally obtained data [4]- [15].

In this PhD, we propose to use the FEM to obtain the *dq*-axis flux linkages ($\lambda_d(i_d, i_q, \theta_r)$, $\lambda_q(i_d, i_q, \theta_r)$) of the SynRM. The FEM is solved for different combinations of *dq*-axis currents (i_d, i_q) and rotor positions (θ_r) as explained before. The stator currents range from 0 up to the rated

value. Then, three-dimensional look-up tables (LUTs) are built for the *d* and *q*-axis flux linkages. The LUTs are employed in the simulated control scheme of the SynRM as described in Fig. 2.9. This method of implementing the λ_d and λ_q in the modelling of the SynRM is simple, efficient and very fast (few seconds) for accurate studies on SynRMs with fixed geometry [20]–[22]. However, it takes a long time to generate the LUTs from FEM. But this has to be done only once for a given machine. Note that, the different inductances in (2.11) and (2.12) (L_{dd}, L_{dq}, L_{qd} and L_{qq}) can be identified from FEM, but it will make the LUTs more complex. Consequently, we prefer to use in the LUTs the λ_d and λ_q as functions of i_d, i_q, θ_r. From the LUTs, (2.11) can be achieved directly based on the required values of i_d, i_q and θ_r. In addition, (2.12) can be obtained by averaging LUTs over the rotor position (θ_r). For the unsaturated case, (2.13) can be obtained by assuming constant values for the L_d and L_q in the linear region of the flux linkages, see Fig. 2.8.

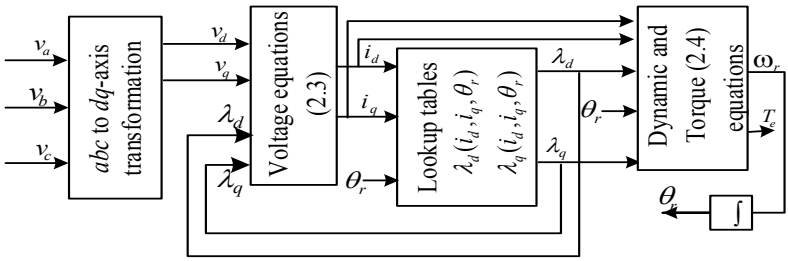

Figure 2.9: Block diagram of the SynRM model with look-up tables.

2.7 Dynamic analysis of the SynRM

In this section, the effect of including and neglecting the magnetic saturation and the rotor position on the SynRM performance i.e. torque capability, synchronization with the supply frequency and power factor is investigated. The study is done first for open loop control. Secondly, closed loop control of the SynRM is studied.

2.7.1 Open loop *V/f* control method

The dynamic model of the SynRM presented in **Sections 2.3** and **2.6** is implemented for the three different models of the *dq*-axis flux linkages

(2.11)-(2.13). In the saturated models 1 and 2, the $\lambda_d(i_d, i_q, \theta_r)$ and $\lambda_q(i_d, i_q, \theta_r)$ are obtained from the LUTs that are generated from the FEM. In the unsaturated model 3, the values of L_d and L_q are selected in the linear region of λ_d and λ_q i.e. neglecting the magnetic saturation and rotor position effects (see Fig. 2.8), resulting in L_d=0.0203 H and L_q=0.0051 H. The moment of inertia of the SynRM is computed from FEM and is about 0.01 kg.m^2, whilst the friction coefficient is assumed to be 0.0002 kg.m^2/s.

The Voltage per Hertz (V_b/f_b) open loop control method is utilized to synchronize the SynRM with the supply frequency. The rated voltage (V_b) and frequency (f_b) of the machine are 220 V and 200 Hz respectively. The DC bus voltage of the inverter is 680 V. The switching frequency of and the sampling time are 6.6 kHz (33 times the rated frequency of the SynRM) and 20 μs respectively. Note that the rated frequency doesn't have to be 50 Hz, as this machine (without rotor cage) cannot run direct-on-line on the power grid. The block diagram of the employed open loop controlled system is depicted in Fig. 2.10. The performance of the SynRM based on these three models is compared to show the impact of the magnetic saturation and rotor position.

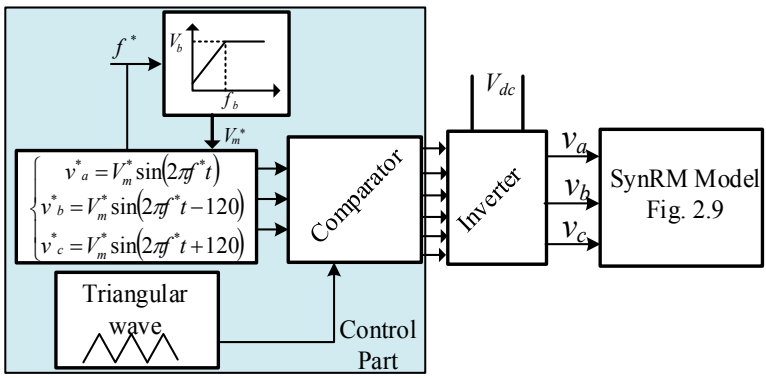

Figure 2.10: Block diagram of the V_b/f_b open loop control of the SynRM.

Figure 2.11 shows the simulated run-up response of the SynRM for the three models i.e. considering the magnetic saturation and rotor position effects for model 1, considering only the magnetic saturation effect with neglected rotor position effect for model 2, and use the unsaturated values for model 3. The load is changed as a stepwise

function with values x= 63%, y= 100% and z= 170% of the SynRM rated load (15.85 N.m) as shown in Fig. 2.11-(a). The reference speed is the rated speed (6000 rpm). At the beginning, the SynRM is synchronized with the supply frequency by the V_b/f_b method without loading.

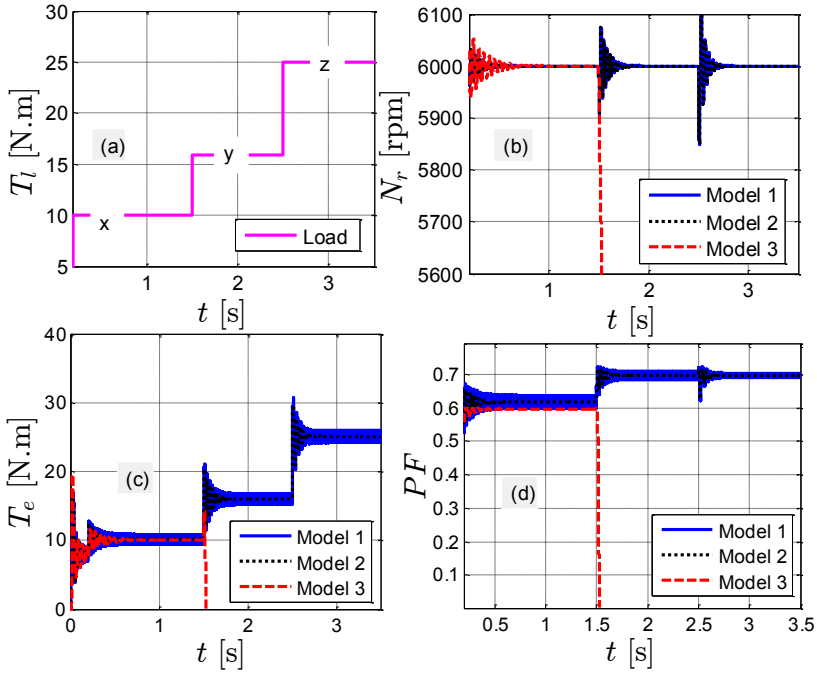

Figure 2.11: Simulated run-up response of the SynRM: (a) load torque profile, (b) motor speed, (c) motor output torque and (d) motor power factor). The three models are: with saturation and rotor position effect (model 1, blue-solid line), with only saturation effect (model 2, black-dotted line) and unsaturated (model 3, red-dashed line).

After the synchronization of the motor, the load characteristic of Fig. 2.11-(a) is applied. It is noticed in Fig. 2.11-(b) and (c) that the SynRM works stably and still synchronizes with the supply frequency using the model 1 or 2 for the different loads. However, for the unsaturated model 3, it doesn't work stably for the rated load or higher loads. In addition, the power factor of the saturated models 1 and 2 is better than that of unsaturated model 3 as seen in Fig. 2.11-(d). Both the better torque

capability and the higher power factor of the SynRM in models 1 and 2 are thanks to the higher saliency ratio (L_d/L_q) compared to model 3 where the inductances are constant values. The oscillations in model 1 (blue-solid line) are mainly due to the rotor position (θ_r) dependence of λ_d and λ_q (see Figs. 2.5 and 2.6). This can be understood by comparing the curves of model 1 (blue-solid line) with model 2 (black-dotted line), where the position effect is neglected, i.e where λ_d and λ_q are averaged over θ_r. The higher oscillations at the instant of the step change in the load are due to the assumed damping coefficient, which is rather low.

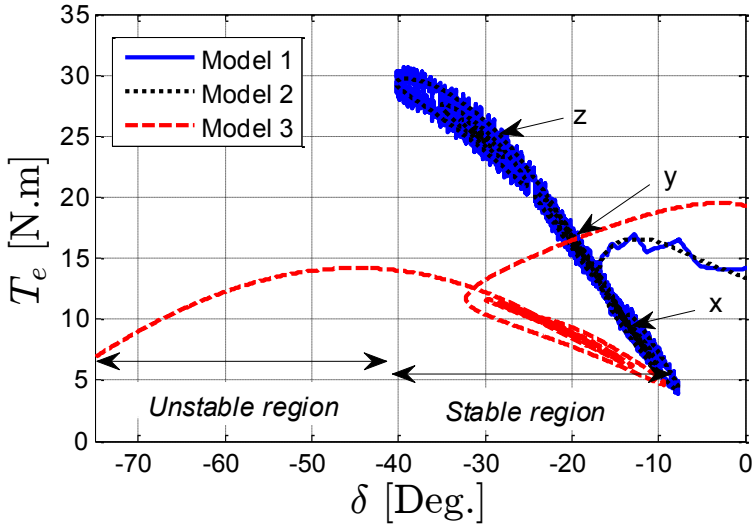

Figure 2.12: The simulated variation of the motor torque with the load angle for the three models at 6000 rpm: with saturation and position effect (blue-solid line), with only saturation effect (black-dotted line) and unsaturated (red-dashed line).

Figure 2.12 manifests the simulated variation of the SynRM torque with the load angle for the three models at the rated speed and for the similar load characteristic of Fig. 2.11-(a). It is evident that the machines including saturation (model 1 and 2) have a higher torque capability (30 N.m), compared to the unsaturated one (14 N.m). In addition, there is no influence on the SynRM torque capability or the stability region of the operation when neglecting the rotor positon effect (black-dotted and blue-solid curves). The stability region is the region

where the load angle is less or equal than 45°. From Figs. 2.11 and 2.12, we learn two things: 1) it is necessary to include the magnetic saturation in the modelling of the SynRM and 2) it is not necessary to include the rotor position effect in the modelling: it only leads to a somewhat higher variation in the SynRM output torque and an increased harmonic content compared to model 2, but it has the same stability limits and dynamic behaviour.

2.7.2 Closed loop field oriented control method

The SynRM under study has a transversally laminated rotor without cages in the flux-barriers. Hence, this type of electric machines is not self-starting and a control method is always necessary to drive the SynRM properly. Closed loop controlled methods are always preferred in the SynRM control due to the better stability issues, compared to the open loop controlled methods [23], [24]. Several closed loop control methods have been presented in the literature for SynRM operation. e.g. field oriented control (FOC) and direct torque control (DTC) [25]–[28]. Here, the SynRM is controlled by the field oriented control method (FOC) based on a space vector pulse width modulation. The control part of Fig. 2.10 is replaced by the vector controlled block diagram described in Fig. 2.13. As can be seen, two reference values are required for the FOC i.e. the *d*-axis current component (i_d*) and the motor speed (ω*). To minimize the SynRM losses and/or to enhance the efficiency, it is mandatory to control the SynRM to work at the maximum torque per Ampère (MTPA) value.

To clarify the importance of including the magnetic saturation effect on the value of i_d* and its influence on the machine output torque, FEM results for the adopted SynRM are presented here. Figure 2.14 shows the output torque of the SynRM as function of the current angle α (see Fig. 2.2) at the rated conditions i.e. a speed of 6000 rpm and different stator currents up to the rated value (I_m=30 A). The corresponding values of i_d and i_q are reported in Fig. 2.15. The blue dash-dotted line in Figs. 2.14 and 2.15 represents the locus of the MTPA. On this locus, the current angle has different values. Also, the value of i_d* is not constant and depends on the required output torque. The red-dotted line shows the MTPA locus in case of neglecting the magnetic saturation in the control of the SynRM. Here, the current angle is constant and equals 45°. From Fig. 2.14, it is observed that the SynRM can produce a higher output torque in the models 1 and 2 that consider saturation: about 8%

higher at the rated conditions, compared with model 3, which is neglecting saturation.

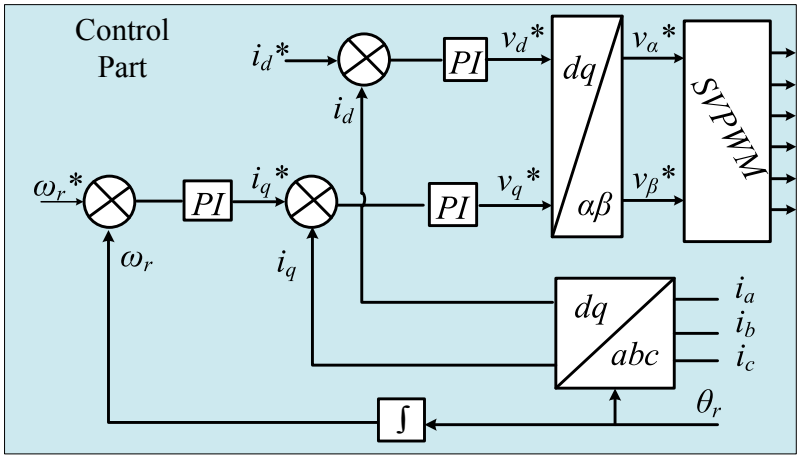

Figure 2.13: Block diagram of the field oriented controlled closed loop method.

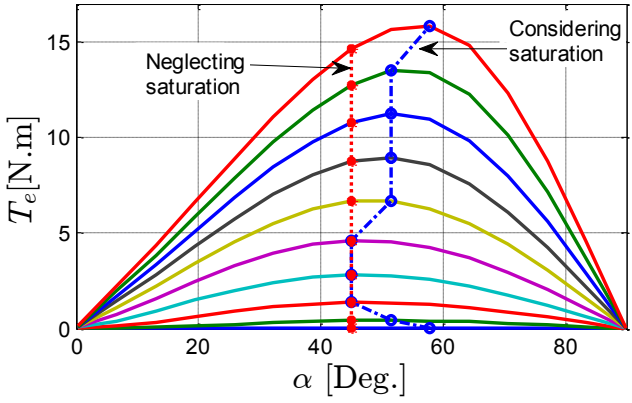

Figure 2.14: The variation of the SynRM output torque as a function of the current angle for different stator currents up to the rated value and at 6000 rpm using FEM.

In the literature, several mathematical and analytical methods to set the value of i_d* can be found e.g. [6], [5] and [8]. However, these methods have several assumptions e.g. that the L_d and L_q saturate to the

same level or neglecting the cross-saturation effect. In addition, mathematical constants have to be obtained and for some cases these constants are complex and difficult. Here, we propose to use the FEM which is explained in **Sections 2.4 and 5** to obtain a relation between the required output torque of the SynRM and i_d* in a LUT [20]–[22]. This method is simple and accurate. In addition, no mathematical equations are needed. The only disadvantage -as mentioned before- is it takes a long time to generate the LUTs from FEM. However, it is done only once.

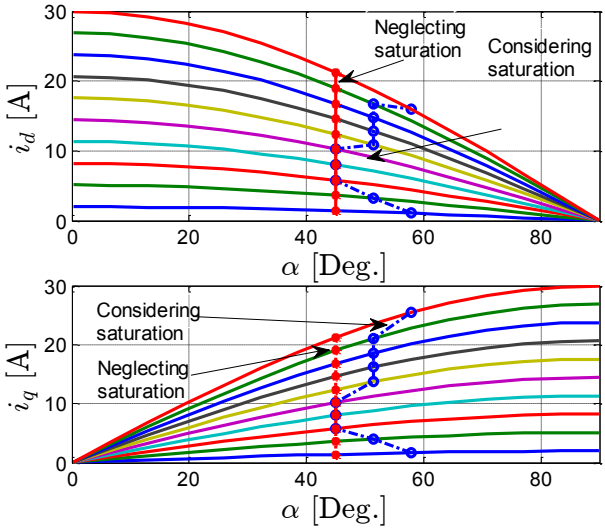

Figure 2.15: The variation of the SynRM *d* and *q*-axis current components as a function of the current angle for different stator currents up to the rated value.

The SynRM model (Fig. 2.9) using the *dq*-axis flux linkages of model 2 (**Section 2.6**), i.e. including only the magnetic saturation with neglecting the rotor position influence, will be compared in the FOC at the same conditions for the following two situations;

- **Situation 1:** i_d* is obtained by FEM and a one dimensional look-up table is generated where i_d*= i_d* (T_e) at the MTPA value (the blue dash-dotted line in Figs. 2.14 and 2.15). Here, the magnetic saturation effect on the control is considered.

- **Situation 2:** i_d* set equal to i_q* and thus the value of the current angle is 45° (the red-dotted line in Figs. 2.14 and 2.15). Here, the magnetic saturation is neglected.

The applied load torque is a stepwise function with 63%, 100% and 126% of the SynRM rated load (15.85 N.m) as seen in Figs. 2.14 and 2.16. The reference speed is the rated speed (6000 rpm). The DC bus voltage is 680 V. The switching frequency of the inverter and the sampling time are 6.6 kHz (33 times the rated frequency of the SynRM) and 20 μs respectively. The PI controller parameters are selected by a trial and error method. The gain and time constant of the speed controller are 20 and 0.01 s, and the gain and time constant of the torque controller are 2 and .05 s.

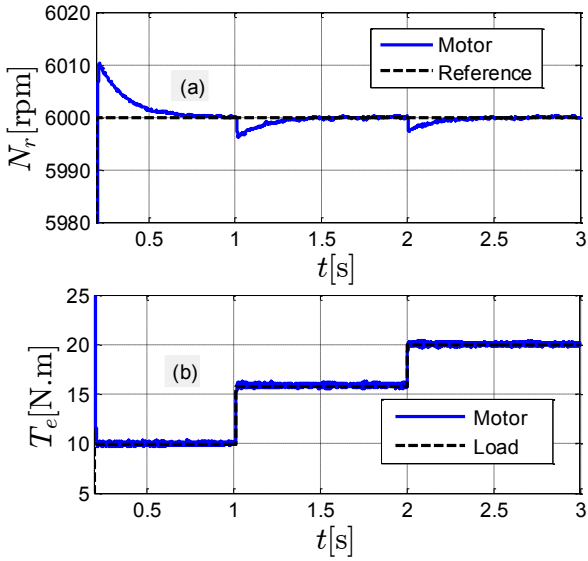

Figure 2.16: Simulated run-up response ((a) speed and (b) torque) of the SynRM considering the saturation effect on the value of i_d*.

For situation 1, Fig. 2.16 shows the simulated run-up response of the SynRM considering the magnetic saturation effect on i_d* at rated speed and for different loads. The corresponding currents (i_d and i_q) are reported in Fig. 2.17. It is clear that the value of i_d* is varied depending

on the required load torque to satisfy the MTPA condition. In addition, the motor speed follows accurately the reference value for the different loads. The motor can work stably at a load torque of 126% of the rated value. Note that, the ripples in the motor curves are due to the inverter PWM. Figure 2.18 shows the three phase currents of the machine for different loads. It can be seen that the current increases with increasing load torque.

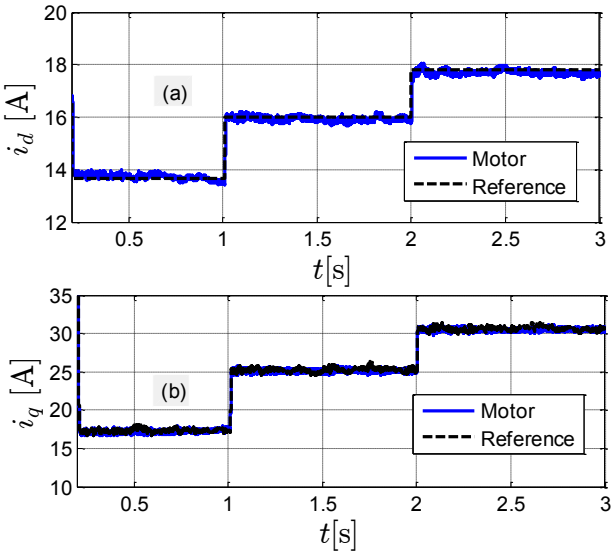

Figure 2.17: Simulated response of the i_d (a) and i_q (b) components of the SynRM considering the saturation effect on the value of i_d* at 6000 rpm.

For situation 2, Fig. 2.19 shows the simulated run-up response of the SynRM neglecting the magnetic saturation effect on the value of i_d* at the rated speed and for different loads. The response of the currents i_d and i_q is reported in Fig. 2.20. For the same conditions of situation 1, the SynRM modeled via model 2 can work at the rated speed only at 63% of the rated load for the given load characteristics of Fig. 2.16. This is clear in Figs. 2.19 and 2.20 (t <= 1 s). However, at the rated load or at higher load, the motor cannot work stably any more at the rated speed. The motor cannot follow the reference speed and therefore, a very high i_q value (limited in the simulation by 100 A) is required as shown in Figs. 2.19 and 2.20 (t=1 s to 1.3 s). This is because the required

load torque is higher than the torque capability of the SynRM at the given i_d* as seen in Fig. 2.14. In this case, the motor must operate in the flux weakening region to work at the rated speed as shown in Figs. 2.19 and 2.20 (t>1.3 s). Alternatively, the DC bus voltage has to increase, but this solution may be not applicable in the real world. The variation of the DC bus voltage may be applicable in photovoltaic systems in which there are no batteries used [29], [30]. Figure 2.21 shows the three phase currents of the machine for different loads. It can be seen that the current increases with increasing load torque.

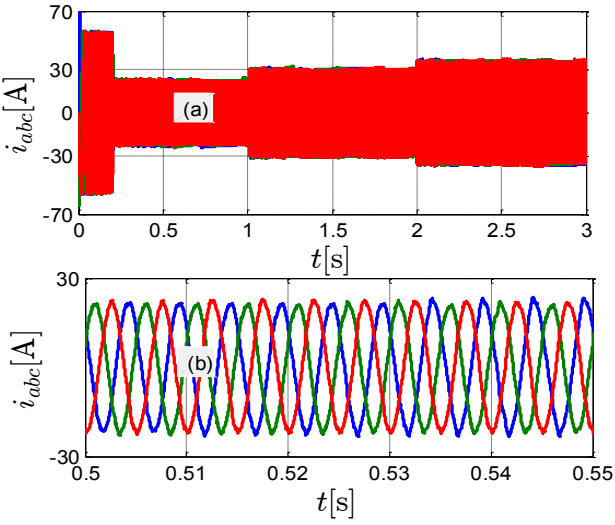

Figure 2.18: Three phase currents i_{abc} (a) of the SynRM at several loads with including the magnetic saturation effect of i_d* and a zoom of i_{abc} (b).

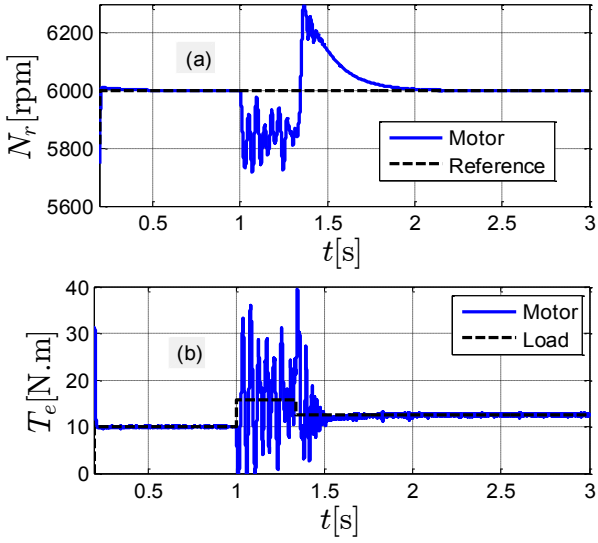

Figure 2.19: Simulated run-up response ((a) speed and (b) torque) of the SynRM neglecting the saturation effect on the value of i_d*.

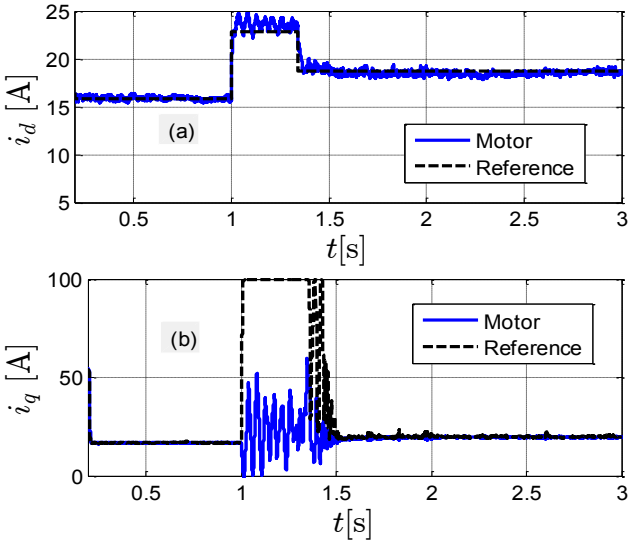

Figure 2.20: Simulated response of i_d (a) and i_q (b) components of the SynRM neglecting the saturation effect on the value of i_d*.

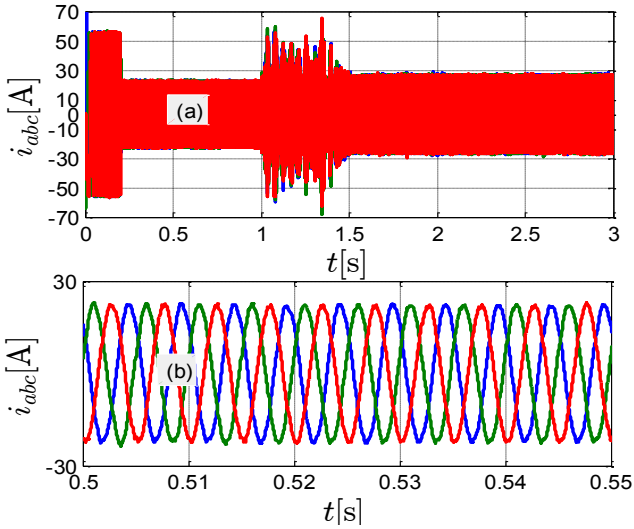

Figure 2.21: Three phase currents i_{abc} (a) of the SynRM at several load torques with neglecting the magnetic saturation and a zoom of i_{abc} (b).

2.8 Performance of the SynRM at different speeds including flux weakening

As usual in electrical machine control, two regions of speeds are considered. In the first region, the speed of the machine is less than or equal to the rated (base) speed. In this region, the applied voltage (V_b) changes proportionally with the frequency (f_b) so that V_b/f_b is constant. In the second region, the speed of the motor is higher than the rated value and V_b is kept constant at the rated value [31].

In this section, we show the influence of including and neglecting the magnetic saturation in the inductances of the SynRM model at steady state operation for several speeds. In this analysis, the SynRM performance is investigated in open loop control. Model 3, with unsaturated L_d and L_q is compared with model 2, where the magnetic saturation is included. Two cases of the unsaturated model 3 are investigated.

The first case considers three different q-axis inductance (L_q) values while the d-axis inductance (L_d) value is fixed. The values of L_q are 0.0051 H, 0.0037 H and 0.0032 H and L_d=0.0203 H. The selection of

L_d=0.0203 H is to represent approximately the average value of L_d in the linear region (neglecting saturation and cross-saturation effects) of the *d*-axis flux linkage, see Fig 2.8. The selection of the three *q*-axis inductance values is to represent approximately the average value of L_q in the linear, knee and saturated regions of the *q*-axis flux linkage respectively, see Fig. 2.8. The second case considers three different *d*-axis inductance (L_d) values while the *q*-axis inductance (L_q) value is fixed. The values of L_d are 0.0110 H, 0.0152 H and 0.0203 H and the value of L_q is 0.0051 H. The following paragraphs give a brief summary of the results. A detailed analysis of these two cases is provided in the **Appendix A.**

Figure 2.22 and Fig. 2.23 show the results of the first and second case respectively.

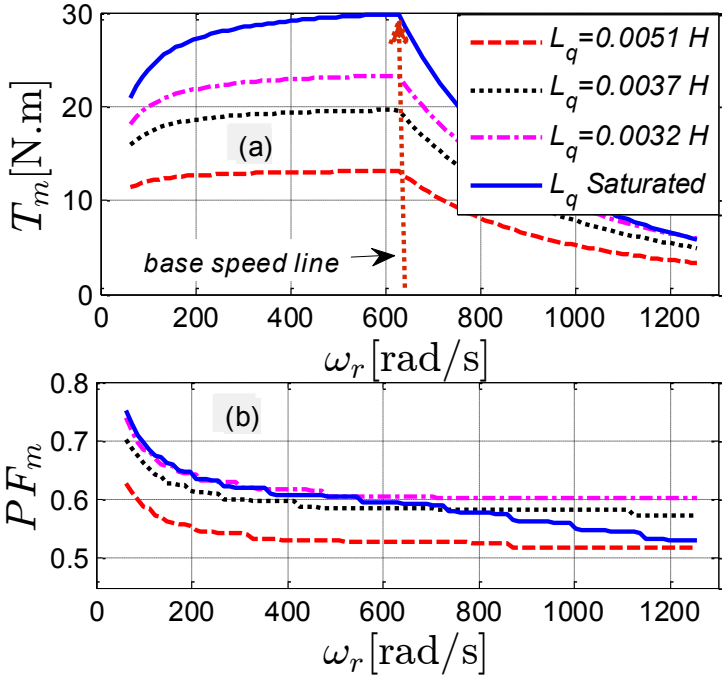

Figure 2.22: Variation of SynRM maximum torque T_m (a) and power factor PF_m at T_m (b) with different speeds ω_r for unsaturated (different L_q and L_d=0.0203 H) and saturated (blue solid-line) machines. (a) and (b) have the same legend.

Fig. 2.22 shows the variation of the maximum torque T_m of the SynRM at different speeds from 10% up to 200% of the rated value for the saturated (Model 2) and unsaturated (L_q= 0.0051 H, 0.0037 H and 0.0032 H at L_d=0.0203 H) machines. The region below the curves in Fig. 2.22-(a) as well as in Fig. 2.23-(a) represents the region where the machine can work stably and synchronize with the supply frequency, while the region above the curves shows the instability region (in the direction of the plotted arrow in the figures). The stability region of the unsaturated machine increases with decreasing L_q because of increasing the saliency ratio (L_d/L_q). Moreover, the machine considering the magnetic saturation has the larger stability region (the blue solid-line) for all the considered speeds.

The machine power factor at the maximum torque T_m for different speeds is shown in Fig. 2.22-(b). The machine considering the magnetic saturation (blue solid-line) has a better power factor compared to the unsaturated cases for all speeds less or equal than the rated value. However, the machine with L_q=0.0032 H (magenta dashed-line) has the best power factor for speeds higher than the rated value.

Figure 2.23-(a) illustrates the variation of the maximum torque T_m of the SynRM as a function of the speed, ranging from 10% to 200% of the rated value. Curves are shown for saturated (Model 2) and unsaturated (L_d=0.0110 H, 0.0152 H and 0.0203 H at L_q=0.0051 H) machines. It is evident that the machine including the magnetic saturation (blue solid line) has a higher stability region. On the other hand, the variation of the L_d at constant L_q has a lower influence on the stability region compared to Fig. 2.22 where the L_q varies at constant L_d. Figure 2.23-(b) shows the variation of the power factor of the SynRM for different speeds at the maximum torque T_m. The saturated machine has the best power factor for all the considered speeds.

Notice that the maximum torque (T_m) in Figs. 2.22 and 2.23 should be constant for all speeds up to the rated value. However, it has a slightly lower values for low speeds compared to the value at rated speed. This influence may be due to the inaccurate representation of the stator resistance and the error in the *V/f* control for low speeds.

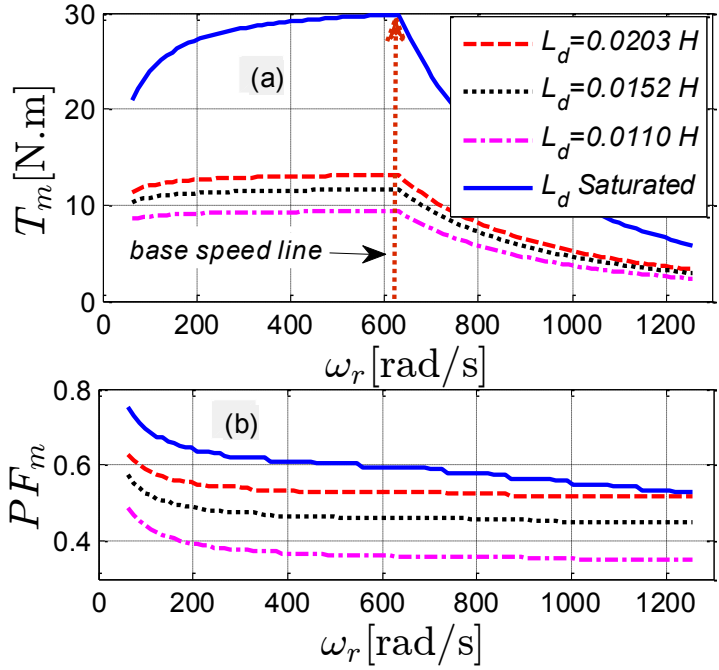

Figure 2.23: Variation of SynRM maximum torque T_m (a) and power factor PF_m at T_m (b) with different speed ω_r for unsaturated (different L_d and L_q=0.0051 H) and saturated (blue solid-line) machines. (a) and (b) have the same legend.

2.9 Conclusions

This chapter has investigated deeply the modelling of SynRMs, taking into account the magnetic saturation and rotor position effects in open loop and closed loop controlled methods. Moreover, the stability limits of operation for the SynRM have been indicated. A simple and very fast efficient model for the SynRM has been proposed based on an accurate representation of the *dq*-axis flux linkages. The *dq*-axis flux linkages are computed from FEM, considering the magnetic saturation and rotor position effects. Look-up tables (LUTs) are generated for the *dq*-axis flux linkages and can be used in the simulations of the SynRM, obtaining an accurate prediction for its performance and control.

Three models of the *dq*-axis flux linkages are investigated based on an open loop controlled method:

- **Model 1:** Considering the magnetic saturation and rotor position effects.
- **Model 2:** Considering only the magnetic saturation, without the rotor position effect.
- **Model 3:** Considering constant values for both L_d and L_q.

It is found that the SynRM torque capability and stability operation region depend mainly on the *dq*-axis flux linkages characteristics. Including magnetic saturation in the model of a SynRM is mandatory to have an accurate prediction of its performance (output torque, power factor and stable region of operation). This means choosing constant inductances (L_d and L_q) to represent the SynRM in a very simple way, is not good enough and can lead to a large deviation in the prediction of the torque capability compared with the real motor. However, the rotor position has almost no influence on the SynRM torque capability or stability region.

In the closed-loop controlled method, it is noticed that considering the magnetic saturation effect on the control of the SynRM results in an 8% increase in the output torque compared to neglecting the saturation effect for the same conditions.

Finally, the SynRM torque capability and power factor have been indicated at several speeds from 10% up to 200% of the rated value; showing the necessity of including the magnetic saturation in the SynRM modelling for accurate performance prediction.

Biography

[1] M. N. Ibrahim, P. Sergeant, and E. M. Rashad, “Synchronous reluctance motor performance based on different electrical steel grades,” *IEEE Trans. Magn.*, vol. 51, no. 11, pp. 1–4, Nov. 2015.

[2] G. Pellegrino, F. Cupertino, and C. Gerada, “Automatic design of synchronous reluctance motors focusing on barrier shape optimization,” *IEEE Trans. Ind. Appl.*, vol. 51, no. 2, pp. 1465–1474, Mar. 2015.

[3] M. N. Ibrahim, P. Sergeant, and E. M. Rashad, “Relevance of including saturation and position dependence in the inductances for accurate dynamic modeling and control of SynRMs,” *IEEE Trans. Ind. Appl.*, vol. 53, no. 1, pp. 151–160, Jan. 2017.

[4] E. Levi, “Saturation modelling in d-q axis models of salient pole synchronous machines,” *IEEE Trans. Energy Convers.*, vol. 14, no. 1, pp. 44–50, Mar. 1999.

[5] T. Lubin, H. Razik, and a. Rezzoug, “Magnetic saturation effects on the control of a synchronous reluctance machine,” *IEEE Trans. Energy Convers.*, vol. 17, no. 3, pp. 356–362, 2002.

[6] S. Yamamoto, T. Ara, and K. Matsuse, “A method to calculate transient characteristics of synchronous reluctance motors considering iron loss and cross-magnetic saturation,” *IEEE Trans. Ind. Appl.*, vol. 43, no. 1, pp. 47–56, 2007.

[7] A. Vagati, M. Pastorelli, F. Scapino, and G. Franceschini, “Impact of cross saturation in synchronous reluctance motors of the transverse-laminated type,” *IEEE Trans. Ind. Appl.*, vol. 36, no. 4, pp. 1039–1046, 2000.

[8] E. M. Rashad, T. S. Radwan, and M. A. Rahman, “A maximum torque per ampere vector control strategy for synchronous reluctance motors considering saturation and iron losses,” *Conf. Rec. 2004 IEEE Ind. Appl. Conf. (39th IAS Annu. Meet.*, vol. 4, pp. 2411–2417, 2004.

[9] H. Mahmoud and N. Bianchi, “Eccentricity in synchronous reluctance motors-Part I: analytical and finite-element models,” *IEEE Trans. Energy Convers.*, vol. 30, no. 2, pp. 745–753, Jun. 2015.

[10] H. Mahmoud and N. Bianchi, “Nonlinear analytical model of eccentric synchronous reluctance machines considering the iron saturation and slotting effect,” *IEEE Trans. Ind. Appl.*, vol. 53, no. 3, pp. 2007–2015, May 2017.

[11] M. Degano, H. Mahmoud, N. Bianchi, and C. Gerada, “Synchronous reluctance machine analytical model optimization and validation through finite element analysis,” in *2016 XXII International Conference on Electrical Machines (ICEM)*, 2016, pp. 585–591.

[12] I. Torac and A. Argeseanu, “Analytical model of the synchronous reluctance motor with axially laminated rotor for optimization purpose,” in *2008 11th International Conference on Optimization of Electrical and Electronic Equipment*, 2008, pp. 27–32.

[13] A. Tessarolo, M. Degano, and N. Bianchi, “On the analytical estimation of the airgap field in synchronous reluctance machine,” in *2014 International Conference on Electrical Machines (ICEM)*, 2014, pp. 239–244.

[14] T. Hubert, R. Steckel, M. Reinlein, A. Kremser, and H.-G. Herzog, “Nonlinear reluctance network method for synchronous reluctance machine analysis,” in *2015 18th International Conference on Electrical Machines and Systems (ICEMS)*, 2015, pp. 904–910.

[15] M. Ferrari, N. Bianchi, and E. Fornasiero, “Analysis of rotor saturation in synchronous reluctance and PM-assisted reluctance motors,” *IEEE Trans. Ind. Appl.*, vol. 51, no. 1, pp. 169–177, Jan. 2015.

[16] A. Vagati, “The synchronous reluctance solution: a new alternative in AC drives,” in *Proceedings of IECON’94 - 20th Annual Conference of IEEE Industrial Electronics*, vol. 1, pp. 1–13.

[17] P. C. Krause, O. Wasynczuk, and S. D. Sudhoff, “Analysis of electric machinery and drive systems,” *Second Ed. Wiley, Interscience, John Wiley Sons. INC. Publ.*, 2002.

[18] N. Bianchi, E. Fornasiero, and W. Soong, “Selection of PM flux linkage for maximum low-speed torque rating in a PM-assisted synchronous reluctance machine,” *IEEE Trans. Ind. Appl.*, vol. 51, no. 5, pp. 3600–3608, Sep. 2015.

[19] N. Chen, S. L. Ho, and W. N. Fu, “Optimization of permanent magnet surface shapes of electric motors for minimization of cogging torque using FEM,” *IEEE Trans. Magn.*, vol. 46, no. 6, pp. 2478–2481, Jun. 2010.

[20] L. Queval and H. Ohsaki, “Nonlinear abc-model for electrical machines using N-D lookup tables,” *IEEE Trans. Energy Convers.*, vol. 30, no. 1, pp. 316–322, Mar. 2015.

[21] M. Mohr, O. Biro, A. Stermecki, and F. Diwoky, “An improved physical phase variable model for permanent magnet machines,” in *2012 XXth International Conference on Electrical Machines*, 2012, pp. 53–58.

[22] A. Kilthau and J. M. Pacas, “Parameter-measurement and control

of the synchronous reluctance machine including cross saturation," in *Conference Record of the 2001 IEEE Industry Applications Conference. 36th IAS Annual Meeting (Cat. No.01CH37248)*, vol. 4, pp. 2302–2309.

[23] G. Jalali, S. Ahmed, H. Kim, and Z. Pan, "Instability detection and protection scheme for efficiency optimized v/f driven synchronous reluctance motors (SynRM)," in *2016 IEEE Energy Conversion Congress and Exposition (ECCE)*, 2016, pp. 1–6.

[24] Z. Hou, J. Huang, H. Liu, M. Ye, Z. Liu, and J. Yang, "Diagnosis of broken rotor bar fault in open- and closed-loop controlled wye-connected induction motors using zero-sequence voltage," *IET Electr. Power Appl.*, vol. 11, no. 7, pp. 1214–1223, Aug. 2017.

[25] H. F. Hofmann, S. R. Sanders, and A. EL-Antably, "Stator-flux-oriented vector control of synchronous reluctance machines with maximized efficiency," *IEEE Trans. Ind. Electron.*, vol. 51, no. 5, pp. 1066–1072, Oct. 2004.

[26] L. Liu, X. Du, and S. Shen, "Indirect field-oriented torque control of induction motor considering magnetic saturation effect: error analysis," *IET Electr. Power Appl.*, vol. 11, no. 6, pp. 1105–1113, Jul. 2017.

[27] R. Morales-Caporal and M. Pacas, "Encoderless predictive direct torque control for synchronous reluctance machines at very low and zero speed," *IEEE Trans. Ind. Electron.*, vol. 55, no. 12, pp. 4408–4416, Dec. 2008.

[28] S. Kang and S. Sul, "Highly dynamic torque control of synchronous reluctance motor," *IEEE Trans. Power Electron.*, vol. 13, no. 4, pp. 793–798, Jul. 1998.

[29] M. Nabil, S. M. Allam, and E. M. Rashad, "Performance improvement of a photovoltaic pumping system using a synchronous reluctance motor," *Electr. Power Components Syst.*, vol. 41, no. 4, pp. 447–464, Feb. 2013.

[30] M. Nabil, S. M. Allam, and E. M. Rashad, "Modeling and design considerations of a photovoltaic energy source feeding a synchronous reluctance motor suitable for pumping systems," *Ain Shams Eng. J.*, vol. 3, no. 4, pp. 375–382, Dec. 2012.

[31] H. Hadla and S. Cruz, “Predictive stator flux and load angle control of synchronous reluctance motor drives operating in a wide speed range,” *IEEE Trans. Ind. Electron.*, vol. 64, no. 9, pp. 6950–6959, Sep. 2017.

Chapter 3
Design Methodology of the SynRM

3.1 Introduction

This chapter presents an overview of the design of SynRMs. The main focus is on the rotor design, in particular on the geometry of the flux-barriers. The influence of the flux-barrier parameters on the SynRM performance indicators is investigated. The investigated performance indicators are saliency ratio, output torque and torque ripple. In addition, easy-to-use parametrized equations are proposed to select the two most crucial parameters of the rotor i.e. the flux-barrier angle and width for each of the flux barriers. The proposed equations are compared with three existing equations found in literature. At the end of the chapter, an optimal rotor design is obtained based on an optimized technique coupled with FEM. The optimal rotor is checked mechanically for the robustness against stress and deformations.

3.2 Literature overview about SynRM design

The stator design of electric machines with a rotating field depends on the type of the employed windings: distributed or concentrated windings. Basically, the distributed windings are always adopted for SynRMs because of several advantages such as low spatial harmonics, low torque ripple and high power factor [1], [2]. Consequently, the stator design with distributed windings of the SynRM is similar to that of conventional induction machines. Therefore, the main focus in this

chapter is given to the rotor part of SynRMs, and also the literature study further in this section is devoted exclusively to rotor design.

It is well-known that the SynRM performance depends mainly on the ratio between the direct and quadrature axis inductances (L_d/L_q) as shown in **Chapter 2**. The inductances are strongly affected by the design of the rotor geometrical parameters, in particular the parameters of the flux-barrier. There are several parameters in the rotor that have to be selected optimally. These parameters are the flux-barrier angle, with, position and length as well as the flux-barrier ribs as will be shown later in Fig. 3.1 [3]. To obtain an optimal SynRM performance, choosing the optimal value for the many geometric parameters of the rotor is very complex. Therefore, an optimization technique is always necessary to optimize the performance indicators i.e. maximize the saliency ratio of the machine, hence the output torque and to minimize the torque ripple [4]. There are three possibilities to couple the optimized technique with the SynRM model to obtain the performance indicators (saliency ratio, output torque and torque ripple) [5]-[11]. The first possibility is to make a parameterized analytical approach for the SynRM, in which all the stator and rotor parameters as well the magnetic material saturation behavior and rotor position dependence have to be included [5]-[7]. The second possibility is to build the SynRM model using FEM [8]–[10]. The latter model is much more simple and accurate in predicting the SynRM performance compared to the analytical one. However, it takes a very huge computation time [11], [12]. A third option, in order to reduce the FEM computation time, is to use the analytical approach coupled to the FEM to obtain optimized flux-barrier parameters. Here, a FEM with the optimized parameter set of the analytical approach is built for refinement [13]. This is an efficient method but evidently requires the effort to develop two models.

In [3], simulations and experiments using a 200 W prototype SynRM were reported for optimizing the design of the flux-barriers and other aspects of the motor. The influence of the number of flux-barriers, the ratio of flux-barrier width to rib width, as well as the ratio of rib width to output torque were presented that have a huge influence on the SynRM performance indicators. In [4], the effect of rotor geometrical parameters on the *dq*-axis inductances of a SynRM is investigated. In addition, an optimum design method coupled with FEM is presented to improve the saliency ratio of the SynRM. In [14], the influence of three

quantities has been investigated in terms of the output torque and torque ripple: the number of stator slots, the number of rotor poles and the number of flux-barrier layers. This paper proved that the combination of these three parameters is very important with respect to torque and torque ripple. It was found that, for every stator slot number, there is preferred number of flux-barrier layers. In addition, an asymmetrical design for the flux-barrier positions with respect to the stator teeth was proposed. This leads to a reduction in the machine torque ripple.

Moreover, some papers have presented some simple approaches and/or parametrized equations to quickly obtain a suitable rough design of a good SynRM rotor. This rough design can then be used in the detailed optimization with FEM [15]–[18]. The benefit of this approach is to reduce the CPU time of the design, by reducing the number of FEM calculations. It is evident that the flux-barrier widths and angles have a huge influence on the SynRM performance indicators [19]. Therefore, a great interest for finding an easy method to choose these two parameters was considered [16]. In [15], a general formula was proposed for selecting the number of flux-barrier layers and for determining the flux-barrier angles for any number of stator slots to minimize the torque ripple. This method is very simple and effective. However, the resulting torque ripple is still a bit high: around 26% as proved in [20]. In [16], simple methods to choose the flux-barrier angles and widths were suggested. However, these methods give a rough estimation only; afterwards, still a FEM sensitivity analysis is required to fine–tune the value of angle β to obtain a low torque ripple. The authors of [17] combined both methods of [15] and [16] and added additional factors to make a generalized formula. The additional factors are the number of stator and rotor slots as well the stator and rotor slot openings. Nevertheless, the torque ripple is still high and for some cases is higher than both [15] and [16]. Moreover, an interesting work was presented in [18] to choose a preliminarily design for the flux-barrier widths. However, the influence of different stator slots was not considered. Therefore, further research is needed to find out a simple method to choose the preliminarily flux-barrier angles and widths of the SynRM for low torque ripple and better average torque.

3.3 Design methodology for the reference SynRM

In this PhD, we study in particular SynRM in detail: the SynRM described in **Chapter 2,** of which one pole of the rotor is shown in Fig. 3.1. The flux-barrier parameters of this reference design are listed in Table 3.1.

The parameters to optimize are the flux barrier angle θ_{bi}, width W_{bi}, length L_{bi} and position p_{bi}. In addition, the flux-barrier ribs have a huge influence on the SynRM performance. However, the selection of the rib thickness is a compromise between the electromagnetic and mechanical robustness [17]. The aforementioned parameters are chosen because literature study (**Section 3.2**) has shown that these are the most dominant for the SynRM performance indicators. The following parameters are fixed: the rotor outer diameter (D_r) and the shaft diameter (D_{sh}).

The performance indicators, which are also the optimization goals, are saliency ratio, output torque and torque ripple.

The FEM presented in **Chapter 2** is parametrized to be used to obtain the performance indicators of SynRM. As mentioned before, sinusoidal currents are applied in this analysis. This means that the effects of harmonics on the torque ripple and average torque is neglected.

Table 3.1: parameters of the flux-barriers of a reference design.

Parameter	Value	Parameter	Value
θ_{b1}	7.5°	W_{b1}	6 mm
θ_{b2}	20.5°	W_{b2}	4 mm
θ_{b3}	33.5°	W_{b3}	3 mm
L_{b1}	25 mm	p_{b1}	23.5 mm
L_{b2}	19 mm	p_{b2}	36 mm
L_{b3}	12 mm	p_{b3}	46 mm

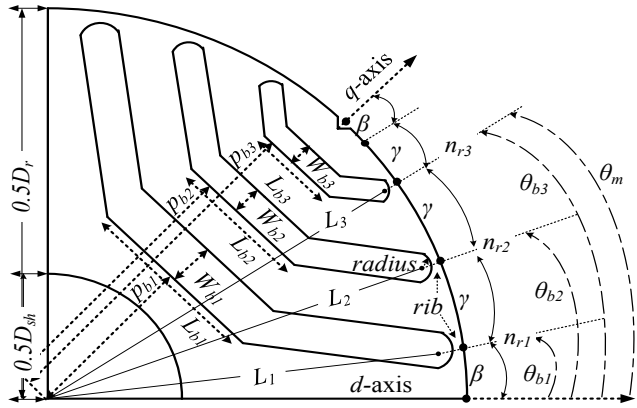

Figure 3.1: One pole of the SynRM rotor geometry.

3.4 Sensitivity analysis of the flux-barrier geometry

The sensitivity analysis of the flux-barrier geometrical parameters is presented in this section. The main objectives of the sensitivity analysis are to 1) understand the influence of the flux-barrier parameters on the SynRM performance and 2) show if it is possible to obtain a good SynRM rotor design.

As mentioned in the previous section, the analysis is done for the reference machine of **Chapter 2** (Fig. 3.1, Table 3.1). For the sensitivity analysis of the SynRM, the stator dimensions, air gap length, the outer diameter (D_r) of the rotor and the lengths (L_1, L_2 and L_3) shown in Fig. 3.1, are fixed. Only the rotor flux-barrier geometrical parameters have been changed. For each of the three barriers, there are 4 studied parameters: the angle θ_{bi}, the width W_{bi}, the length L_{bi} and the position p_{bi} with i=1:3. In order to study the sensitivity of the rotor flux-barriers on the SynRM performance, only one variable of the rotor flux-barrier dimensions - e.g. the flux-barrier width - is varied within specified constraints, while the other dimensions are kept constant. As there are three flux-barriers, this leads to a three-dimensional response space. E.g. in case of the flux-barrier width, we obtain a function of W_{b1}, W_{b2} and W_{b3}. The characteristics of the SynRM are computed using 2D-FEM at the rated speed (6000 rpm). The stator current is the rated value (21.21 A) at a current angle α=56.5° which corresponds to the maximum output torque value of a reference design (**Chapter 2**). The flux paths and flux density distribution of one pole of the SynRM using

FEM are shown in Fig. 3.2. It is clear that some regions are saturated e.g. the flux-barrier ribs.

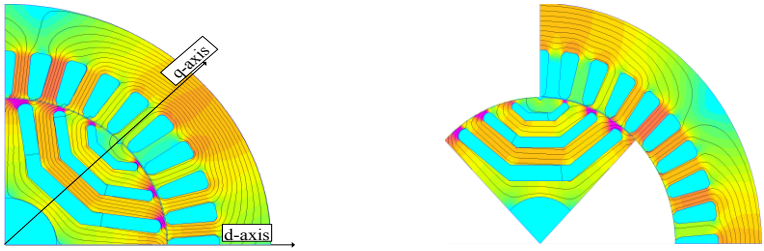

θ_r=0° θ_r=45°

Figure 3.2: Flux paths of one pole of the reference SynRM using FEM with different positions at rated current and current angle α=56.5°.

3.4.1 The effect of the flux-barrier angles θ_{bi}

The adopted SynRM has three flux-barriers per pole with the angles as shown in Fig. 3.1. The three flux-barrier angles (θ_{b1}, θ_{b2} and θ_{b3}) are measured in degrees from the *d*-axis line to the center of the flux-barrier. The range of the parameters is given in Table 3.2. As mentioned before, all the other rotor variables are kept constant and equal to the reference values given in Table 3.1.

Figure 3.3 shows the variation of the SynRM saliency ratio for different flux-barrier angles at the rated conditions. The maximum and the minimum saliency ratios in the considered parameter range are approximately 5.25 and 4.35 (about 20.69% difference, compared to the minimum value) respectively. When looking to e.g. the top right subfigure, the saliency ratio of the SynRM decreases with increasing both θ_{b2} and θ_{b3}. On the other hand, when comparing the 4 Subfigures (having the same color scale), the saliency ratio increases with increasing θ_{b1} till approximately 7.5 degrees and then decreases again. In fact, the variation of the saliency ratio with the flux-barrier angles has two main reasons. The first reason is the variation of the *d*-axis flux path area. With increasing both θ_{b1}, θ_{b2} and θ_{b3}, the *d*-axis flux obtains a somewhat larger useful cross-section of magnetic material. This can be seen by comparing Subfigs. 2 and 1. In the region of small θ (region close to horizontal axis with $0<\theta_m<35°$), a lot of flux is passing. Here,

the magnetic cross section increases with increasing θ_{b1}, θ_{b2} and θ_{b3}. In the region $35°<\theta_m<45°$, not much d-axis flux is present (Subfig. 1). Here, the magnetic cross section reduces. The total d-axis flux and by consequently the L_d slightly increase. This first reason suggests an increasing saliency ratio, in contrast with Subfig. 4. The second reason is the variation of the area and the magnetic saturation level of the flux-barrier ribs (see: Subfig. 1) which has a direct effect on the q-axis inductance value. With increasing θ_{b1}, θ_{b2} and θ_{b3} but especially with increasing θ_{b1}, the available magnetic cross section for q-axis flux strongly increases, causing the L_q to increase much more than L_d. This leads to a lower saliency ratio as observed in Subfig. 4.

Table 3.2: The constraints on the flux-barrier angles.

Variable	Minimum	Maximum
θ_{b1}	5°	10°
θ_{b2}	16.5°	20.5°
θ_{b3}	26°	35°

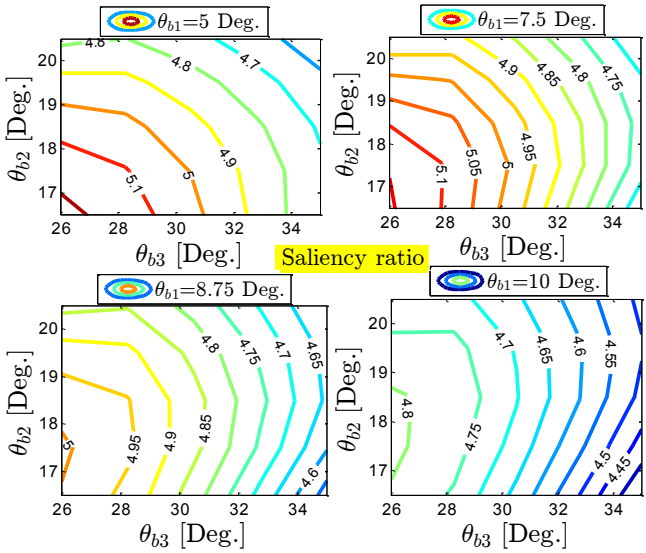

Figure 3.3: Saliency ratio of the reference SynRM versus different flux-barrier angles at rated conditions.

Figure 3.4 indicates the computed average torque of the SynRM based on the Maxwell stress tensor method for different flux-barrier angles. The computed maximum and minimum torque values are 16.08 N.m and 14.61 N.m (about 10.04% difference, compared to the minimum value) respectively. Clearly, there is one optimal value of the flux-barrier angles that realizes the maximum torque: see Subfigs. 2 and 3 for $\theta_{b1} = 7.5°$ and $\theta_{b1} = 8.75°$. For rather low θ_{b1}, the SynRM torque decreases with increasing both θ_{b2} and θ_{b3}. There is a more or less linear relationship between θ_{b2} and θ_{b3} in order to have high torque. For high $\theta_{b1} > 8.75°$, also θ_{b2} and θ_{b3} should increase but the obtained torque remains lower than for $\theta_{b1} < 8.75°$. Note that, the markers of red circles in Fig. 3.4 will be used later.

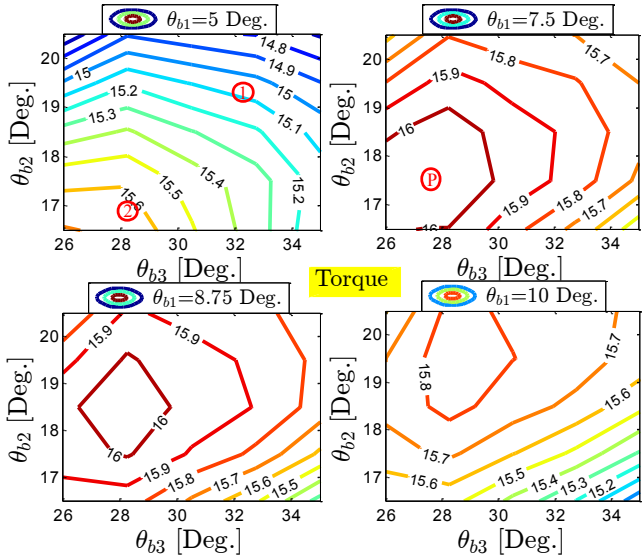

Figure 3.4: Output torque of the reference SynRM versus different flux-barrier angles at rated conditions.

Figure 3.5 describes the torque ripple (in percent) of the SynRM due to the variation of the flux-barrier angles. It can be seen that there is a huge effect on the torque ripple. The maximum and the minimum torque ripple values are 66.9% and 12.3% respectively. The difference on the torque ripple is enormous: the maximum value is more than 4 times the minimum value. It is a result of the interaction between the spatial harmonics of the magneto-motive force (MMF) of the stator

currents and the rotor geometry, in particular the flux-barrier angles. It is evident that for the flux-barrier angles that are corresponding to the stator slot openings, θ_{b1}=10°, θ_{b2}=20° and θ_{b3}=30°, the SynRM torque ripple is very high: more than 60%. In addition, when moving the flux-barrier angles away from the stator slot openings, the torque ripple of SynRM reduces to a minimum value indicated by the symbol Ⓜ in Fig. 3.5. This can be seen for θ_{b1}=7.5°, θ_{b2}=17° and θ_{b3}=27°.

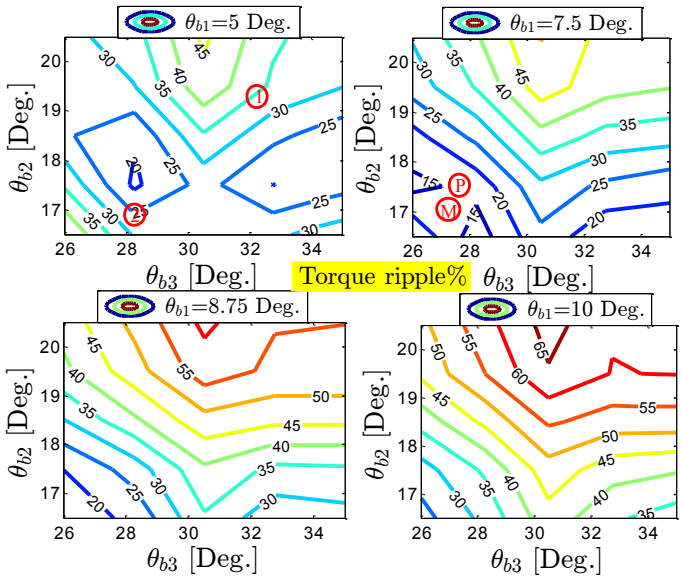

Figure 3.5: Torque ripple (in percent) of the reference SynRM versus different flux-barrier angles at rated conditions.

3.4.2 The effect of the flux-barrier widths W_{bi}

The flux-barrier widths W_{b1}, W_{b2} and W_{b3} are defined as shown in Fig. 3.1. The range of the flux-barrier widths is given in Table 3.3. The flux-barrier angles: θ_{b1}=7.5°, θ_{b2}=17.5° and θ_{b3}=27.5° are selected based on the first case (**Section 3.3.1**). Again, all the other rotor parameters are kept constant and equal to their value in the reference design given in Table 3.1.

Figure 3.6 shows the variation of the SynRM saliency ratio for different flux-barrier widths at rated conditions. The maximum and the minimum saliency ratios are approximately 5.51 and 2.64 (about 109% difference, compared to the minimum value) respectively. It is obvious

that the saliency ratio increases with increasing flux-barrier widths W_{b1}, W_{b2} and W_{b3}. This is mainly due to the increasing q-axis magnetic reluctance. In addition, the d-axis flux path area decreases. Therefore, the d-axis inductance decreases a bit too. However, the effect on the q-axis is much stronger so that the saliency ratio increases with increasing flux-barrier widths.

Table 3.3: The constraints on the flux- barrier widths.

Variable	Minimum	Maximum
W_{b1}	2 mm	8 mm
W_{b2}	1 mm	6 mm
W_{b3}	1 mm	4 mm

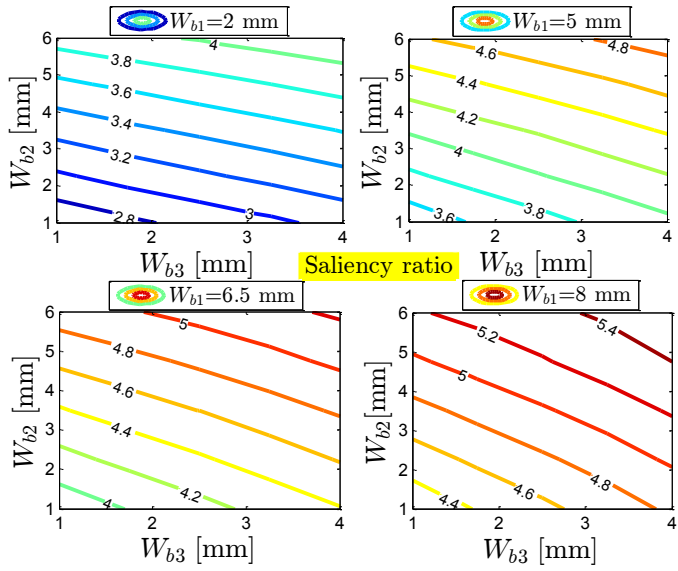

Figure 3.6: Saliency ratio of SynRM versus different flux-barrier widths at rated conditions.

The computed torque of the SynRM for different flux-barrier widths is clarified in Fig. 3.7. It is noticed that the flux-barrier widths have a large effect on the SynRM torque. The SynRM torque depends mainly on the saliency ratio L_d/L_q which in turn depends on the barrier width.

The computed maximum and minimum torque values are 16.06 N.m and 12.21 N.m (about 31.5% difference, compared to the minimum value) respectively. In general, the SynRM torque increases with increasing the flux-barrier widths. Furthermore, it can be deduced that the variation of W_{b1} has a much higher effect on the SynRM torque compared to the variation of both W_{b2} and W_{b3}.

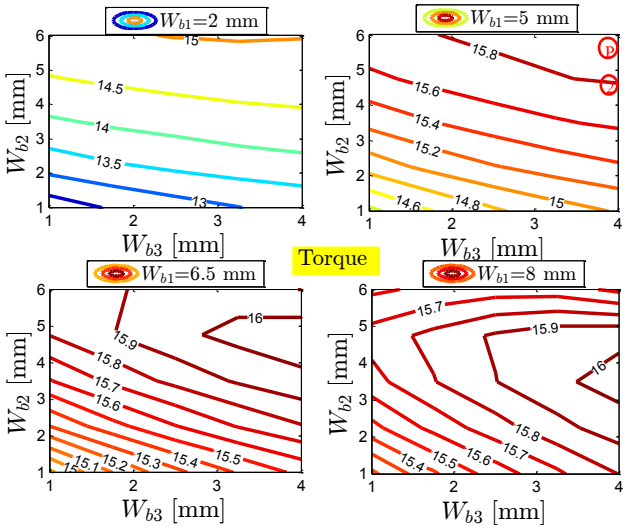

Figure 3.7: Output torque of the reference SynRM versus different flux-barrier widths at rated conditions.

Figure 3.8 displays the torque ripple (in percent) versus the variation of the flux-barrier widths. The maximum and the minimum torque ripple percentage values are 26.52% and 10.50% (about 152.5% difference, compared to the minimum value) respectively. The difference in the torque ripple is large and can be explained in a similar way as in paragraph **3.4.1**. An important conclusion here is that the torque ripple seems to remain very low regardless of the choice of the barrier width parameters.

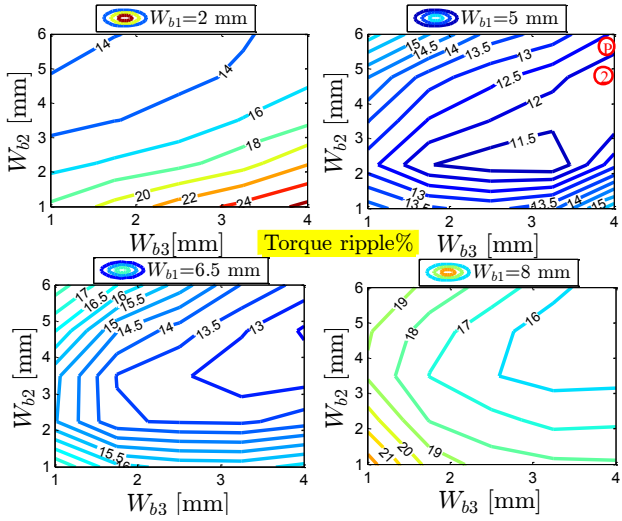

Figure 3.8: Torque ripple (in percent) of the reference SynRM versus different flux-barrier widths at rated conditions.

3.4.3 The effect of the flux-barrier lengths L_{bi}

The flux-barrier lengths L_{b1}, L_{b2} and L_{b3} are defined as shown in Fig. 3.1. The constraints on the flux-barrier lengths are given in Table 3.4. The flux-barrier angles (θ_{b1}=7.5°, θ_{b2}=17.5° and θ_{b3}=27.5°) and widths (W_{b1}=7 mm, W_{b2}=4.5 mm and W_{b3}=4 mm) have been selected based on the previous two cases (**3.3.1** and **3.3.2**). All the other rotor parameters are kept constant and equal to the values in Table 3.1.

Table 3.4: The constraints on the flux-barrier lengths.

Variable	Minimum	Maximum
L_{b1}	15 mm	40 mm
L_{b2}	5 mm	30 mm
L_{b3}	5 mm	15 mm

Figure 3.9 shows the variation of the SynRM saliency ratio for different flux-barrier lengths. It is clear that there is an effect on the saliency ratio due to different flux-barrier lengths. The maximum and the minimum saliency ratios are approximately 5.70 and 5.21 (about

9.39% difference, compared to the minimum value) respectively. This means that the effect of L_{b1}, L_{b2} and L_{b3} on the saliency ratio is rather low. The saliency ratio of the SynRM increases with an increased L_{b1} till a specified limit and then decreases again. Concerning L_{b2}, there seems to be an optimum value. For L_{b3}, an important observation is that its effect is almost negligible. In fact, the variation of the saliency ratio is mainly due to the variation of the *d*-axis magnetic reluctance.

Figure 3.10 describes the computed output torque of the SynRM for different flux-barrier lengths. The computed maximum and minimum torque values are 16.07 N.m and 14.25 N.m (about 13% difference, compared to the minimum value) respectively. In general, the SynRM torque increases with increasing the L_{b1} and L_{b2}. Also here, the effect of L_{b3} is negligible.

Figure 3.11 illustrates the variation of the torque ripple (in percent) versus the flux-barrier lengths. It can be noticed that there is a quite strong effect of the flux-barrier lengths on the torque ripple values, although much less than the effect of the flux-barrier angles. The maximum and minimum torque ripple percentage values are 24.55% and 14.03% (about 75% difference, compared to the minimum value) respectively.

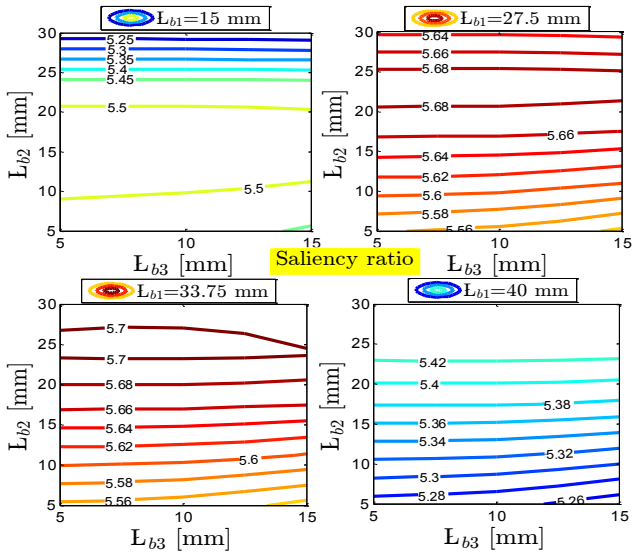

Figure 3.9: Saliency ratio of the reference SynRM versus different flux-barrier lengths at rated conditions.

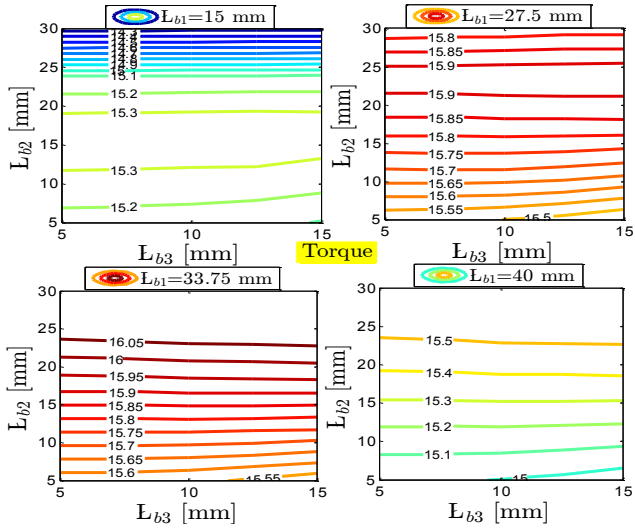

Figure 3.10: Output torque of the reference SynRM versus different flux-barrier lengths at rated conditions.

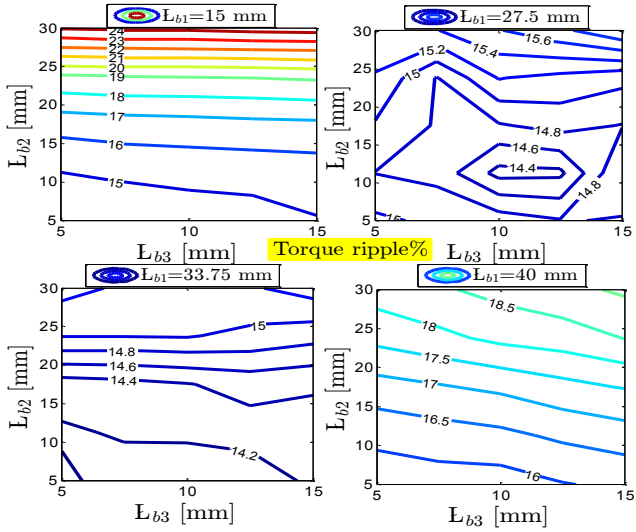

Figure 3.11: Torque ripple (in percent) of the reference SynRM versus different flux-barrier lengths at rated conditions.

3.4.4 The effect of the flux-barrier positions P_{bi}

The flux-barrier positions p_{b1}, p_{b2} and p_{b3} are defined as shown in Fig. 3.1. The flux-barrier positions are varied as given in Table 3.5. The flux-barrier angles (θ_{b1}=7.5°, θ_{b2}=17.5° and θ_{b3}=27.5°), widths (W_{b1}=7 mm, W_{b2}=4.5 mm and W_{b3}=4 mm) and lengths (L_{b1}=33.5 mm, L_{b2}=24 mm and L_{b3}=15 mm) have been selected based on the previous three cases.

Table 3.5: The constraints on the flux-barrier positions.

Variable	Minimum	Maximum
p_{b1}	18 mm	25 mm
p_{b2}	33 mm	38 mm
p_{b3}	45 mm	47 mm

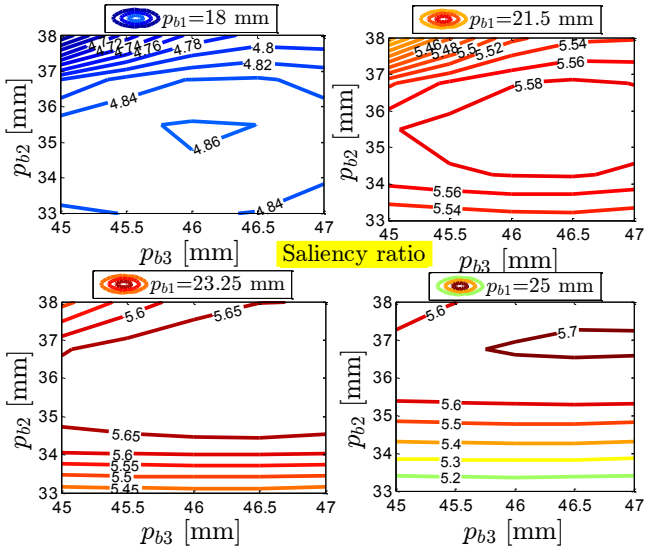

Figure 3.12: Saliency ratio of the reference SynRM versus different flux-barrier positions at rated conditions.

Figure 3.12 shows the variation of the SynRM saliency ratio for different flux-barrier positions. The maximum and the minimum saliency ratios are approximately 5.71 and 4.62 (about 23.6%

difference, compared to the minimum value) respectively. It is clear that the saliency ratio increases with increasing p_{b1}. However, the influence of p_{b2} depends on p_{b1}. On the other hand, the effect of p_{b3} can be neglected. The variation of the flux-barrier positions leads to a variation of mainly the *d*-axis magnetic reluctance, hence, the saliency ratio.

Figure 3.13 shows the computed torque of the SynRM for different flux-barrier positions. The computed maximum and minimum torque values are 16.08 N.m and 13.39 N.m (about 20% difference, compared to the minimum value) respectively. The variations of p_{b1} and p_{b2} have a notable effect on the SynRM torque. However, the effect of p_{b3} can be neglected.

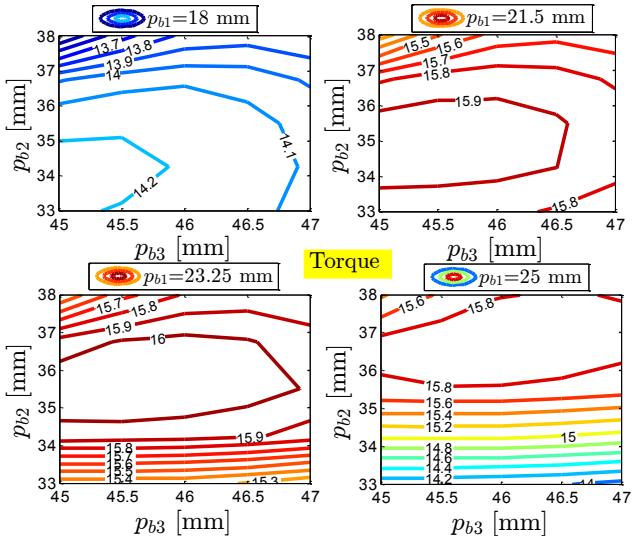

Figure 3.13: Output torque of SynRM versus different flux-barrier positions at rated conditions.

The variation of the torque ripple percentage value due to different flux-barrier positions is reported in Fig. 3.14. The torque ripple decreases with increasing the flux-barrier positions. The maximum and minimum torque ripple percentage values are 25% and 14.5% (about 72% difference, compared to the minimum value) respectively.

From Figs. 3.9 to 3.14, the flux-barrier positions are chosen to be p_{b1}=23.5 mm, p_{b2}=36 mm and p_{b3}=46 mm (similar to the reference values given in Table 3.1). The SynRM performance indicators

(saliency ratio, torque and torque ripple) which are corresponding to the selected three barrier parameters as a result of the aforementioned sensitivity analysis are 6.5, 16.3 N.m and 12.5% respectively. This result will be compared later with the SynRM performance indicators of an optimal rotor design to show how far the sensitivity analysis method compared to the optimal method.

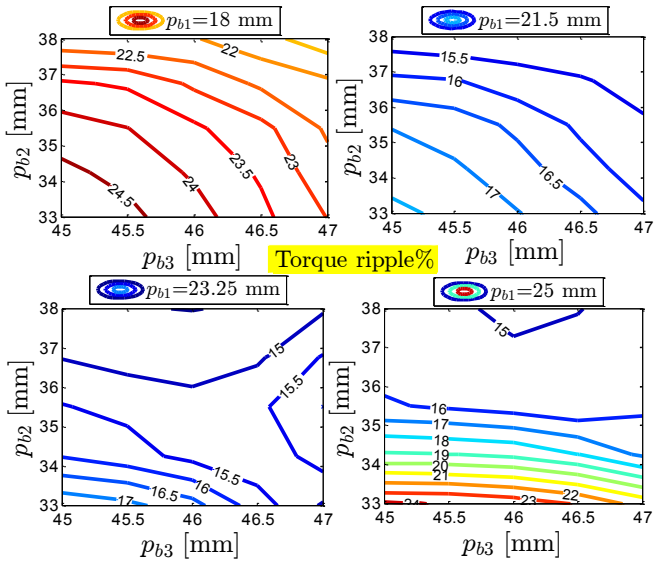

Figure 3.14: Torque ripple (in percent) of the SynRM versus different flux-barrier positions at rated conditions.

3.5 Easy-to-use equations for selecting the flux-barrier angle and width

As shown before, the two crucial rotor design parameters of the SynRM are the flux-barrier angles and widths. This is because the flux-barrier angles have a huge influence on the SynRM torque ripple, and the flux-barrier widths have a strong effect on the SynRM average torque [18]. Therefore, we propose simple approaches and/or parametrized equations for a better selection of these two SynRM rotor parameters to be used in the optimization with FEM and/or the sensitivity analysis. This will reduce the consumption of computation time to obtain a good SynRM rotor design.

In the following paragraph, three existing methods to choose the flux-barrier angle and one existing method for the flux-barrier width are compared with the proposed method. The accuracy of the methods is benchmarked for several machines.

3.5.1 Selection of the flux-barrier angle and width

(a) Flux-barrier angle selection

Three methods described in literature are presented here to choose the flux-barrier angles in order to obtain a preliminarily design for the SynRM with low torque ripple [15]–[18].

- The first method [15] simply correlates the number of stator slots n_s and rotor slots n_r per pole pair as follows:

$$n_r = n_s \pm 4 \tag{3.1}$$

  where n_r and n_s must be even and the rotor pitch angle (γ) is constant between the flux-barriers as sketched in Fig. 3.15-a.
- The second method was investigated in [16] and it is a refinement of the first method. The authors introduced an additional angle β, see Fig. 3.15-b, to generalize [15]. This angle β is used to control the value of the rotor slot pitch angle γ as follows:

$$\gamma = \frac{\frac{\pi}{2P} - \beta}{n_{layer} + 0.5} \tag{3.2}$$

  where n_{layer} is the number of flux-barrier layers and P is the number of pole pairs.
- The third method was presented in [17] by assuming that $\beta=\gamma/2$ in (3.2). In addition, the authors added an additional factor N, which is equal to n_s/n_r to generalize the method for different numbers of stator and rotor slots as follows:

$$\gamma = \frac{\frac{\pi}{2P}}{N\left(n_{layer} + 1\right)} \tag{3.3}$$

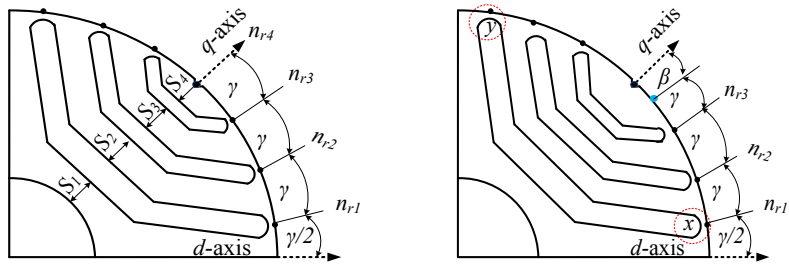

(a) First method (b) Second method

Figure 3.15: Geometrical parameters of a SynRM rotor with 4 poles and three flux-barriers according to the first method [15] and the second method [16].

More literature is published about the flux-barrier design, allowing to improve the SynRM torque ripple. The previous methods for selecting the flux-barrier angles, use equally spaced rotor slots, see Fig. 3.15, like that of the stator slots distribution. Nevertheless, asymmetrical rotor slot angles can be used too as investigated in [21]. It is proved in the literature that the torque ripple of a SynRM can be reduced by selecting unequally spaced rotor slots [21]. In addition, a method to reduce the torque ripple of SynRMs is given in [17]; the flux-barrier angles, see circles in Fig. 3.15-b, should be selected such that when the first end (x) moves towards the opening of the corresponding stator slot, the second end (y) moves away from the opening of the corresponding stator slot opening at the same time. This results in positive and negative torque pulsations during the motor operation. Eventually, the positive and negative torque pulsations may cancel each other, resulting in a reduced torque ripple for the SynRM.

As a result of the aforementioned literature methods, we propose an angle β, see Fig. 3.1, and use it to control the rotor slot pitch angle γ. Here, the slot pitch angle γ of the first flux-barrier layer closest to the *d*-axis (see Fig. 3.15) is not equal to the pitch angles between the other flux-barrier layers. This results in two easy-to-use parametrized equations for choosing the flux-barrier angles. The proposed method is generalized for any number of flux-barrier layers and poles as follows:

$$\beta = \frac{\pi}{4Pn_{layer}} \tag{3.4}$$

$$\gamma = \left(\frac{1}{n_{layer}}\right)\left(\frac{\pi}{2P} - 2\beta\right) \tag{3.5}$$

where n_{layer} is the number of flux-barrier layers, γ is the rotor slot pitch angle and β is an angle as sketched in Fig. 3.15. The proposed method considers that the rotor and stator slot openings are identical because this helps in reducing the torque ripple of the SynRM [17].

(b) Flux-barrier width selection

In order to choose the flux-barrier width of the SynRM rotor, the authors of the second method, which is mentioned before, presented an easy equation given by [16], [18]:

$$W_{bt} = K_{wq} * W_{it} \tag{3.6}$$

where W_{bt} is the total flux-barrier width ($W_{b1} + W_{b2} + W_{b3}$ in Fig. 3.15) and W_{it} is the total iron width in the q-axis direction. The width of the different flux-barriers is equal. They proved by several FEM simulations that the optimum value for K_{wq} is around 0.6-0.7.

It is evident that (3.6) does not consider the effect of the stator teeth width. Therefore, we propose the following simple equation in which the effect of the stator teeth width is included:

$$W_b = \frac{W_{tq} - W_{th}(n_{layer} + 1)}{n_{layer}} \tag{3.7}$$

where W_b and W_{th} are the width of the flux-barrier and the stator teeth respectively; W_{tq} is the total width of the iron in the q-axis direction and n_{layer} is the number of flux-barrier layers.

The total width W_{tq} in the q-axis direction is computed by:

$$W_{tq} = \frac{D_r - D_{sh}}{2} \tag{3.8}$$

where D_r and D_{sh} are the rotor outer diameter and the shaft diameter respectively. The width of all the flux-barriers is equal as in (3.6). In addition, the width of the rotor iron segment (S_1, S_2, S_3 and S_4 in Fig. 3.15-a) is equal to the stator teeth width.

3.5.2 Accuracy of the easy-to-use equations

In order to compare the methods existing in literature with the proposed one, the sensitivity analysis on the flux-barrier angles and widths presented in **Section 3.4** is used. The results of the proposed method, given by (3.4) and (3.5), and the aforementioned three methods, given by (3.1), (3.2) and (3.3) are allocated in Figs. 3.4 and 3.5 in **Section 3.4**. The abbreviations Ⓟ, ①, ② and ③ refer to the proposed, first, second and third methods respectively. Note that only the flux-barrier angles are different between the several methods and the other geometrical parameters are constant. Besides Figs. 3.4 and 3.5, the output torque and the torque ripple of the SynRM designs based on the different methods are listed in Table 3.6. The output torque and torque ripple of SynRM based on both methods ① and ② are approximately displayed in Figs. 3.4 and 3.5 at θ_{b1}=5°. In addition, the output torque and torque ripple based on the method ③ cannot be displayed in Figs. 3.4 and 3.5 because the flux-barrier angles based on this method are out of the considered range. However, their values are mentioned in Table 3.6 and lead to a SynRM design with high torque ripple. From Figs. 3.4, 3.5 and Table 3.6, it is clear that the proposed method Ⓟ gives a flux-barrier angle design with the lowest torque ripple of about 12.63%. On the other hand, the average torque based on the proposed method Ⓟ is much better, compared to the others. It is important to point out that the exact values of torque and torque ripple mentioned in Table 3.6 may not be indicated in Figs. 3.4 and 3.5, because the contour plots show only the trends of the variation of the parameters. Note that the results shown in Figs. 3.4 and 3.5 consider the flux-barrier end arc is equal to half of the flux barrier width, given in Table 3.1. While for the proposed and the existing methods, the flux-barrier end arc is equal to the slot opening. The variation of the flux-barrier end arc also has a slight influence on the average torque and torque ripple.

The proposed method Ⓟ is not only validated for a SynRM rotor with three flux-barrier layers, but also for four and five flux-barrier layers and compared with the three existing methods ①, ② and ③. This is to show its effectiveness for both odd and even numbers of flux-barrier layers. It is important to highlight that the comparison between the different methods is done for similar electromagnetic and geometrical parameters. Only the flux-barrier angles are chosen based on the method.

Table 3.6: Comparison between proposed Ⓟ and 3 existing methods for selecting flux-barrier angles of three barriers.

Variable	Ⓟ	①	②	③
θ_{b1}	7.5°	6.43°	5.62°	3.75°
θ_{b2}	17.5°	19.28°	16.87°	11.25°
θ_{b3}	27.5°	32.14°	28.12°	18.75°
Torque, N.m	15.63	15.04	15.41	14.50
Torque ripple	12.63%	36.3%	23.38%	42.34%

Table 3.7: Comparison between proposed Ⓟ and 3existing methods for selecting flux-barrier angles of four barriers.

Variable	Ⓟ	①	②	③
θ_{b1}	5.62°	5°	4.5°	4°
θ_{b2}	14.06°	15°	13.5°	12°
θ_{b3}	22.50°	25°	22.5°	20°
θ_{b4}	30.39°	35°	31.5°	28°
Torque, N.m	16.72	16.03	16.36	16.5
Torque ripple	25.45%	71.66%	20.24%	31.8%

In Table 3.7, it is clear that the proposed method Ⓟ gives a SynRM with four barriers rotor with a torque ripple of 25.45% which is lower than both methods ① and ③ and a bit more than method ②. Note that in case of a four flux-barrier rotor, the method ① is not valid. Therefore, it gives a flux-barrier angle design with a very high torque ripple: about 71.6%. For the four-barrier rotor, the average torque of the SynRM based on the proposed method Ⓟ turns out to be much better than the other methods. For five barriers (Table 3.8), it is obvious that the proposed method Ⓟ gives a SynRM with the lowest torque ripple and highest average torque compared to the existing methods. The torque ripple is about 20.30 % based on the proposed method Ⓟ. From

Tables 3.6, 3.7 and 3.8, it is clear that the proposed method, given by (3.5) and (3.6), gives better results than the existing methods, given by (3.1), (3.2) and (3.3), for the different number of flux-barrier layers.

Table 3.8: Comparison between proposed Ⓟ and 3 existing methods for selecting flux-barrier angles of five barriers.

Variable	Ⓟ	①	②	③
θ_{b1}	4.5°	4.09°	3.75°	4.16°
θ_{b2}	11.7°	12.27°	11.25°	12.45°
θ_{b3}	18.9°	20.45°	18.75°	20.83°
θ_{b4}	26.1°	28.63°	26.25°	29.16°
θ_{b5}	33.3°	36.81°	33.75°	37.50°
Torque, N.m	16.49	15.89	16.17	15.83
Torque ripple	20.30%	30.95%	24%	30.7%

3.6 Optimal design of the SynRM

A complete design of an electric machine contains the electromagnetic, mechanical and thermal behaviors. As mentioned before, the stator design of SynRM is the same as for an induction machine. Therefore, in this section an optimal selection of the rotor flux-barrier parameters is given. Moreover, a mechanical analysis is presented to check the robustness of the optimal rotor design. A brief information about the thermal behavior of the SynRM is addressed.

3.6.1 Electromagnetic design

The rotor flux-barrier parameters (12 parameters in total), shown in Fig. 3.1, have been optimized to obtain a compromise between a high output torque and a low torque ripple SynRM. For each of the three barriers, there are four parameters: the angle θ_{bj}, the width W_{bj}, the length L_{bj} and the position p_{bj} with j=1:3. Hence, this gives twelve rotor variables in total. The constraints on the twelve variables of the three flux-barriers are shown in Table 3.9. Note that – in contrast to the line searches in

the sensitivity analysis of **Section 3.4** – we now consider a full optimization of all 12 parameters together.

The FEM (**Section 2.4**) of the SynRM coupled with a Latin hypercube sampling technique is employed to obtain the optimal flux-barrier parameters [22], [23]. The twelve rotor parameters given in Table 3.9 are varied within the considered constrains by the optimization technique. Then the SynRM performance indicators are obtained. Figure 3.16 shows the variation of the motor output torque versus the torque ripple (in percent) for many SynRMs with different values of the twelve flux-barrier variables at the rated conditions. It is noticed that the selection of the rotor parameters has a strong effect on both the SynRM output torque and torque ripple. This is mainly caused by the dependency of the SynRM performance on the inductance difference (the difference between the *d* and *q*-axis inductances, L_d-L_q) which is a function of the rotor variables. A Pareto front line for the output torque and torque ripple values of several SynRMs is drawn in Fig. 3.16. The line is almost horizontal. This means that the torque ripple can be minimized to about 10% almost without sacrificing the output torque.

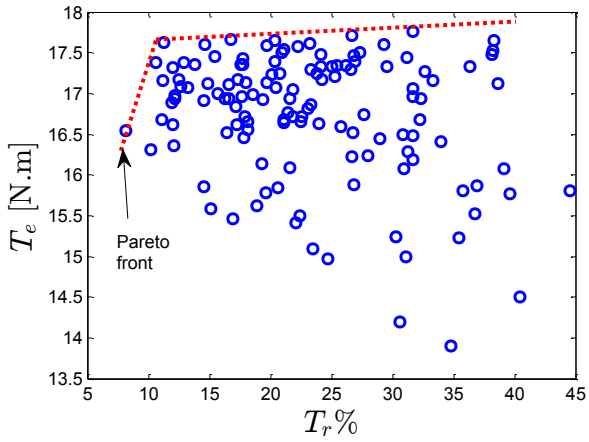

Figure 3.16: Output torque versus torque ripple for SynRM with different flux-barrier variables (Table 3.9) at the rated conditions

A selection for the twelve rotor parameters is shown in Table 3.10 to obtain an optimal SynRM performance. This selection is a good

comprise between the high output torque (17.76 N.m) and the low torque ripple (10%) as reported in Fig. 3.16.

Table 3.9: Constraints on the three flux-barrier variables.

Variable	Minimum	Maximum
θ_{b1}	5°	10°
θ_{b2}	16.5°	20.5°
θ_{b3}	26°	35°
W_{b1}	1mm	8 mm
W_{b2}	1 mm	6 mm
W_{b3}	1 mm	4 mm
L_{b1}	5 mm	40 mm
L_{b2}	5 mm	30 mm
L_{b3}	5 mm	15 mm
p_{b1}	18 mm	25 mm
p_{b2}	33 mm	38 mm
p_{b3}	42 mm	47 mm

Table 3.10: Optimal flux-barrier parameters of SynRM.

Parameter	Value	Parameter	Value
θ_{b1}	8.08°	W_{b1}	5.5 mm
θ_{b2}	16.43°	W_{b2}	3.5 mm
θ_{b3}	28.4°	W_{b3}	3.5 mm
L_{b1}	28.85 mm	p_{b1}	22.75 mm
L_{b2}	28 mm	p_{b2}	35.5 mm
L_{b3}	13.5 mm	p_{b3}	44.2 mm

Figure 3.17 compares the output torque and torque ripple of the SynRM design based on the easy-to-use proposed method (**Section 3.5**) and the optimal one. For the machine of the rotor design using the proposed method, all the parameters are fixed to the reference parameters given in Table 3.1 expect to the flux-barrier angles and widths. The flux-barrier angles and widths are selected based on the proposed equations (3.4), (3.5), (3.7) and (3.8). The resulting average torque and torque ripple of the SynRM with the optimal rotor design are about 17.76 N.m and 10 % respectively, as seen in Fig. 3.17 compared to 16.65 N.m and 11.5 % for the proposed method and compared to 16.3 N.m and 12.5% for the sensitivity analysis method (**Section 3.4**). This means that the design of the flux-barrier angles and widths based on the proposed method is close to the optimal choice.

A complete investigation of the optimal SynRM design will be shown in the next Chapters.

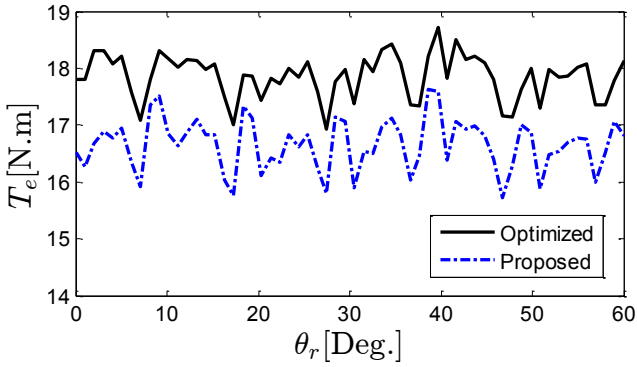

Figure 3.17: SynRM output torque versus the rotor position at the rated conditions, for the optimized SynRM, and for the SynRM designed via the proposed method with easy-to-use equations

3.6.2 Mechanical validation of the optimal rotor

The mechanical check for the robustness of the rotor design, especially the critical points such as the flux-barrier ribs is necessary. This is because the rotation forces may cause deformation in such points. The rotor deformation is a challenge in SynRMs because of the small length of the airgap and flux-barrier ribs as well.

FEM is used to emulate the stresses (Von-Mises stress) and deformations on the rotor design. The mechanical properties of the rotor iron laminations (M330-50A) are given in Table 3.11 [24].

Figures 3.18 to 3.21 show the applied load by means of centrifugal forces, stress and deformation for the optimal rotor at 6000 rpm (double rated speed). It is clear that the maximum stress is 235 MPa which is lower than the limit given (355 MPa) in Table 3.11 for the rotor material. This means that there is a safety margin of about 35%, which is acceptable based on the literature [17], [18]. The maximum deformation is 20 micrometer as seen in Fig. 3.21. This is only about 6.6% of the air gap length and also of the minimum flux-barrier rib.

Table 3.11: Mechanical specifications of rotor steel (M330-50A).

Parameter	Quantity	Unit
Yield stress	355	MPa
Tensile stress	490	MPa
Elasticity	$2.1e^{11}$	Pa
Poisson's ratio	0.29	

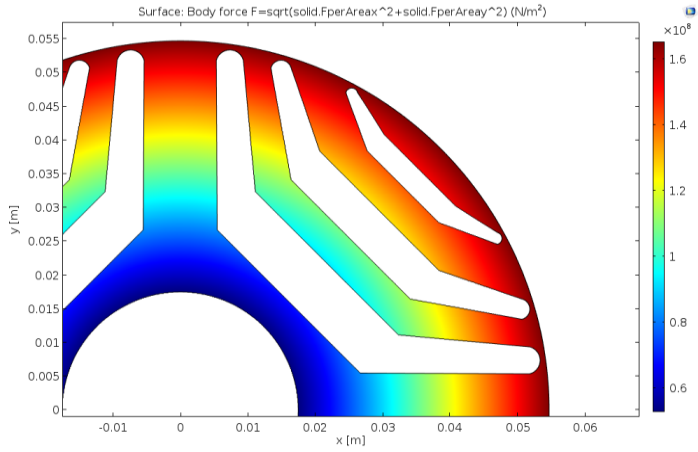

Figure 3.18: Applied force density per meter axial length, only considering centrifugal force, for the optimized SynRM rotor at 6000 rpm (double rated speed).

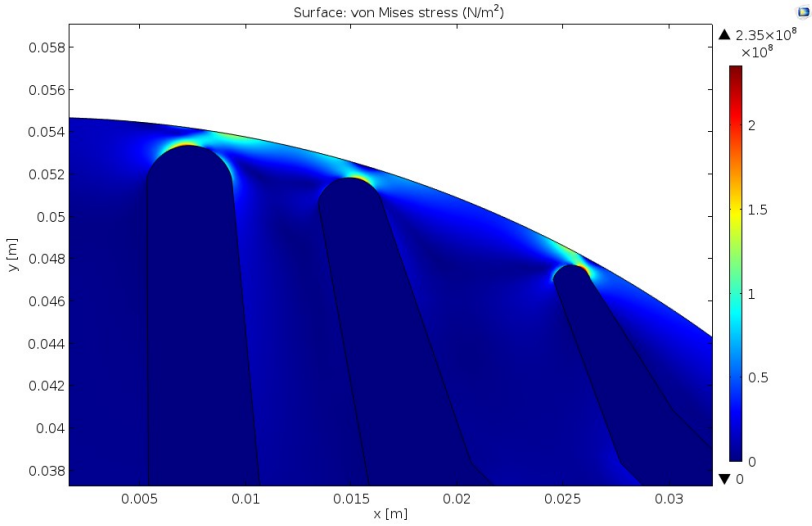

Figure 3.19: Von Mises stress showing a maximum of 235 MPa, for the optimized rotor at 6000 rpm. Zoom in of the geometry. The color scale is NOT truncated.

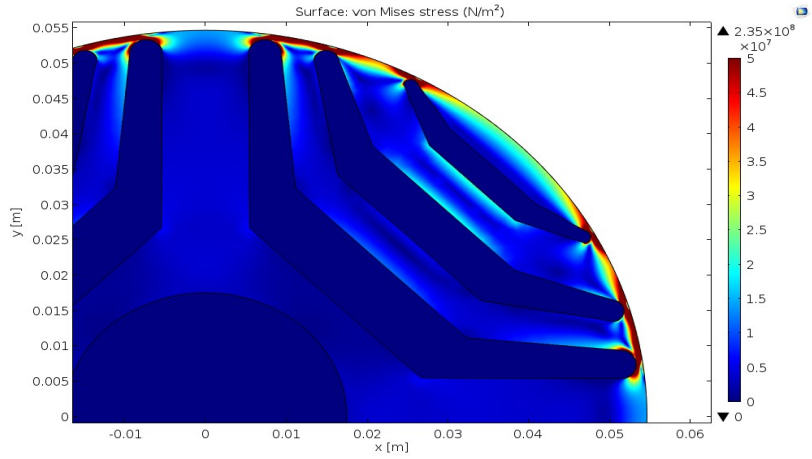

Figure 3.20: Von Mises stress showing a maximum of 235 MPa, for the optimized machine at 6000 rpm. The color scale is truncated to 50 MPa for clear visibility.

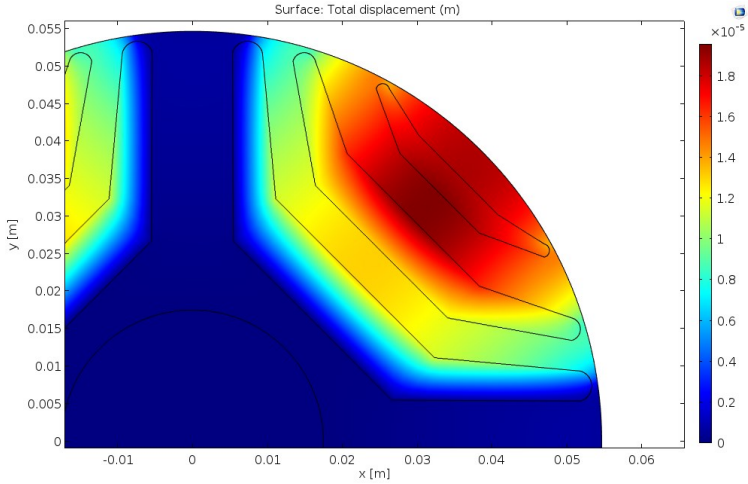

Figure 3.21: Deformation showing a maximum of almost 20 micrometer, for the optimized machine at 6000 rpm.

3.6.3 Thermal analysis of the optimal SynRM

A high current density in the stator windings results in high copper losses and by consequence high hot-spot temperatures. To transfer the generated heat to the ambient, fins on the stator housing are commonly used. In addition, forced air cooling is employed by using a shaft mounted fan. This is to improve heat transfer from the housing fins and sometimes from the end winding and rotor surfaces. However, for high current density, the air forced cooling approach may not be sufficient and other cooling methods may be required. A water jacket in the stator housing is another possible way that enables an effective heat transfer from the stator winding active part to the coolant [25]–[29].

As we mentioned before, the stator of the SynRM is an induction motor stator that has been designed taking into account the thermal issues. The optimization of the rotor of the SynRM results in a machine with still almost the same mechanical rated power as the original induction machine. In addition, as the rotor of SynRM has much lower losses than that of the corresponding induction machine, we can be sure that no overheating will occur as long as we stick to the same rated current in the stator, the same rated speed and approximately the same mechanical power. This means that there is no need to investigate the thermal part of the SynRM. Consequently, we do not focus our study in the thermal of this machine.

For the prototype machines, the forced air cooling method is employed by using a shaft mounted fan.

3.7 Conclusions

This chapter has presented the design of synchronous reluctance motors (SynRMs), in particular the rotor design. A sensitivity analysis of the flux-barrier geometry in the rotor of SynRM is done and the effects of different rotor geometry parameters on the machine performance indicators (the saliency ratio, output torque and torque ripple %) are shown as in Table 3.12. The influence of the highest rotor parameter on the performance indicators is highlighted in the Table 3.12.

Table 3.12: Influence of flux-barriers variation on the SynRM.

Parameter	*Saliency ratio*	*Torque, N.m*	*Torque ripple%*
Different angles, θ_{bi}	20.69%	10%	444%
Different widths, W_{bi}	109%	31.5%	152.5%
Different lengths, L_{bi}	9.4%	13%	75%
Different positions, p_{bi}	23.6%	20%	72%

Moreover, a simple method (parametrized equations) for choosing the two most crucial rotor parameters of SynRMs i.e. the flux-barrier angle and width is proposed. The proposed approach is compared to three existing methods in the literature for different numbers of flux-barrier layers i.e. 3, 4 and 5 per pole. It is proved that the proposed method is effective in choosing the flux-barrier angles and widths. The SynRM torque ripple and average torque based on the proposed method are better than the considered literature methods. This results in a good SynRM design. This "starting point" design can be further optimized via FEM based optimization routines. Thanks to a good "starting point", the required computation time for the optimization is reduced.

Finally, an optimized technique coupled with FEM to obtain an optimal selection for the flux-barrier parameters has been investigated. An optimal rotor design for the SynRM is obtained. The optimal rotor

is checked mechanically towards the robustness, showing an acceptable mechanical design.

Biography

[1] C. M. Spargo, B. C. Mecrow, J. D. Widmer, C. Morton, and N. J. Baker, "Design and validation of a synchronous reluctance motor with single tooth windings," *IEEE Trans. Energy Convers.*, vol. 30, no. 2, pp. 795–805, Jun. 2015.

[2] C. M. Spargo, B. C. Mecrow, J. D. Widmer, and C. Morton, "Application of fractional-slot concentrated windings to synchronous reluctance motors," *IEEE Trans. Ind. Appl.*, vol. 51, no. 2, pp. 1446–1455, Mar. 2015.

[3] H. Kiriyama, S. Kawano, Y. Honda, T. Higaki, S. Morimoto, and Y. Takeda, "High performance synchronous reluctance motor with multi-flux barrier for the appliance industry," in *Conference Record of 1998 IEEE Industry Applications Conference. Thirty-Third IAS Annual Meeting (Cat. No.98CH36242)*, vol. 1, pp. 111–117.

[4] H. Azizi and A. Vahedi, "Rotor geometry parameter optimization of synchronous reluctance motor using taguchi method," *Prz. Elektrotechniczny*, pp. 197–201, 2013.

[5] D. Prieto, P. Dessante, J. Vannier, B. Dagusé, X. Jannot, and J. Saint-Michel, "Multi-physic analytical model for a saturated permanent magnet assisted synchronous reluctance motor," *IET Electr. Power Appl.*, vol. 10, no. 5, pp. 356–367, May 2016.

[6] N. Bianchi and B. J. Chalmers, "Axially laminated reluctance motor: analytical and finite-element methods for magnetic analysis," *IEEE Trans. Magn.*, vol. 38, no. 1, pp. 239–245, 2002.

[7] M. H. Mohammadi, T. Rahman, R. Silva, M. Li, and D. A. Lowther, "A efficient algorithm for rotor design optimization of synchronous reluctance machines," *IEEE Trans. Magn.*, vol. 52, no. 3, pp. 1–4, Mar. 2016.

[8] M. Nashiki, A. Satake, Y. Kawai, T. Yokochi, and S. Okuma, "A new flux-barrier-type reluctance motor with a slit rotor," *IEEE Trans. Ind. Electron.*, vol. 46, no. 6, pp. 1199–1206, 1999.

[9] M. N. Ibrahim, P. Sergeant, and E. M. Rashad, "Synchronous reluctance motor performance based on different electrical steel grades," *IEEE Trans. Magn.*, vol. 51, no. 11, pp. 1–4, Nov. 2015.

[10] J. Lee, I. Lee, Y. Cho, and T. Yun, "Characteristics analysis and optimum design of anisotropy rotor synchronous reluctance motor using coupled finite element method and response surface methodology," *IEEE Trans. Magn.*, vol. 45, no. 10, pp. 4696–4699, Oct. 2009.

[11] D. Prieto, P. Dessante, J.-C. Vannier, X. Jannot, and J. Saint-Michel, "Analytical model for a saturated permanent magnet assisted synchronous reluctance motor," in *2014 International Conference on Electrical Machines (ICEM)*, 2014, pp. 72–78.

[12] A. Hemeida and P. Sergeant, "Analytical modeling of surface pmsm using a combined solution of maxwells equations and magnetic equivalent circuit," *IEEE Trans. Magn.*, vol. 50, no. 12, pp. 1–13, Dec. 2014.

[13] C. Gutfrind, X. Jannot, J. C. Vannier, P. Vidal, and D. Sadarnac, "Analytical and FEM magnetic optimization of a limited motion actuator for automotive application," in *The XIX International Conference on Electrical Machines - ICEM 2010*, 2010, pp. 1–6.

[14] K. Wang, Z. Q. Zhu, G. Ombach, M. Koch, S. Zhang, and J. Xu, "Torque ripple reduction of synchronous reluctance machines," *COMPEL - Int. J. Comput. Math. Electr. Electron. Eng.*, vol. 34, no. 1, pp. 3–17, Jan. 2015.

[15] A. Vagati, M. Pastorelli, G. Francheschini, and S. C. Petrache, "Design of low-torque-ripple synchronous reluctance motors," *IEEE Trans. Ind. Appl.*, vol. 34, no. 4, pp. 758–765, 1998.

[16] R.-R. Moghaddam and F. Gyllensten, "Novel high-performance synrm design method: an easy approach for a complicated rotor topology," *IEEE Trans. Ind. Electron.*, vol. 61, no. 9, pp. 5058–5065, Sep. 2014.

[17] S. Taghavi and P. Pillay, "A novel grain-oriented lamination rotor core assembly for a synchronous reluctance traction motor with a reduced torque ripple algorithm," *IEEE Trans. Ind. Appl.*, vol. 52, no. 5, pp. 3729–3738, Sep. 2016.

[18] R. R. Moghaddam, *Synchronous Reluctance Machine (SynRM) in Variable Speed Drives (VSD) Applications*. KTH Royal Institute of Technology, 2011.

[19] M. J. Kamper, "Effect of rotor dimensions and cross magnetisation on Ld and Lq inductances of reluctance synchronous machine with cageless flux barrier rotor," *IEE Proc. - Electr. Power Appl.*, vol. 141, no. 4, p. 213, 1994.

[20] S. Bolognani, H. Mahmoud, and N. Bianchi, "Fast synthesis of permanent magnet assisted synchronous reluctance motors," *IET Electr. Power Appl.*, vol. 10, no. 5, pp. 312–318, May 2016.

[21] M. Sanada, K. Hiramoto, S. Morimoto, and Y. Takeda, "Torque ripple improvement for synchronous reluctance motor using an asymmetric flux barrier arrangement," *IEEE Trans. Ind. Appl.*, vol. 40, no. 4, pp. 1076–1082, Jul. 2004.

[22] P. S. Shin, S. H. Woo, Y. Zhang, and C. S. Koh, "An application of Latin hypercube sampling strategy for cogging torque reduction of large-scale permanent magnet motor," *IEEE Trans. Magn.*, vol. 44, no. 11, pp. 4421–4424, Nov. 2008.

[23] J. B. Kim, K. Y. Hwang, and B. I. Kwon, "Optimization of two-phase in-wheel IPMSM for wide speed range by using the Kriging model based on Latin hypercube sampling," *IEEE Trans. Magn.*, vol. 47, no. 5, pp. 1078–1081, May 2011.

[24] "isovac high-perm 330-50 A Data sheet • February 2015 Electrical steel," 2015.

[25] S. Pickering, P. Wheeler, F. Thovex, and K. Bradley, "Thermal design of an integrated motor drive," in *IECON 2006 - 32nd Annual Conference on IEEE Industrial Electronics*, 2006, pp. 4794–4799.

[26] P. Zheng, R. Liu, P. Thelin, E. Nordlund, and C. Sadarangani, "Research on the cooling system of a 4QT prototype machine used for HEV," *IEEE Trans. Energy Convers.*, vol. 23, no. 1, pp. 61–67, Mar. 2008.

[27] C. Kral, A. Haumer, and T. Bauml, "Thermal model and behavior of a totally-enclosed-water-cooled squirrel-cage induction machine for traction applications," *IEEE Trans. Ind. Electron.*, vol. 55, no. 10, pp. 3555–3565, Oct. 2008.

[28] Z. Huang, S. Nategh, V. Lassila, M. Alakula, and J. Yuan, “Direct oil cooling of traction motors in hybrid drives,” in *2012 IEEE International Electric Vehicle Conference*, 2012, pp. 1–8.

[29] S. Nategh, Z. Huang, A. Krings, O. Wallmark, and M. Leksell, “Thermal modeling of directly cooled electric machines using lumped parameter and limited CFD analysis,” *IEEE Trans. Energy Convers.*, vol. 28, no. 4, pp. 979–990, Dec. 2013.

Chapter 4

Influence of the Electrical Steel Grade on the SynRM Performance

4.1 Introduction

This chapter studies the effect of different steel grade on the SynRM performance i.e. output torque, power factor, torque ripple, iron losses and efficiency. Four different steel grades M600-100A, M400-50A, M330P-50A and NO20 are considered. All the electromagnetic and geometrical parameters of the SynRM are kept constant in this chapter. Only the material characteristics are varied.

4.2 Overview about electrical steel grade

The most used electrical steel that is employed in the core of the electric machines and transformers is an iron alloy. Apart from the iron, the silicon is a significant element in the electrical steel. This is because increasing the percentage of silicon up to about 6% leads to a reduction in the core losses and increases the electrical resistivity of the steel. Eventually, this leads to an improved efficiency for the electric machines and transformers [1].

Two types of the electrical steels can be found [1]:

- **Grain oriented electrical steel:** The grains of this material are oriented in a predefined direction. The magnetic properties of

this type of steel along the rolling direction (RD) are much better than the properties along the transverse direction (TD). Evidently, these materials are not isotropic: their behavior depends on the direction of the magnetic field and flux density vector. The grain oriented steels are normally employed in power transformers and recently in axial flux machines.

- **Non-oriented electrical steel:** These materials are more or less isotropic: only a small difference between the behavior in the rolling and transverse direction is observed. This material is employed in all different kinds of electric machines.

In the literature, several papers have investigated the influence of different electrical steel grades on the performance, in particular the output torque and efficiency, of electric machines [1]–[7]. In [2], the influence of soft magnetic material on the efficiency of a permanent magnet synchronous machine was investigated. It was shown that the efficiency of 1.5 kW PMSM has been increased by about 2% when replacing the stator iron of M800-50A by M235-35A. The first material has significantly higher electromagnetic losses than the second one, but also a higher thermal conductivity. The influence of four electrical steel grades on the temperature distribution in direct-drive PM synchronous generators for 5 MW wind turbines was given in [3]. It was found that for a direct-drive generator with 50 pole pairs, - a low number of pole pairs for a direct-drive generator - the thermal conductivity of the steel grade has a major influence on the temperature distribution due to the low electrical frequency. In addition, for a generator with a high number of pole pairs, e.g. 150 pole pairs, the magnetic properties of the electrical steel grade have a dominant influence on the temperature distribution. The performance and iron losses of an axial flux permanent-magnet synchronous machine (AFPMSM) were compared for both nonoriented (NO) and grain-oriented (GO) materials in [4]. It was found that the iron losses of the GO material are lower than the NO by about a factor 7 at the same speed. In addition, the GO material resulted in a 10% higher torque for the same current. Thanks to the 10% higher torque-to- current ratio, it is possible to reduce the copper losses by about 20%. In [5], a comparison of the performance of a direct-drive and single stage gearbox permanent magnet synchronous generator (PMSG) for wind energy based on two steel grades was presented. It was proved analytically that there is about 1% difference in the annual efficiency of two optimized generators using different steel grades. The design of highly efficient high-speed induction motors with optimally

exploited magnetic materials was investigated in [6]. Two steel grades were employed in two optimized 20-kW 30000-rpm induction machines, i.e. one incorporating a cobalt-iron alloy (Vacoflux 50), and the other one using silicon steel (M270-35A). It was shown that the air-gap flux-density in the Vacoflux 50 machine is about 20% higher than in the machine equipped with M270-35A. This leads to an increased torque density and efficiency of the Vacoflux 50 machine.

4.3 Characteristics of the four steel grades

In this section, the characteristics of the four employed steel grades are given. The four steel grades are NO20, M330P-50A, M400-50A and M600-100A. It is clear that these materials have different specific loss values and a different thickness. M600-100A for example has 1.0 mm thickness and maximally 6.0 W/kg losses at 50 Hz and 1.5 T. The magnetic characteristics of these four steel grades are obtained experimentally based on *Epstein* measurements of the laminations [1]. The single-valued *BH* curves of the four materials are shown in Fig. 4.1.

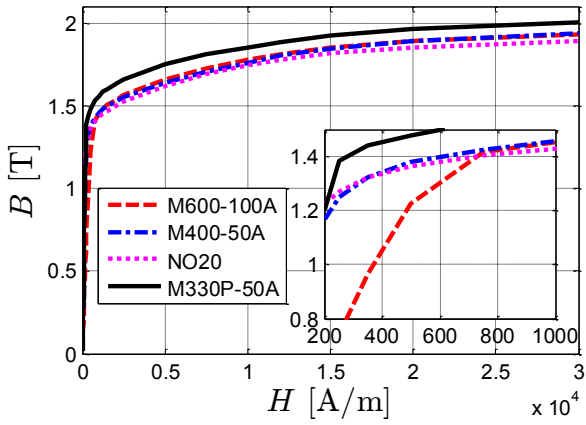

Figure 4.1: *BH* curves of the four considered magnetic material grades M600-100A, M400-50A, NO20 and M300P-50A.

Figure 4.1 shows the *BH* curves of the four electrical steel grades. It is obvious that M330P-50A has a higher flux density (B) for magnetic fields (H) higher than 250 A/m. Figure 4.2 shows the relative

permeability of the four materials as a function of the flux density B. Clearly, NO20 and M600-100A have the highest and lowest permeability compared to the other materials for H less than 250 A/m respectively. In addition, the flux-level saturation of M330P-50A is much higher than the other materials. This is expected to have an influence on the inductances of the SynRM, hence the overall performance.

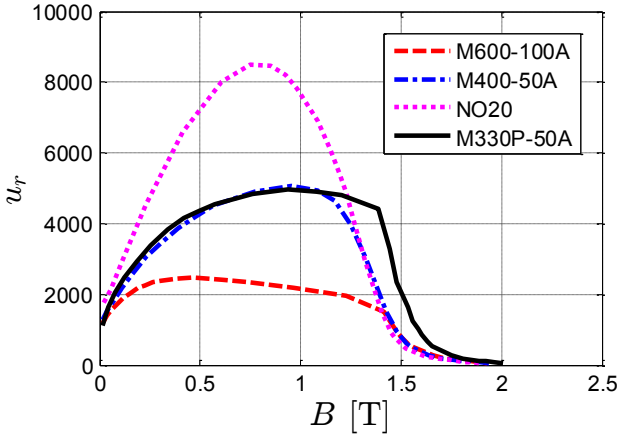

Figure 4.2: Relative permeability μ_r versus flux density B of M600-100A, M400-50A, NO20 and M300P-50A.

Figures 4.3 to 4.6 report the measured and the fitted iron losses curves of the four electrical steel grades (NO20, M330P-50A, M400-50A and M600-100A) for several frequencies. The nonlinear least squares method is used for fitting the irons losses. In this method, the difference in the measured and computed losses is divided by the frequency. This gives better fitting at low frequency (e.g. 50 Hz) but worse fitting at high frequency (e.g. 700 Hz). At 100 or 200 Hz, the fitting is reliable. This is the key point because these frequencies are dominant frequencies in our application. It is obvious from Figs. 4.3 to 4.6 that for the same frequency and flux density level, the iron losses of the materials differ too much. This means that the efficiency of the electric machine is affected by the electrical steel grade. The influence of different steel grades on the SynRM performance will be compared in the next section. Furthermore, it is observed that the fitted and measured curves of the losses of the four materials are matching very

well for lower frequencies: up to 200 Hz in the figures. However, for higher frequencies, there is a bit difference between the measured and the fitted curves.

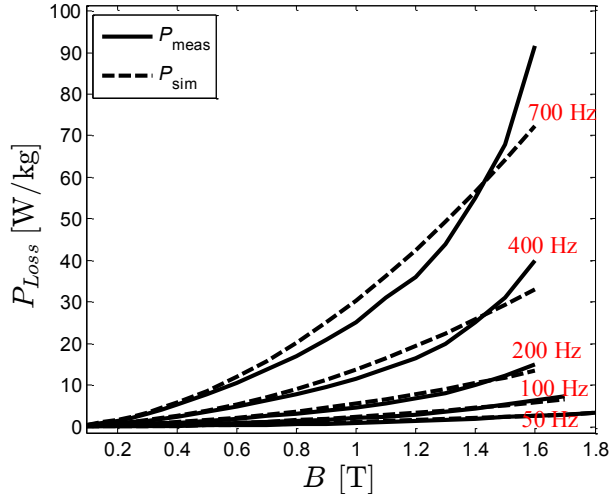

Figure 4.3: The iron losses of NO20 versus the flux density for several frequencies (50 Hz, 100 Hz, 400 Hz and 700 Hz).

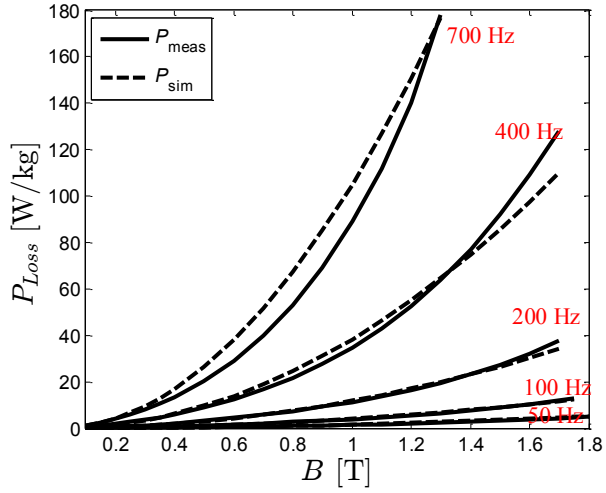

Figure 4.4: The iron losses of M330P-50A versus the flux density for several frequencies (50 Hz, 100 Hz, 400 Hz and 700 Hz).

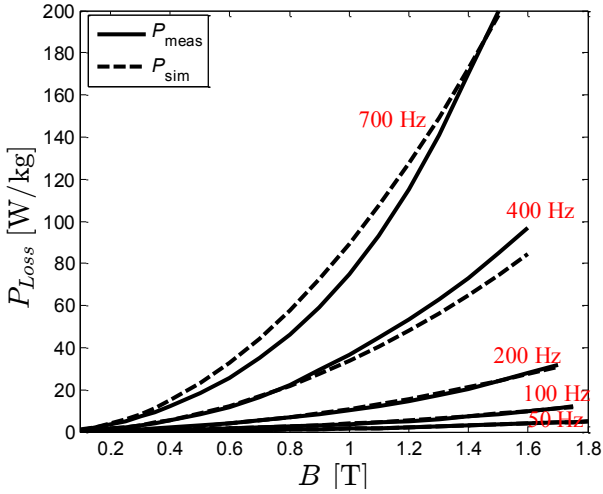

Figure 4.5: The iron losses of M400-50A versus the flux density for several frequencies (50 Hz, 100 Hz, 400 Hz and 700 Hz).

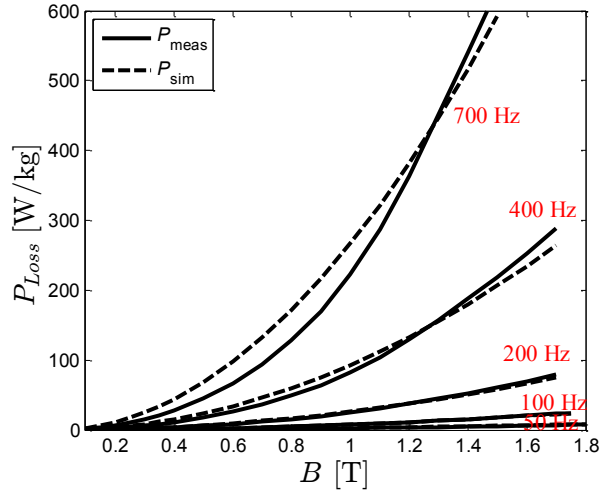

Figure 4.6: The iron losses of M600-100A versus the flux density for several frequencies (50 Hz, 100 Hz, 400 Hz and 700 Hz).

The iron losses in this thesis are calculated based on the statistical loss theory of Bertotti in the time domain as described in (4.1) [8]. The theory depends on loss separation into hysteresis, classical and excess losses. The geometry of the machine is divided into small segments. The magnetic flux density B for every segment has been obtained using the FEM at different rotor positions θ_r. This results in a machine without induced currents in the time domain waveforms $B_x(t)$, $B_y(t)$. In fact, the number of rotor positions that is used for the loss calculation for the SynRM has a strong effect on the loss value. This is due to the dependency of the magnetic reluctance of the SynRM on the rotor position. It is found that 300 rotor positions are enough for the model to obtain approximately the correct amount of losses in the machine. In other words, if the number of rotor positions increases to more than 300, the difference in the losses calculation is very small and this will lead to an increased computation time. The computed iron losses are based on the time vectors of the flux density [$B_x(t)$, $B_y(t)$] for each geometry segment of 300 rotor positions. Evidently, the fundamental frequency of these waveforms at the rated speed is the rated value in the stator and 0 Hz in the rotor. Both waveforms have a high harmonic content, causing iron loss in the rotor to be nonzero.

$$\left.\begin{aligned} P_{hyst} &= a_M B_p^{\alpha_M} f \\ P_{class}(t) &= b_M \left|\frac{dB}{dt}\right|^2 \\ P_{exc}(t) &= c_M \left(\sqrt{1 + d_M \left|\frac{dB}{dt}\right|} - 1\right)\left|\frac{dB}{dt}\right| \\ P_{iron} &= (P_{hyst} + P_{class} + P_{exc})\rho_i \end{aligned}\right\} \tag{4.1}$$

where a_M, α_M, b_M, c_M, d_M and ρ_i are material dependent parameters. ρ_i is density of the material and f is the frequency of the applied field.

The material parameters of (4.1) are obtained based on the measured and fitted loss curves presented before. It is worth mentioning that the accuracy of the loss model depends mainly on the material parameters.

4.4 Performance of the SynRM using different steel grades

In this section, the influence of the four electrical steel grades presented in **Section 4.3** on the SynRM performance (saliency ratio, output power, power factor, torque ripple and efficiency) is investigated. The SynRM geometry of Table 2.1 (**Chapter 2**) and the flux-barrier parameters of Table 3.1 (**Chapter 3**) are again used in this chapter.

The FEM of **Section 2.4** (**Chapter 2**) is combined with an experiment-based magnetic material model to study the effect of the four steel grades on the performance of the SynRM. All the results are computed at the same current and speed, namely the rated values (21.21 A and 6000 rpm) of the SynRM. In addition, the same geometry, mesh nodes and elements are considered. The number of nodes and elements of the FEM model are approximately 31238 and 56371 respectively. In the FEM simulations, the SynRM is working in torque control mode. This means that *dq*-axis currents are given and the motor is rotated at fixed speed.

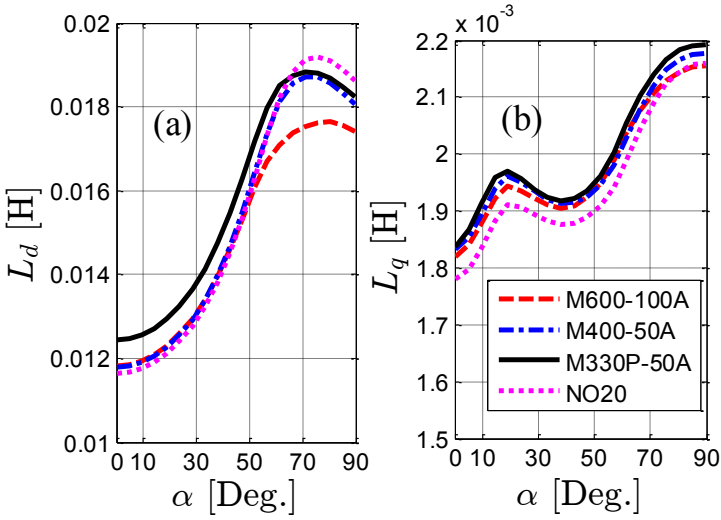

Figure 4.7: *dq*- axis inductances (L_d(a), L_q(b)) of the SynRM versus current angle α for four steel grades.

Figure 4.7 shows the variation of *d* and *q*-axis inductances (L_d, L_q) of the SynRM for different current angles under the four steel grades. The current angle is the angle between the stator current space vector with respect to the *d*-axis of the motor, see Fig. 2.2 (**Chapter 2**). It is noticed that for a similar current angle, the *dq*-axis inductances of SynRM vary for all the electrical steel grades. This is because the permeability of the materials is different as seen in Fig. 4.2. The saliency ratio (L_d/L_q) of the four machines is shown in Fig. 4.8. Clearly, there is a significant difference in the saliency ratio of the SynRM because of the material grade. The M330P-50A gives the largest saliency ratio while M600-100A gives the smallest value for a current angle less than the maximum power angle. This is indeed due to different saturation behavior (Fig. 4.1) between the materials. This has a direct effect on the saliency ratio as mentioned before. Consequently, the difference in saliency ratio of the materials shown in Fig. 4.8 will definitely make a variation on the motor performance as described on Fig. 4.9. This figure shows the motor output power for different current angles at rated speed (6000 rpm) under the four material grades. It is evident that M330P-50A yields the highest output power which is about 8% higher than for M600-100A because it has the higher saliency ratio, see Fig. 4.8.

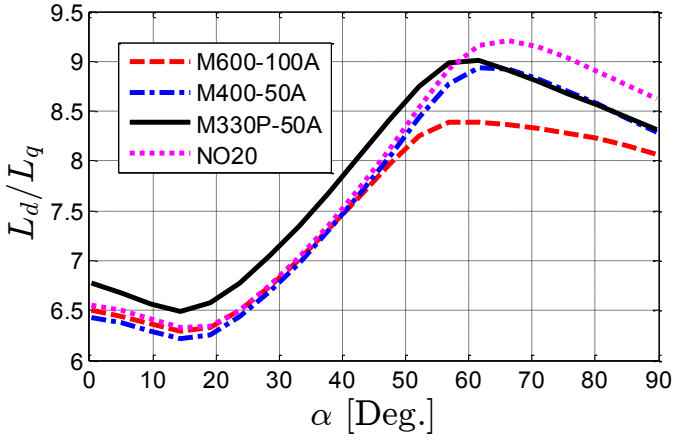

Figure 4.8: Saliency ratio L_d/L_q of SynRM versus current angle α for four steel grades.

Figure 4.10 shows the variation of the motor power factor as a function of the current angle for different materials. It is clear that the material grade has almost no influence on the power factor of the motor. This is because the difference in saliency ratio of the materials has a non-significant influence on the power factor angle, see Fig. 2.1. Furthermore, the power factor increases with increasing the current angle till an optimal value, then starts to decrease again. Note that, the maximum output power angle of SynRM (Fig. 4.9) is not the maximum power factor angle (Fig. 4.10).

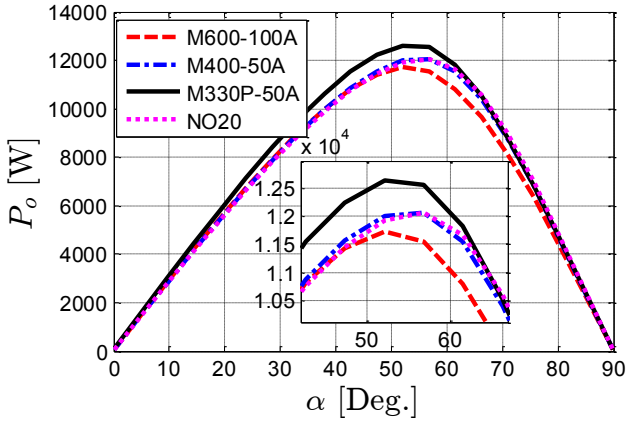

Figure 4.9: Output power P_o of SynRM versus current angle α for four steel grades at 6000 rpm.

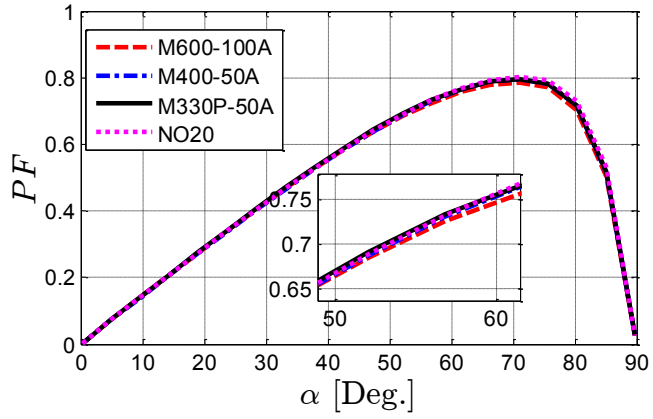

Figure 4.10: Power factor *PF* of SynRM versus current angle α for four steel grades at 6000 rpm.

Figure 4.11 shows the torque ripple (in percent) of the SynRM as a function of the current angle for different materials. It can be noticed that there is no difference in the torque ripple of the SynRM between the different materials. This is because the torque ripple depends mainly on the motor geometry, which is the same for all materials. However, the SynRM geometry under study has a rather high torque ripple: around 50% at the maximum power angle.

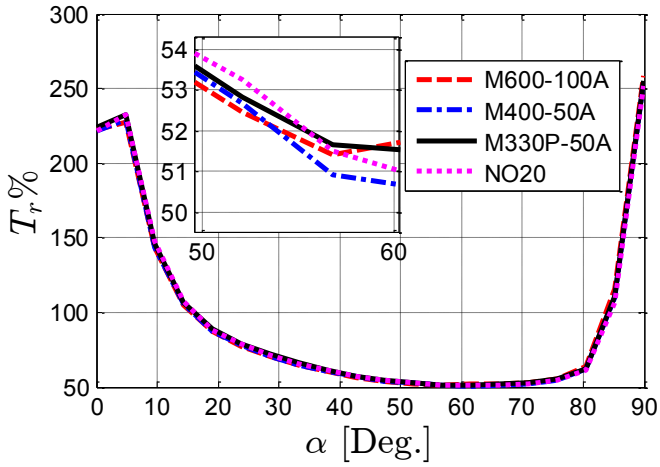

Figure 4.11: Torque ripple T_r% of SynRM versus current angle α for several steel grades at 6000 rpm.

Figure 4.12 shows the three phase flux linkages of the SynRM as a function of the mechanical rotation angle for different steel grades. It is clear that M330P-50A and M600-100A have the highest and lowest flux linkage respectively. This is due to the saliency ratio difference.

In order to compute the efficiency of the SynRM based on the different electrical steel grades, the iron losses calculation is necessary. The loss model presented **Section 4.3** is used to calculate the different iron loss components in the machine [8].

The iron losses are computed at the maximum power angle that is approximately 52^{o}: see Fig. 4.9. Moreover, several characteristics for the SynRM are included in Table 4.1. From the table, it can be noticed that NO20 gives the highest efficiency, which is about 9% point higher than for M600-100A. This is thanks to the low iron losses of NO20

compared with M600-100A (see Figs.4.3 and 4.6). The losses of NO20 machine are about 15.2% of the losses of M600-100A. However, the lower loss grades are more expensive both in raw material cost and in cutting cost [7]. In a rough approximation, the lowest loss grade will have more or less double cost compared to highest loss grade [7].

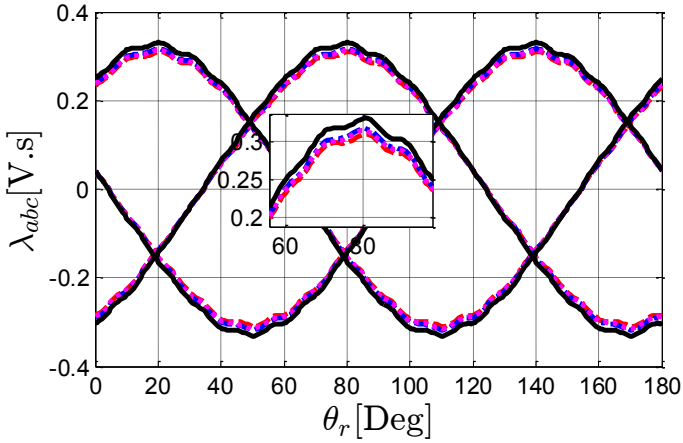

Figure 4.12: Three phase flux linkages *abc* of SynRM versus mechanical rotor angle θ_r for four steel grades at 6000 rpm. The legend is similar to Fig. 4.11.

Table 4.1: SynRM characteristics using different steel grades at current angle of 52°.

Factor	***Steel Grade***			
	NO20	***M330P-50A***	***M400-50A***	***M600-100A***
Iron loss(W)	221.20	667.50	527.70	1451
P_o (kW)	11.973	12.670	12.054	11.772
η%	96.567	93.560	94.273	87.668
T_r%	51.34	50.72	50.58	50.05
(L_d - L_q) (H)	0.0144	0.0152	0.0145	0.0141
PF	0.687	0.690	0.686	0.684
T_e (N.m)	19.05	20.16	19.18	18.73

For some applications, the power density is more important than the efficiency. Among the 4 considered materials, the highest output power, torque and power factor can be achieved using M330P-50A. This is due to the higher saliency ratio, see Fig. 4.8.

4.5 Conclusions

This chapter has presented the influence of different electrical steel grades on the performance of a synchronous reluctance motor (SynRM). Four different steel grades (NO20, M330P-50A, M400-50A and M600-100A) with different loss and thickness are studied. It is observed that the *dq*-axis inductances of the motor are affected by the material properties due to different permeability and magnetic saturation level. Hence, the SynRM performance varies because it depends mainly on the saliency ratio. It is found that M330P-50A has the highest output power which is about 8% higher than for M600-100A for the considered steel grades. In addition, the material grade has almost no influence on the power factor of the motor. The SynRM torque ripple doesn't depend on the material properties because it depends mainly on the motor geometry.

Moreover, the electrical steel grade has a great effect on the iron loss and hence the efficiency of the SynRM. The losses of the NO20 SynRM are about 15.2% of the M600-100A SynRM. Hence, the NO20 SynRM gives the highest efficiency, which is about 9% higher than for M600-100A.

Finally, it can be concluded that the higher permeability and low loss grade makes the material more favorable for the SynRM. However, its cost will be high.

Biography

[1] A. Abdallh, "An inverse problem based methodology with uncertainty analysis for the identification of magnetic material characteristics of electromagnetic devices," *PhD thesis*, Ghent University, 2012.

[2] I. Hofman, P. Sergeant, and A. Van den Bossche, "Influence of soft magnetic material in a permanent magnet synchronous

machine with a commercial induction machine stator," *IEEE Trans. Magn.*, vol. 48, no. 4, pp. 1645–1648, Apr. 2012.

[3] D. Kowal, P. Sergeant, L. Dupré, and L. Vandenbossche, "The effect of the electrical steel properties on the temperature distribution in direct-drive PM synchronous generators for 5 MW wind turbines," *IEEE Trans. Magn.*, vol. 49, no. 10, pp. 5371–5377, Oct. 2013.

[4] D. Kowal, P. Sergeant, L. Dupré, and A. Van den Bossche, "Comparison of the electrical steel grade on the performance of the direct-drive and single stage gearbox permanent-magnet machine for wind energy generation, based on an analytical model," *IEEE Trans. Magn.*, vol. 46, no. 2, pp. 279–285, Feb. 2010.

[5] D. Kowal, L. Dupré, P. Sergeant, L. Vandenbossche, and M. De Wulf, "Influence of the electrical steel grade on the performance of the direct-drive and single stage gearbox permanent-magnet machine for wind energy generation, based on an analytical model," *IEEE Trans. Magn.*, vol. 47, no. 12, pp. 4781–4790, Dec. 2011.

[6] M. Centner and U. Schafer, "Optimized the electromagnetic steel selections and performance impact assessments of synchronous reluctance motors," *IEEE Trans. Ind. Electron.*, vol. 57, no. 1, pp. 288–295, Jan. 2010.

[7] C.-T. Liu, H.-Y. Chung, and S.-Y. Lin, "On the electromagnetic steel selections and performance impact assessments of synchronous reluctance motors," *IEEE Trans. Ind. Appl.*, vol. 53, no. 3, pp. 2569–2577, May 2017.

[8] G. Bertotti, "General properties of power losses in soft ferromagnetic materials," *IEEE Trans. Magn.*, vol. 24, no. 1, pp. 621–630, 1988.

Chapter 5
Combined Star-Delta Windings

5.1 Introduction

This chapter compares the combined star-delta winding with the conventional star winding. A simple method to calculate the equivalent winding factor is proposed. In addition, the modelling of a SynRM with combined star-delta winding is given. Furthermore, at the end of this chapter, the effect of different winding layouts on the performance (output torque, power factor and efficiency) of SynRMs is presented.

5.2 Overview about combined star-delta winding

With the wide diversity of different motor types, the main interest in recent research is dedicated to develop an energy-efficient motor design with the highest possible torque density [1], [2]. One of the main techniques to improve the machine torque density is to increase the fundamental winding factor through innovative winding layouts [3]. Among several configurations, the so-called combined star-delta winding layout was proposed in literature several years ago. As far as we know, the first reference on this topic was a patent issued in 1918 [4]. The combined star-delta winding can be made by equipping the stator with two winding sets having a 30^0 spatial phase shift [5]. This can be simply achieved e.g. by splitting the 60^0 phase belt of a conventional three-phase winding into two parts, each spanning 30^0.

In literature, the combined star-delta winding is adopted in different applications [6]–[9]. In [7], combined star-delta connected windings were used to increase the performance of the axial flux permanent magnet machines with concentrated windings. It was found that the output power of the combined star-delta winding is much higher than the output power of the conventional star winding by 7.8% and 7.2% for simulations and measurements respectively. This is because winding factor increases by about 3.5%. In addition, the total losses of the axial-flux PM machine were the same for the combined star-delta and conventional star connected windings. Therefore, the efficiency is slightly increased: 0.2% point compared to the convention star connection. The complete theory and analysis of the combined star-delta three phase windings based on the magneto-motive force spatial harmonics and equivalent winding factors calculation are investigated in [8]. The per-phase winding was divided in three series-connected parts. For example, for one phase, the first portion contains two in-phase corresponding coils placed under two adjacent pole pairs. The second and the third portions have a shifted angle in the magnetic axis of 20° electrically. It was proved that connecting the inner delta in clockwise or counterclockwise direction leads to two different space angles between the star and delta systems. In this way, two different steps in the airgap flux level were observed. The validity of the theoretical analysis was checked by two experimental tests on a squirrel cage induction motor and a permanent magnet synchronous generator with a specially designed stator winding. In [9], the design strategy for implementing combined star-delta windings was outlined and applied to a 1.25 MW, 6 kV induction motor. It was shown that the torque and efficiency of the induction motor are improved by about 0.2% and 0.4% respectively using the combined star-delta windings, compared to the conventional star connection. This may seem a small increase, but it almost doesn't increase the cost of the motor. The combined star-delta winding is not only applied for three phase machines but also for multiple phase machines [10]–[12]. Dynamic and steady-state models of a five phase induction motor equipped with combined star-delta stator winding connection are given in [12] and [10] respectively. It is shown in [12] that the combined star-delta connection gives superior performance over both the star and delta connection in a five phase induction machine.

5.3 Winding configurations analysis

There are two types of the combined star-delta (Y-Δ) windings: the star-delta parallel connection and the combined star-delta series connection as shown in Fig. 5.1-a and 5.1-b respectively. The combined star-delta parallel connection has some practical difficulties: 1) the effective number of turns in series and the cross-section area of the conductors of the star and delta component windings have to be exactly equal, and 2) the space geometry of the two windings have to be equal in order to achieve a similar winding impedance. Otherwise, circulating currents will likely occur, resulting in excessive losses and reduced machine efficiency. Therefore, this type of winding was not eventually recommended in the literature. Consequently, the series connection of a combined star-delta winding is always adopted in the different applications [6], [8], [9].

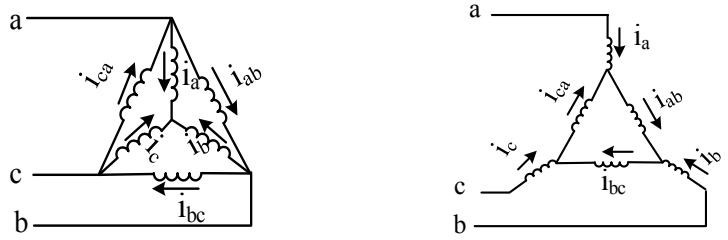

a) star-delta parallel connection. b) star-delta series connection.

Figure 5.1: Combined star-delta winding connections.

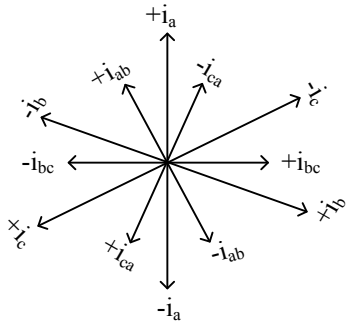

Figure 5.2: Currents phasor diagram of the combined star-delta connected windings.

The combined star-delta series connection is adopted in this work where the star component is connected between the supply and the inner delta as shown in Fig.5.1-b. This connection results in a phase shift of 30° between the star and delta components. The combined star-delta coils are arranged to reach a current distribution along the SynRM stator circumference similar to that of six phase windings. The current phasors for the balanced star-delta series connected windings are shown in Fig. 5.2. There is a factor √3 difference of the vector length of the six phasors due to the ratio between the star and delta currents. By consequence, the number of turns of the star winding coils has to be 1/√3 of the number of turns of the delta winding coils in order to generate an equal magneto-motive force (MMF). However, obtaining the ratio of √3 between the turns of the two windings may be difficult due to fabrication issues. This may not be an obstacle: other winding ratios may be chosen that approximate √3 [8]. Moreover, the cross-section of the delta coils can be reduced by a factor √3.

Table 5.1: Fundamental magnitude of MMF and THD of the different connections.

Connection	Slots/pole/phase	Fund. Magnitude of MMF (pu)	THD
Star connection (Y)	Y=3 (s)	1	9.88%
Combined star-delta connection (Y-Δ)	Y=2, Δ=1 (ssd)	1.0311	8.38%
	Y=1, Δ=2 (sdd)	1.0308	8.38%
	Y=2, Δ=1 (sds)	0.9689	11.05%
	Δ=2, Y=1 (dds)	1.0308	8.38%
	Δ=1, Y=2 (dss)	1.0311	8.38%
	Δ=2, Y=2 (dsd)	0.9687	11.05%

In the following analysis, the main focus is devoted to a 36-slot, 4-pole, 3-phase machine as an example. This corresponds to a number of slots/pole/phase (q) equal to 3. For q=3, the three slots belong to one phase in the conventional star-connected winding (s), while for the combined star-delta winding, several connection possibilities can be

made as given in Table 5.1. The symbols s (or Y) and d (or Δ) represent the equipped slots of star and delta coils respectively. The abbreviation of the different connections is given in brackets e.g. (ssd) means that two slots are used for the star-connected winding set and the remaining slot for the delta-connected winding set. The fundamental magnitude and the total harmonic distortion in percent (THD) of the magneto-motive force (MMF) of the different winding connections are listed in Table 5.1 as well, assuming sinusoidal currents and a single layer winding in both star and delta coils. It is evident that both the fundamental MMF component and THD are different between the connections. Clearly, the ssd and sdd, as well as the dss and dds connections have a similar fundamental MMF component and an identical harmonic spectra when the effect of circulating currents in the delta coils is neglected. In addition, they give a higher gain in MMF of about 3% compared to the conventional star connection (s). Furthermore, their THD values are lower due to the significant suppression of the low order harmonics, especially the 5^{th} and 7^{th}.

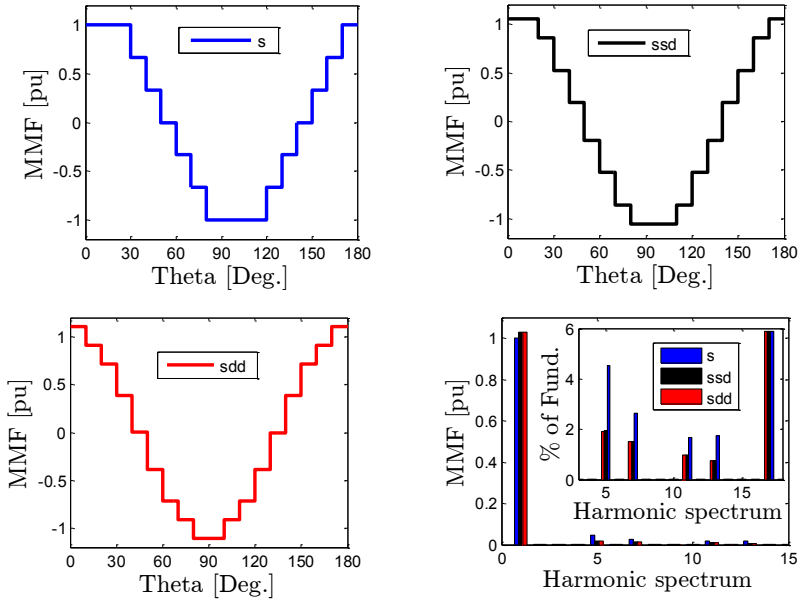

Figure 5.3: MMF (in per unit) as a function of circumferential angle (Theta) of s, ssd and sdd connections with sinusoidal currents at time=0.

This can be noticed in Fig. 5.3 in which the MMF distribution is plotted for s, ssd and sdd connections at the same time instant. Interestingly enough, the MMF distribution of ssd and sdd is much better in the former case compared to the s connection. The increase of the fundamental MMF component of the ssd and sdd connections will lead to a higher torque density compared to the conventional s connection for the same copper volume. Hence, the machine efficiency may also increase. In essence, the dds and dss layouts are similar to the ssd and sdd layouts respectively. However, the star and delta sub windings should be connected such that the phase angle between the three-phase currents in the two winding sets should be leading rather than lagging. On the other hand, the other possible star-delta connections (sds and dsd) have a low MMF magnitude and a higher THD compared with s connection. Consequently, sds and dsd connections will not be considered in the following study.

5.4 Winding factor calculation of the proposed layout

The winding layouts of the proposed s, ssd and sdd windings are sketched in Fig. 5.4 for a single pole-pair using a single layer layout.

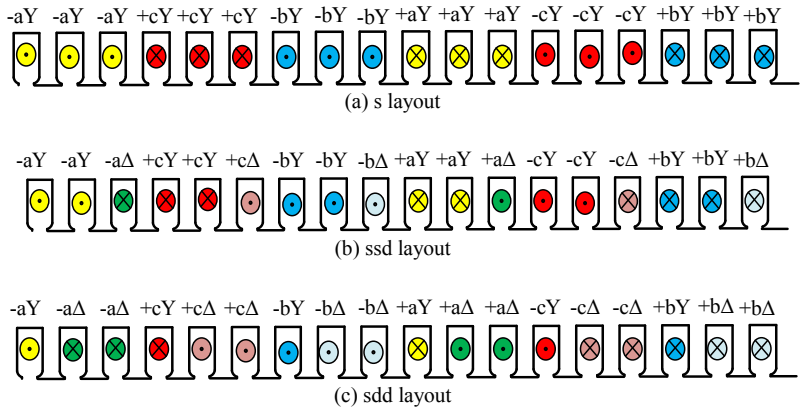

Figure 5.4: Winding layout of (a) s, (b) ssd and (c) sdd connections.

In the combined star-delta connection, in order to generate an equal MMF from the two winding sets, the number of turns of the delta section has to be higher than the star section by a factor √3 as mentioned before. For the prototype machine, the number of turns of the star coils has been selected to be 26. Hence, the number of turns of the delta coils will be 45. Since the copper volume per slot remains the same, the conductor cross sectional area of this winding set will be also lower by the same factor compared to the conventional star case. Therefore, the cross-section area of the delta and star conductors are selected as 0.884 mm^2 and 1.573 mm^2 respectively. The corresponding connections between the star and delta coils are shown in Fig. 5.5. The aΔ, bΔ and cΔ represent the delta coils connected between (aY and bY), (bY and cY) and (cY and aY) respectively as shown in Fig. 5.1-b and Fig. 5.5.

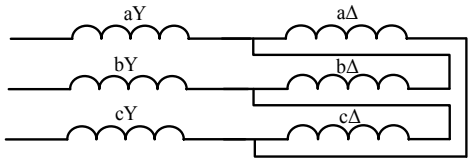

Figure 5.5: Combined star-delta series connection.

The star of slot (SoS) phasor diagram for the induced EMFs across different coils and the terminal voltage phasors are shown in Fig. 5.6. It is clear that the equivalent winding factor for each case can be simply given by [13]–[18]:

$$K_w = \frac{E_{aY}}{3E} \tag{5.1}$$

where, E is the induced EMF magnitude across each coil of the star winding set and E_{aY} is the equivalent phase voltage magnitude of the three-phase stator terminals. Based on (5.1), the calculated winding factors for the three possible connections are given in Table 5.2. The calculation of these factors assumes that the number of turns of the delta coil is exactly √3 times the number of turns of the star one. Obtaining the winding factor using SoS, which is usually used in most available literature, will be tedious for a higher number of coils with different possible coil shares between the star and delta winding section [18].

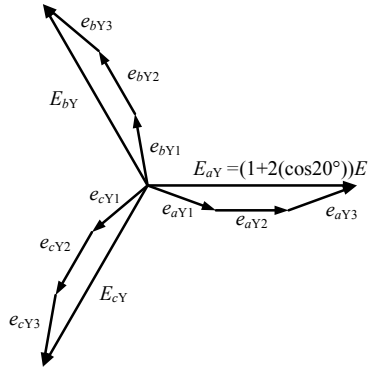

(a) s layout

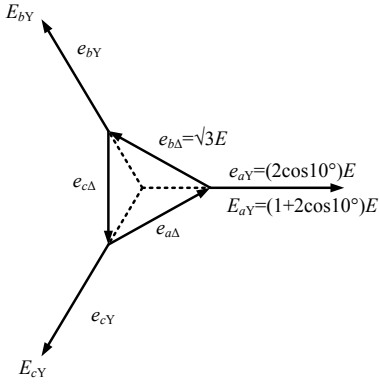

(b) ssd layout

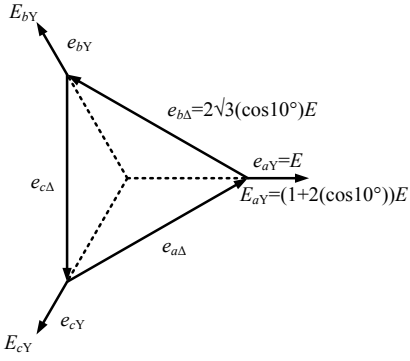

(c) sdd layout

Figure 5.6: Star of slot (SoS) phasor diagram for different connections.

Table 5.2: Equivalent winding factor for each connection.

Connection	s	ssd	sdd
K_w using (5.1)	$\frac{1+2\cos(20°)}{3}$ =0.9598	$\frac{1+2\cos(10°)}{3}$ =0.9899	$\frac{1+2\cos(10°)}{3}$ =0.9899
K_w using (5.6)	0.9598	0.9896	0.9894

Alternatively, in the following, a simpler technique is therefore proposed to provide a closed form for the equivalent winding factor of a combined star-delta connection. Instead of using SoS, the equivalent winding factor of any three-phase winding layout comprising q coils per phase per pole can be simply found from the ratio between the fundamental component of the total MMF and the fundamental component of a three-phase machine with full pitch concentrated winding and having the same number of turns per phase, as given by [14], [16]:

$$K_w = \frac{F_{Y\Delta 1}}{\frac{3}{2}\frac{4N_c}{2\pi}qI} \tag{5.2}$$

where $F_{Y\Delta 1}$ is the fundamental component of the total MMF distribution, N_c is the number of turns per coil for the conventional three-phase winding, q is the number of slots per phase per pole, and I is the line current magnitude.

It is known that in a conventional three-phase distributed winding, the phase belt is 60°. To rewind a three-phase stator with a combined star-delta winding, the phase belt of each phase is split into two portions, as shown in Fig. 5.7, where the number of coils for the star and delta sections are x and y respectively. If the angle between any two successive slots is β, the magnetic axis of each winding set is identified by the red dashed lines in Fig. 5.7 for the two winding sets. Hence, the phase belt angle $q\beta$=60° and the angle between the magnetic axes of the two sets will be $q\beta/2$=30°.

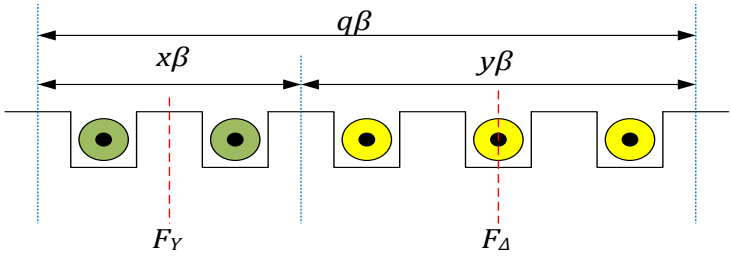

Figure 5.7: Phase belt span comprising x star coils and y delta coils.

If the machine line current (star winding phase current) is Ie^{j0°, the corresponding phase current of the delta winding should be $(I/\sqrt{3})e^{-j30^\circ}$. Hence, the space phasor of the fundamental component of the MMF generated by each winding set can be found as [8]:

$$\overline{F_Y} = \frac{3}{2}\frac{4}{\pi}\frac{xN_Y}{2}\frac{\sin\left(x\frac{\beta}{2}\right)}{x\sin\left(\frac{\beta}{2}\right)}e^{j\theta}Ie^{j0} \tag{5.3}$$

$$\overline{F_\Delta} = \frac{3}{2}\frac{4}{\pi}\frac{yN_\Delta}{2}\frac{\sin\left(y\frac{\beta}{2}\right)}{y\sin\left(\frac{\beta}{2}\right)}e^{j\left(\theta-\frac{q\beta}{2}\right)}\frac{I}{\sqrt{3}}e^{-j30^\circ} \tag{5.4}$$

where θ is the peripheral angle.

The fundamental total MMF of the two windings is the phasor summation of the two space phasors and is given by:

$$\overline{F_{Y\Delta}} = \frac{3}{\pi}\left(N_Y\frac{\sin\left(x\frac{\beta}{2}\right)}{\sin\left(\frac{\beta}{2}\right)} + \frac{N_\Delta}{\sqrt{3}}\frac{\sin\left(y\frac{\beta}{2}\right)}{\sin\left(\frac{\beta}{2}\right)}\right)e^{j\theta}Ie^{j0} \tag{5.5}$$

Hence, the equivalent winding factor can be simply calculated from (5.2) by taking the number of turns per coil of the conventional three-phase machine N_c=N_Y.

$$K_w = \frac{1}{q\sin\left(\frac{\beta}{2}\right)}\left(\sin\left(x\frac{\beta}{2}\right)+\frac{N_\Delta}{\sqrt{3}N_Y}\sin\left(y\frac{\beta}{2}\right)\right) \tag{5.6}$$

Table 5.3: Equivalent winding factor for different values of q and different possible connections.

q	Connection	Winding factor	Maximum gain
2	s	0.9659	1.035
	sd	0.9996	
3	s	0.9598	1.031
	ssd	0.9896	
	sdd	0.9894	
4	s	0.9577	1.035
	sssd	0.9828	
	ssdd	0.9911	
	sddd	0.9824	
5	s	0.9567	1.0335
	ssssd	0.9781	
	sssdd	0.9888	
	ssddd	0.9886	
	sdddd	0.9777	
6	s	0.9561	1.035
	ssssssd	0.9747	
	sssddd	0.9859	
	sssddd	0.9895	
	ssdddd	0.9856	
	sddddd	0.9742	

The ratio N_Δ/N_Y ideally equals √3, hence the ideal value for the winding factor is given by:

$$K_w = \frac{1}{q\sin\left(\frac{\beta}{2}\right)}\left(\sin\left(x\frac{\beta}{2}\right)+\sin\left(y\frac{\beta}{2}\right)\right) \tag{5.7}$$

Since the number of turns of each coil should be approximated to the nearest integer value, therefore, (5.6) would preferably be used. Based on (5.6), the winding factors of both possible connections for the adopted 36-slot, 4-pole stator are calculated and added to Table 5.2.

It is also interesting to generalize the calculation of the winding factor for different values of *q, x*, and *y*, which can be now easily done using (5.6). The calculated values of the winding factor for q =2 to 6 are given in Table 5.3. It is clear that the torque density gain is maximized when $x \cong y$. The maximum torque gain equals 3.5% when $x \cong y$.

5.5 Modelling of SynRM using combined star-delta winding

The detailed model of a SynRM with the conventional three phase winding is given in **Chapter 2**. Therefore, in this section, the modelling of a SynRM using the combined star-delta connection is given briefly. The dq^s-axis current components in a stationary reference frame as a function of the six components of the star-delta currents (Fig. 5.2) can be described as follows [13]:

$$\begin{bmatrix} i_q^s \\ i_d^s \end{bmatrix} = K_t \begin{bmatrix} 1 & -\frac{1}{2} & -\frac{1}{2} & \frac{\sqrt{3}}{2} & 0 & \frac{\sqrt{3}}{2} \\ 0 & \frac{\sqrt{3}}{2} & -\frac{\sqrt{3}}{2} & -\frac{1}{2} & 1 & -\frac{1}{2} \end{bmatrix} \begin{bmatrix} i_a \\ i_b \\ i_c \\ i_{ab} \\ i_{bc} \\ i_{ca} \end{bmatrix} \tag{5.8}$$

The dq^s-axis current components can be transformed to the rotor reference frame (dq^r) as follows:

$$\begin{bmatrix} i_q^r \\ i_d^r \end{bmatrix} = \begin{bmatrix} \cos(\theta_f) & \sin(\theta_f) \\ -\sin(\theta_f) & \cos(\theta_f) \end{bmatrix} \begin{bmatrix} i_q^s \\ i_d^s \end{bmatrix} \tag{5.9}$$

where θ_f is the reference frame angle.

In order to obtain the value of the factor K_t in (5.8) of the Clarke transformation, the space vector length of the three currents of star and delta coils should have the same magnitude. There are two possibilities to obtain the same vector magnitude between the star and delta currents. The first is to convert the space vector length of the delta currents to be equal to the space vector length of the star currents. This can be done by multiplying the delta currents by √3. The second is to convert the space vector length of the star currents to the space vector length of the delta currents. This can be done by multiplying the star currents by the factor (1/√3). We choose the second option, then the factor K_t in (5.8) will be 2/6.

The previous transformation matrices can be used for the *dq*-axis flux linkages of the combined star-delta connected windings. To use the same value of K_t=2/6 for the flux linkage transformation, the space vector length of the three flux linkages of star and delta coils should have the same magnitude. To obtain the same vector magnitude between star and delta flux linkages, the same two methods can be used as for the currents, but with a factor X√3 instead of √3. The factor X depends on the layout of combined star-delta connection: sdd or ssd. In case of sdd the factor X is 2. This originates from the fact that there are two times as much delta coils compared to star coils. While in case of ssd the factor X is 0.5. This is because the number of star coils is twice the number of delta coils.

The electromagnetic torque T_e of the SynRM in case of the combined star-delta connection can be written as follows [19]:

$$T_e = \frac{3}{2} K_1 P(\lambda_d(i_d, i_q) i_q - \lambda_q(i_d, i_q) i_d) \tag{5.10}$$

where P is the number of pole pairs, i_d, i_q, λ_d and λ_q are the direct (d) and quadrature (q) axis current (i) and flux linkage (λ) components respectively.

The factor K_1 in (5.10) depends on the winding type. In case of a

conventional star winding, the factor K_1 equals 1, while in case of combined star-delta windings, the factor K_1 depends on the space vector length of the currents and the flux linkages. As we have chosen to convert the star vector length to delta, the factor K_1 equals 3/2 for sdd and 3 for ssd respectively.

Except the presented equations before, the remaining of the SynRM modelling given in **Chapter 2** remains valid, including the vector diagram.

5.6 Comparison of star and combined star-delta winding for the prototype SynRM

In this section, the performance (output torque, power factor, torque ripple and efficiency) of the SynRM is investigated under the proposed winding layouts i.e. s, ssd and sdd connections. The geometrical parameters of Table 2.1 (Chapter 2) and the optimal rotor parameters of Table 3.10 (**Chapter 3)** are employed in the following study. In addition, the main electromagnetic and geometrical parameters of the prototype is listed Table 5.5.

Table 5.4: Parameters of the adopted SynRM.

Parameter	Value	Parameter	Value
Number of rotor flux barriers per pole	3	**Active axial length**	140 mm
Number of stator slots/pole pairs	36/2	**Air gap length**	0.3 mm
Number of phases	3	**Rated voltage**	380 V
Stator outer/inner diameter	180/110 mm	**Rated output power**	5.5 kW
Rotor steel	M330-50A	**Rated speed**	3000 rpm
Stator steel	M270-50A	**Rated current**	12.23 A

It is shown in **Chapter 4** that the selection of the steel grade has a great influence on the efficiency of SynRMs. As the majority of the iron losses in SynRMs is in the stator core, we have selected a better grade for the stator than for the rotor: the prototype SynRM uses the material grades M270-50A and M330-50A for the stator and rotor cores respectively. This selection is a compromise between the losses and the manufacturing cost of the prototypes. The performance of the SynRM is analysed using FEM by MAXWELL ANSYS software in transient mode. The current controlled inverter is emulated by three current sources carrying three-phase sinusoidal currents. The currents in the delta coils are calculated using an external circuit-based simulator similar as in Fig. 5.8. This way, the unavoidable harmonic current components circulating in the delta section are taken into consideration.

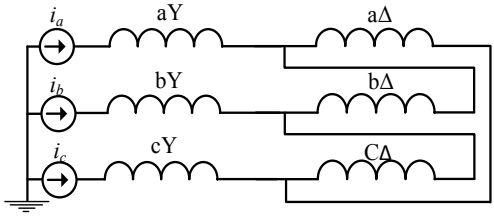

Figure 5.8: Combined star-delta winding coupled to three phase current sources.

Figure 5.9 shows the SynRM output torque as a function of the current angle for several current magnitudes up to the rated value (12.23 A) at rated speed (3000 rpm). The current angle represents the phase angle of the injected star currents, as shown in **Chapter 2**. The SynRM torque increases with the current angle till a certain maximum value is achieved, and then decreases again. The current angle that corresponds to maximum output torque represents the optimal current angle in terms of a maximal torque-to-current ratio, i.e. it maximizes the torque production for the same stator current. It is obvious from Fig. 5.9 that the optimal current angle is different for the several curves shown. It predominately depends on the amplitude of the stator current: a higher current angle is optimal for a higher current. This is explained by the changing magnetic saturation behaviour of the core material with a stator current variation. Furthermore, the SynRMs with s and sdd connections have approximately the same optimal current angle e.g. at

rated current, the optimal current angle is 56.5°. However, the optimal current angle of the SynRM with ssd connection (46.5° at rated current) has a 10° phase advance shift compared to the other two connections. This is equal to the shift in the total MMF magnetic axis corresponding to each winding layout.

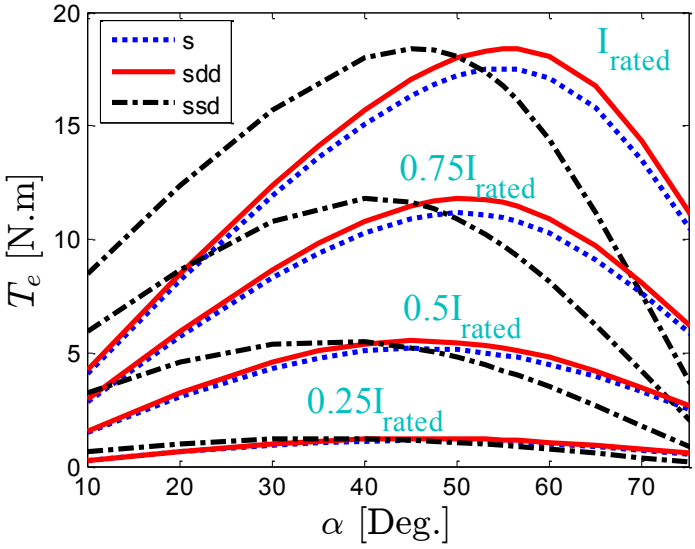

Figure 5.9: SynRM output torque (T_e) as a function of current angle (α) for several stator currents at rated speed.

Let's now focus on the amplitude of the torque in Figs. 5.9 and 5.10. At rated current, Fig. 5.9 shows that the calculated maximum torque is 17.47 N.m for the s connection and 18.38 N.m for both the ssd and sdd connections. Figure 5.10 shows the variation of the SynRM torque as a function of the rotor position at the rated conditions. The increase in the SynRM torque is about 5.2% using both ssd and sdd connections compared to the conventional star connection. This is thanks to the corresponding enhancement in the winding factor, as explained in **Section 5.4,** which increases the airgap flux density, resulting in an improved torque density. Figure 5.11 shows the flux-density distribution of the SynRM using s, ssd and sdd connections at the rated conditions and rotor position θ_m = 0°, corresponding to the most left point of Fig. 5.10. It is clear that both star-delta connections have a

higher flux-density compared to the star connection, in particular in the stator yoke.

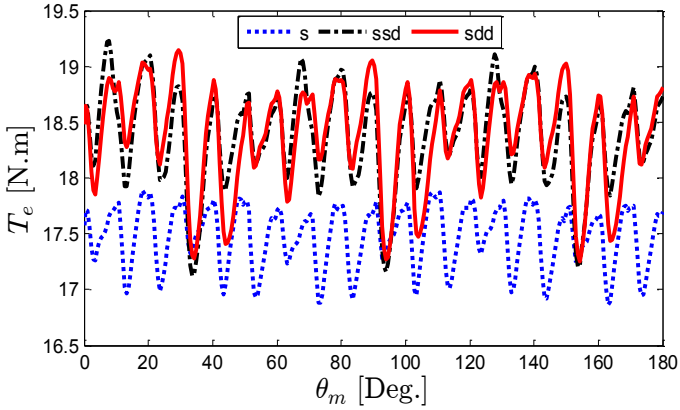

Figure 5.10: SynRM output torque (T_e) as a function of mechanical rotor angle (θ_m) at rated conditions and optimal current angle.

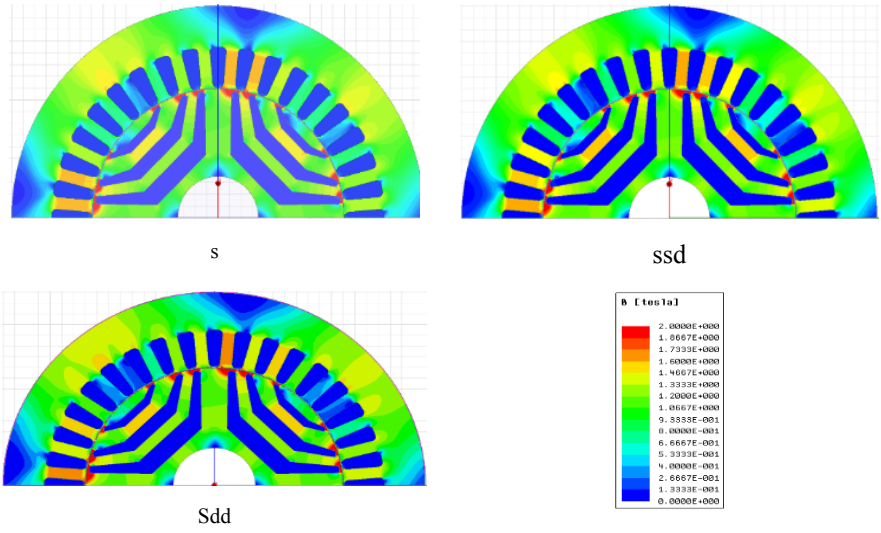

Figure 5.11: Flux density distribution of the SynRM for s, ssd and sdd connections at rated conditions and θ_m=0.

Moreover, it is worth noticing in Fig. 5.9 that the difference (in percent) in the output torque between the star and star-delta winding

configurations at the optimal current angle is generally current dependent. This can be clearly seen from Fig. 5.12. Fig. 5.12(a) shows the difference in the output torque (in percent) between the star and star-delta winding connections as a function of the line current at the optimal current angle and rated speed. It is clear that the torque gain (in percent) decreases with the increase in the stator current. To explain the reduction in torque gain, the difference (in percent) in the difference between the direct (d) and quadrature (q) axes inductances (L_{dq}) of the two winding configurations is plotted in Fig. 5.12(b). Clearly, the increase in the stator current level affects L_{dq}% due to core saturation, which in turn affects the achievable output torque for a certain RMS stator current.

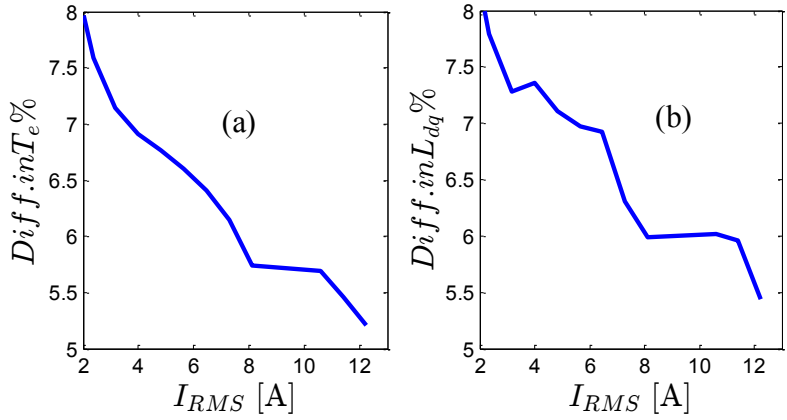

Figure 5.12: The difference in the torque %) and (b) the difference in L_{dq}% as a function of stator current (RMS) at optimal current angles and rated speed.

Figure 5.13 shows the relation between the current angle and the torque ripple (in percent) under rated current and speed. The torque ripple magnitudes at the optimal current angle are 5.62%, 10.26% and 9.62% for the s, ssd and sdd connections respectively, as shown in Fig. 5.13. The increase in the torque ripple% of both ssd and sdd windings compared to star case is mainly due to the induced harmonic current components circulating in the delta sub winding, which give rise to a pulsating third harmonic flux component in the air gap. Although it does not contribute to average torque production, it negatively affects the torque ripple magnitude. This is in contrast to Fig. 5.3 because the

MMF distributions of Fig. 5.3 is plotted assuming sinusoidal currents in both star and delta coils. A harmonic spectrum analysis for the currents of the different connections will come later.

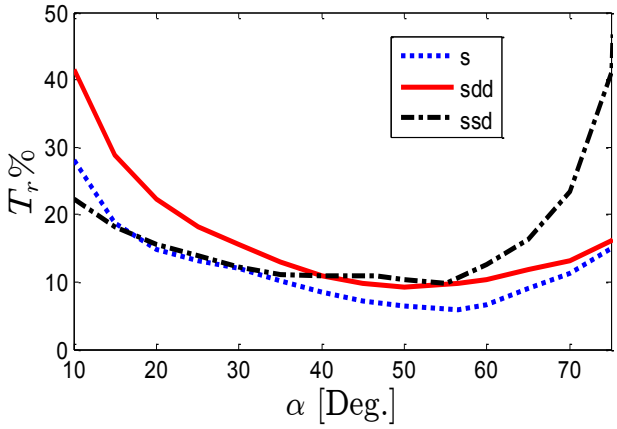

Figure 5.13: SynRM torque ripple T_r (in percent %) as a function of current angle (α) at rated current and speed.

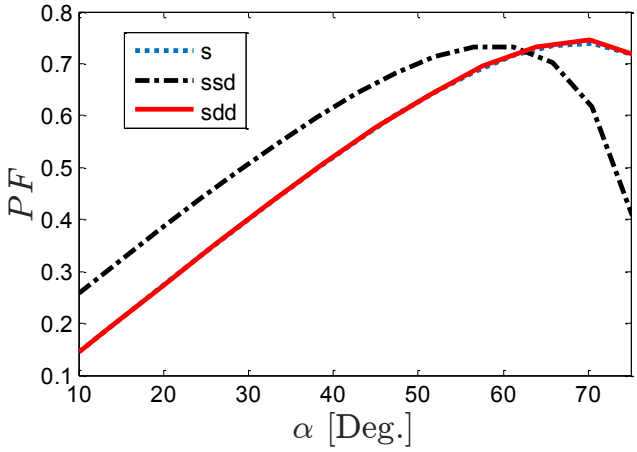

Figure 5.14: SynRM power factor (*PF*) as a function of current angle (α) at rated current and speed.

The variation of the SynRM power factor as a function of the current angle for the three connections at rated conditions is shown in Fig. 5.14. It is noticed that the effect of the stator winding layout on the SynRM

power factor can be merely neglected; e.g. at rated conditions, the optimal current angle of s and ssd is about 56.5° and for ssd is about 46.5° as shown in Fig. 6. The corresponding machine power factor of the s, ssd and sdd windings will then be 0.679, 0.681 and 0.683 respectively, which is fair to be assumed the same.

Figure 5.15 shows the currents in the star and delta coils of the three connections at the rated conditions and optimal current angle. The star currents are enforced as pure sinusoidal currents as mentioned before in all the different connections, while the delta currents in the combined star-delta windings are computed based on FEM. It is evident that the delta coils have circulating currents. The harmonic spectrum of the currents is reported in Fig. 5.16. Apart from the fundamental component, the dominant harmonic component is the 3rd: about 12.9% and 11.2% of the fundamental component of ssd and sdd respectively. These harmonics are negatively affected the torque ripple as observed before in Fig. 5.13.

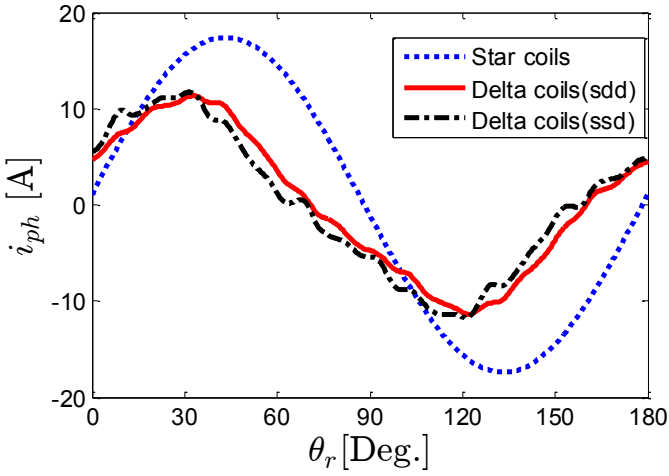

Figure 5.15: Currents of star and delta coils at rated conditions and optimal current angle.

Figure 5.17 shows the line flux linkage of the s, ssd and sdd connections at the rated conditions and optimal current angle. It is observed that both combined star-delta configurations have a similar maximum flux linkage: about 0.920 V.s. In addition, the maximum flux

linkage of both combined star-delta connections is higher than the flux linkage of the s winding by about 10%. This is indeed thanks to the improved winding factor of the combined star-delta connection. The line voltage of the three connections is shown in Fig. 5.18 for rated current and speed at optimal current angle. It is obvious that the combined star-delta windings have a bit higher voltage than s winding as a result of the higher flux linkage, see Fig. 5.17.

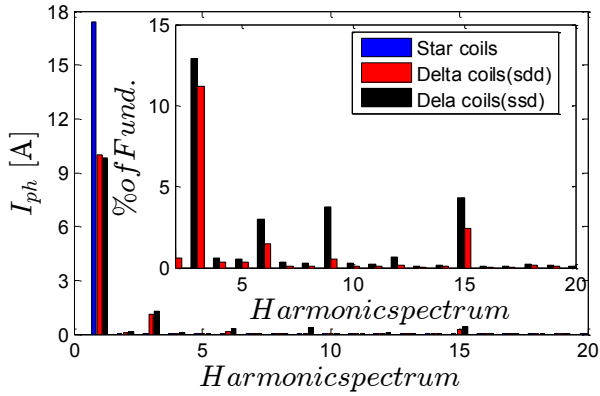

Figure 5.16: Harmonic spectrum of currents in star and delta coils at rated conditions and optimal current angle.

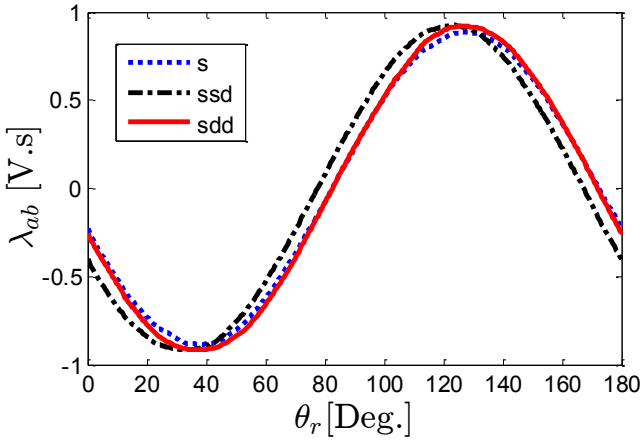

Figure 5.17: Line-to-line flux linkage of the s and sdd connections at rated conditions and optimal current angle.

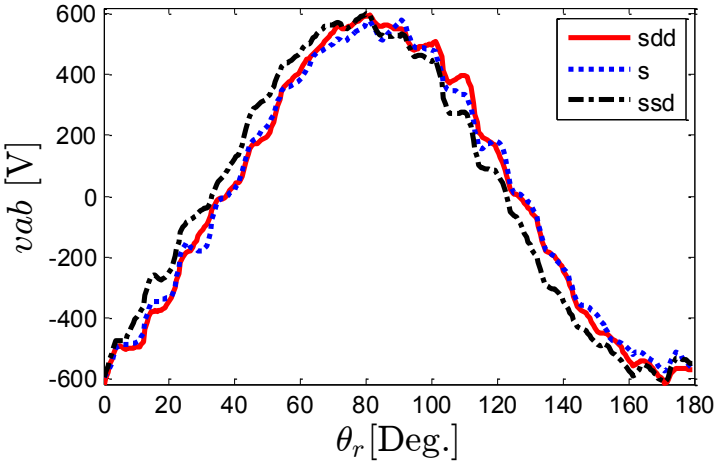

Figure 5.18: Line-to-line voltage of the s and sdd connections at rated conditions and optimal current angle.

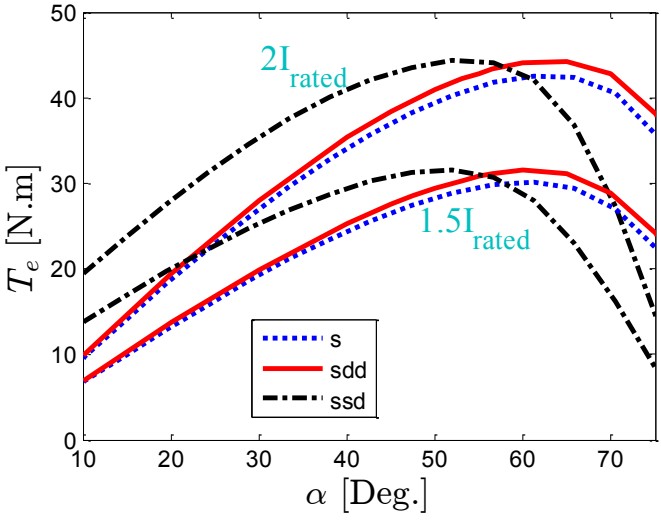

Figure 5.19: SynRM output torque (T_e) as a function of current angle (α) for overload situations: 1.5 and 2 times the rated current at 1000 rpm (1/3 of rated speed).

For some applications, e.g. electric vehicles, overloading is required for some cases, especially at low speeds. Figure 5.19 reports the overloading behaviour of the SynRM using the three connections at

1000 rpm (1/3 of rated speed). The variation of the SynRM torque is studied as a function of the current angle for 1.5 and 2 times the rated current. The result is shown in Fig. 5.19. Obviously, the optimal current angle has been shifted to a larger value compared to the one at the rated current (Fig. 5.9). This is because the variation of the q-axis inductance with increasing current becomes very low compared to the variation of the d-axis inductance for overload currents. In the q-axis direction, the flux-barrier ribs are heavily saturated, forcing the flux-lines to pass through the flux-barriers. These barriers are air, so that the q-axis inductance remains almost constant with increasing current. The d-axis however is almost saturated for these overload currents. Therefore, the d-axis inductance decreases with increasing stator current. We know that the torque is proportional to $(L_d\text{-}L_q)i_d i_q$. Consequently, as a high d-axis current reduces L_d significantly, it is more effective to increase i_q than i_d. This results in a large increase in the optimal current angle as observed in Fig. 5.19. Moreover, both the combined star-delta windings have a higher output torque compared to the star one: about 4.3% and 4.4% for the 1.5 and 2 times rated current cases respectively. Clearly, the achievable torque gain under overloading condition (4.3% and 4.4%) is lower compared to the rated current case (5.2%), which is mainly due to core saturation.

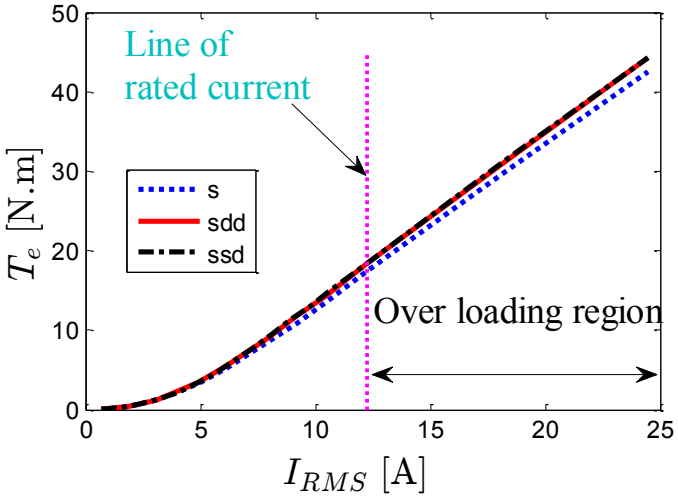

Figure 5.20: SynRM output torque (T_e) as a function of stator current (*RMS*) at optimal current angles and at 1000 rpm (1/3 of rated speed).

Figure 5.20 shows the variation of the SynRM torque as a function of the stator RMS current at the optimal current angles for the s, ssd and sdd windings. It is observed that the variation of the SynRM torque as a function of the stator current for the over rated current region can be assumed linear.

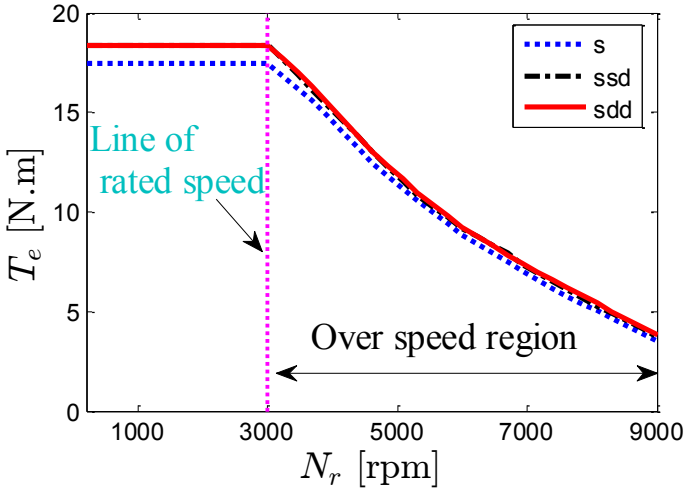

Figure 5.21: SynRM output torque (T_e) as a function of speed (N_{rpm}) at rated current and optimal current angles.

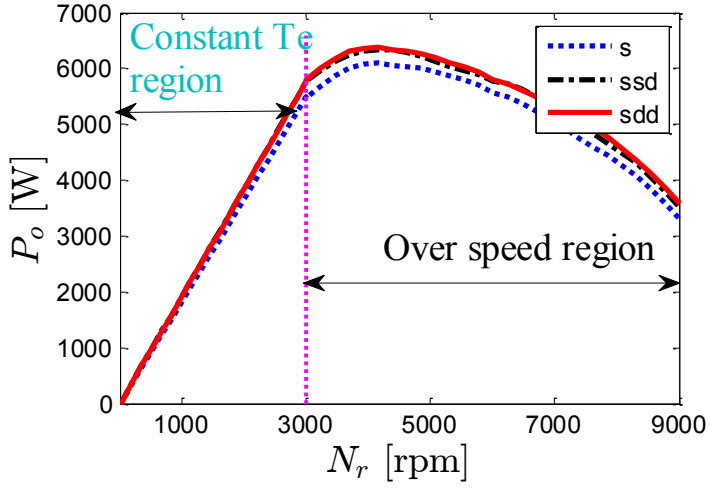

Figure 5.22: SynRM output power (P_o) as a function of speed (N_{rpm}) at rated current and optimal current angles.

The following paragraph investigates the influence of speed, including speeds above the rated one. The SynRM output torque and power as function of the speed at the optimal current angles and rated current are shown in Figs. 5.21 and 5.22 respectively. Notice that the optimal current angle for speeds up to the rated value (3000 rpm) is the angle of the maximum torque while for speeds above the rated value, the optimal current angle is the angle that keeps the stator voltage approximately at its rated voltage. For speeds up to the rated value, the increase in the SynRM torque of star-delta connections is constant and equal to 5.2% (as mentioned before). This is because the optimal current angle is fixed, hence the difference in L_{dq} (Fig. 5.12), resulting in a fixed gain in the torque. However, for speeds more than the rated value, the stator current is fixed at the rated value and the current angle varies in order to keep the stator voltage at the rated value. This results in an increase in the current angle to reduce the airgap flux, hence the SynRM output torque decreases as shown in Fig. 5.23. Consequently, the gain in the SynRM torque of the combined star-delta connection varies with the speed as well. The torque gain increases from about 5.2% at the rated speed to about 9.5% at 3 times the rated speed. Fig. 5.24 shows that the power factor varies for speeds above rated speed, but there is no difference in the power factor between the different winding connections.

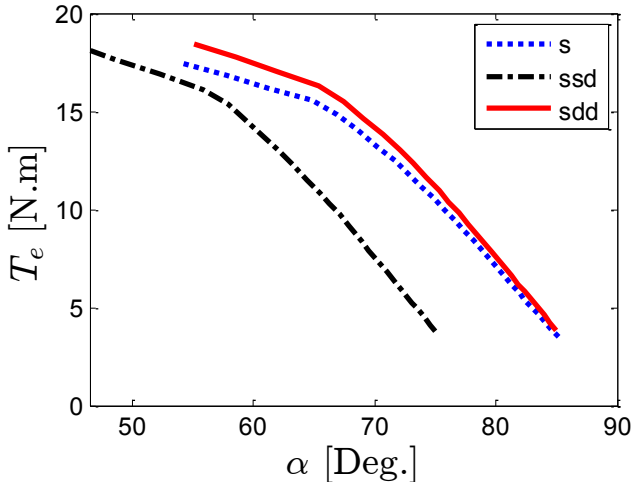

Figure 5.23: SynRM output torque (T_e) as a function of current angle (α) for speeds higher than the rated value (3000) at the optimal current angle.

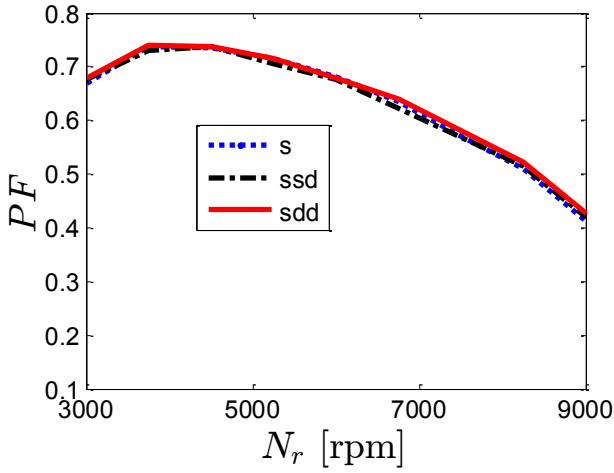

Figure 5.24: SynRM power factor (*PF*) as a function of speed (N_{rpm}) at optimal current angles.

The simulated efficiency and total losses of the SynRM using the s, ssd and sdd connections are reported in Fig. 5.25. The figure shows the efficiency and losses as a function of the speed at the optimal current angles. The efficiency is simply calculated based on the computed output power and the total estimated losses (copper and iron losses) of the machine. The mechanical losses are neglected in this comparison. To find the iron losses, the magnetic flux density *B* is computed using FEM for several points and positions, and then the iron losses are calculated as in [20]. The copper losses are computed based on the measured winding resistance of the machine and the current amplitude. The current amplitude is chosen the same for each winding connection. Note that the copper losses are similar in the star and the delta windings. This is because in the delta-connected coils, the increase in the number of turns by a factor √3 and the reduction in the cross-section area by a factor √3 is compensated by a lower current, also by a factor √3. Figure 25a indicates that the SynRM efficiency of the ssd and sdd is slightly higher than the efficiency in case of the s connection. The losses in Figure 25b are not much different between the three types of connection. This means that the increase in the efficiency is mainly due to the increase in the output torque (Fig. 5.12). Zoom in to show the difference in the SynRM efficiency and losses between the different windings is reported in Fig. 5.26. The small difference in the total losses

of the SynRMs occurs due to circulating harmonic currents when either ssd or sdd connections are used. This can be observed in Fig. 5.27 as well. In this figure, the machine efficiency and losses are shown for different stator current at the rated speed and optimal current angles.

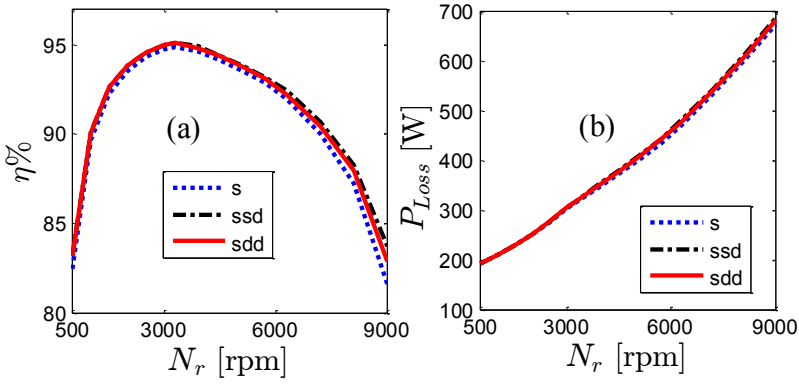

Figure 5.25: (a) SynRM efficiency and (b) total losses as a function of speed (N_{rpm}) at optimal current angles (only copper and iron losses are taken into account).

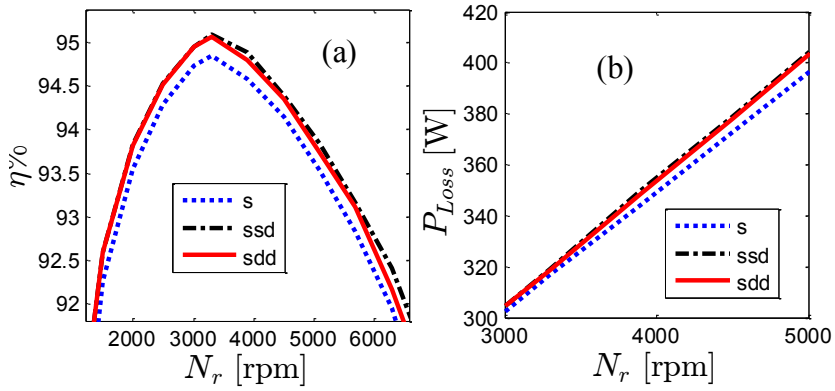

Figure 5.26: (a) Zoom in of SynRM efficiency and (b) zoom in of total losses as a function of speed (N_{rpm}) at optimal current angles (only copper and iron losses are taken into account).

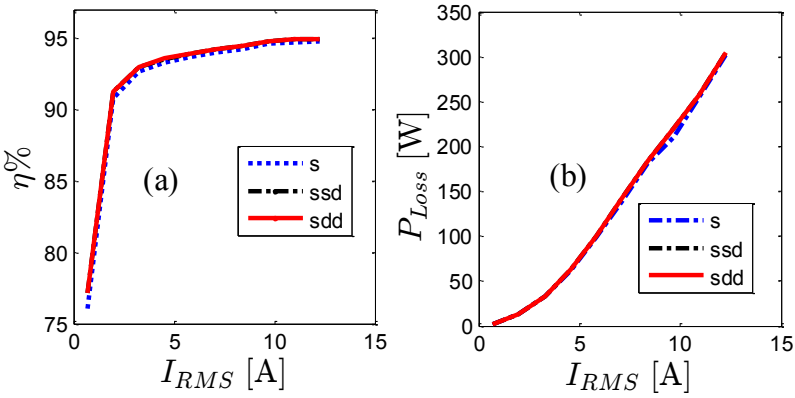

Figure 5.27: (a) The simulated efficiency and (b) total losses as a function of stator current (*RMS*) at optimal current angles and rated speed.

5.7 Conclusions

This chapter has investigated the combined star-delta winding configurations. A simple method to calculate the winding factor of the different winding configurations is proposed. The dynamic modelling of a SynRM using a combined star-delta winding is given. Furthermore, the SynRM performance (torque, power factor, torque ripple and efficiency) using two combined star-delta winding layouts in comparison with a conventional star-connected winding is presented for a prototype machine. The combined star-delta winding configurations are named star-star-delta (ssd) and star-delta-delta (sdd) connections. Here, "star-star-delta" means that the conductors in 2 of the 3 slots per pole per phase belong to the star connected windings, and the conductors in the third slot belong to the delta connected windings. It is found that the difference between the ssd and sdd combined star-delta connections is very small in terms of the machine performance. This is observed over a wide range of speed and current. Nevertheless, when compared with a conventional star connection, both ssd and sdd windings correspond to a torque gain of 5.2% under rated conditions. This gain decreases in the overloading range due to core saturation, but it increases up to 8% under small loads. In the constant power range (above rated speed), the torque gain increases to approximately 9.5% at 3 times the rated speed. The effect of the winding configuration on the

machine power factor and on the core loss is negligible up to 3 times rated speed and 2 times rated current. Nevertheless, the machine efficiency for a combined star-delta connection is improved by 0.26% point at rated load, and even more under light loading.

Biography

[1] A. T. De Almeida, F. J. T. E. Ferreira, and A. Q. Duarte, "Technical and economical considerations on super high-efficiency three phase motors," *IEEE Trans. Ind. Appl.*, vol. 50, no. 2, pp. 1274–1285, Mar. 2014.

[2] F. Ferreira, G. Baoming, and A. de Almeida, "Stator winding connection-mode management in line-start permanent magnet motors to improve their efficiency and power factor," *IEEE Trans. Energy Convers.*, vol. 28, no. 3, pp. 523–534, Sep. 2013.

[3] A. S. Abdel-Khalik, S. Ahmed, and A. M. Massoud, "Effect of multilayer windings with different stator winding connections on interior PM machines for EV applications," *IEEE Trans. Magn.*, vol. 52, no. 2, pp. 1–7, Feb. 2016.

[4] J. K. Kostko, "Polyphase reaction synchronous motors," *J. Am. Inst. Electr. Eng.*, vol. 42, no. 11, pp. 1162–1168, Nov. 1923.

[5] J. Y. Chen and C. Z. Chen, "Investigation of a new AC electrical machine winding," *IEE Proc. - Electr. Power Appl.*, vol. 145, no. 2, p. 125, 1998.

[6] M. N. Ibrahim, P. Sergeant, and E. M. Rashad, "Combined star-delta windings to improve synchronous reluctance motor performance," *IEEE Trans. Energy Convers.*, vol. 31, no. 4, pp. 1479–1487, Dec. 2016.

[7] H. Vansompel, P. Sergeant, L. Dupré, and A. Bossche, "A combined wye-delta connection to increase the performance of axial-flux PM machines with concentrated windings," *IEEE Trans. Energy Convers.*, vol. 27, no. 2, pp. 403–410, Jun. 2012.

[8] M. V. Cistelecan, F. J. T. E. Ferreira, and M. Popescu, "Adjustable flux three-phase AC machines with combined multiple-step star-delta winding connections," *IEEE Trans. Energy Convers.*, vol. 25, no. 2, pp. 348–355, Jun. 2010.

[9] Y. Lei, Zh. Zhao, Sh. Wang, D. G. Dorrell, and W. Xu, "Design and analysis of star–delta hybrid windings for high-voltage induction motors," *IEEE Trans. Ind. Electron.*, vol. 58, no. 9, pp. 3758–3767, Sep. 2011.

[10] A. S. Abdel-Khalik, S. Ahmed, and A. M. Massoud, "Steady-state mathematical modeling of a five-phase induction machine with a combined star/pentagon stator winding connection," *IEEE Trans. Ind. Electron.*, vol. 63, no. 3, pp. 1331–1343, Mar. 2016.

[11] A. S. Abdel-Khalik, S. Ahmed, and A. M. Massoud, "Low space harmonics cancelation in double-layer fractional slot winding using dual multiphase winding," *IEEE Trans. Magn.*, vol. 51, no. 5, pp. 1–10, May 2015.

[12] A. S. Abdel-Khalik, S. Ahmed, and A. M. Massoud, "Dynamic modeling of a five-phase induction machine with a combined star/pentagon stator winding connection," *IEEE Trans. Energy Convers.*, vol. 31, no. 4, pp. 1645–1656, Dec. 2016.

[13] P. C. Krause, O. Wasynczuk, and S. D. Sudhoff, "Analysis of electric machinery and drive systems," *Second Ed. Wiley, Interscience, John Wiley Sons. INC. Publ.*, 2002.

[14] J. Yang, G. Liu, W. Zhao, Q. Chen, Y. Jiang, L. Sun, and X. Zhu, "Quantitative comparison for fractional-slot concentrated-winding configurations of permanent-magnet vernier machines," *IEEE Trans. Magn.*, vol. 49, no. 7, pp. 3826–3829, Jul. 2013.

[15] Y. Yokoi, T. Higuchi, and Y. Miyamoto, "General formulation of winding factor for fractional-slot concentrated winding design," *IET Electr. Power Appl.*, vol. 10, no. 4, pp. 231–239, Apr. 2016.

[16] F. Magnussen and C. Sadarangani, "Winding factors and Joule losses of permanent magnet machines with concentrated windings," in *IEEE International Electric Machines and Drives Conference, 2003. IEMDC'03.*, vol. 1, pp. 333–339.

[17] O. Misir, S. M. Raziee, N. Hammouche, C. Klaus, R. Kluge, and B. Ponick, "Calculation method of three-phase induction machines equipped with combined star-delta windings," in *2016 XXII International Conference on Electrical Machines (ICEM)*, 2016, pp. 166–172.

[18] J. Yang, G. Liu, W. Zhao, Q. Chen, Y. Jiang, L. Sun, and X. Zhu, "Quantitative Comparison for Fractional-Slot Concentrated-Winding Configurations of Permanent-Magnet Vernier Machines," *IEEE Trans. Magn.*, vol. 49, no. 7, pp. 3826–3829, Jul. 2013.

[19] A. Vagati, "The synchronous reluctance solution: a new alternative in AC drives," in *Proceedings of IECON'94 - 20th Annual Conference of IEEE Industrial Electronics*, vol. 1, pp. 1–13.

[20] M. N. Ibrahim, P. Sergeant, and E. M. Rashad, "Synchronous reluctance motor performance based on different electrical steel grades," *IEEE Trans. Magn.*, vol. 51, no. 11, pp. 1–4, Nov. 2015.

Chapter 6
Permanent Magnet Assisted SynRM

6.1 Introduction

This chapter investigates the influence of inserting permanent magnets in the rotor of SynRMs. In addition, the performance (output torque, torque ripple, power factor and efficiency) of four prototype SynRMs is compared. The four prototypes have identical stators and rotors lamination iron stacks, but different windings and with and without PMs in the rotor.

6.2 Overview of PMaSynRMs

The power factor of a "conventional" SynRM – "conventional" means without magnets on the rotor – is rather poor, requiring a high kVA inverter [1]. This means that the low cost of the SynRM may be compensated by a more expensive inverter [2]. In order to improve the power factor and to enhance the torque density and efficiency of SynRMs, permanent magnets are inserted in the rotor flux-barriers, resulting in a PM-assisted SynRM (PMaSynRM) [3]. Ferrite PMs are always employed in a PMaSynRM to reduce the machine cost compared to the conventional permanent magnets synchronous machines (PMSMs) [3]–[5]. The latter type of machines uses stronger and more expensive permanent magnets, usually NdFeB or SmCo rare earth magnets. In spite of their lower flux density (about 0.4 T at maximum), ferrite magnets have advantages too: 1) they can work at

higher temperatures without losing the magnetization compared to PMSMs with rare-earth magnets and 2) they are available on the market at low prices. This indeed increases the reliability of PMaSynRMs.

In literature, much research work on PMaSynRMs can be found [1]–[12]. In [1], an analysis on the characteristics of *dq*-axis inductances (L_d, L_q) of PMaSynRM was presented. It is proved that adding ferrite PMs in the *q*-axis direction of the machine results in an improved saliency ratio (L_d/L_q). This means that the whole machine performance (torque density, power factor and efficiency) is improved. In addition, it is verified by hysteresis loss analysis that the additional loss caused by the ferrite PMs is almost negligible. The rotor design of SynRMs with and without magnets was given in [2]. In addition, the impact of three rotor designs i.e. reference, optimal and optimal with PMs in the center of flux-barriers on the performance of SynRM was investigated. Furthermore, the influence of the different rotors on the magnetic saturation of the machine was studied. It was found that the torque density and the efficiency of the SynRM at the rated conditions increased by about 9.5% and 0.18% respectively when replacing the reference rotor by the optimal one, and by 15% and 0.55% respectively when inserting ferrite PMs in the center of the optimal rotor. In addition, the power factor of the optimal SynRM increased by 17.6% with inserted PMs. For the machine studied in [2], the SynRM efficiency and power factor can reach 95.63% and 0.93 respectively, by filling the whole flux-barriers of the rotor with ferrite PMs. In [3], the design and optimization of a PMaSynRM for an electric vehicle was presented for two different duty cycles. The two duty cycles are the city driving and a mixed driving operation. A global optimization is used to evaluate the most effective machine design. It was shown that the global optimization over the driving cycle leads to an increase of the efficiency. An analytical procedure to select the amount of PMs for a maximum low-speed torque rating was given in [4]. In addition, a FEM analysis was considered to include the iron saturation as well. It was found that a power factor above 0.8 can be obtained by choosing the amount of the ferrite PM flux to be about 3 times the *q*-axis flux due to the nominal current. In addition, it was shown that a high torque and a unity power factor can be obtained by choosing a proper amount of PM flux linkage. However, such a solution can't be achieved by ferrite PMs. It requires strong PMs such as rare earth magnets. The performance of a low power and speed PMaSynRM for high efficiency and wide constant power operation was examined in [7]. The rated power and

speed are about 60 W and 600 rpm respectively. It was shown that the PMaSynRM can offer a wide constant-power speed range up to 5 times the rated speed and a high efficiency operation in the constant power operating region. In [8], the influence of the PM volume (flux level) on the PMaSynRM performance was analyzed, considering a fixed lamination geometry and stack length. In addition, an optimization of the PMs for a PMaSynRM with a wide constant power speed range was given. The main conclusion of this paper is that the PM volume depends on the requirements of the application and it has to be carefully designed. The performance of a high power density PMaSynRM with ferrite magnets was evaluated in [9]. It is shown that by tapering the flux barriers and incorporating center ribs, the PMaSynRM can achieve sufficiently good mechanical properties to operate in the high-speed region and in addition, it can resist the demagnetization problem. Furthermore, a PMaSynRM was proposed with almost equal power density and constant power speed range compared to the PMSM used in Toyota Prius 2003. Moreover, the proposed PMaSynRM has a 90.0% efficiency for a wide operating range with a maximum of 97.0%. Detailed experimental validations for the performance of the proposed PMaSynRM were given in [12]. A design and optimization of a high speed PMaSynRM for traction applications was investigated in [10]. The study considers both highway and city driving cycles. It is shown that the torque ripple and losses can be introduced in the optimization process as additional objective functions. The analysis emphasized that an optimum solution for the torque ripple may not be necessarily a good solution for the losses. Various experimental tests on SynRM and PMaSynRM were presented in [11]. It is shown that inserting PMs in the rotor leads to a 10% increase in the SynRM torque at low speed and 50% in field weakening operation. The influence of rotor skewing is studied as well, showing a decrease in the torque ripple to about one third. However, the machine torque is slightly decreased. Moreover, it is evident that the SynRM power factor is improved in the whole operating regions when PMs are inserted in the rotor.

The work presented in this chapter investigates the performance of a SynRM with different stator winding connections and ferrite PMs inserted in the rotor. Two stator winding connections are employed: the conventional star connection and the combined star delta connection presented in **Chapter 5**.

6.3 Principle of inserting PMs in a SynRM

As shown in the earlier chapters, the performance of a SynRM depends mainly on the saliency ratio, i.e. the ratio of the *d*- and *q*-axis inductances (L_d/L_q). The L_d is related to the main flux of the machine and corresponds to the magnetizing inductance. L_q is a result of the flux obstructed by the flux-barriers and it has a quite low value. The ideal SynRM output torque can be obtained when the L_q tends to zero. This is because the SynRM output torque is proportional to (L_d-L_q). This can be understood simply from (2.6) and the vector diagram of the SynRM shown in Fig. 2.2 in **Chapter 2**.

In order to reduce the L_q value and hence to improve the SynRM performance, PMs with a low flux density are always inserted in the rotor flux-barriers of the conventional SynRM. This leads to the well-known PMaSynRM [7], [13]. The PM flux saturates the flux barrier ribs of the rotor as sketched in Fig. 6.1. This means that a lower *q*-axis current is required. Consequently, the power factor of the machine increases as well i.e. the required kVA inverting rating decreases [4]. Besides the improvement in the power factor of the machine, the PMs contribute significantly in the machine output torque [5].

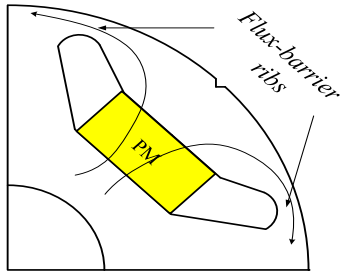

Figure 6.1: Saturation of the flux-barrier ribs as a result of the PM flux.

In general, the PMaSynRM is obtained by simply inserting PMs in the rotor flux-barriers of a SynRM. It is possible that the flux-barrier is partially or fully filled with PM material [2]. Several possible ways can be found in literature for partially filling the flux-barriers with PMs [14]–[16]. The PMs can be inserted in the center, outer and both center and outer of the flux-barriers as in [3], [16] and [14] respectively.

The more PM material in the flux-barrier, the better output torque and power factor can be obtained. However, there is an optimum value that achieves a compromise between the cost and the performance of the machine.

The dynamic model of a PMaSynRM is similar to that of the conventional SynRM (**Chapter 2**) with some modifications as a result of the inserted PMs. The main modifications are related to the voltage and torque equations [2], [17]. The steady state voltage and torque equations are given by:

$$\begin{cases} V_d = R_s I_d - \omega_r P \psi_q + \omega_r P \psi_{pm} \\ V_q = R_s I_q + \omega_r P \psi_d \end{cases} \tag{6.1}$$

$$T_e = \frac{3}{2} P(\psi_d I_q - \psi_q I_d + \psi_{pm} I_d) \tag{6.2}$$

The torque (6.2) can be expressed as a function of the saliency difference (L_d-L_q) as follows:

$$T_e = \frac{3}{2} P((L_d - L_q) I_d I_q + \psi_{pm} I_d) \tag{6.3}$$

where ψ_{pm} is the flux linkage of the PMs.

The vector diagram of the PMaSynRM is plotted in Fig. 6.2. It is evident that increasing the PM flux (ψ_{pm}) reduces the angle (ϕ) between the voltage and current vectors. This improves the machine power factor. Furthermore, the PM torque component (6.3) increases, resulting in an increased machine output torque. In contrast to a PMSM, the dominant torque component is coming from the saliency difference (L_d-L_q) of the PMaSynRM (the first term in (6.3)), but not from the PM flux component (the last term in (6.3)).

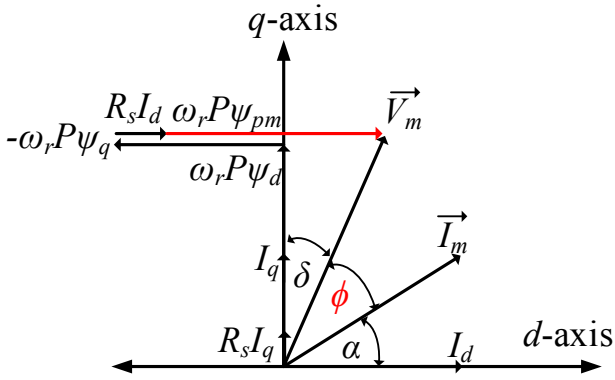

Figure 6.2: Vector diagram of the PMaSynRM.

6.4 Performance comparison of SynRM and PMaSynRM prototypes

In this section, the performance (output torque, power factor and efficiency) of SynRMs and PMaSynRMs is compared. In order to have a fair comparison, two stator and two rotor prototypes are studied and tested. The two stators and two rotors have identical geometries of the iron lamination stacks. Two distributed winding configurations are used on the stator: the first configuration is the conventional star connected winding and the second one is the combined star-delta connection (sdd) presented in **Chapter 5**. The rotors have three flux-barriers per pole: one rotor is made without ferrite PMs and the second one is made with PMs. Figure 6.3 shows a one pole of the geometries of the S and Sd prototypes. The a, b and c windings represent the star coils (aY, bY and cY), while the ab, bc and ca windings represent the delta coils (aΔ, bΔ and cΔ) as in **Chapter 5**. The ferrite PMs are inserted in the centre of the flux-barrier as sketched in Fig. 6.4; the black arrow shows the magnetization direction of the PMs. The ferrite PM type is Y30BH with the parameters listed in Table 6.1. The geometrical and electromagnetic parameters of the machine are given in **Chapter 5**.

With the two stators and two rotors, four prototype SynRMs can be obtained. These four machines are listed in Table 6.2. The abbreviations given in Table 6.2 are used in the remaining of the text.

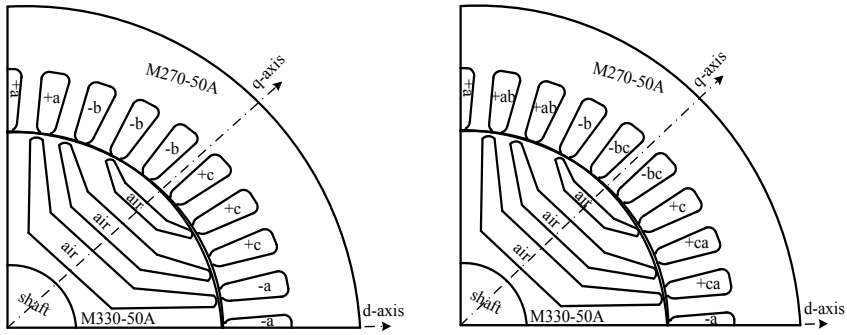

(a) S prototype (b) Sd prototype

Figure 6.3: One pole geometry of S and Sd prototype SynRMs.

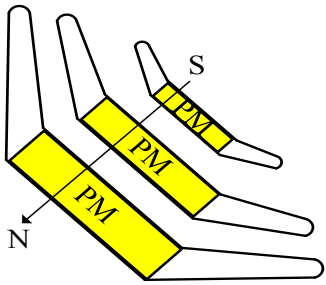

Figure 6.4: Flux-barriers with inserted ferrite PMs.

Table 6.1: Ferrite PM properties at 20° C.

Parameter	Value	Parameter	Value
Remanence, B_r	0.39 T	Maximum energy, BH_{max}	25 kJ/m^3
Coercivity, H_c	234 kA/m	Temperature coefficient	-0.2%/°C (0-100°C)

Table 6.2: SynRM abbreviations.

Machine		Abbreviation
Stator winding	**Rotor**	
Conventional star connection, Fig. 6.3-a	Flux-barriers without PMs, Fig. 6.3	S
Combined star-delta connection, Fig. 6.3-b	Flux-barriers without PMs, Fig. 6.3	Sd
Conventional star connection, Fig. 6.3-a	Flux-barriers with ferrite PMs, Fig. 6.3	S-PM
Combined star-delta connection, Fig. 6.3-b	Flux-barriers with ferrite PMs, Fig. 6.3	Sd-PM

Four SynRMs are modelled using 2D-MAXWELL ANSYS software. The goal is to compare their performance i.e. output torque, torque ripple, power factor, losses and efficiency. In the simulation, in the stator, three phase sinusoidal currents are enforced into the windings to simply emulate the current controlled inverter that supplies the SynRM. For the Sd machines, the three sources are connected to the star coils as shown in Fig. 5.8 in **Chapter 5**. Consequently, the currents in the delta coils are not enforced; they are computed by the FEM. Note that in the delta coils, triplen harmonics of the current occur as observed in **Chapter 5**. These circulating currents are taken into account in the simulation. The rotor is rotated at a fixed speed.

Figure 6.5 shows the output torque of the 4 SynRMs as a function of the current angle at rated speed (3000 rpm) and for half and full rated current (12.23 A). For half rated current at the optimal current angles, it is observed that the output torque of the Sd-PM, S-PM and Sd machines increases by about 41.85%, 34.55% and 6.41% respectively compared to the S machine. The optimal current angle represents the angle of the stator current vector with respect to the *d*-axis, see Fig. 6.2 that achieves the maximum output torque. It is evident from Fig. 6.5 that the optimal current angle is not a fixed value and depends on the stator current level and on the saturation behaviour of the machine core as well. This can be noticed in Fig. 6.5 by comparing the different curves of several machines and current levels. Furthermore, the output torque of the Sd-PM machine is higher than the S-PM by about 5.42%

at the optimal current angles. This means that the amount of the increase in the output torque of the two machines with reluctance rotor (S and Sd) and the two machines with PM-assisted rotor (S-PM and Sd-PM) at the optimal current angles is not constant. This is because of the different *dq*-axis currents and the saturation in the machine core.

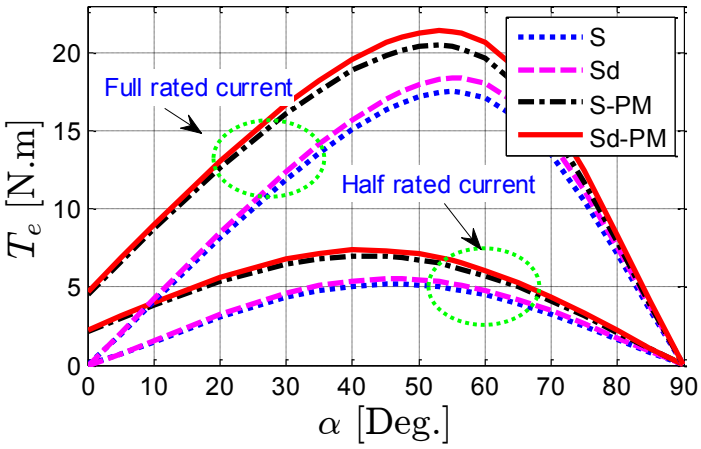

Figure 6.5: SynRM output torque (T_e) as a function of current angle (α) at rated speed.

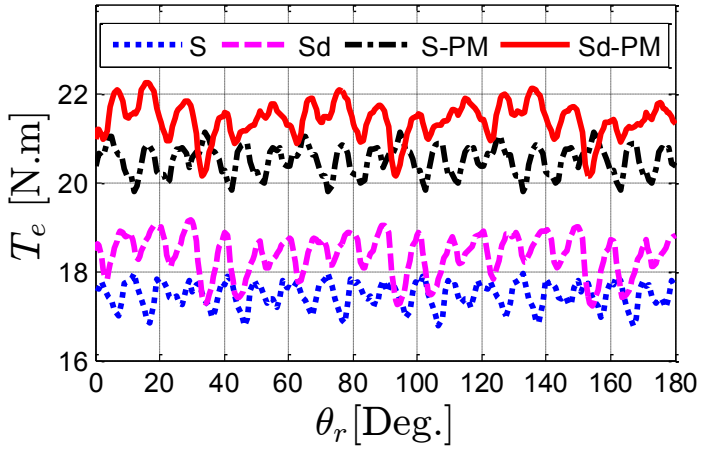

Figure 6.6: SynRM output torque (T_e) as a function of mechanical rotor angle (θ_m) at rated conditions and optimal current angles.

On the other hand, for full rated current, it is clear from Fig. 6.5 that the output torque of the Sd, S-PM and Sd-PM machines is higher than the torque of the S machine by about 5.02%, 17.01% and 22.37% respectively at the optimal current angles. This can be seen also in Fig. 6.6 in which the output torque of the 4 machines is plotted for several rotor positions. An interesting observation here is that the increase in the output torque of the Sd, S-PM and Sd-PM machines compared to the S machine is not a constant value; it is current dependent. The flux density distribution of 4 machines at θ_r=0° of Fig. 6.6 is shown in Fig. 6.7. It is clear that the Sd-PM machine has regions with much higher flux density compared to the other machines, in particular in the stator yoke.

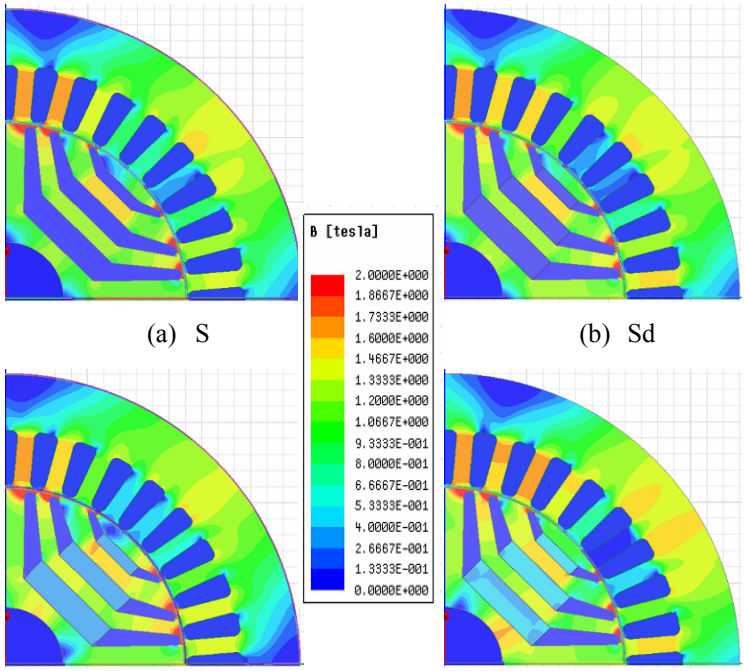

Figure 6.7: Flux density distribution of the 4 prototypes at rated current and optimal current angles.

Figure 6.8 shows the output torque of the 4 machines as a function of the stator current at the optimal current angles and rated speed. The

difference of the output torque (in percent) of the Sd-PM, S-PM and Sd machines compared to the S machine is reported in Fig. 6.9. Clearly, both machines with PMs in the rotor (Sd-PM and S-PM) have much higher output torque compared to the S machine. The Sd-PM machine has an increase in the output torque of about 22.37% for rated current and of about 150% for low current, compared to the S machine. This is mainly thanks to the inserted ferrite PMs in the rotor. Furthermore, the difference in the output torque of the Sd-PM, S-PM and Sd machines compared to the S machine decreases with the increase in the stator current. This is due to the decrease in the saliency ratio difference with the increase in the current as shown in Fig. 6.10. For low current, the PM flux reduces the *q*-axis inductance of the machine much more than for high current. This indeed results in the decrease of the saliency ratio difference with the increase in the stator current. The similar shape of the curves of Figs. 6.9 and 6.10 indicates that the torque gain is almost completely caused by the saliency difference.

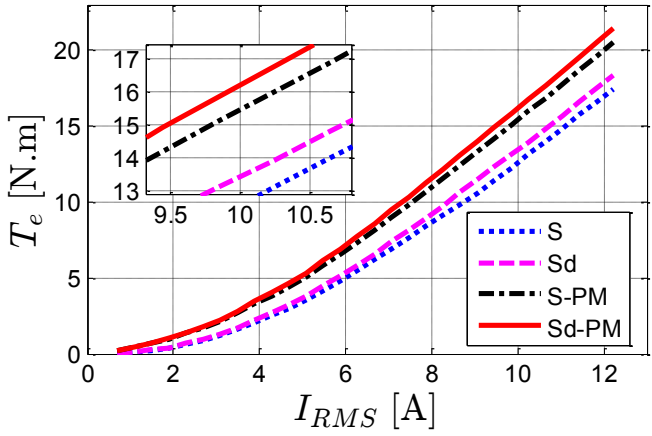

Figure 6.8: SynRM output torque (T_e) as a function of stator current (*RMS*) at optimal current angles and rated speed.

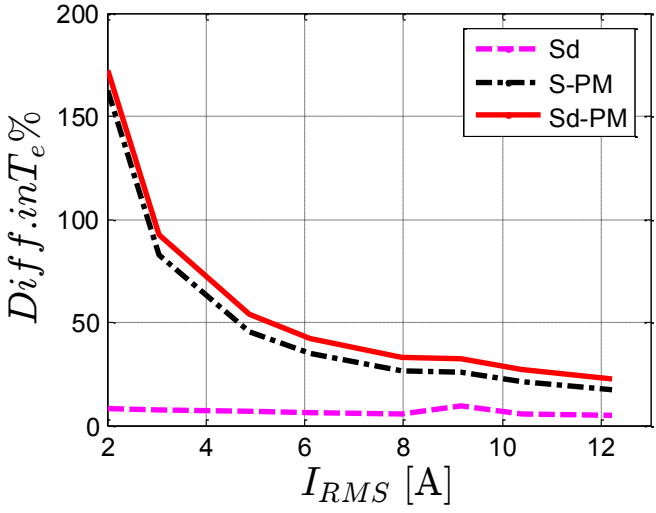

Figure 6.9: Difference in the output torque % (T_e) as a function of stator current (*RMS*) at optimal current angles and rated speed of SynRMs.

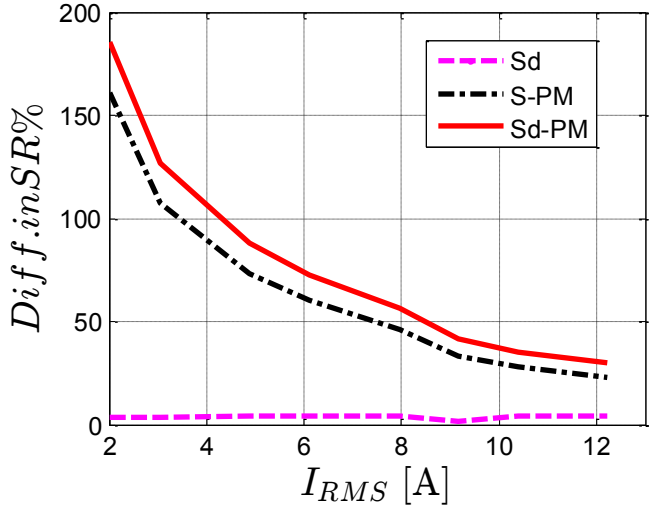

Figure 6.10: Difference in the saliency ratio % (*SR*) as a function of stator current (*RMS*) at optimal current angles and rated speed of SynRMs.

Figure 6.11 shows the variation of the torque ripple (in percent) as a function of the current angle at the rated conditions of the 4 machines. It is observed that the torque ripple of the 4 machines decreases with the increase in current angle till an optimal angle, and then increases again. The value and the current angle at which the minimum occurs is different for the 4 machines. This is due to the fact that the torque ripple depends on both the amount of spatial harmonics of the magneto-motive force (MMF) and the machine average torque. Both the harmonics and the average torque of the 4 machines are different. By comparing the torque ripple of the 4 machines, it can be noticed that the machines with combined star-delta connected stator have a higher torque ripple compared to the machines with star winding. This is due to the harmonics of the delta coils. The torque ripple increases from about 6.4% (star connection) to about 9.5% (star-delta connection). For the 4 machines, Fig. 6.12 shows the variation of the torque ripple (in percent) for different stator currents, at rated conditions and optimal current angles. It is seen that the SynRM torque ripple decreases with increasing stator current. This is mainly because of the increase in the output torque and the fact that the ripple is given in percent of the torque. In absolute peak-to-peak value, the ripple increases linearly with the increase in the stator current as presented in [18]. In addition, the Sd machines have a higher torque ripple than the S machines. This is because of the harmonics in the delta coils as mentioned before.

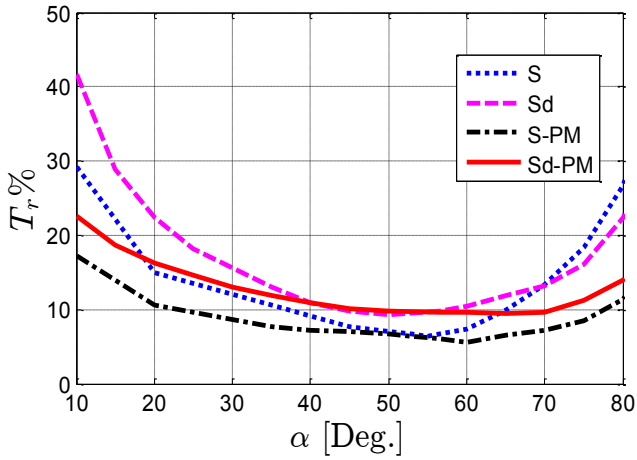

Figure 6.11: SynRM torque ripple (T_r %) as a function of current angle (α) at rated current and speed.

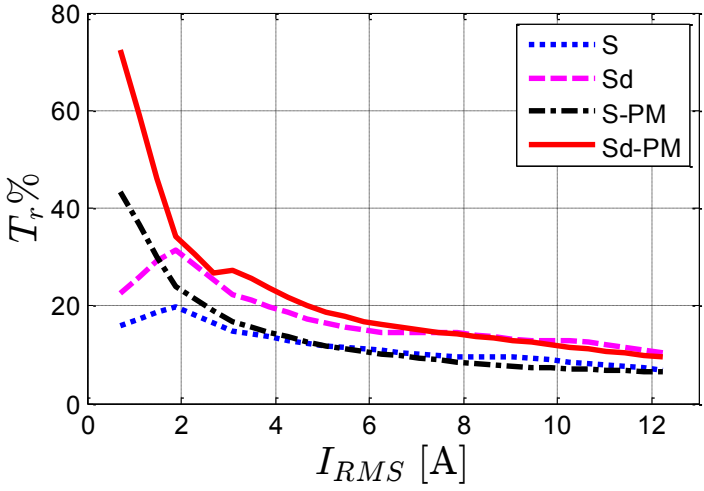

Figure 6.12: SynRM torque ripple % (T_r) as a function of stator current (*RMS*) at optimal current angles and rated speed.

The power factor of the 4 SynRMs as a function of the current angles for rated conditions is shown in Fig. 6.13. It is observed that the SynRM power factor increases with the increase in the current angle till an optimal value is achieved. This is because of the increase in the saliency ratio. Notice that the maximum value is at higher current angle than for the maximum torque in Fig. 6.5. We know that the power factor is proportional to the phase angle between the stator voltage and current vector i.e. ϕ in Fig. 6.2. With increasing the current angle for a fixed stator current amplitude, L_d increases significantly and L_q decreases to almost a constant value. Therefore, the *d*-axis flux component (related to L_d) has a main contribution on the variation of the voltage vector as in (6.1), this results in a decreased phase angle between the voltage and current of the machine, hence the power factor increases. This is different in case of the SynRM torque where the torque is proportional to the difference between the L_d and L_q as well as the current angle for a fixed stator current as in (6.3). With neglecting the saturation in the inductances, the maximum torque of the SynRM occurs at a current angle of 45° in SynRMs. With including the magnetic saturation, this angle shifts slightly. In case of a PMaSynRM, the current angle of the maximum power factor is higher than that of SynRM, as seen in Fig. 6.13. This is because of adding PMs which contributes to the *d*-axis voltage component. Increasing the *d*-axis voltage component increases

the phase angle between the voltage and current vectors as in Fig. 2.6. Consequently, the current angle of the maximum power factor is larger in PMaSynRMs than in SynRMs. Figure 6.13 confirms findings in other studies in literature e.g. [14] that adding PMs in the rotor increases the power factor dramatically. However, the figure shows that there is almost no influence on the machine power factor when using a combined star-delta connection instead of the conventional star connection, both for the machines with and without ferrite PMs. This is because the combined star-delta winding has a non-significant influence on the phase shift between the stator current and voltage vectors.

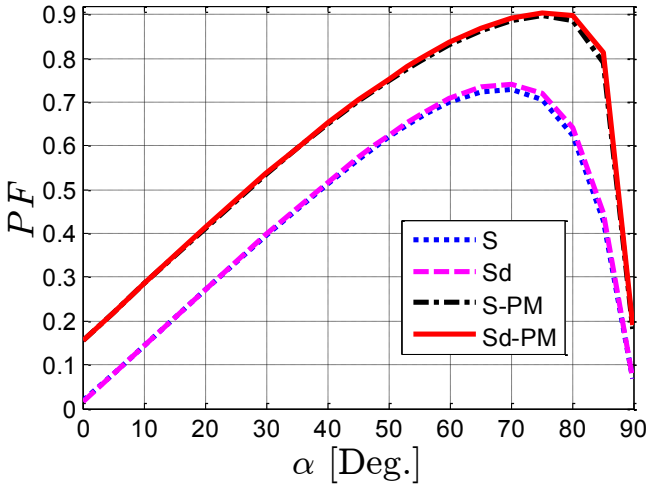

Figure 6.13: SynRM power factor (*PF*) as a function of current angle (α) at rated current and speed.

The variation of the power factor of the 4 SynRMs as a function of the stator current is reported in Fig. 6.14. The simulations are done at the optimal current angles and at rated speed. We already know from Fig. 6.13 that the ferrite PMs increase the power factor significantly. In addition, we learn from Fig. 6.14 that the gain in power factor becomes lower at high stator currents. In Fig. 6.9, we have seen a similar behaviour for the torque: i.e. that the gain in torque becomes lower too at high stator currents. For low stator current, the PM flux linkage is dominant compared to the machine flux components (ψ_d and ψ_q in Fig. 6.2), hence the phase angle between the voltage and current is very low,

resulting in a high power factor. However, with increasing stator current, the machine flux increases while the PM flux remains the same, resulting in an increase in the power factor angle. Hence the power factor decreases as noticed in Fig. 6.14.

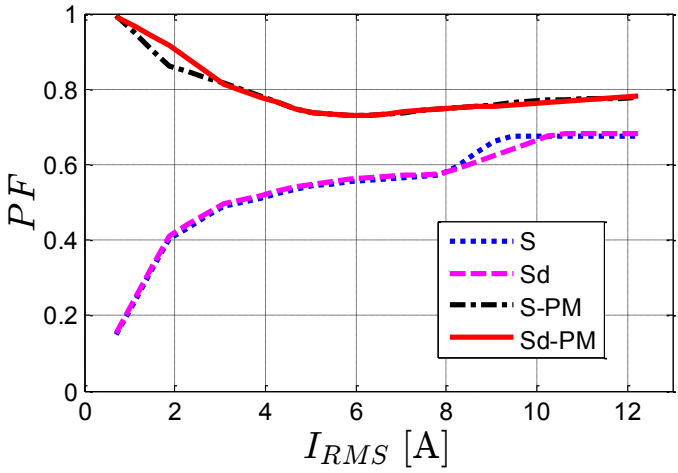

Figure 6.14: SynRM power factor (*PF*) as a function of stator current (*RMS*) at optimal current angles and rated speed.

The simulated SynRM efficiency of the 4 SynRMs as a function of the stator current at the optimal current angles and for half and full rated speed is reported in Fig. 6.15. The efficiency calculation includes only the copper and iron losses of the machine. The copper losses are computed based on the measured winding resistance of the machine and the current amplitude. The current amplitude is chosen the same for each machine. Note that the copper losses are similar in the star and the delta windings. This is because in the delta-connected coils, the increase in the number of turns by a factor $\sqrt{3}$ and the reduction in the cross-section area by a factor $\sqrt{3}$ is compensated by a lower current, also by a factor $\sqrt{3}$. The iron losses are computed using the magnetic flux density *B* resulting from FEM calculations for several points and positions. Then the iron losses are obtained as described in **Chapter 4** [19].

Figure 6.15 shows a slight increase in the machine efficiency using the combined star-delta winding instead of the star winding: about 0.33% point higher at the maximum efficiency. Moreover, the efficiency of the machine is increased with inserting PMs in the rotor. This is clear when comparing the efficiency of the Sd-PM machine with the S machine under rated current: about 1.25% point higher for half rated speed and 0.82% point for full rated speed. The low difference in the efficiency between the machines can be understood from Fig. 6.16. This figure shows the computed total losses of the 4 machines for half and rated speeds. The strong increase with current indicates that the copper losses (which are the same for the machines) are dominant. It is clear that the losses are approximately similar; only a slight increase in the losses of the SynRMs having combined star-delta windings occurs due to circulating harmonic currents.

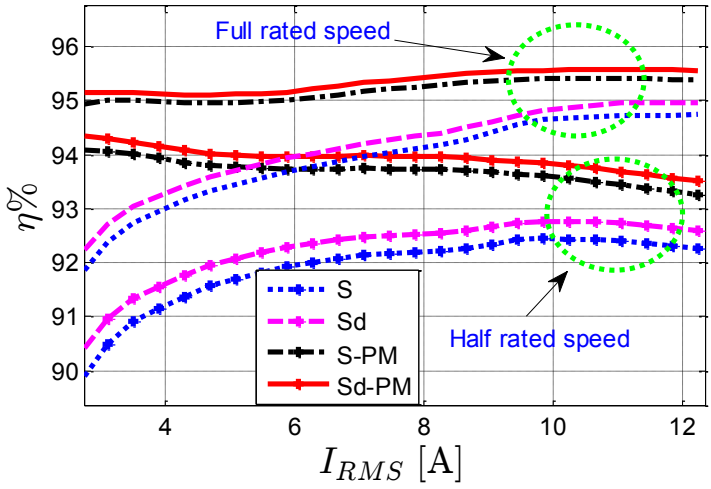

Figure 6.15: The simulated efficiency as a function of stator current (*RMS*) at optimal current angles (only copper and iron losses are taken into account).

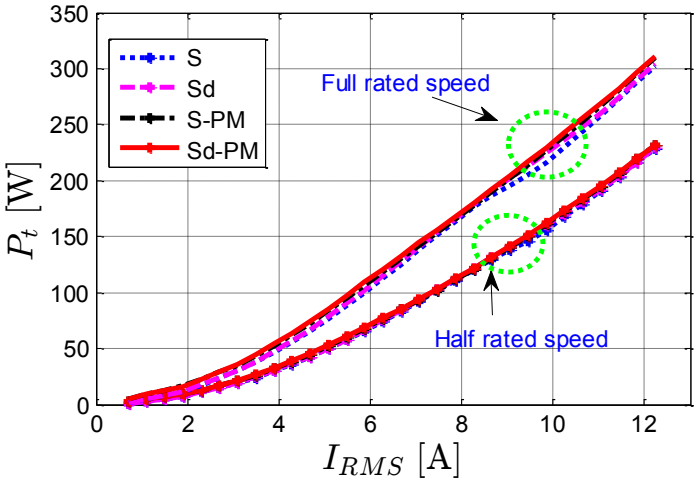

Figure 6.16: The simulated total losses (copper +iron) as a function of stator current (*RMS*) at optimal current angles.

The simulated efficiency maps of the four SynRMs are shown in Figs. 6.17 to 6.20. At a given speed, the stator current varies up to the rated value at the optimal current angles. Then the efficiency is calculated as mentioned before in Fig. 6.15. It is clear that the efficiency of SynRM increased a bit using combined star-delta winding. In addition, it increases significantly with inserted PM in the rotor. The maximum efficiency of Sd-PM machine is about 95.5% compared to 94.74% for S, 94.95% for Sd and 95.40% for S-PM machines.

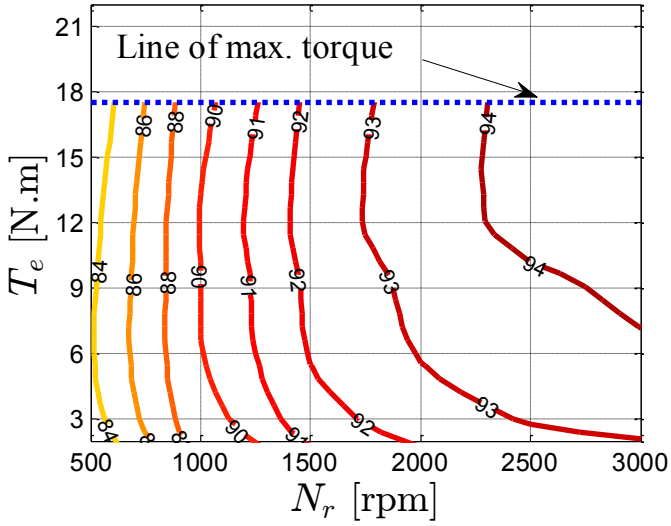

Figure 6.17: The simulated efficiency map of S SynRM at optimal current angles (only copper and iron losses are taken into account).

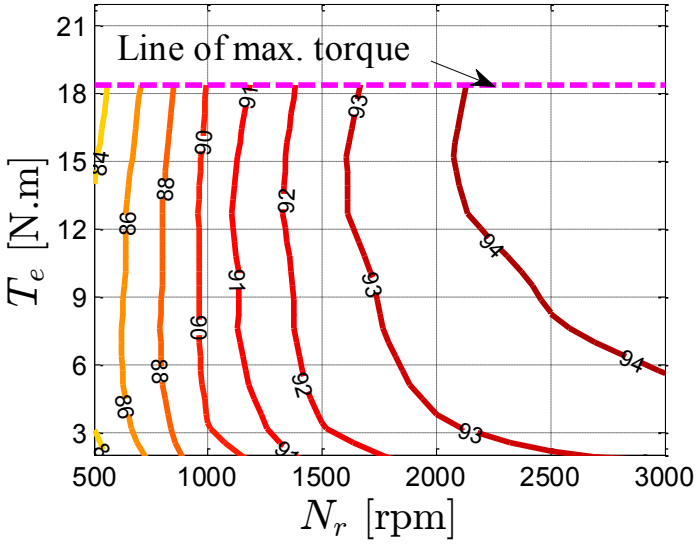

Figure 6.18: The simulated efficiency map of Sd SynRM at optimal current angles (only copper and iron losses are taken into account).

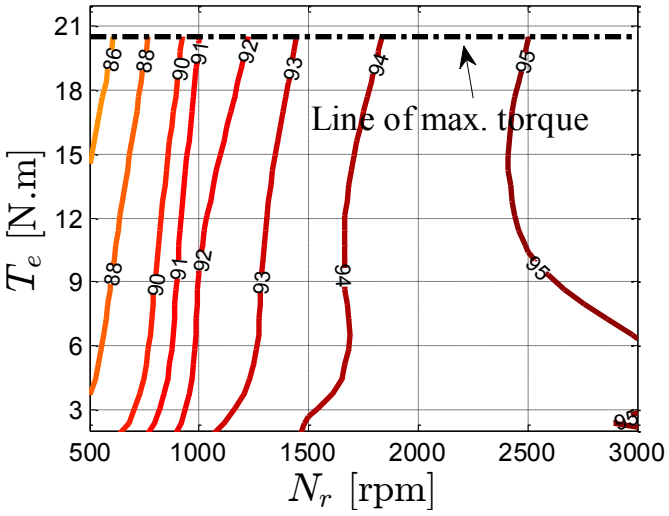

Figure 6.19: The simulated efficiency map of S-PM SynRM at optimal current angles (only copper and iron losses are taken into account).

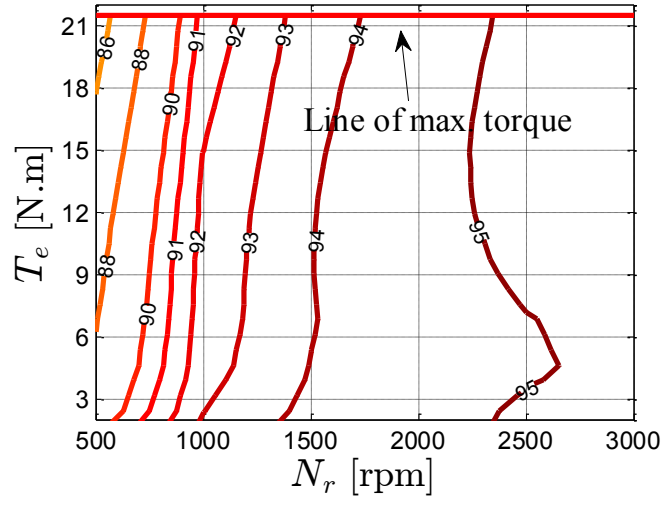

Figure 6.20: The simulated efficiency map of Sd-PM SynRM at optimal current angles (only copper and iron losses are taken into account).

6.5 Conclusions

This chapter has investigated the influence of inserting permanent magnets (PMs) inside the flux-barriers of SynRMs. The performance (output torque, power factor, efficiency) of four SynRMs has been compared; they have identical iron laminations in the stator and rotors. Two different winding layouts are used: the conventional star winding and the combined star-delta winding. In addition, two rotors are considered: one with ferrite PMs in the center of the rotor flux-barriers and the second one without magnets.

For the same copper volume and current, the machine with the combined star-delta winding and with ferrite PMs inserted in the rotor corresponds to an approximately 22% increase in the torque at rated current and speed compared to the machine with conventional star connection, and no magnets in the rotor. This enhancement is mainly thanks to adding the ferrite PMs in the rotor and the improvement in the winding factor of the combined star-delta winding. In addition, the torque gain increases up to 150% for low current compared to the conventional star connection with reluctance rotor. Moreover, the efficiency of the machine is increased with inserting PMs in the rotor. The Sd-PM machine has about 1.25% point higher for half rated speed and about 0.82% point higher for full rated speed, compared to the S machine under rated current. An interesting observation here is that the efficiency of the machine with combined star-delta connection and PM assisted rotor (Sd-PM) increases significantly in partial loads. Furthermore, the power factor of the machines with PMs inserted in the rotor (Sd-PM and S-PM) is very high for partial load compared to the machines without PM (Sd and S).

Biography

[1] J. H. Lee, J. Ch. Kim, and D. S. Hyun, “Effect analysis of magnet on Ld and Lq inductance of permanent magnet assisted synchronous reluctance motor using finite element method,” *IEEE Trans. Magn.*, vol. 35, no. 3, pp. 1199–1202, May 1999.

[2] M. N. Ibrahim, P. Sergeant, and E. M. Rashad, “Rotor design with and without permanent magnets and performance evaluation of synchronous reluctance motors,” *ICEMS2016*, pp.

1–7, 2016.

[3] E. Carraro, M. Morandin, and N. Bianchi, “Traction PMASR motor optimization according to a given driving cycle,” *IEEE Trans. Ind. Appl.*, vol. 52, no. 1, pp. 209–216, Jan. 2016.

[4] N. Bianchi, E. Fornasiero, and W. Soong, “Selection of PM flux linkage for maximum low-speed torque rating in a PM-assisted synchronous reluctance machine,” *IEEE Trans. Ind. Appl.*, vol. 51, no. 5, pp. 3600–3608, Sep. 2015.

[5] M. Obata, S. Morimoto, M. Sanada, and Y. Inoue, “Performance of PMASynRM with ferrite magnets for EV/HEV applications considering productivity,” *IEEE Trans. Ind. Appl.*, vol. 50, no. 4, pp. 2427–2435, Jul. 2014.

[6] N. Bianchi, S. Bolognani, D. Bon, and M. Dai Pre, “Rotor flux-barrier design for torque ripple reduction in synchronous reluctance and pm-assisted synchronous reluctance motors,” *IEEE Trans. Ind. Appl.*, vol. 45, no. 3, pp. 921–928, 2009.

[7] S. Morimoto, M. Sanada, and Y. Takeda, “Performance of PM-assisted synchronous reluctance motor for high-efficiency and wide constant-power operation,” *IEEE Trans. Ind. Appl.*, vol. 37, no. 5, pp. 1234–1240, 2001.

[8] M. Barcaro, N. Bianchi, and F. Magnussen, “Permanent-magnet optimization in permanent-magnet-assisted synchronous reluctance motor for a wide constant-power speed range,” *IEEE Trans. Ind. Electron.*, vol. 59, no. 6, pp. 2495–2502, Jun. 2012.

[9] S. Ooi, S. Morimoto, M. Sanada, and Y. Inoue, “Performance evaluation of a high-power-density PMASynRM with ferrite magnets,” *IEEE Trans. Ind. Appl.*, vol. 49, no. 3, pp. 1308–1315, May 2013.

[10] M. Degano, E. Carraro, and N. Bianchi, “Selection criteria and robust optimization of a traction PM-assisted synchronous reluctance motor,” *IEEE Trans. Ind. Appl.*, vol. 51, no. 6, pp. 4383–4391, Nov. 2015.

[11] N. Bianchi, E. Fornasiero, M. Ferrari, and M. Castiello, “Experimental comparison of PM-assisted synchronous reluctance motors,” *IEEE Trans. Ind. Appl.*, vol. 52, no. 1, pp. 163–171, Jan. 2016.

[12] S. Morimoto, Shohei O., Y. Inoue, and M. Sanada, “Experimental evaluation of a rare-earth-free PMASynRM with ferrite magnets for automotive applications,” *IEEE Trans. Ind. Electron.*, vol. 61, no. 10, pp. 5749–5756, Oct. 2014.

[13] M. Ferrari, N. Bianchi, and E. Fornasiero, “Analysis of rotor saturation in synchronous reluctance and PM-assisted reluctance motors,” *IEEE Trans. Ind. Appl.*, vol. 51, no. 1, pp. 169–177, Jan. 2015.

[14] W. Zhao, D. Chen, T. A. Lipo, and B.-I. Kwon, “Performance improvement of ferrite-assisted synchronous reluctance machines using asymmetrical rotor configurations,” *IEEE Trans. Magn.*, vol. 51, no. 11, pp. 1–4, Nov. 2015.

[15] B. Nikbakhtian, S. Talebi, P. Niazi, and H. A. Toliyat, “An analytical model for an N-flux barrier per pole permanent magnet-assisted synchronous reluctance motor,” in *2009 IEEE International Electric Machines and Drives Conference*, 2009, pp. 129–136.

[16] R. Vartanian, H. A. Toliyat, B. Akin, and R. Poley, “Power factor improvement of synchronous reluctance motors (SynRM) using permanent magnets for drive size reduction,” in *2012 Twenty-Seventh Annual IEEE Applied Power Electronics Conference and Exposition (APEC)*, 2012, pp. 628–633.

[17] M. N. Ibrahim, P. Sergeant, and E. M. Rashad, “Influence of rotor flux-barrier geometry on torque and torque ripple of permanent-magnet-assisted synchronous reluctance motors,” in *2016 XXII International Conference on Electrical Machines (ICEM)*, 2016, pp. 398–404.

[18] M. N. Ibrahim, P. Sergeant, and E. M. Rashad, “Relevance of including saturation and position dependence in the inductances for accurate dynamic modeling and control of SynRMs,” *IEEE Trans. Ind. Appl.*, vol. 53, no. 1, pp. 151–160, Jan. 2017.

[19] M. N. Ibrahim, P. Sergeant, and E. M. Rashad, “Synchronous reluctance motor performance based on different electrical steel grades,” *IEEE Trans. Magn.*, vol. 51, no. 11, pp. 1–4, Nov. 2015.

Chapter 7

Experimental Validation of the Prototype SynRMs

7.1 Introduction

This chapter shows the experimental validation of the aforementioned simulated results. A complete overview about the employed laboratory setup is given. Eventually, measurements on five prototype SynRMs are obtained.

7.2 Overview about the experimental setup

In this section, an overview about the employed experimental setup is presented. The experimental setup is shown in Fig. 7.1 and consists of a 9.3 kW, 2905 rpm induction motor coupled with the prototype SynRM under test. A torque sensor (DR-2112-R) is mounted between the two machines to measure the SynRM output torque. In addition, an incremental encoder (DHO514) of 1024 samples/revolution is placed on the induction motor shaft to measure the speed of the system. Three LA 25-NP current sensors measure the SynRM currents with the required bandwidth for the control system. Furthermore, the SynRM is supplied by a three-phase voltage source inverter, consisting of a Semikron IGBT module and a controlled DC supply. A four-channel power analyzer (Tektronix PA4000) is connected between the Semikron IGBT module and the SynRM to measure and analyze the

electrical components i.e. voltage, current, power and power factor. The induction motor is controlled by a commercial inverter CFW11 to be used as a prime mover or as a braking load.

The complete block diagram of the field oriented control is shown in Fig. 7.2. The SynRM can work either in a speed or a torque control mode. In speed control mode, the conventional field oriented control (FOC) method is used to drive the SynRM [1]. In this case, the induction motor is emulated as a braking load. In torque control mode of the SynRM, the speed control loop of the FOC shown in Fig. 7.2 is removed. Then, the reference values i_d* and i_q* are given. In this situation, the induction motor is used as a prime mover to keep the speed of the SynRM constant at the desired value.

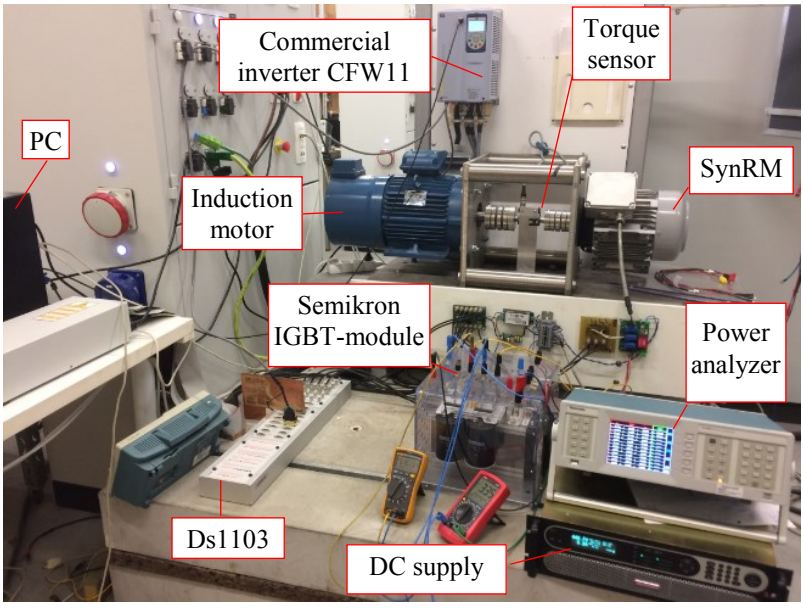

Figure 7.1: A photograph of the complete experimental setup.

For data acquisition and to run the control algorithm of the whole setup (Fig. 7.2), a dSPACE 1103 platform is employed for the SynRM. The platform controls the Semikron IGBT module that supplies the SynRM by giving the 6 switching signals to the Semikron IGBT module. This approach makes it possible to adjust several parameters such as the current vector angle α (or the i_d and i_q current components),

the switching frequency, the parameters of the PI controllers, and the DC bus voltage. For the induction motor, the commercial software of the CFW11 inverter is used to give set points of speed (in rpm) or torque (in percent of the rated value) to the commercial inverter online by the computer.

The space vector pulse width modulation (SVPWM) technique is implemented by the dSPACE 1103 platform and used to control the switches of the Semikron IGBT module for the SynRM. In the experiments, the default switching frequency of the inverter is set to 6.6 kHz with a sampling time of 20 μs. The DC bus voltage of the inverter is set to a default value of 600 V. Both the switching frequency and the DC bus voltage are variable, but it is explicitly mentioned when values other than the default are selected.

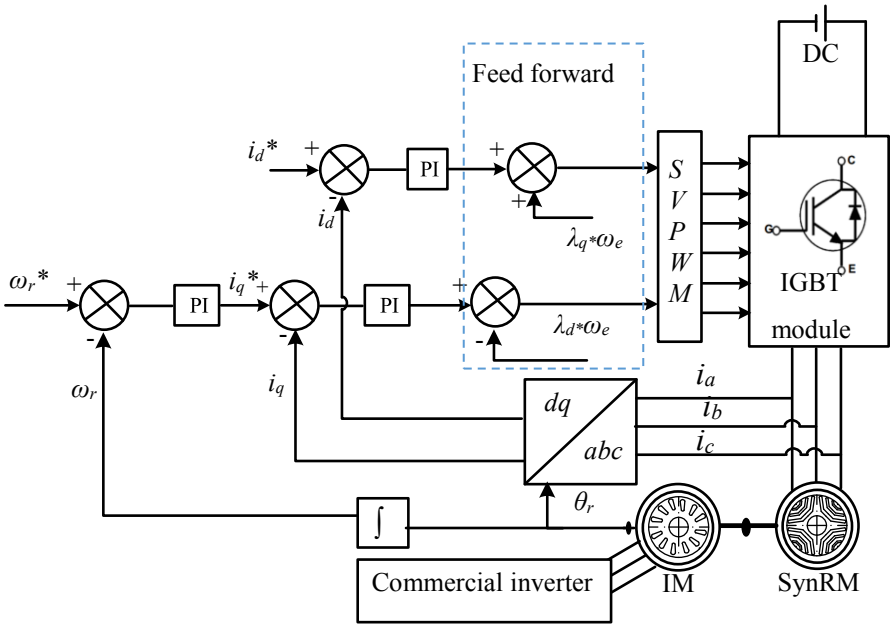

Figure 7.2: The block diagram of the field oriented control of SynRM.

7.3 Parameters of the PI controllers

Three proportional integral (PI) controllers are used in the field oriented control method as seen in Fig. 7.2; one for the speed control loop and the remaining two for the *dq*-axis currents control loops. Eventually, three times two PI parameters (K_p, K_i) are required. In this thesis, the parameters (K_p, K_i) of every PI controller are obtained separately by experimental tests.

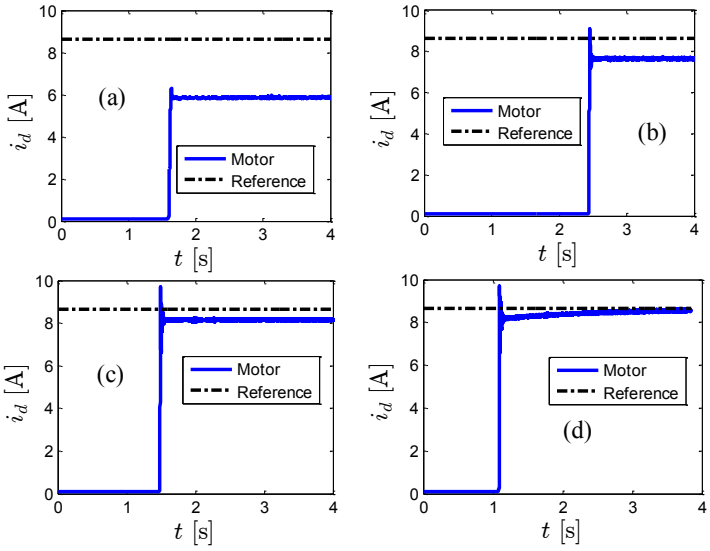

Figure 7.3: *d*- axis current as a function of time. (a) k_{pd}=10, K_{id}=0, (b) k_{pd}=20, K_{id}=0 , (c) k_p=30, K_{id}=0 and (d) k_{pd}=20, K_{id}=5.

The parameters of the current control loops have to be identified firstly, then the parameters of the speed control loop. At first, we start to obtain the PI parameters of the *d*-axis current loop. The remaining two loops (*q*-axis current and speed loops) are disconnected from the block diagram shown in Fig. 7.2. A set value (i_d*) as a step function is given with an initially selected value for K_p. Then, the feedback signal (i_d) is recorded as shown in Fig. 7.3-a. Based on the feedback signal of i_d, the K_p will be increased or decreased to reduce the error between the feedback and set point signals. Once the response of the feedback signal seems stable with a steady state error as seen in Fig. 7.3-c, then a

selected value of K_i is inserted. The K_i value will be decreased or increased based on the response of the feedback signal as observed in Fig. 7.3-d. Eventually, the K_p and K_i values of the i_d current control loop are known. A similar approach can be done for the i_q current control loop.

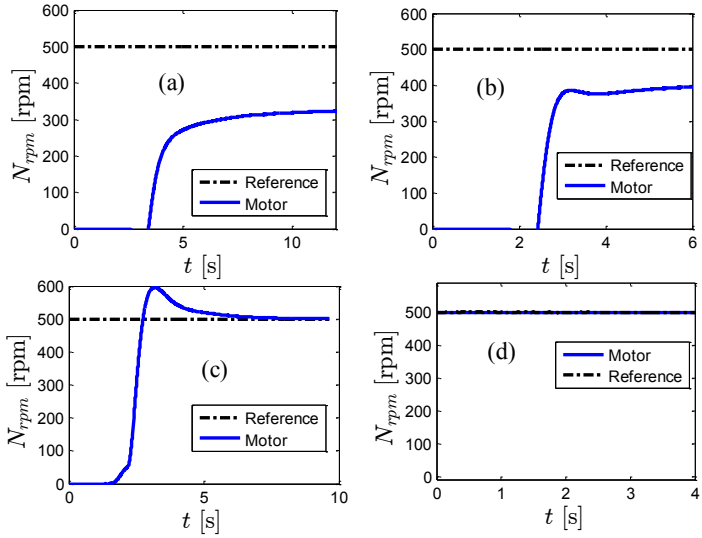

Figure 7.4: Motor speed as a function of time. (a) k_{ps}=0.005, K_{is}=0, (b) k_{ps}=0.01, K_{is}=0, (c) k_{ps}=0.02, K_{is}=0.01 and (d) k_{ps}=0.02, K_{is}=0.02.

Once the PI controller parameters of the current control loops are obtained, then the parameters of the speed control loop can be obtained. Again, an initially selected value of K_p for the speed control loop is given, and the behavior of the motor speed is observed as shown in Fig. 7.4-a. The K_p value of the speed control loop will be increased or decreased based on the response of the motor speed. Once the motor is rotating in a stable way with a steady state error as seen in Fig. 7.4-b, then the K_i value of the speed control loop is inserted, observing the motor behavior as observed in Fig. 7.3-c. Eventually, the parameters of the three PI controllers are obtained.

To improve the stability of the SynRM against the variation of the speed and current, when constant PI parameters are used, feed forward loops for both *d* and *q* current control loops are employed [2], [3]. This

is due to the fact that both the *dq*-axis flux linkages (λ_d, λ_q) of the SynRM vary nonlinearly with the currents (i_d, i_q), as seen in **Chapter 2**. The values of λ_d and λ_q are obtained by FEM and stored in look-up tables, as presented in **Chapter 2**. Then, these look-up tables are used in the experimental tests.

7.4 Prototype SynRMs

Five prototype SynRMs have been tested experimentally using the complete laboratory setup shown in Figs. 7.1 and 7.2. All the prototypes have similar sizes i.e. outer-inner stator/rotor diameters, airgap and stack lengths as shown in Fig. 7.5.

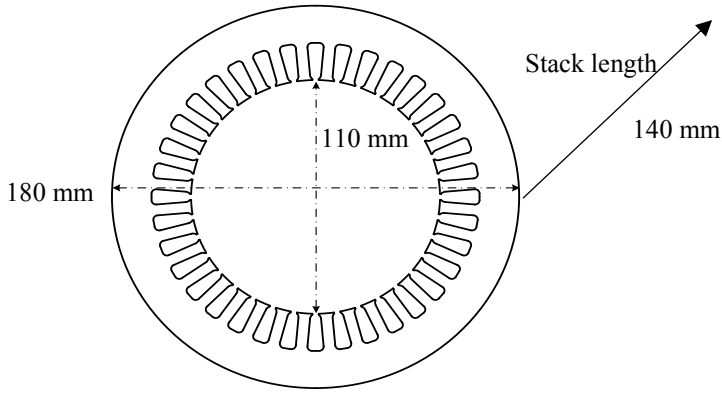

Figure 7.5: SynRM stator geometry.

The first prototype is called the reference machine. The stator winding is the conventional star winding with 15 turns/slot. The stator and rotor iron type is M400-50A. This machine is designed by a manufacturing company. The parameters of this machine are given in Table 2.1 (**Chapter 2**).

The remaining four prototypes have identical laminated iron stacks in the stator and rotor. Two different stator windings are used: one with a conventional star winding and the second one with a combined star-delta winding. The combined star-delta winding has per pole and per phase one slot for star coils and two slots for delta coils (sdd) as shown in **Chapter 5**. The number of turns of the star and delta coils is 26 and

45 turns/slot respectively. Two rotors are employed; one rotor contains ferrite permanent magnets while the second one does not have magnets. The parameters of the rotor without PMs have been optimally selected as shown in **Chapter 3**. Then the rotor with PMs is simply obtained by inserting ferrite PMs in the center of the flux-barriers as seen in **Chapter 6**. The stator and rotor steel grades are M270-50A and M330-50A respectively. A photograph of the prototypes is shown in Fig. 7.6. The parameters of the four machines are given in Table 3.10 (**Chapter 3),** table 5.4 (**Chapter 5**) and Table 6.1 (**Chapter 6**). All the windings of the prototypes have two parallel groups.

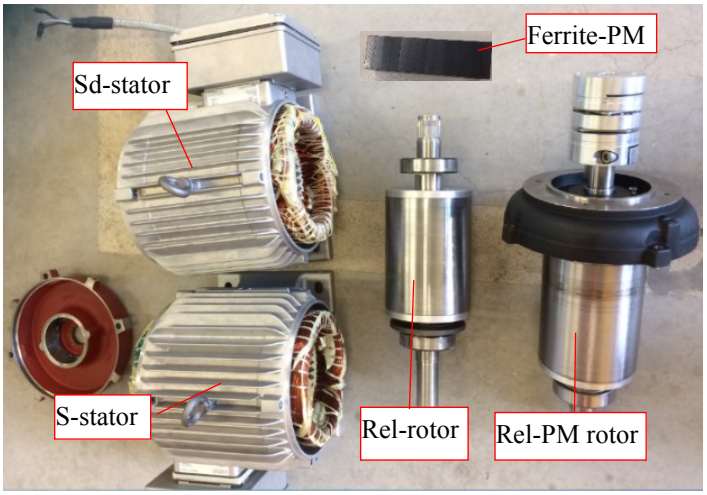

Figure 7.6: A photograph of the prototypes, where S is a conventional star connected stator, Sd is a combined star-delta connected stator, Rel is a conventional rotor without PMs and Rel-PM is a rotor with PMs.

Figures 7.7 and 7.8 show the rotor geometries of the reference and optimized prototypes respectively. Notice that, the rotor flux-barrier parameters of the prototypes are different.

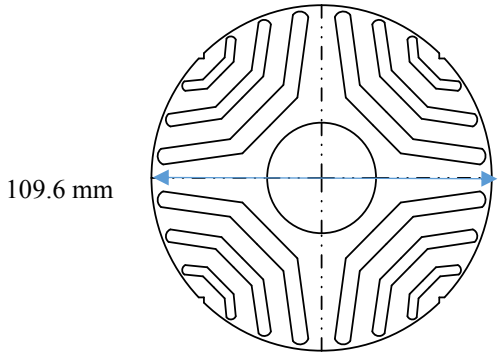

Figure 7.7: Rotor geometry of the reference prototype machine.

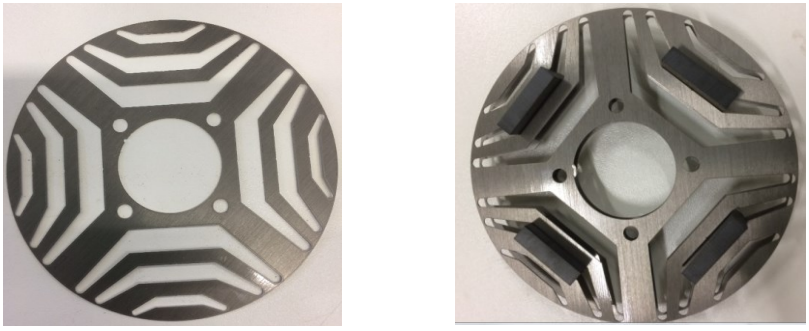

(a) Without magnets (b) With magnets

Figure 7.8: Rotor geometries of the optimal prototype design.

7.5 Inductance measurements

Several methods can be found in the literature to measure the SynRM inductances [4]–[7]. One method is called the *VI* method. Here, a voltage is injected with an angular frequency ω_e in two phases in series. The line voltage and current of the SynRM are measured at standstill as shown in Fig. 7.9 [4], [5]. Then, the inductances between two phases can be obtained by:

$$L_{ab} = \frac{1}{\omega_e}\sqrt{\left(\frac{V}{I}\right)^2 - 4R_s^2} \tag{7.1}$$

where V and I are the line voltage and current respectively and R_s is the resistance of one phase winding.

The voltage and current are measured at two rotor positions i.e. the d-axis where the magnetic reluctance is minimum (the inductance is maximum L_d) and the q-axis where the magnetic reluctance is maximum (the inductance is minimum L_q). The d and q-axis positions are identified by rotating the SynRM rotor slowly and observing the measured voltage and current. The minimum and maximum measured currents belong to the d and q axis positions respectively. Eventually, the L_d, L_q, ψ_d and ψ_q can be obtained by:

$$L_d = \frac{L_{ab_{\max}}}{2}, \ \psi_d = L_d I_d \tag{7.2}$$

$$L_q = \frac{L_{ab_{\min}}}{2}, \ \psi_q = L_q I_q \tag{7.3}$$

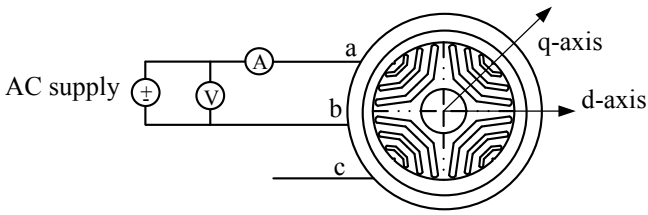

Figure 7.9: Measuring the inductances of a SynRM using the *VI* method.

It is clear that this method is simple and easy to implement because only two measuring devices are required to measure the line voltage and current. However, some errors on the measurements are expected due to the limited accuracy of the measuring devices as well as the inaccuracy in identifying the correct d and q axis rotor positions. In addition, this method does not take into account the effect of cross-saturation on the measured dq-axis inductances.

7.6 Measurements on the reference prototype SynRM

First, the validation of the simulated results of the reference prototype SynRM is given. This machine has been used in the work presented in **Chapter 2**, **4** and **8.** The geometrical and electromagnetic parameters of the reference prototype are given in Table 2.1.

The *dq* axis flux linkages ($\psi_d(i_d, 0)$, $\psi_q(0, i_q)$) of the reference prototype are obtained by the *VI*-method at standstill. The end winding effect on the simulated *dq* axis flux linkages has been included as in [8]. The simulated and measured *dq*-axis flux linkages versus the corresponding currents of the SynRM are shown in Fig. 7.10. It is clear that the correspondence between the simulated and measured results is good.

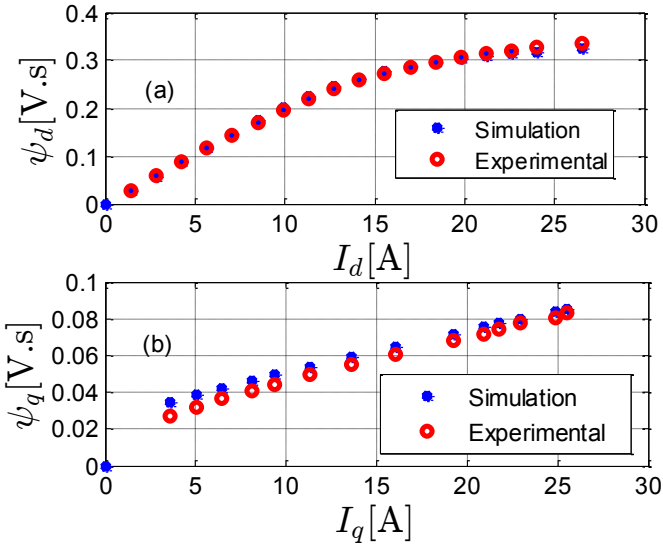

Figure 7.10: Simulated and measured *dq*- axis flux linkages ($\psi_d(i_d, 0)$, $\psi_q(0, i_q)$) of the reference prototype SynRM as a function of different currents at standstill.

Figure 7.11 shows the computed and measured *dq*-axis flux linkages for different loads at a constant *d*-axis reference current i_d*=14.2 A. The

measured and simulated results have been obtained at 2500 rpm for different loading conditions. It is noticed that the effect of cross saturation on the *d*-axis flux linkage is very small because i_d*=14.2 A is located in the linear region of the *d*-axis flux linkage (Fig. 2.5). This is similar as expected from the simulation results given in **Chapter 2**. In addition, it is clear that the *q*-axis flux linkage increases linearly with increasing the loading (i_q), similar to expected simulated results.

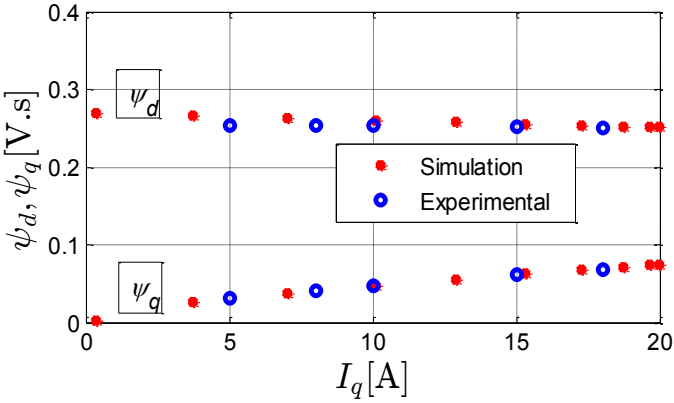

Figure 7.11: Computed and measured *dq*- axis flux linkages ($\psi_d(14.2\ A,\ i_q)$, $\psi_q(14.2\ A,\ i_q)$) of the reference prototype SynRM for different loads at 2500 rpm.

Figure 7.12 (a) shows the measured (fundamental component) and the computed phase voltage of the SynRM for different current angles α at fixed stator current (I_m=20 A) and fixed speed (2500 rpm). It is clear that the phase voltage decreases with increasing current angle. This is due to the decreasing *d*-axis current, which has the highest contribution on the phase voltage. The measured and computed power factors of the SynRM are shown in Fig. 7.12-(b). Figure 7.12 shows a good matching between the simulated and measured results.

Figure 7.13 shows the computed and measured output torque of the SynRM for different loads at constant i_d*=14.2 A (the case of Fig. 7.11). The output torque of the machine increases approximately linearly with the stator current. Figures 7.11 and 7.13 prove that the cross saturation effect in the reference prototype SynRM is considered properly in the simulated results.

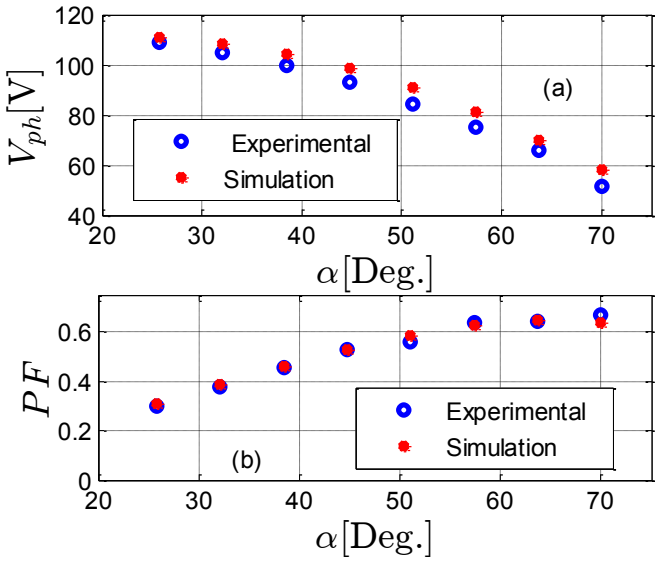

Figure 7.12: Measured and computed (a) phase voltage and (b) power factor of the reference SynRM versus the current angle at I_m=20 A and 2500 rpm.

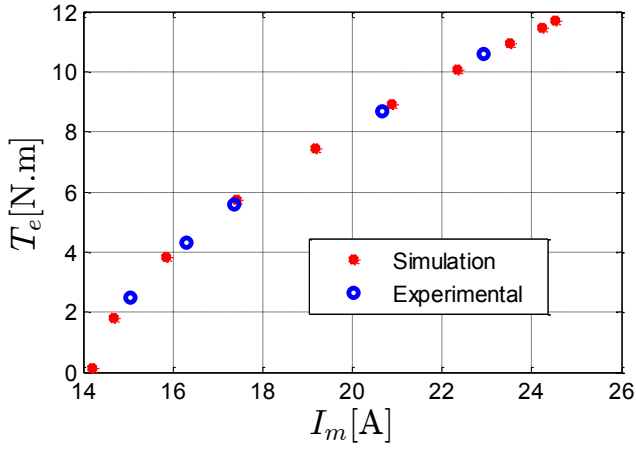

Figure 7.13: Computed and measured output torque of the reference prototype SynRM for different stator currents at i_d*=14.2 A and 2500 rpm.

Figure 7.14 shows the measured and computed output torque of SynRM as a function of the current angle at speed of 2500 rpm and a

current (I_m=20 A). It is clear that the output torque of the SynRM increases with increasing current angle till an optimal value is achieved and then decreases again as can be deduced from (2.6) in **Chapter 2**. It is obvious that the maximum output torque of the SynRM does not occur at the current angle of 45°. This proves that it is mandatory to control the SynRM in order to achieve a maximum torque per Ampere. The current angle can also be chosen in order to optimize the SynRM losses and efficiency.

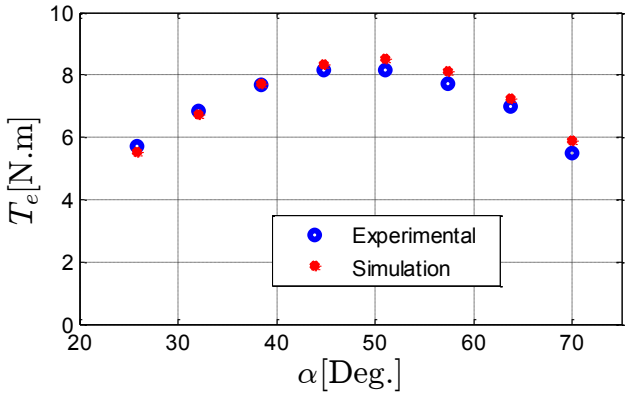

Figure 7.14: Measured and computed output torque of the reference prototype SynRM versus the current angle at I_m=20 A and 2500 rpm.

The efficiency of the reference prototype SynRM is reported in Fig. 7.15. There is some difference between the measured and computed efficiency. This is due to some reasons: 1) the model of the simulation is supplied by sinusoidal current while the machine is supplied by a PWM inverter in the experimental, causing additional PWM losses, 2) the mechanical losses are not included in the simulations, 3) the error in the measurements and 4) the error in the parameters of the loss model of the core material has a great influence as well.

The measured efficiency map of the reference prototype SynRM drive is reported in Fig. 7.16. The speeds range up to 40% of the rated speed due to the limitation of the experimental setup. The measured torque is up to the rated value. The current angle is adjusted at the optimal value based on the look-up table as presented in **Chapter 2**. The efficiency is the ratio of the SynRM output mechanical shaft power

to the electrical DC input power of the inverter. Hence, it takes into account also the losses in the inverter, and gives the total drive efficiency. It can be seen that the efficiency reaches about 85% for low speed and power (at about 40 % of the rated speed and power).

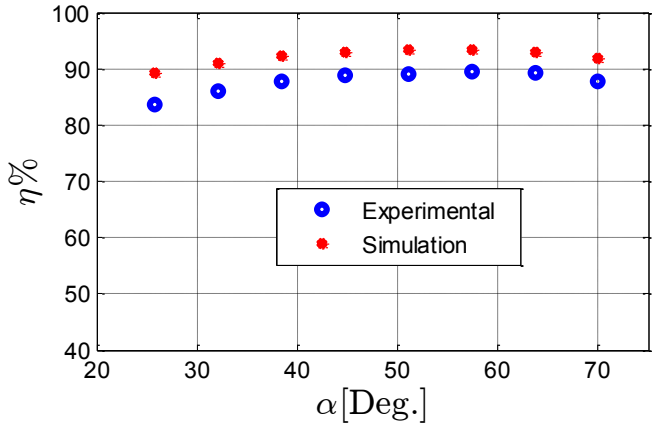

Figure 7.15: Efficiency of the reference prototype SynRM versus the current angle at I_m=20 A and 2500 rpm.

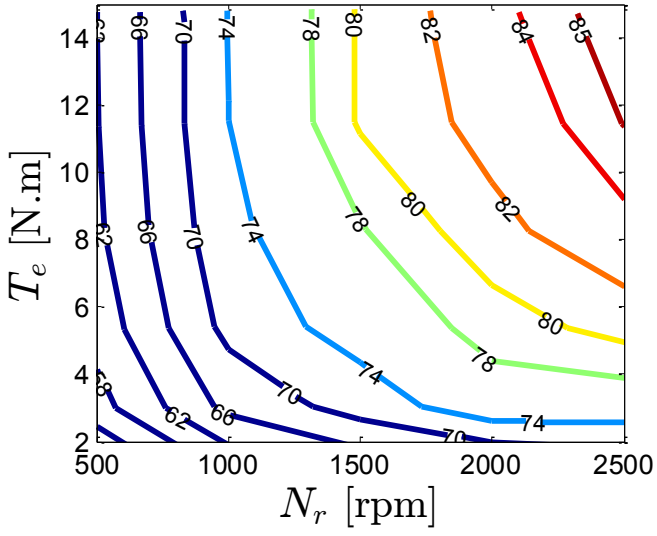

Figure 7.16: Measured efficiency map of the reference prototype SynRM drive at the optimal current angles.

7.7 Measurements on four optimized prototype SynRMs

The second part in the experimental validation is for the four prototypes presented in **Chapters 3, 5** and **6**. We recall that these prototypes are the result of the design optimization starting from the reference machine. The abbreviations of the 4 prototypes are presented in Table 6.2 in **Chapter 6**. The geometrical and electromagnetic parameters of the four optimized prototypes are given in Tables 3.10 (**Chapter 3**) and 5.4 (**Chapter 5**) and 6.1 (**Chapter 6**). Note that some of the measured data in this section include an interpolation.

Figure 7.17 shows the measured and simulated output torque of 4 prototypes as a function of the current angle at half the rated current and speed. The simulated and measured results correspond very well. Furthermore, the difference in the maximum output torque of the four machines validates the findings of Fig. 6.9 (**Chapter 6**) that the difference in the output torque between the machines is current dependent.

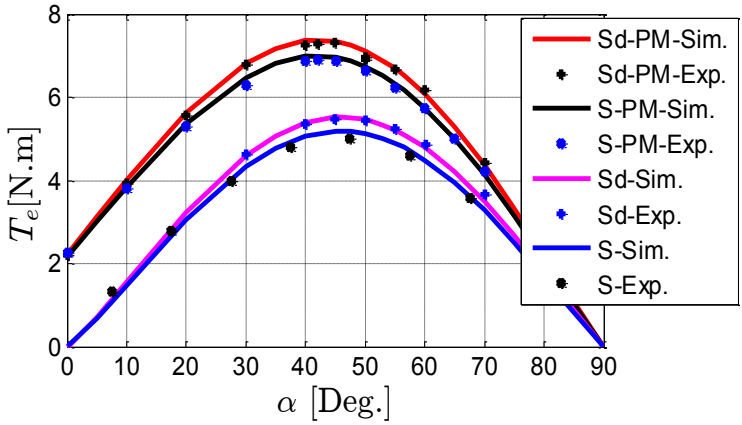

Figure 7.17: The output torque (T_e) of 4 optimized prototype SynRMs as a function of the current angle (α) at half rated current and speed.

The measured and simulated output torque and power factor of the 4 optimized prototype SynRMs as a function of the stator current at the

optimal current angles and rated speed are reported in Figs. 7.18 and 7.19 respectively. Good matching between the simulated and measured results is noticed.

The measured total losses of the 4 optimized prototypes as a function of the stator current at full rated speed is shown in Figure 7.20. The measured losses are the difference between the measured output and input powers of the machine. The difference in losses of the 4 prototypes is not significant, similar to trends of simulated results in Fig. 6.16 (**Chapter 6**). However, the simulated losses are lower than the measured losses. The reason -as mentioned before- is that the mechanical and PWM losses are not considered in the simulation. In addition, the computed iron losses may be underestimated because degradation of the material properties by cutting and press fitting is not included.

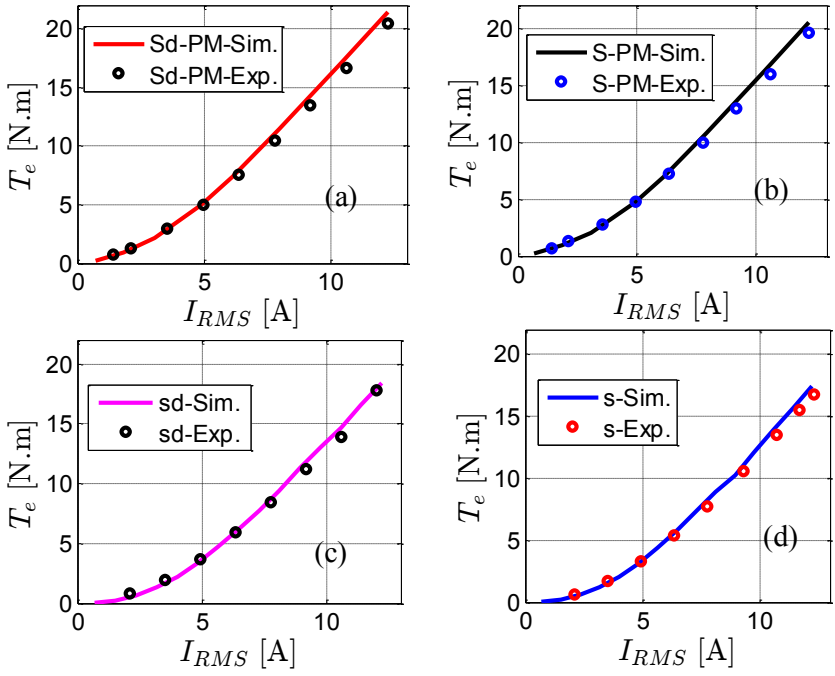

Figure 7.18: Output torque (T_e) of the 4 optimized prototypes as a function of stator current (*RMS*) at the optimal current angles and rated speed.

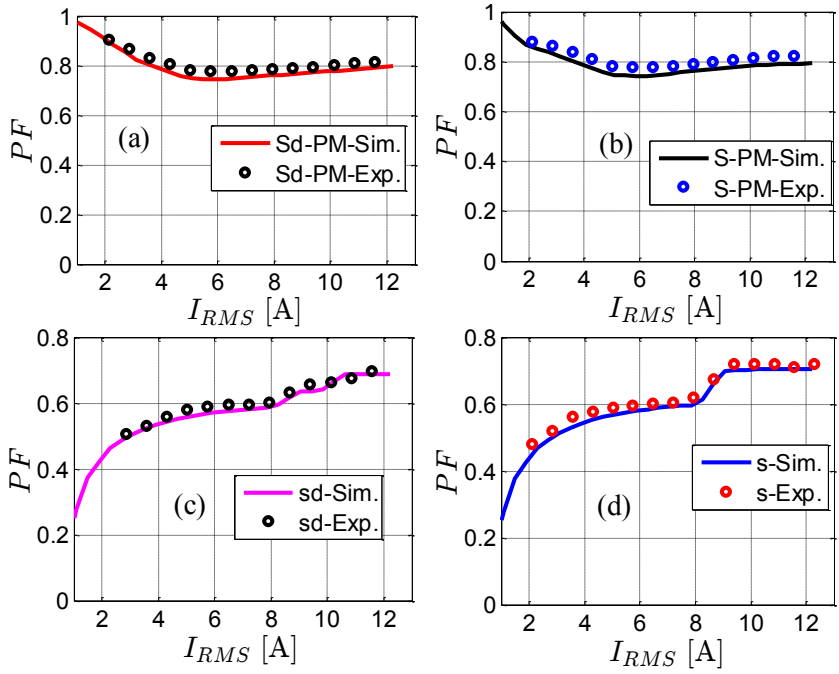

Figure 7.19: Power factor (*PF*) of the 4 optimized prototypes as a function of stator current (*RMS*) at the optimal current angles and rated speed.

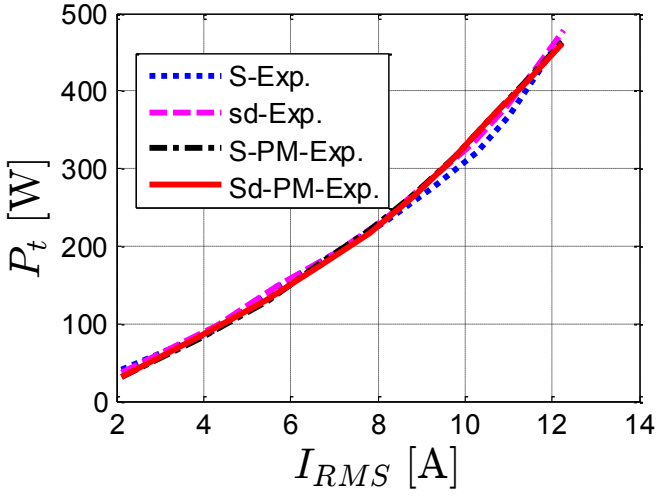

Figure 7.20: The measured losses of the 4 optimized prototypes at optimal current angles and rated speed (3000 rpm).

Figure 7.21 reports the measured efficiency of the four optimized prototypes for several loading currents at the optimal current angles and at the rated speed (3000 rpm). It is clear that the efficiency of SynRM improves slightly using the combined star-delta winding and improves significantly by adding PMs in the rotor, similar to trends of simulated results in Fig. 6.15 (**Chapter 6**). The Sd-PM machine has the highest efficiency: about 93.60% at the rated current. This is higher than the required minimum for the IE4 super premium efficiency class [9]: about 92.50% for a 4-pole 5.5 kW induction motor. The rated efficiency for the other machines is: 92.10% for the S machine, 92.36% for the Sd machine and 93.29% for the S-PM machine.

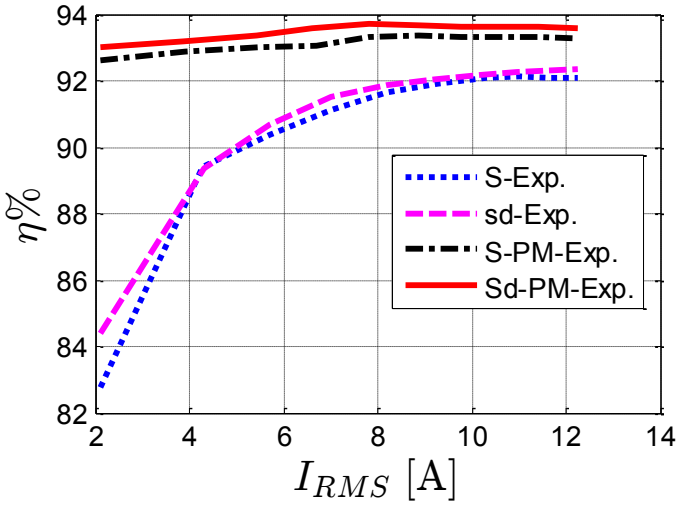

Figure 7.21: The measured efficiency of the 4 optimized prototypes at optimal current angles and rated speed (3000 rpm).

Figures 7.22 to 7.25 report the measured efficiency maps of the whole drive system (prototype + inverter) at optimal current angles for speeds and currents up to the rated values (3000 rpm, 12.23 A). A shown before in **Chapter 6**, the maximum output torque of the 4 machines is different and the Sd-PM machine gives the highest output torque. In general and in correspondence with literature [10]–[12], adding ferrite PMs in the rotor of the SynRM increases the machine efficiency. It is worth noting that the efficiency of the Sd-PM machine (Fig. 7.25) is much better than

for the other machines in the whole operating range, but especially at low loads. This is because the output torque of the Sd-PM is much higher than the output torque of the other machines for the same currents. This happens especially for low currents as depicted in Fig. 6.9 **(Chapter 6)**. By comparing the machines regarding the winding configuration, the machines with combined star-delta windings have a better efficiency compared to the machines with the conventional star windings, especially under partial loads. This is because of the increased torque-to-current ratio.

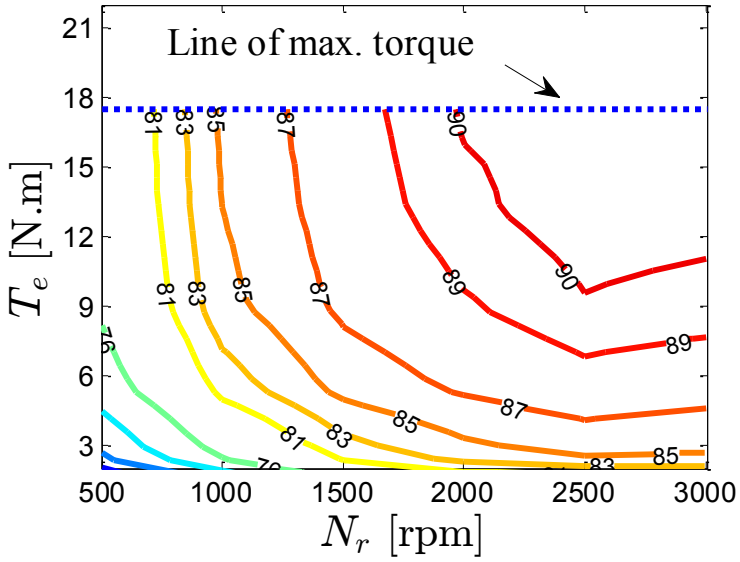

Figure 7.22: Measured efficiency map of the whole drive system using the S machine at optimal current angles up to the rated values.

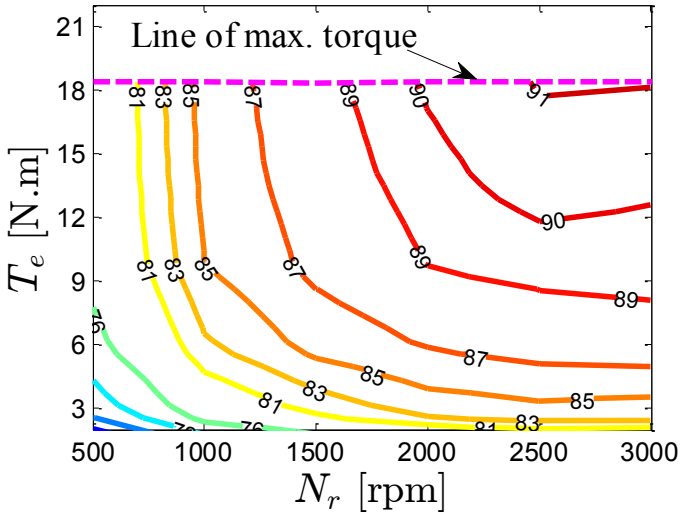

Figure 7.23: Measured efficiency map of the whole drive system using the Sd machine at optimal current angles up to the rated values.

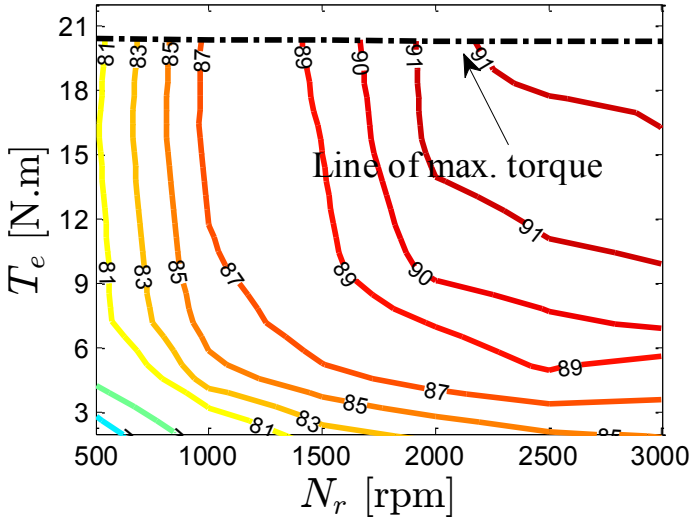

Figure 7.24: Measured efficiency map of the whole drive system using the S-PM machine at optimal current angles up to the rated values.

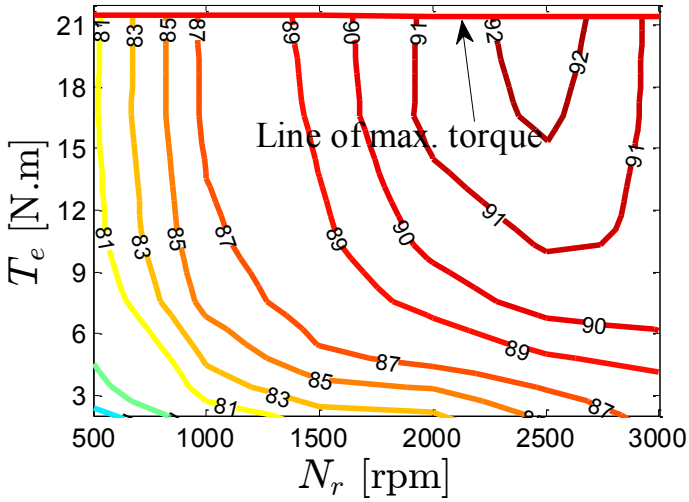

Figure 7.25: Measured efficiency map of the whole drive system using the Sd-PM machine at optimal current angles up to the rated values.

7.8 Conclusions

This chapter has presented the experimental measurements of one reference and four optimized prototype SynRMs. The measurements are used to validate the theoretical work presented in this thesis. It is shown that there is a good matching between the simulated and measured results for the five prototypes.

Biography

[1] T. Matsuo and T. A. Lipo, "Field oriented control of synchronous reluctance machine," in *Proceedings of IEEE Power Electronics Specialist Conference - PESC '93*, pp. 425–431.

[2] A. Fratta, C. Petrache, G. Franceschini, and G. P. Troglia, "A simple current regulator for flux-weakened operation of high performance synchronous reluctance drives," in *Proceedings of 1994 IEEE Industry Applications Society Annual Meeting*, pp.

649–657.

[3] F. De Belie, “Vectorregeling van synchrone machines met permanente-magneetbekrachtiging zonder mechanische positiesensor,” *PhD Thesis*, Ghent University, 2010.

[4] H. Khang, J. Kim, J. Ahn, and H. Li, “Synchronous Reluctance Motor drive system parameter identification using a current regulator,” in *2008 Twenty-Third Annual IEEE Applied Power Electronics Conference and Exposition*, 2008, pp. 370–376.

[5] H. V. K. and J. W. A. S. H. Hwang, J. M. Kom, “Parameter identification of a synchronous reluctance motor by using a synchronous PI current regulator at a standstill,” *J. power electonic. Vol. 10, No. 5*, pp. 491–497, 2010.

[6] R. Dutta and M. F. Rahman, “A comparative analysis of two test methods of measuring Ld- and Lq-axes inductances of interior permanent-magnet machine,” *IEEE Trans. Magn.*, vol. 42, no. 11, pp. 3712–3718, Nov. 2006.

[7] A. Chiba, F. Nakamura, T. Fukao, and M. A. Rahman, “Inductances of cageless reluctance-synchronous machines having nonsinusoidal space distributions,” *IEEE Trans. Ind. Appl.*, vol. 27, no. 1, pp. 44–51, 1991.

[8] J. Pyrhönen, T. Jokinen, and V. and Hrabovcová, *Design of rotating electrical machines*. Wiley, 2008.

[9] A. T. De Almeida, F. J. T. E. Ferreira, and A. Q. Duarte, “Technical and economical considerations on super high-efficiency three phase motors,” *IEEE Trans. Ind. Appl.*, vol. 50, no. 2, pp. 1274–1285, Mar. 2014.

[10] M. Degano, E. Carraro, and N. Bianchi, “Selection criteria and robust optimization of a traction PM-assisted synchronous reluctance motor,” *IEEE Trans. Ind. Appl.*, vol. 51, no. 6, pp. 4383–4391, Nov. 2015.

[11] M. Barcaro, N. Bianchi, and F. Magnussen, “Permanent-magnet optimization in permanent-magnet-assisted synchronous reluctance motor for a wide constant-power speed range,” *IEEE Trans. Ind. Electron.*, vol. 59, no. 6, pp. 2495–2502, Jun. 2012.

[12] M. Ferrari, N. Bianchi, and E. Fornasiero, “Analysis of rotor saturation in synchronous reluctance and PM-assisted reluctance

motors," *IEEE Trans. Ind. Appl.*, vol. 51, no. 1, pp. 169–177, Jan. 2015.

Chapter 8
PV Pumping System Utilizing SynRM

8.1 Introduction

This chapter proposes an efficient and low cost PV pumping system employing a SynRM. The proposed system doesn't have a DC-DC converter that is often used to maximize the PV output power, nor has it storage (battery). Instead, the system is controlled in such a way that both the PV output power is maximized and the SynRM works at the maximum power per Ampère, using a conventional three phase pulse width modulated inverter. At the beginning, the design of the proposed system is presented. Then, the modelling of all components of the system is given. Finally, the performance of the proposed system is shown.

8.2 Overview of PV pumping systems

Recently, renewable energy sources have obtained an increasing attention for electric power applications in order to reduce the dependency on the conventional energy sources. This is because of several advantages of the renewable energy sources such as: 1) free and inexhaustible, 2) clean and 3) easy and cheap maintenance [1]–[4]. Solar photovoltaic (PV) systems are one of the most promising renewable energy systems today and in the coming years. This is owing to the greatest availability of the sun radiation compared to the other energy sources. In addition, the prices of the PV modules are decreasing

more and more thanks to the advancement in the manufacturing technology of the solar cells [1].

The solar PV systems can be divided into two main types; standalone (off grid) and grid-connected systems. The standalone PV systems are employed in several developing countries e.g. Egypt, Sudan, Algeria, India etc. [2], [5]–[8], especially in remote rural areas where the connection to the grid is not possible or costly [1], [4]. Several developing countries, in particular African countries, have an excellent availability of the sun. The average irradiation level of the sun is around 600 W/m^2 e.g. for Egypt [9], [10]. This makes the standalone PV solar system to be a promising candidate, especially for pumping applications. A detailed analysis about the investigations on site specific application and performance of PV pumping systems in different countries is given in [2]. The conclusion from the analysis given in [2] is that the PV water pumping system is an effective, sustainable and easy way for water requirements in irrigations and house needs. However, the efficiency and cost of the PV pumping system are still big challenges. Therefore, several literature research is available, seeking to increase the total efficiency and to reduce the total cost of the PV pumping system.

Several authors have investigated the selection of the electric motor that is used in the PV pumping system [2]–[4], [9]–[18]. In the past, the PV pumping system was based on brushed DC motors [11], [19]–[24]. These motors can be simply directly coupled to the PV supply via a DC-DC converter. The transient and steady state performances of direct coupling of several types of DC motors (series, shunt, and separately excited) to a PV supplied water pumping system were investigated in [19]–[24]. The papers investigated the influence of different irradiation levels, different loading conditions and several system controllers. It was found that the separately excited and permanent magnet DC motors are more suitable than the shunt and series DC machines for PV water pumping systems [22]–[26]. Nevertheless, DC motors suffer from several disadvantages related to the brush contacts and commutator. This requires frequent maintenances and increases running cost that reduces the reliability and efficiency of the system [25]–[27]. Therefore, brushless machines are gaining the most interest in pumping systems thanks to their advantages such as low maintenance, high efficiency and low cost [4].

In the literature, several publications were presented for pumping systems based on brushless DC motors (BDCMs) [12], [13], induction motors (IMs) [27], permanent-magnet synchronous motors (PMSMs) [14] and switched reluctance motors (SRMs) [15]. A PV pumping system based on BDCM has been studied intensively in the literature, thanks to its merits such as high reliability and ruggedness, better performance for a wide range of speed, and high efficiency. A single stage PV array fed BDCM driven a water pump is investigated in [28]. This system does not use the conventional DC-DC converter. However, there is a need for three hall sensors to accomplish the electronic commutation to drive the system at the maximum power point of the PV array. The IMs are used in PV pumping systems with an inverter but without DC-DC converter in [29], [30]. However, the efficiency of the IMs is still a problem and it diminishes under light loading because the excitation losses dominate [17]. The aforementioned disadvantages motivate the researchers to prefer the PMSMs. The authors of [14] presented a standalone PV pumping system employing a PMSM. However, they neglected the inverter losses in their analysis. In addition, the prices of the PMs are high and the demagnetization due to the weather conditions – in particular the high ambient temperature – is a problem.

For pumping systems in developing countries, SynRMs have several advantages compared to other types of brushless machines: a rugged construction and low cost because there are no windings, cage and magnets in the rotor. In addition, the efficiency of SynRMs is better than the efficiency of IMs, but it is inferior compared to PMSMs [31]. However, only few research work was published considering the PV pumping systems using SynRMs [3], [4], [32]. In [3], the authors studied the modelling and design considerations for a PV supply feeding a SynRM for a pumping system. In addition, they presented a simple control strategy to improve the system performance in [4]. However, they employed a SynRM with axially laminated caged rotor, which increases the losses and complicates its manufacturing. They simply assumed in the modelling of the SynRM that the inductances are constant values, neglecting the magnetic saturation effect. This gives a non-accurate calculation for the SynRM output power, hence the total power of the system [18]. In addition, neither the motor geometry nor the number of PV modules was optimized. Moreover, they employed a boost converter to maximize the output power of the PV supply, which increases the cost and complexity of the system. Recently, the authors

of [32] presented an analysis and design for a PV pumping system using a SynRM. However, they also used the DC-DC boost converter to maximize the PV output power.

The literature lacks the accurate study of a SynRM with variable but uncontrolled DC-bus voltage (no DC-DC converter) for PV supplied pumping systems. This is the motivation in this PhD to study the PV pumping system based on SynRMs in order to improve the total system efficiency and the total cost.

8.3 Design of the proposed system

In order to reduce the cost and/or the losses of the proposed PV system, neither a DC-DC converter, nor storage (battery) is employed. The proposed PV pumping system consists of the following components:

A) Centrifugal pump;

B) Three phase SynRM;

C) Three phase voltage source inverter with control system;

D) PV array

The block diagram of the proposed system is shown in Fig. 8.1.

To start the design of the different components mentioned in Fig. 8.1, it is necessary to achieve the requirements of the pumping application. The proposed system is used for pumping water for irrigation and human needs. The required amount of water is assumed to equal 500 m^3/day. It is assumed that the average number of hours during which the motor can work properly is 10 hours/day. Therefore, the average flow rate of the pump should be 50 m^3/h. The height difference (the head) of the water is assumed to be 50 m. The average power can be computed based on the flow rate and the height difference.

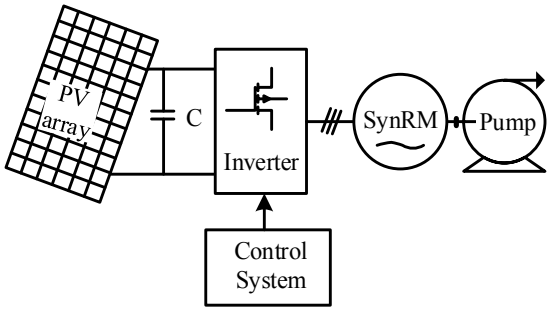

Figure 8.1: Block diagram of the proposed system.

A) Design of the centrifugal pump

The output power of the pump can be computed by:

$$P_p = \frac{\rho g}{3600} QH \tag{8.1}$$

where ρ is the water density (kg/m^3), g is the gravitational constant (9.81 m/s^2), Q is the flow rate (m^3/h) and H is the total head (m) of the pump.

The head-flow rate (HQ) characteristic of the centrifugal pump can be obtained using this relation [33]:

$$H = a_o \omega_r^2 + a_1 \omega_r Q + a_2 Q^2 \tag{8.2}$$

where a_o, a_1 and a_2 are constants, depending on the pump geometry. ω_r is the motor speed (rad/s).

With a desired flow rate of the pump (Q) of 50 m^3/h - as mentioned before - and the total head of the pump (H) of 50 m, the mechanical output power of the pump is equal to 6.8 kW. Consequently, the input mechanical power of the pump can be obtained. It equals 8 kW with an estimated pump efficiency of 85%.

B) Design of the SynRM

It is clear from subsection A) that the minimum required output power of the SynRM to achieve the pumping requirements is 8 kW. As known, the output power of the PV array depends on the irradiation and temperature conditions. This means that the motor will not operate at the rated power for the whole operation period. Hence, a margin factor

for the design of motor output power is necessary. The solar irradiation level of Egypt, as an example, ranges from 3.2 kWh/m^2/day to about 8.1 kWh/m^2/day with an approximately annual average of 5.9 kWh/m^2/day [10]. The margin factor can be calculated, assuming it approximately to be 1.4. Therefore, the rated motor output power is selected to be 11 kW.

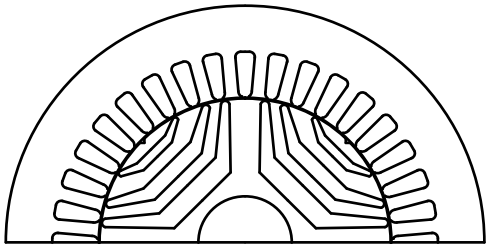

Figure 8.2: Half of SynRM geometry.

The target mechanical output power of the SynRM is 11 kW. The stator design of SynRM is similar to the induction motor stator. The number of slots and poles are selected to be 36 and 4 respectively. For the windings, conventional three phase distributed windings are considered in which two parallel groups of 15 turns/slot are used. The proposed rated speed is 6000 rpm and the full load stator current is 21.12 A. The proposed speed is quite high so that the size of the motor remains small. This is a benefit because the motor can fit in a smaller drill hole. The airgap length is 0.3 mm. The transverse laminated rotor type with three flux-barriers per pole is considered. Half of the SynRM geometry is shown in Fig. 8.2. The most crucial parameters of the SynRM – as shown in **Chapter 3** – are the flux-barrier parameters (12 parameters in total) that are sketched in Fig. 8.3.

In order to maximize the output power of the SynRM and to minimize the torque ripple, an optimization is done to choose the optimal value of the 12 flux-barrier parameters. The optimization is done based on a parametrized 2D-FEM as presented in details in **Chapter 3**. This means that the optimization is done only at one specific point, assuming sinusoidal current in the machine windings. The optimization goals are low torque ripple% and high output torque. The optimization is also subject to a number of constraints: the outer diameter is fixed to 180 mm and the rated speed is 6000 rpm.

The optimal selection of the 12 flux-barrier parameters is given in Table 8.1 that is a good compromise between the low torque ripple (10%) and the high output power (11.15 kW).

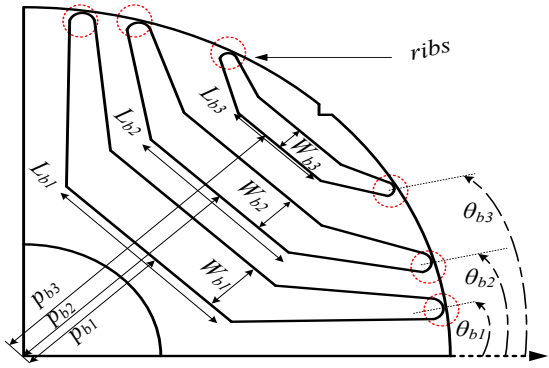

Figure 8.3: Flux-barrier parameters of the SynRM.

Table 8.1: Optimal selection of the flux-barrier parameters of the SynRM.

Flux-barrier Parameter	Value	Flux-barrier Parameter	Value
θ_{b1}	8.08°	W_{b1}	5.5 mm
θ_{b2}	16.43°	W_{b2}	3.5 mm
θ_{b3}	29.4°	W_{b3}	3.5 mm
L_{b1}	29.85 mm	p_{b1}	22.75 mm
L_{b2}	28 mm	p_{b2}	35.5 mm
L_{b3}	13.5 mm	p_{b3}	44.2 mm

At first, the performance of the designed SynRM is examined using 2D FEM at a speed of 6000 rpm. Three phase sinusoidal currents are injected in the machine windings while rotating the rotor by a fixed step. Then the output power, power factor and torque ripple (in percent) are calculated.

Figure 8.4 shows the output power of the designed SynRM as a function of the current angle for several stator currents at the rated speed. We recall that the current angle is the angle between the stator current vector and the *d*-axis as defined in **Chapter 2**. Evidently, for fixed stator current amplitude, both *d* and *q* axis currents vary with the current angle and this results in a different SynRM output power. This means that it is necessary to control the SynRM to give the maximum output power. The point of maximum output power is highlighted with a red circle in the Fig. 8.4. In fact, the value of the current angle at which the maximum power of SynRM occurs, depends on the saturation behavior of the machine, as explained in **Chapter 2**. The power factor and the torque ripple% of the machine as a functions of current angle at rated speed and current are reported in Figs. 8.5 and 8.6 respectively. It can be seen that the power factor and torque ripple at the maximum power point are 0.69 and 10% respectively.

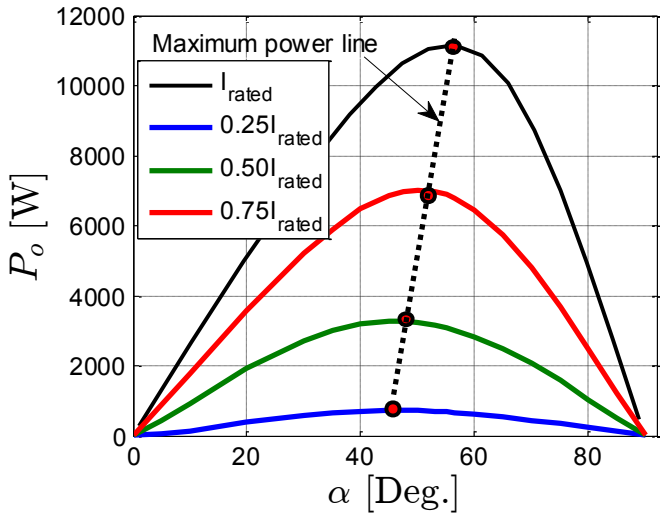

Figure 8.4: Current angle (α) versus output power (P_o) of the SynRM at rated speed and several currents up to the rated current.

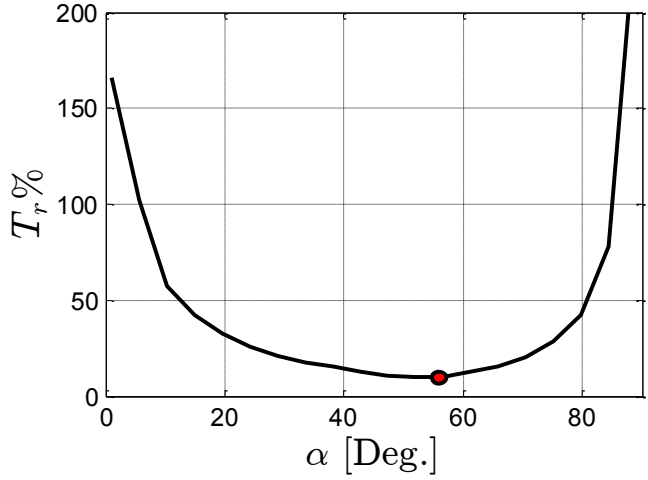

Figure 8.5: Current angle (α) versus torque ripple ($T_r\%$) of the SynRM at rated conditions.

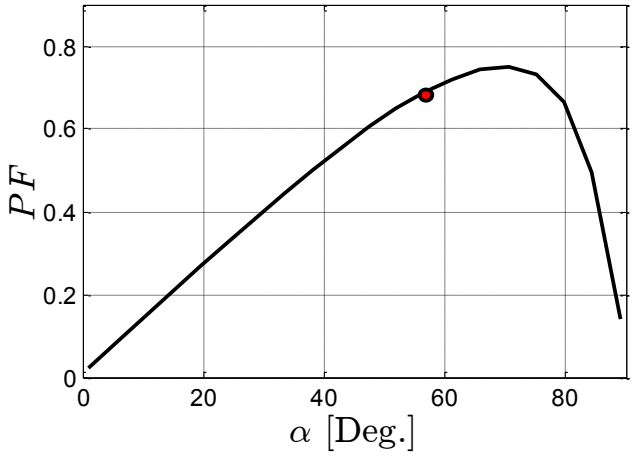

Figure 8.6: Current angle (α) versus power factor (PF) of the SynRM at rated conditions.

The iron losses of the machine are calculated using the statistical losses theory of Bertotti based on FEM. The detailed loss model is given in **Chapter 4**. The iron losses of the machine are 398 W and the copper losses are 205 W, with sinusoidal currents (no PWM ripple). This results in a SynRM efficiency of 94.87% at rated current and speed and at the maximum torque per Ampère operating point of the SynRM.

C) Design of the three phase inverter

A conventional three phase voltage source inverter is used in the proposed system. The inverter consists of three legs with 2 IGBTs per leg. The schematic diagram of the inverter is shown in Fig. 8.7.

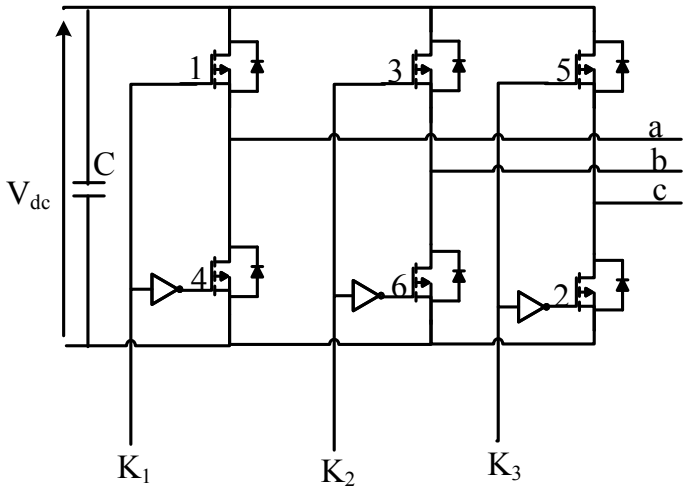

Figure 8.7: Schematic diagram of the voltage source inverter.

The kVA rating of the inverter can be computed based on the rated power and power factor of the SynRM. The inverter rating is selected to be 20 kVA based on the output power (11kW), efficiency (94.87%) and power factor (0.69) of the SynRM and assuming a margin factor of about 1.3. The DC bus voltage and current of the inverter are 1000 V and 20 A respectively, to achieve the required motor voltage and current. The efficiency of the inverter is assumed to be 96%. The DC bus capacitor is assumed to 200 μF [13].

D) Design of the PV array

The PV module parameters given in Table 8.2 are used to design the whole PV array. The characteristics of the PV module at different irradiation levels (G=200 W/m^2, 400 W/m^2 and 1000 W/m^2) and temperatures (T=25°C, 35°C and 45°C) are shown in Figs. 8.8 and 8.9 respectively. It is clear that the influence of the irradiation level

variation on the PV output power is much larger than the temperature variation.

Table 8.2: PV module specifications.

Maximum power, P_{max}	135 W
Open circuit voltage, V_{oc}	22.1 V
Short circuit current, I_{sc}	9.37 A
Short circuit current temperature coefficient, k_i	5.02e-3 A/°C
Short circuit voltage temperature coefficient, k_v	8e-2 V/°C
Reference temperature, T_{ref}	25°C

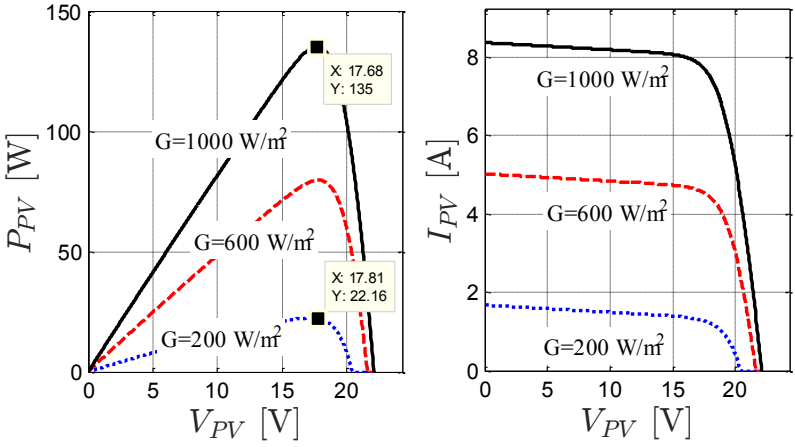

Figure 8.8: PV module characteristics at different irradiation levels (G=200 W/m^2, 400 W/m^2 and 1000 W/m^2) and constant temperature (T=25°C).

From the previous steps (A, B and C), the required output power of the PV can be computed based on the machine input power. The PV output power at the standard conditions (G=1000 W/m^2, T=25°C) is selected to be 12.25 kW. This results in a total number of 92 PV modules of 135 W each (see Table 8.2). Based on the necessary rated phase voltage of the SynRM and by consequence the DC bus voltage of the inverter, the PV modules can be arranged in series and parallel. This

leads to a PV array of 46 series modules with 2 parallel strings. The characteristics of the PV array are reported in Fig. 8.10 for different irradiation levels and at T=25°C. The green dash dotted line in Fig. 8.10 represents the maximum power point line of the PV array (a) and the corresponding voltage and current of the array (b).

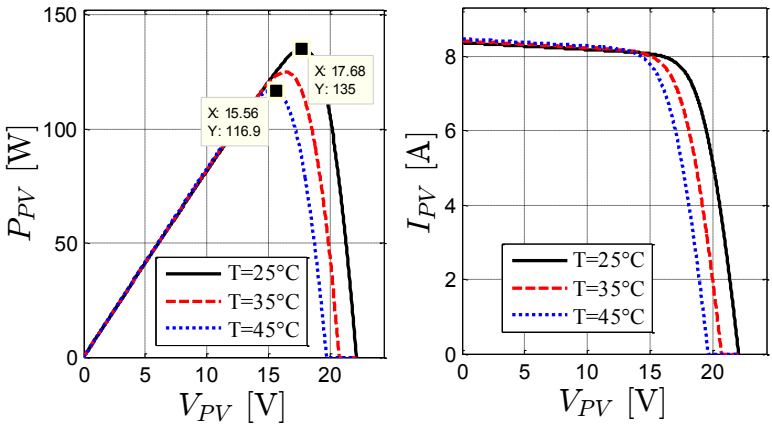

Figure 8.9: PV module characteristics at different temperatures (T=25°C, 35°C and 45°C) and constant irradiation level (G=1000 w/m^2).

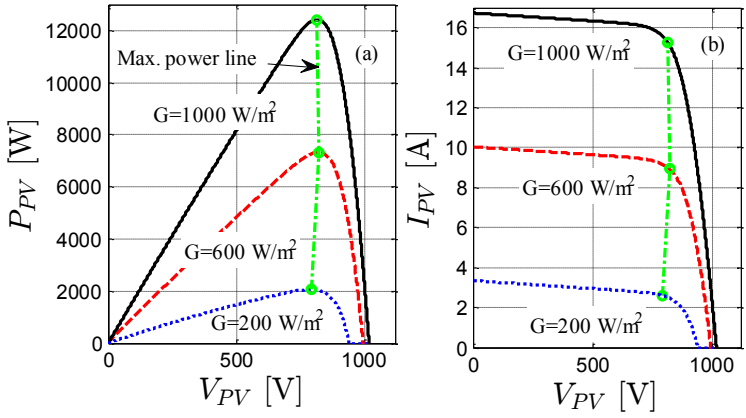

Figure 8.10: The PV array characteristics at different irradiation levels (G=200 W/m^2, 400 W/m^2 and 1000 W/m^2) and T=25°C.

8.4 Modelling of the proposed system

In this section, the mathematical model of the components of the proposed system is given.

(a) PV array model

The single diode PV cell model shown in Fig. 8.11 is used. The practical PV module consists of several connected PV cells. The current-voltage (*I-V*) relation of the PV module can be formulated by [3], [4]:

$$I_{PV} = I_{ph} - I_o\left[\exp\left(\frac{V_{PV} + R_s I_{PV}}{V_t a}\right) - 1\right] - \frac{V_{PV} + R_{sm} I_{PV}}{R_{pm}} \qquad (8.3)$$

where I_{pv} and V_{pv} are the current and voltage of the PV module; I_o and I_{ph} are the saturation and photocurrents; V_t is the thermal voltage of the module; a is the diode ideality factor and R_{sm} and R_{pm} are the series and parallel resistance of the module.

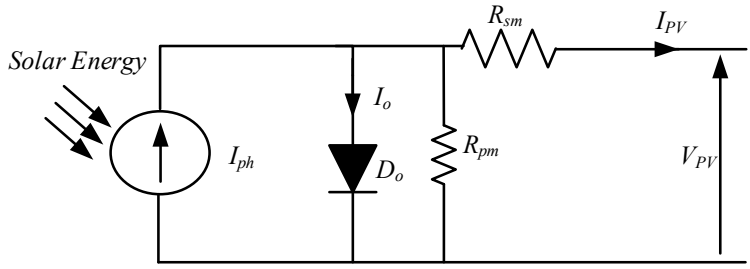

Figure 8.11: Single diode PV cell equivalent circuit.

The photocurrent (I_{ph}) depends mainly on the solar irradiation and cell temperature, which is described as [34]:

$$I_{ph} = \left(I_{sc} + k_i\left(T_c - T_{ref}\right)\right)G \qquad (8.4)$$

where I_{sc} is the module short-circuit current at 25°C and 1000 W/m^2, k_i is the temperature coefficient of the short-circuit current (A/°C), T_{ref} is the cell reference temperature and G is the solar irradiation level (W/m^2).

Moreover, the diode saturation current varies with the cell temperature, which is described as [34]:

$$I_o = I_{rs}\left(\frac{T_c}{T_{ref}}\right)^3 \exp\left(\frac{qE_G}{kA}\left(\frac{1}{T_{ref}} - \frac{1}{T_c}\right)\right) \tag{8.5}$$

where I_{rs} is the cell reverse saturation current at the reference temperature and the solar insolation and E_G is the bang-gap energy of the semiconductor used in the cell.

The PV array is a series and parallel connection of the modules. Hence for given numbers of series (N_s) and parallel (N_p) modules, the equivalent *I-V* relation can be as follows [34]:

$$I_{PV} = I_{ph}N_p - I_o N_p\left[\exp\left(\frac{V_{PV} + R_{sm}I_{PV}\left(\frac{N_s}{N_p}\right)}{V_t a N_s}\right) - 1\right] - \frac{V_{PV} + R_{sm}I_{PV}\left(\frac{N_s}{N_p}\right)}{R_{pm}\left(\frac{N_s}{N_p}\right)} \tag{8.6}$$

(b) Three phase inverter model

The output voltage of the inverter can be expressed as function of the PV array voltage as follows [4]:

$$\begin{aligned} v_{an} &= \frac{1}{3}(2K_1 - K_2 - K_3)V_{dc} \\ v_{bn} &= \frac{1}{3}(-K_1 + 2K_2 - K_3)V_{dc} \\ v_{cn} &= \frac{1}{3}(-K_1 - K_2 + 2K_3)V_{dc} \end{aligned} \tag{8.7}$$

With K_1, K_2 and K_3 the switching states of the 3 inverter legs, being either 1 or 0. When the switch state (K_1, K_2 or K_3) equals 1, it means that the corresponding upper switch is ON while the lower one is OFF and vice versa.

(c) SynRM model

The SynRM model given in details in **Chapter 2** is used in this system. The following equations are implemented [18]:

$$\left.\begin{aligned} v_d &= R_s i_d + p\psi_d(i_d, i_q) - \omega_r P \psi_q(i_d, i_q) \\ v_q &= R_s i_q + p\psi_q(i_d, i_q) + \omega_r P \psi_d(i_d, i_q) \\ T_e &= \frac{3}{2} P(\psi_d(i_d, i_q) i_q - \psi_q(i_d, i_q) i_d) \end{aligned}\right\} \tag{8.9}$$

where the symbols have the same meaning as defined in **Chapter 2**: v, i, ψ and T_e represent the voltage, current, flux linkage and electromagnetic torque of the SynRM; d and q refer to the direct and quadrature axis components; R_s is the SynRM stator resistance; P and p are the number of pole pairs and differential operator and ω_r is the rotor mechanical speed. Here, the saturation and cross-saturation of the dq-axis flux linkages of the machine are considered. This is done by generating lookup tables (LUTs) for the dq-axis flux linkages as function of the dq-axis current components using FEM. The detailed explanation of the accurate SynRM modeling is presented in **Chapter 2**.

(d) Centrifugal pump model

The torque (T_{cp}) speed (ω_r) behavior of the centrifugal pump is expressed by [15], [16], [28]:

$$T_{cp} = K_p \omega_r^2 \tag{8.10}$$

where K_p is the proportionality constant of the pump and ω_r is the rotational speed of the rotor in rad/s. The K_p value is calculated based on the rated torque and speed offered by the motor.

8.5 Performance of the proposed system

The complete block diagram of the proposed system is sketched in Fig. 8.12. In order to drive the SynRM to work stably, the conventional vector controlled technique is employed in which two reference signals are necessary as presented in **Chapter 2** and sketched in the block diagram of **Chapter 7** (Fig. 7.2). The first reference signal is the speed while the second one is the *d*-axis current (i_d*). In addition, in order to control the system to work efficiently, both the maximum power line of the PV array (green dash dotted line in Fig. 8.10) and the maximum torque per Ampère locus of the SynRM have to be coincided (black dotted line in Fig. 8.4). This can be done by obtaining: 1) the reference speed of the system from the proposed maximum power point tracking (MPPT) algorithm shown in Fig. 8.12 and 2) the reference *d*-axis current from the generated LUT using FEM as shown in **Chapter 2** [18].

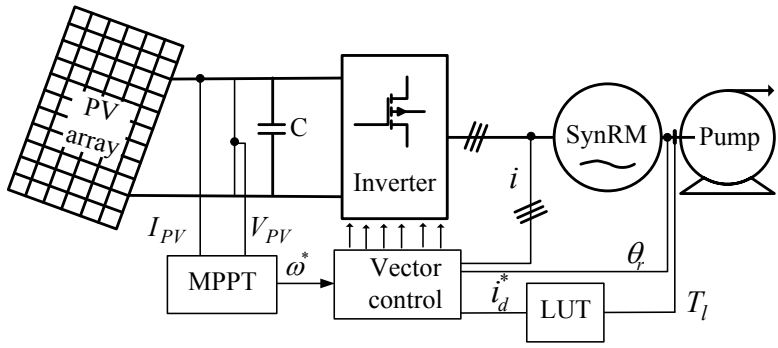

Figure 8.12: The complete block diagram of the proposed system.

The proposed maximum power point tracking algorithm is sketched in Fig. 8.13. This algorithm uses the perturbation and observation strategy. First, the voltage and current of the PV array are measured. Then the output power of the PV array can be calculated. The present value at time instant *m* of the PV power and voltage are compared with the previous values at time instant *m*-1; the time difference between the two instants is one sample time (1e-5 s). Eventually, the reference speed of the system at which the output power of the PV array is maximum can be obtained using the MPPT algorithm shown in Fig. 8.12 and 8.13.

On the other hand, based on the load torque of the pump, the reference current (i_d*) can be obtained from the LUT that is generated by FEM. The reference current (i_d*) controls the SynRM to work at the maximum torque per Ampère.

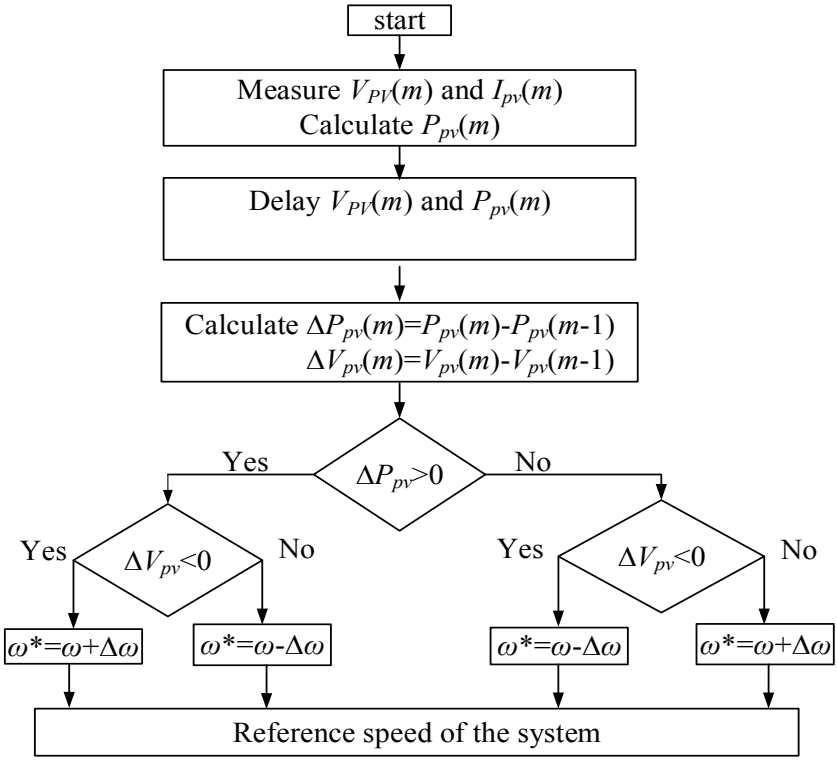

Figure 8.13: The proposed maximum power point tracking algorithm at time instant *m*.

The proposed system shown in Fig. 8.12 is simulated for three different irradiation levels: 200 W/m^2, 600 W/m^2 and 1000 W/m^2. Figure 8.14 reports the reference speed calculated by the MPPT algorithm that maximizes the PV output power at the given conditions (irradiation level and temperature). In addition, in Fig. 8.14, the SynRM speed can be seen as well: it follows accurately the reference speed of the system.

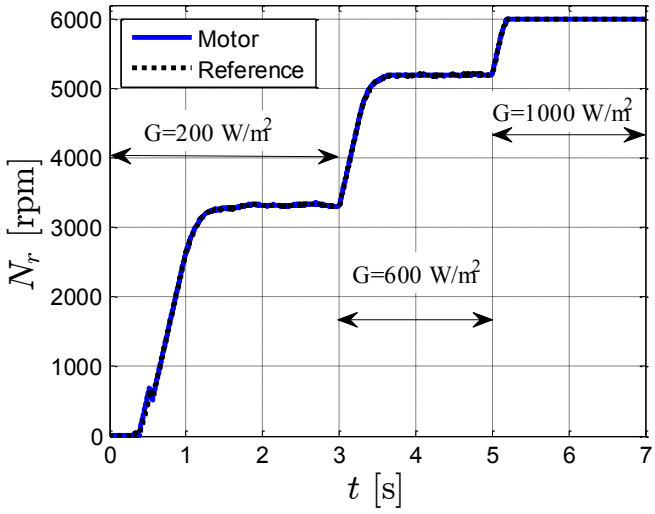

Figure 8.14: Reference and SynRM speeds of the proposed system for three irradiation levels (200 w/m^2, 600 W/m^2 and 1000 W/m^2) and at 25°C.

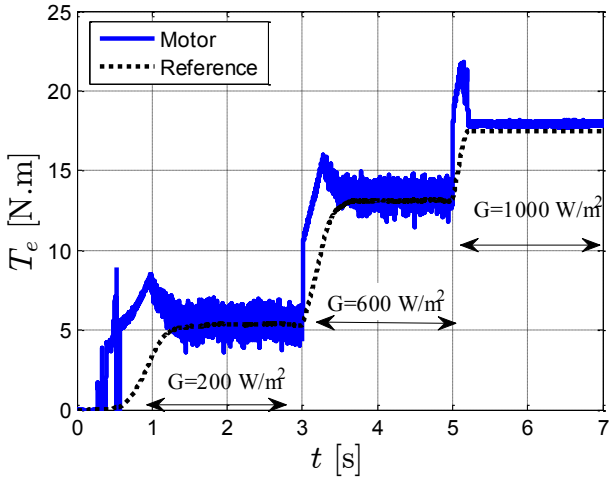

Figure 8.15: Reference and SynRM torques of the proposed system for three irradiation levels (200 w/m^2, 600 W/m^2 and 1000 W/m^2) and at 25°C.

Figure 8.15 shows the reference torque and the motor output torque for different irradiation levels. The reference load torque is the required load torque of the pump that depends on the motor speed as in (8.10).

It is obvious that with increasing the irradiation level, the motor speed increases, hence also the load torque becomes higher. The figure shows that the motor gives the required load torque successfully. The ripples in the motor output torque are due to the PWM of the inverter.

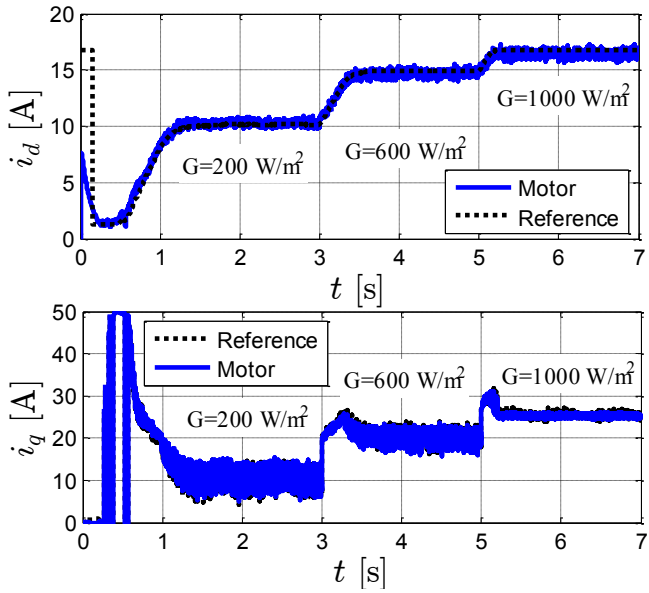

Figure 8.16: *dq*- axis currents of SynRM for three irradiation levels (200 w/m^2, 600 W/m^2 and 1000 W/m^2) and at 25°C.

The *dq*-axis currents of the system are shown in Fig. 8.16. They are obtained according to the scheme in Fig. 8.12. From the irradiated solar power, the required pump torque and speed are known. The reference current i_d* is generated from the lookup table based on the required pump torque to achieve the maximum torque per Ampère of the SynRM (black dotted line in Fig. 8.4, and the "LUT"-block in Fig. 8.12). The reference current i_q* is given by the controller of the speed loop. It is clear in Fig. 8.16 that the *dq*-axis currents of the motor follow accurately the reference values. The three-phase currents of the motor for the three irradiation levels are shown in Fig. 8.17. It is obvious that with increasing the irritation level, the motor speed increases and hence the pump load increases too. This results in an increase in the motor current to achieve the required pump load. A zoom in of the three-phase currents at G=1000 W/m^2 is displayed in Fig. 8.18. At G=1000 W/m^2,

the motor works at the rated speed and produces the rated torque as seen in Figs. 8.14 and 8.15. Consequently, the motor absorbs the rated current (I_m=30 A).

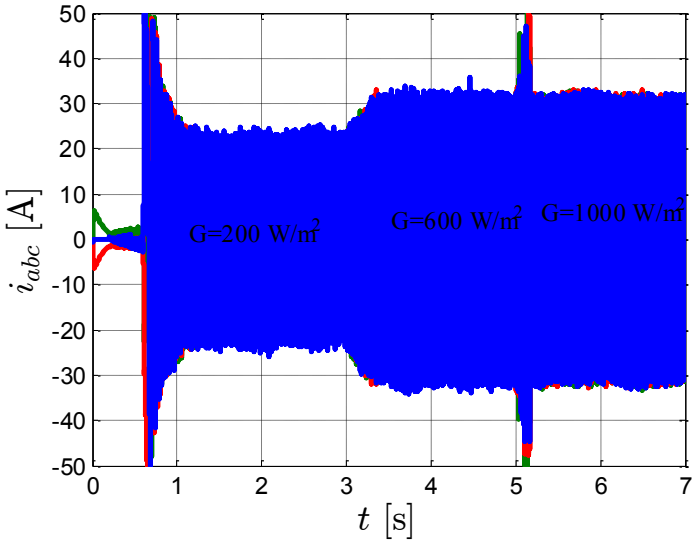

Figure 8.17: Three-phase currents of SynRM for three irradiation levels (200 w/m^2, 600 W/m^2 and 1000 W/m^2) and at 25°C.

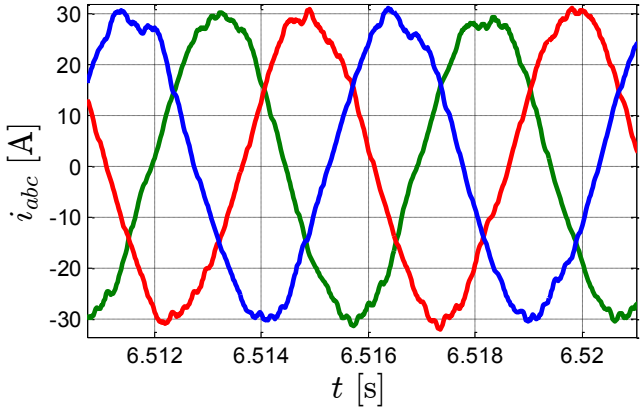

Figure 8.18: Zoom in of three-phase currents of SynRM irradiation level of 1000 W/m^2 at 25°C.

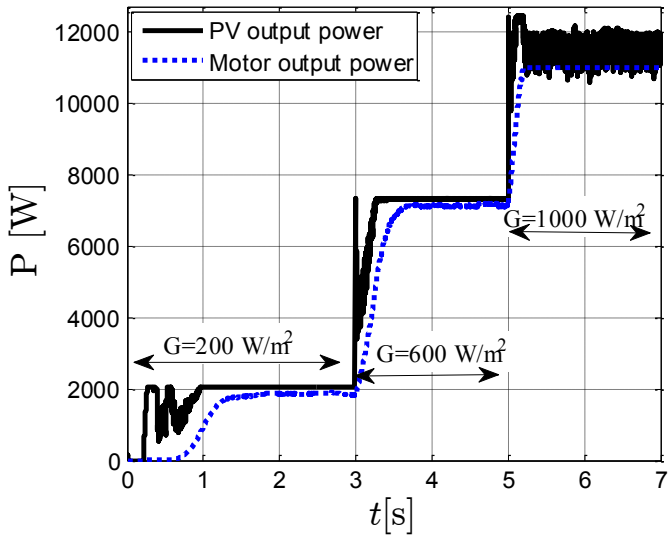

Figure 8.19: PV output power and motor input power at three irradiation levels (200 w/m^2, 600 W/m^2 and 1000 W/m^2) and at 25°C.

The PV and the SynRM output powers are shown in Fig. 8.19 for different irradiation levels at 25°C. It is observed that the PV array works at the maximum available power at the different irradiation levels. This can be seen by comparing the PV output power of Fig. 8.19 with the PV characteristic of Fig. 8.10. Note that the ripples in the PV output power at G=1000 W/m^2 are due to the higher maximum output power of the PV than the maximum power of the motor. In addition, the SynRM works at the maximum power per Ampère for all the different irradiations. This is obvious also when comparing the SynRM output power of Fig. 8.19 at G=1000 w/m^2 with the rated power of the motor in Fig. 8.4. Note that the difference in the power between the PV and the motor in Fig. 8.19 is due to the copper and the friction losses (the friction coefficient is assumed to be 0.0002 kg.m^2/s, similar as in **Chapter 2**).

Figure 8.20 shows the PV maximum output power locus (green dashed line) and the motor maximum input power per Ampère locus coincide for the different irradiation levels. The PV array voltage and current at the maximum power point for different irradiation levels are shown in Fig. 8.21. It is obvious that the voltage and current correspond very well with the maximum power point of Fig. 8.20.

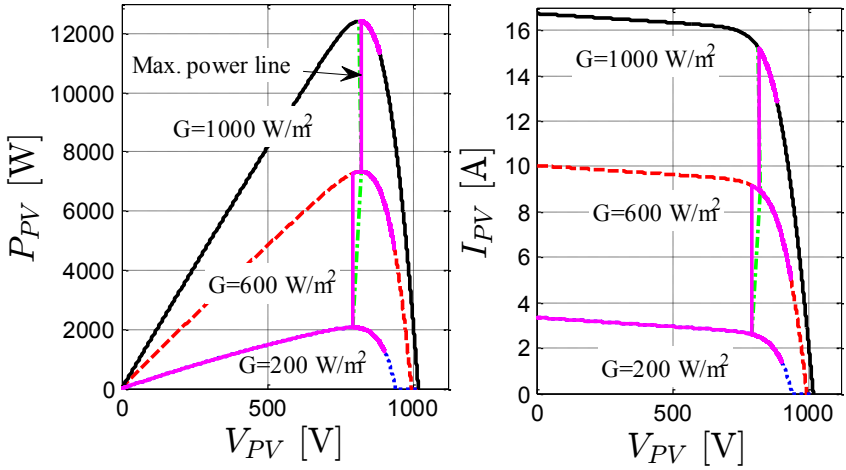

Figure 8.20: The PV array characteristics at different irradiation levels (G=200 W/m^2, 400 W/m^2 and 1000 W/m^2) and T=25°C.

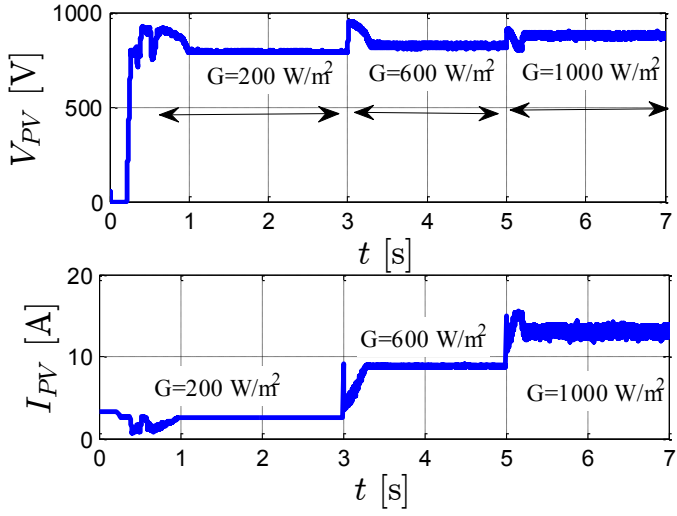

Figure 8.21: Voltage (V_{pv}) and current (I_{pv}) of the PV array for three irradiation levels (200 w/m^2, 600 W/m^2 and 1000 W/m^2) at 25°C.

The pump flow rate is reported in Fig. 8.21. It is clear that the pump flow rate increases with the increase in the SynRM speed. The flow rate amount achieves the required target amount.

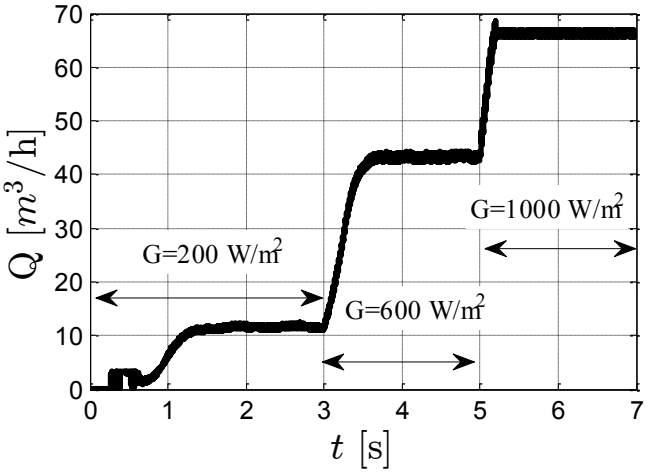

Figure 8.22: The flow rate of the centrifugal pump at three irradiation levels (200 W/m^2, 600 W/m^2 and 1000 W/m^2) and at 25°C.

8.6 Conclusions

This chapter has presented the design and the modelling of a photovoltaic (PV) pumping system utilizing a synchronous reluctance motor (SynRM) and a direct coupling, i.e. a coupling without additional DC-DC converter. The proposed system doesn't have a DC-DC converter, which is often used to maximize the PV output power, nor has it storage (battery). Instead, a simple control algorithm is proposed to control the system in such a way that both the PV output power is maximized and the SynRM works at the maximum torque per Ampère, using a conventional three phase pulse width modulated inverter. The sizing of the components was done based on component models. The optimization of the SynRM is explained in detail, and the optimal control of the system is elaborated. This results in a cheap, reliable and efficient PV pumping system.

Biography

[1] S. S. Chandel, M. Nagaraju Naik, and R. Chandel, "Review of solar photovoltaic water pumping system technology for irrigation and community drinking water supplies," *Renew. Sustain. Energy Rev.*, vol. 49, pp. 1084–1099, Sep. 2015.

[2] V.Ch. Sontake and V. R. Kalamkar, "Solar photovoltaic water pumping system - A comprehensive review," *Renew. Sustain. Energy Rev.*, vol. 59, pp. 1038–1067, Jun. 2016.

[3] M. Nabil, S. M. Allam, and E. M. Rashad, "Modeling and design considerations of a photovoltaic energy source feeding a synchronous reluctance motor suitable for pumping systems," *Ain Shams Eng. J.*, vol. 3, no. 4, pp. 375–382, Dec. 2012.

[4] M. Nabil, S. M. Allam, and E. M. Rashad, "Performance improvement of a photovoltaic pumping system using a synchronous reluctance motor," *Electr. Power Components Syst.*, vol. 41, no. 4, pp. 447–464, Feb. 2013.

[5] E. Mahmoud and H. el Nather, "Renewable energy and sustainable developments in Egypt," *Appl. Energy*, vol. 74, no. 1–2, pp. 141–147, Jan. 2003.

[6] A. A. Hamza and A. Z. Taha, "Performance of submersible PV solar pumping systems under conditions in the Sudan," *Renew. Energy*, vol. 6, no. 5–6, pp. 491–495, Jul. 1995.

[7] A. Hamidat, B. Benyoucef, and T. Hartani, "Small-scale irrigation with photovoltaic water pumping system in Sahara regions," *Renew. Energy*, vol. 28, no. 7, pp. 1081–1096, Jun. 2003.

[8] A. Chaurey, P. M. Sadaphal, and D. Tyaqi, "Experiences with SPV water pumping systems for rural applications in India," *Renew. Energy*, vol. 3, no. 8, pp. 961–964, Nov. 1993.

[9] A. A. Nafeh, "Design and economic analysis of a stand-alone pv system to electrify a remote area household in egypt," *Open Renew. Energy J.*, vol. 2, no. 1, pp. 33–37, Apr. 2009.

[10] E. R. Shouman, E. T. El Shenawy, and M. A. Badr, "Economics analysis of diesel and solar water pumping with case study water pumping for irrigation in Egypt," *Int. J. Appl. Eng. Res. ISSN*,

vol. 11, no. 2, pp. 973–4562, 2016.

[11] S. M. Alghuwainem, "Matching of a DC motor to a photovoltaic generator using a step-up converter with a current-locked loop," *IEEE Trans. Energy Convers.*, vol. 9, no. 1, pp. 192–198, Mar. 1994.

[12] R. Kumar and B. Singh, "BLDC motor driven solar PV array fed water pumping system employing zeta converter," in *2014 IEEE 6th India International Conference on Power Electronics (IICPE)*, 2014, pp. 1–6.

[13] R. Kumar and B. Singh, "BLDC motor-driven solar PV array-fed water pumping system employing zeta converter," *IEEE Trans. Ind. Appl.*, vol. 52, no. 3, pp. 2315–2322, May 2016.

[14] R. Antonello, M. Carraro, Al. Costabeber, F. Tinazzi, and M. Zigliotto, "Energy-efficient autonomous solar water-pumping system for permanent-magnet synchronous motors," *IEEE Trans. Ind. Electron.*, vol. 64, no. 1, pp. 43–51, Jan. 2017.

[15] B. Singh, A. K. Mishra, and R. Kumar, "Solar powered water pumping system employing switched reluctance motor drive," *IEEE Trans. Ind. Appl.*, vol. 52, no. 5, pp. 3949–3957, Sep. 2016.

[16] R. Kumar and B. Singh, "Solar photovoltaic array fed water pump driven by brushless DC motor using Landsman converter," *IET Renew. Power Gener.*, vol. 10, no. 4, pp. 474–484, Apr. 2016.

[17] Z. Yang, F. Shang, I. P. Brown, and M. Krishnamurthy, "Comparative study of interior permanent magnet, induction, and switched reluctance motor drives for EV and HEV applications," *IEEE Trans. Transp. Electrif.*, vol. 1, no. 3, pp. 245–254, Oct. 2015.

[18] M. N. Ibrahim, P. Sergeant, and E. M. Rashad, "Relevance of including saturation and position dependence in the inductances for accurate dynamic modeling and control of SynRMs," *IEEE Trans. Ind. Appl.*, vol. 53, no. 1, pp. 151–160, Jan. 2017.

[19] J. Appelbaum, "Starting and steady-state characteristics of DC motors powered by solar cell generators," *IEEE Trans. Energy Convers.*, vol. EC-1, no. 1, pp. 17–25, Mar. 1986.

[20] H. M. B. Metwally and W. R. Anis, "Dynamic performance of

directly coupled photovoltaic water pumping system using D.C. shunt motor," *Energy Convers. Manag.*, vol. 37, no. 9, pp. 1407–1416, Sep. 1996.

[21] Z. Zinger and A. Braunstein, "Optimum operation of a combined system of a solar cell array and a DC motor," *IEEE Trans. Power Appar. Syst.*, vol. PAS-100, no. 3, pp. 1193–1197, Mar. 1981.

[22] M. M. Saied, "Matching of DC motors to photovoltaic generators for maximum daily gross mechanical energy," *IEEE Trans. Energy Convers.*, vol. 3, no. 3, pp. 465–472, 1988.

[23] W. Z. Fam and M. K. Balachander, "Dynamic performance of a DC shunt motor connected to a photovoltaic array," *IEEE Trans. Energy Convers.*, vol. 3, no. 3, pp. 613–617, 1988.

[24] V. Ch. Mummadi, "Steady-state and dynamic performance analysis of PV supplied DC motors fed from intermediate power converter," *Sol. Energy Mater. Sol. Cells*, vol. 61, no. 4, pp. 365–381, Apr. 2000.

[25] Y. R. Hsiao and B. A. Blevins, "Direct coupling of photovoltaic power source to water pumping system," *Sol. Energy*, vol. 32, no. 4, pp. 489–498, 1984.

[26] S. Singer and J. Appelbaum, "Starting characteristics of direct current motors powered by solar cells," *IEEE Trans. Energy Convers.*, vol. 8, no. 1, pp. 47–53, Mar. 1993.

[27] A. Betka and A. Moussi, "Performance optimization of a photovoltaic induction motor pumping system," *Renew. Energy*, vol. 29, no. 14, pp. 2167–2181, Nov. 2004.

[28] R. Kumar and B. Singh, "Single stage solar PV fed brushless DC motor driven water pump," *IEEE J. Emerg. Sel. Top. Power Electron.*, pp. 1–1, 2017.

[29] P. Packiam, N. K. Jain, and I. P. Singh, "Steady and transient characteristics of a single stage PV water pumping system," *Energy Syst.*, vol. 6, no. 2, pp. 173–199, Jun. 2015.

[30] A. B. Raju, S.Ramesh Kanik, and Rohini Jyoti, "Maximum efficiency operation of a single stage inverter fed induction motor PV water pumping system," in *2008 First International Conference on Emerging Trends in Engineering and Technology*, 2008, pp. 905–910.

[31] A. T. De Almeida, F. J. T. E. Ferreira, and A. Q. Duarte, "Technical and economical considerations on super high-efficiency three phase motors," *IEEE Trans. Ind. Appl.*, vol. 50, no. 2, pp. 1274–1285, Mar. 2014.

[32] A. Varshney and B. Singh, "Performance of SPV array fed pumping system with synchronous reluctance motor drive," in *2016 IEEE 1st International Conference on Power Electronics, Intelligent Control and Energy Systems (ICPEICES)*, 2016, pp. 1–6.

[33] K. Benlarbi, L. Mokrani, and M. S. Nait-Said, "A fuzzy global efficiency optimization of a photovoltaic water pumping system," *Sol. Energy*, vol. 77, no. 2, pp. 203–216, 2004.

[34] M. G. Villalva, J. R. Gazoli, and E. R. Filho, "Comprehensive approach to modeling and simulation of photovoltaic arrays," *IEEE Trans. Power Electron.*, vol. 24, no. 5, pp. 1198–1208, May 2009.

Chapter 9
Conclusions and Future Work

9.1 Conclusions

The PhD focusses on many design aspects of SynRMs and PMaSynRMs, and on a practical application of the SynRM: a PV pumping system. A literature survey shows that a lot of research is published about SynRMs and PMaSynRMs. This PhD studies a number of additional design aspects that are new compared to the state-of-the-art, and that are summarized in the following paragraphs.

The first study is to find out the required level of accuracy of the SynRM model, in order to have a realistic behavior of the waveforms in the simulations of a controlled SynRM drive. Therefore, several state-space models with different accuracy are made, with inductances found from FEM. The drive is the SynRM, supplied by an inverter and controlled via a suitable control algorithm. The relevance of including magnetic saturation and rotor position effects in the mathematical *dq*-axis model of SynRMs is investigated. It leads to three models for the SynRM: 1) an accurate model with inductances that depend on *d*- and *q*-axis current and rotor position; 2) a less accurate model with inductances that only depend on *d*- and *q*-axis current, and 3) an inaccurate model with constant inductances. In addition, the modelling of SynRMs is studied in both open loop and closed loop control, for each of the three models, i.e. considering or neglecting the influence of the magnetic saturation and the rotor position effects. It is shown that including magnetic saturation in the model of a SynRM – as in model

1 and 2 – is mandatory to have an accurate prediction for its performance (output torque, power factor and stable region of operation). Model 1, which includes the dependence on the rotor position, does not add much accuracy compared to model 2. The most simple model 3, which uses constant inductances (L_d and L_q), is not accurate enough and can lead to a large deviation in the prediction of the torque capability compared with the real motor.

In a second study, the influence of geometric flux-barrier parameters on the performance indicators (saliency ratio, output torque and torque ripple) of the SynRM is investigated; more flux-barrier parameters are considered than the common practice in literature. In addition, easy-to-use parametrized equations to select the most crucial parameters of the rotor are proposed. The proposed approach is compared to three existing methods in the literature, and this is done for different numbers of flux-barrier layers i.e. 3, 4 and 5 layers per pole. It is proved that the proposed method is effective in choosing the flux-barrier angles and widths. In addition, it provides a good SynRM in terms of torque ripple and average torque. The resulting design can be used as a start candidate in a further detailed optimization of the machine. Finally, a detailed optimization based on FEM is done to select the optimal flux-barrier parameters. Several flux-barrier parameters (12 in total) are considered in the optimization process. The goal is to obtain an optimal SynRM performance i.e. maximum saliency ratio and hence maximum output torque, and minimum torque ripple. An optimal rotor design is obtained. The mechanical robustness of the optimized rotor is checked for the rated speed of the machine, and is found to be acceptable with sufficient safety margin.

In addition, a comparison of the SynRM performance based on different electrical steel grades is given. Four different steel grades (NO20, M330P-50A, M400-50A and M600-100A) with different loss and thickness are studied. It is observed that the *dq*-axis inductances of the motor are affected by the material properties due to the different permeability. Hence, the SynRM performance varies because it depends mainly on the saliency ratio. It is found that M330P-50A has the highest output power, which is about 8% higher than for M600-100A. Moreover, the electrical steel grade has a great effect on the iron loss and the efficiency of the SynRM. At the rated operating point, the efficiency of the SynRM based on NO20 is about 9% point higher than the efficiency of M600-100A.

Several combined star-delta winding configurations are proposed and compared to the conventional star windings. A simple method to calculate the winding factor of the different winding configurations is proposed. Furthermore, the SynRM performance (torque, power factor, torque ripple and efficiency) using two combined star-delta winding layouts in comparison with a conventional star-connected winding is presented for a prototype machine. It is found that both combined star-delta windings result in approximately the same SynRM performance. This is observed over a wide range of speed and current. Nevertheless, when compared with conventional star windings, the combined star-delta windings correspond to a torque gain of 5.2% under rated conditions. This gain decreases in the overloading range due to core saturation, but it increases up to 8.0% at partial load. In the constant power range (above rated speed), the torque gain increases to approximately 9.5% at 3 times the rated speed. The effect of the winding configuration on the machine power factor and on the core loss is negligible up to 3 times the rated speed and 2 times the rated current. Nevertheless, the machine efficiency for the combined star-delta windings is improved by 0.26% point at rated load, and even more under light load.

Moreover, PMaSynRMs and SynRMs using conventional star and combined star-delta winding connections are compared. For the same copper volume and current, the machine with combined star-delta windings and with ferrite PMs inserted in the rotor – the Sd-PM machine – corresponds to an approximately 22% increase in the output torque at rated current and speed compared to the machine with conventional star windings and with the conventional "magnet-free" reluctance rotor (the S machine). This enhancement is mainly thanks to adding the ferrite PMs in the rotor and the improvement in the winding factor of the combined star-delta winding. In addition, the torque gain increases up to 150% for low currents compared to the machine with the conventional star windings and with the conventional reluctance rotor. Moreover, the efficiency of the machine is increased with inserting PMs in the rotor. The Sd-PM machine has about 1.25% point higher efficiency for half rated speed and about 0.82% point higher efficiency for full rated speed compared with the S machine at rated current. An interesting observation here is that the efficiency of the machine with combined star-delta windings and PM assisted rotor (Sd-PM) increases significantly in partial loads. Furthermore, the power factor of the machines with PMs inserted in the rotor (Sd-PM and S-

PM) is very high for partial load compared to the machines without PMs (Sd and S).

Five prototype SynRMs are manufactured and tested: one reference prototype machine and four optimized machines. These latter four are assembled using two stators – one with conventional star windings and one with combined star-delta windings – and two rotors – one with PMs and one without PMs. The efficiency maps of these prototypes are constructed. The experimental results are used to validate the theoretical analysis.

Finally, a design of a low cost and efficient PV pumping system is proposed, using a SynRM drive. The proposed system doesn't have a DC-DC converter that is often used to maximize the PV output power, nor has it storage (battery). Instead, the system is controlled in such a way that both the PV output power is maximized and the SynRM works at the maximum torque per Ampère, using a conventional three phase pulse width modulated inverter. The efficiency of the employed system is definitely higher than with an induction motor drive. This is because of the high efficiency of the SynRM at part load and at reduced DC voltage.

9.2 Future work

In the future, further research on the shape of the flux-barriers can be done. In this PhD, the research focused only on one barrier shape: a trapezoidal shape. Further research can be focused on the influence of the flux-barrier shape (U, C etc.) on the electromagnetic and mechanical behavior of SynRM.

Another further research activity will be on the flux-weakening region of SynRMs and PMaSynRMs based on the different winding topologies and/or multilayer windings. A trade-off between the machine performance and power electronics switching frequency can be considered to minimize the losses of the whole system. In addition, different steel grades in the stator and rotor can be considered in this research.

A thermal study of the SynRM is very useful to determine the rated power accurately. In this PhD, the stator is taken from an induction

machine, and the same rated power is assumed. However, the optimized SynRM has a better efficiency, especially when using better magnetic material grades (e.g. NO20, see **Chapter 4**), combined star-delta windings (**Chapter 5**), and a rotor with ferrite Permanent Magnets (**Chapter 6**). It is expected that, starting from an induction machine with a given cooling capacity, the rated power of the corresponding SynRM can be increased. A thermal study makes it possible to quantify this increase in rated power.

In contrast to switched reluctance machines (SRMs), synchronous reluctance machines are known to be useful only for rather low mechanical speeds. The reason is the high mechanical stress of the rotor, in particular the "iron bridges" that must be thin for electromagnetic reasons, at high rotational speed. Research can be done to rotor designs that are suitable for high rotational speed, and still guarantee a good efficiency and torque density of the SynRM.

In this PhD, a brief study about PV pumping systems using one prototype SynRM is presented. Further research on PV pumping systems can be done. On the one hand, another prototype SynRM e.g. the one with combined star-delta windings in the stator and PMs inserted in the rotor can be compared with the presented system and/or with the available PV pumping systems in the literature. The total efficiency, total cost and reliability can be considered as the factors of the comparison. On the other hand, a further research can be done on the maximum power point tracking control system.

A last topic is the further research on multiphase SynRMs and PMaSynRMs. A lot of research has been already done on multiphase winding of conventional star connection on SynRMs. In addition, multiphase star-delta windings are investigated intensively, in particular for induction machines. However, the multiphase combined-star delta connections are not studied on SynRMs and PMaSynRMs through the literature. This topic can be a wide area of research for SynRMs and PMaSynRMs. Moreover, other control strategies compared to the conventional field oriented control mentioned in the thesis can be investigated for the different prototypes.

Appendix A
Steady-state analysis of the SynRM

In this section, we show the influence of including and neglecting the magnetic saturation in the inductances of the SynRM model at steady state operation. In addition, the stability limits of the machine are studied as well. In this analysis, the SynRM performance is investigated at the rated voltage and frequency (i.e. 380 V and 200 Hz) in open loop control method. Model 3, with unsaturated L_d and L_q is compared with model 2, where the magnetic saturation is included. Here, the cases of Section 2.8 (**Chapter 2**) are investigated.

A.1 The effect of different *q*-axis inductance (L_q) values

In this case, three different values for L_q= 0.0051 H, 0.0037 H and 0.0032 H at a fixed value for L_d=0.0203 H are considered as unsaturated (constant) SynRMs. The inductances L_d and L_q of the saturated machine have been calculated from the LUT using FEM (Model 2) as mentioned in **Chapter 2**. The selection of the vales of L_d and L_q is explained in **Section 2.8** (**Chapter 2**).

Figures A.1 and A.2 show I_q-L_q and I_d-L_d characteristics for both the saturated and unsaturated machines. It is observed that L_q and L_d (blue solid-lines) of the saturated machine vary nonlinearly with I_d and I_q. The L_q and L_d vary from about 0.0102 H and 0.0190 H, at no load (δ=0°) where i_q=0 A and i_d=12.98 A respectively, to about 0.0025 H and 0.0171 H, at maximum load (δ=45°) with i_q=77 A and i_d=8.73 A respectively. The resistance of the phase winding R_s is very small and hence its effect on the load angle δ can be neglected. The variation of

$L_q(I_d, I_q)$ is stronger than the variation of $L_d(I_d, I_q)$: about 308% and 11% compared to the minimum values respectively. Note that in Fig. A.2, the L_d saturated varies nonmontical as a result of L_d characteristics; the L_d behavior in SynRMs increases with increasing the I_d for low currents and then decreases again.

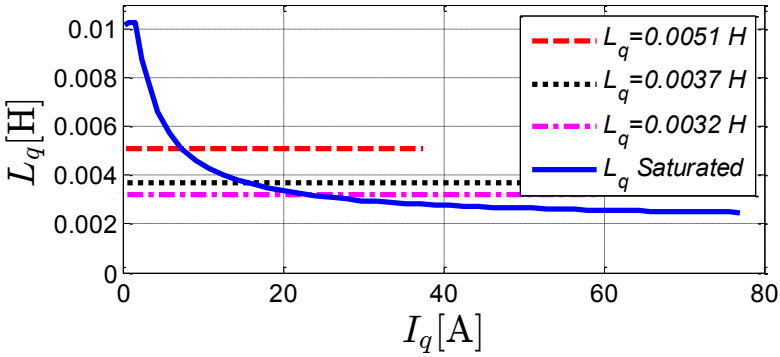

Figure A.1: I_q-L_q characteristics for saturated (blue sold-line) and different unsaturated (red dashed, black dotted and magenta dash dotted-lines) SynRMs.

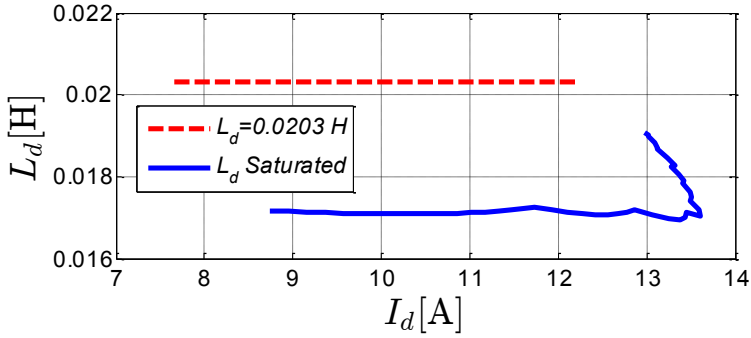

Figure A.2: I_d-L_d characteristics for saturated (blue sold-line) and unsaturated (red dashed-line) SynRMs.

Figures A.3 and A.4 show the variation of I_q and I_d with the load angle δ for both unsaturated (different L_q values at fixed L_d) and saturated machines. It can be seen that I_q increases with decreasing L_q where I_q changes from 34.5 A at the unsaturated case for L_q=0.0051 H (magenta dash dot-line) to about 70.25 A at the saturated case (blue

solid-line) at the maximum load angle (δ=45°). On the other hand, I_d is the same for different L_q, because L_d is fixed for the unsaturated machines. In addition, there is a difference on the I_d as a result of different L_d between the saturated and unsaturated cases. The variation of I_d for different saturated and unsaturated L_d is not much due to the minor change between the saturated and unsaturated L_d (+16%) (see: Fig. A.2).

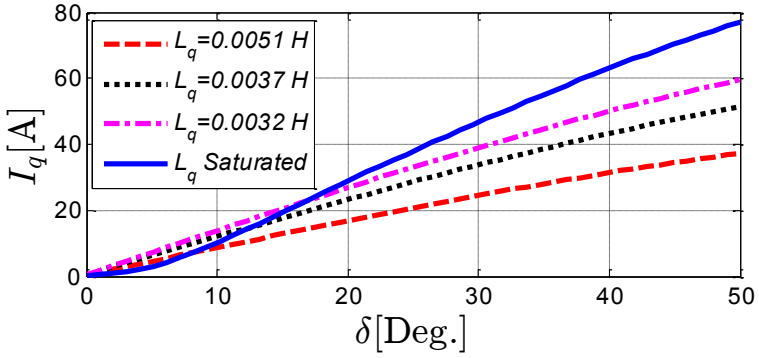

Figure A.3: Variation of I_q with δ for unsaturated q-axis inductances and L_d=0.0203 H, compared to saturated one (blue solid-line).

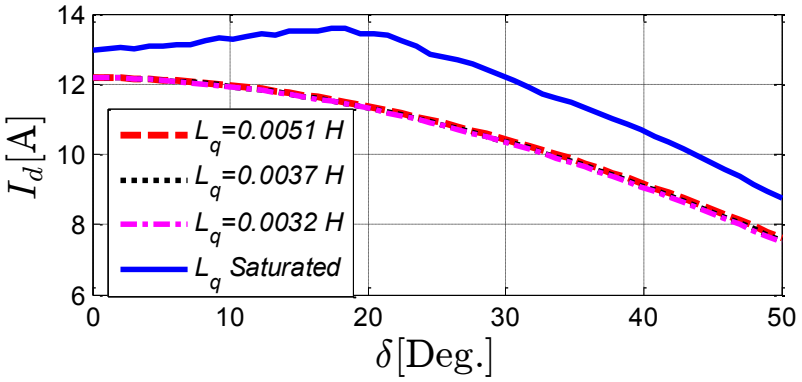

Figure A.4: Variation of I_d with δ for unsaturated q-axis inductances and L_d=0.0203 H, compared to saturated one (blue solid-line).

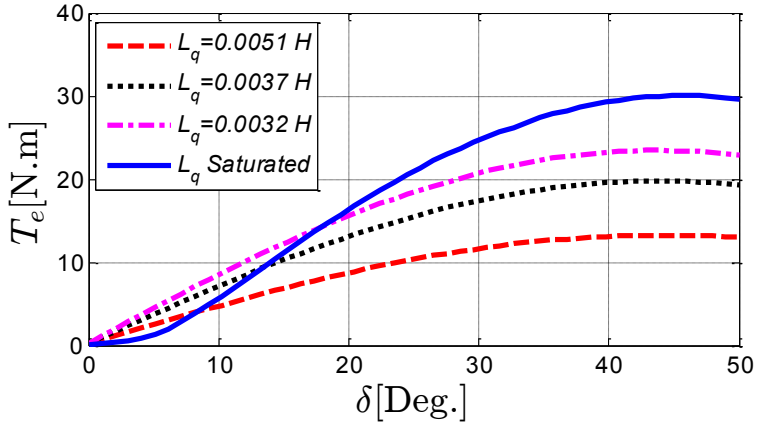

Figure A.5: Variation of T_e with δ for unsaturated q-axis inductances and L_d=0.0203 H, compared to saturated one (blue solid-line).

The variation of the SynRM torque T_e versus the load angle δ for both the unsaturated and saturated cases is depicted in Fig. A.5. Two extreme limiting values for the motor torque stability region can be deduced: from about 13.26 Nm for the unsaturated case at L_q=0.0051 H (magenta dash dotted-line) to about 30 Nm for the saturated case (blue solid-line) at the maximum load angle (δ=45°). This is because the SynRM torque mainly depends on the saliency ratio (L_d/L_q). In addition, there is a huge difference in the stability region of the SynRM between the saturated and the unsaturated cases: about 126% compared to the minimum value at the maximum load angle (δ=45°). The stability region is the region where the load angle is less or equal than 45°. The load angle is a negative value but it is drawn as a positive value in the figures. Figure A.6 indicates the variation of the motor power factor *PF* for different loading angles δ. It is obvious that the difference in the power factor between the machines is huge. The power factor of the SynRM depends on the motor output power which depends on the saliency ratio (L_d/L_q).

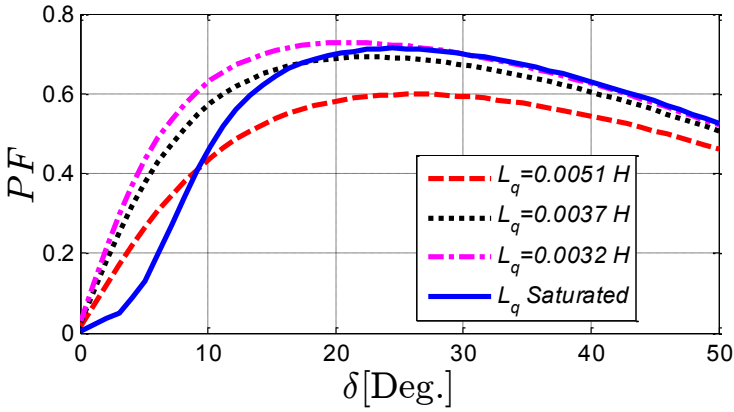

Figure A.6: Variation of PF with δ for unsaturated q-axis inductances and L_d=0.0203 H, compared to saturated one (blue solid-line).

A.2 The effect of different *d*-axis inductance (L_d) values

In this case, three different values for L_d=0.0110 H, 0.0152 H and 0.0203 H at a fixed value for L_q=0.0051 H are treated as the unsaturated machines. As mentioned before, the saturated L_d and L_q have been calculated from the LUTs using FEM as a saturated machine as mentioned in **Chapter 2**. The selection of the vales of L_d and L_q is explained in **Section 2.8** (**Chapter 2**).

Figures A.7 and A.8 show I_d-L_d and I_q-L_q characteristics of the SynRM for both the saturated and unsaturated machines. The variation of the load angle δ with I_d and I_q for different unsaturated d-axis inductances is shown in Figs. A.9 and A.10 respectively. In Fig. A.9, it is noticed that I_d increases with decreasing L_d while I_q is the same for different L_d as seen in Fig. A.10; because L_q is fixed for the unsaturated machines. In addition, there is a huge difference of the I_q between the saturated and unsaturated cases. The saturated machine keeps higher I_q at the rated voltage and speed: about 102% compared to the unsaturated machines at the maximal load angle.

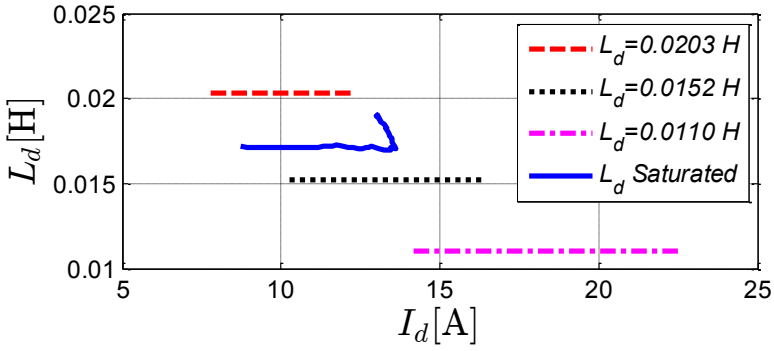

Figure A.7: I_d-L_d characteristics for saturated (blue sold-line) and different unsaturated (red dashed, black dotted and magenta dash dotted-lines) SynRMs.

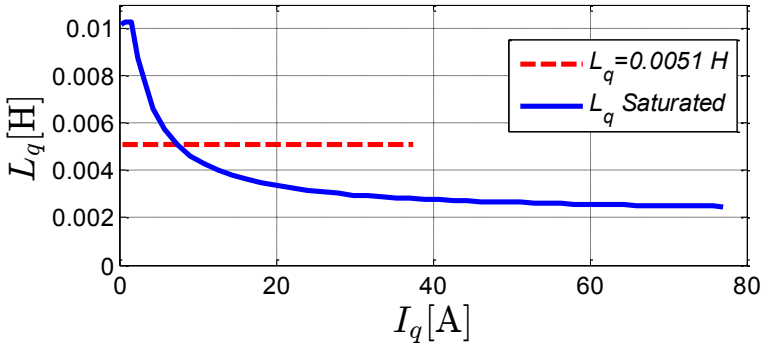

Figure A.8: I_q-L_q characteristics for saturated (blue sold-line) and unsaturated (red dashed-line) SynRMs.

Figure A.11 displays the variation of the motor torque T_e versus the variation of the load angle δ for both saturated and unsaturated machines. The motor stability region can be increased from about 9.5 N.m with the unsaturated machines to about 30 N.m for the saturated case. Moreover, it is obvious that there is a lower effect on the torque capability and the stability region of the SynRM considering different L_d compared with different L_q (Figs. A.1:A.6). This is due to the variation of the saliency ratio (L_d/L_q) as a result of different I_d-L_d and I_q-L_q characteristics.

Fig. A.12 shows the variation of the motor power factor *PF* versus the load angle δ for different unsaturated machines with the saturated

one. Here, it is observed that the saturated SynRM has a higher power factor for higher loads.

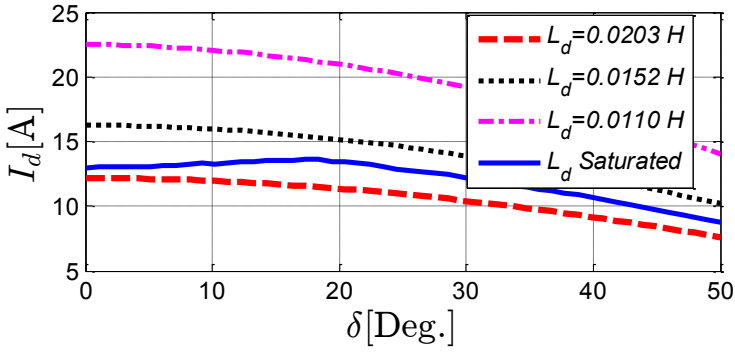

Figure A.9: Variation of I_d with δ for unsaturated (different *d*-axis inductances and L_q=0.0051 H) compared to saturated one (blue solid-line).

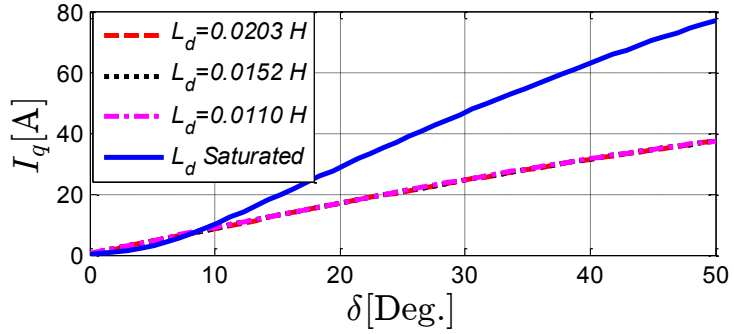

Figure A.10: Variation of I_q with δ for (different *d*-axis inductances and L_q=0.0051 H) compared to saturated one (blue solid-line).

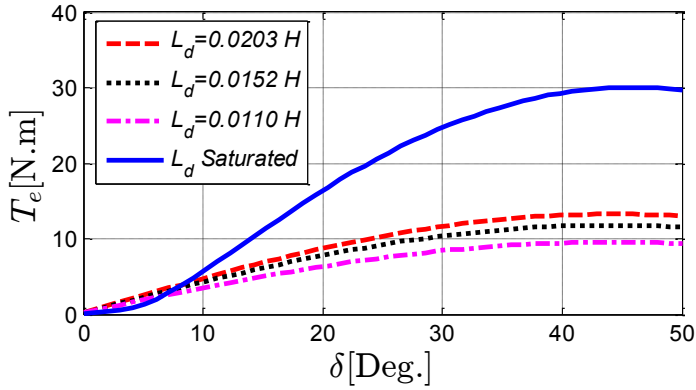

Figure A.11: Variation of δ with T_e for (different d-axis inductances and L_q=0.0051 H) compared to saturated one.

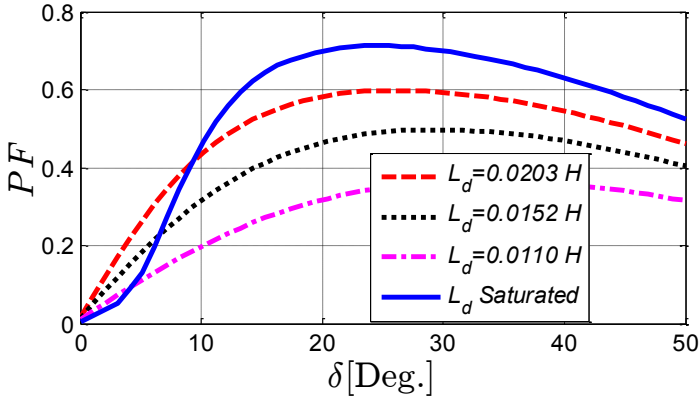

Figure A.12: Variation of δ with PF for (different d-axis inductances and L_q=0.0051 H) compared to saturated one (blue solid-line).